

On the Development and Applications of Automated Searches for Eclipsing Binary Stars

A thesis presented

by

Jonathan Devor

to

The Department of Astronomy

in partial fulfillment of the requirements

for the degree of

Doctor of Philosophy

in the subject of

Astronomy

Harvard University

Cambridge, Massachusetts

13 February 2008

© 2008, by Jonathan Devor

All rights reserved.

On the Development and Applications of Automated Searches for Eclipsing Binary Stars

Abstract

Eclipsing binary star systems provide the most accurate method of measuring both the masses and radii of stars. Moreover, they enable testing tidal synchronization and circularization theories, as well as constraining models of stellar structure and dynamics. With the recent availability of large-scale multi-epoch photometric datasets we were able to study eclipsing binary stars en masse. In this thesis, we analyzed 185,445 light curves from ten TrES fields, and 218,699 light curves from the OGLE II bulge fields. In order to manage such large quantities of data, we developed a pipeline with which we systematically identified eclipsing binaries, solved for their geometric orientations, and then found their components' absolute properties. Following this analysis we assembled catalogs of eclipsing binaries with their models, computed statistical distributions of their properties, and located rare cases for further follow-up, including T-Cyg1-03378, which has unusual eclipse timing variations. Of particular importance are low-mass eclipsing binaries, which are rare yet critical for resolving the ongoing mass-radius discrepancy between theoretical models and observations. To this end, we have discovered over a dozen new low-mass eclipsing binary candidates and spectroscopically confirmed the masses of five of them. One of these confirmed candidates, T-Lyr1-17236, is especially interesting because of its long orbital period. We examined T-Lyr1-17236 in detail and found that it is consistent with the magnetic disruption hypothesis. Both the source code of our pipeline and the complete list of our candidates are freely available.

Contents

Abstract	iii
Acknowledgments	ix
1 Introduction	1
1.1 A Brief Historical Overview of Eclipsing Binary Analysis	4
1.2 A Primer on Parameter Extraction	7
1.3 A Simple Binary Light Curve Generator	11
1.4 Chapter Summaries	15
2 Solutions for 10,000 Eclipsing Binaries in the Bulge Fields of OGLE II Using DEBiL	19
2.1 Introduction	20
2.2 Motivation	22
2.3 Method	26
2.3.1 The First Tier – Finding the Period	27
2.3.2 The Second Tier – DEBiL Fitter	29
2.3.3 Limitations	36
2.4 Tests	38
2.5 Results	39
2.5.1 Population Distributions	44
2.5.2 Extreme Systems	49

2.6	Conclusions	50
2.7	Appendix - Statistical Tests	52
2.7.1	Fitness Score	52
2.7.2	Scatter Score	53
2.7.3	Waviness	54
2.8	Appendix - Density Estimation	55
3	A Novel Approach to Analyzing Eclipsing Binaries in Large Photometric Datasets	63
3.1	Introduction	64
3.2	Express Method for Eclipsing Component Identification (MECI-express)	66
3.3	Method for Eclipsing Component Identification (MECI)	67
3.4	Conclusions	70
4	MECI: A Method for Eclipsing Component Identification	73
4.1	Introduction	74
4.2	Motivation	76
4.2.1	Characterizing the Binary Stellar Population	76
4.2.2	Identifying Low-Mass Main-Sequence EBs	78
4.2.3	EBs as Standard Candles	79
4.3	Method	81
4.3.1	Stage 1: Finding the Orbital Parameters	81
4.3.2	Stage 2: Finding the Absolute Stellar Parameters	83
4.3.3	Assessing the Likelihood of a Binary Pairing	86
4.3.4	Optimization	88
4.4	Testing MECI	89
4.4.1	Observed Systems	90
4.4.2	Simulated Systems	91

4.4.3	Limitations	100
4.5	Conclusions	102
5	Identification, Classifications, and Absolute Properties of 773 Eclipsing Binaries Found in the TrES Survey	103
5.1	Introduction	104
5.2	Method	107
5.3	Results	132
5.3.1	Low-Mass EBs	157
5.3.2	Eccentric EBs	159
5.3.3	Abnormal EBs	168
5.4	Conclusions	171
5.5	Appendix - Rejecting Single-Eclipse EB Models	173
5.6	Appendix - Description of the Catalog Fields	174
6	T-Lyr1-17236: A Long-Period Low-Mass Eclipsing Binary	179
6.1	Introduction	180
6.2	Initial Photometric Observations	182
6.3	Follow-up Photometric Observations	186
6.4	Spectroscopic Observations	190
6.5	Orbital Analysis	195
6.6	Physical Parameters	202
6.7	Chromospheric Activity	207
6.8	Comparison with Models and Conclusions	209
7	Conclusions and Future Work	215
7.1	Low-Mass Candidates with At Least Three RV Measurements	218
7.1.1	T-CrB0-10759	224

7.1.2	T-Cyg1-12664	228
7.1.3	T-Tau0-04859	231
7.1.4	T-Tau0-07388	234
7.2	Low-Mass Candidates with Fewer than Three RV Measurements . . .	237
7.2.1	T-And0-04829	240
7.2.2	T-And0-20382	243
7.2.3	T-CrB0-14232	246
7.2.4	T-Dra0-03021	249
7.2.5	T-Dra0-07116	252
7.3	T-Cas0-07656: A Pulsating Eclipsing Binary	256
7.4	T-Cyg1-03378: A Binary with Large O-C Eclipse Timing Variations .	258
References		266

“The only way to realize the full scientific benefit of our observations is to share the data with our competition.”

–Bohdan Paczyński (1940 - 2007)

For my Family.

Acknowledgments

Alfréd Rényi once said, and many others subsequently paraphrased him, that “a mathematician is a device for turning coffee into theorems.” Indeed, in the hard-nosed professional world we live in, be it academic or otherwise, it is easy to forget all the human elements that must fall into place for one to be able to produce original work.

In the years leading up to graduate school, I was extraordinarily fortunate to be surrounded by friends, family, and teachers who provided me with continuous support and guidance. My parents, who would patiently answer an unending stream of questions from a very persistent child, would later encourage me to follow my heart’s desire, wherever it might lead me. My decision to spend over a half-decade in school to study Astronomy, was never once questioned. However, as so often the case, my path to Astronomy was by no means a straightforward one.

Carl Sagan’s *Cosmos* provided me with the first major push in this direction, and numerous visits to the San Francisco Exploratorium and the Boston Museum of Science cemented my love for the physical sciences at a young age. However, if it was not for an inspirational high school physics teacher named Reuben Tel-Dan, I would probably never have considered further studying physics in college. After serving in the Israeli military, I enrolled at the Hebrew University of Jerusalem, where I would meet a second inspirational teacher—Avishai Dekel. I first met Professor Dekel at a talk he gave during a freshman survey course. In that lecture I was first introduced to the concepts of dark matter, dark energy, and the concordance model of cosmology. He concluded with the current attempts to simulate the Universe at

the grandest scales. I was immediately hooked, and proceeded to work in his group until my graduation. It is due to this experience that I chose to go to graduate school, while most of my friends were pursuing jobs at high tech companies.

My first encounter with Harvard University resulted in a bit of a culture shock due to its immense range of possibilities, both academically and otherwise. In the following years I would make a point of trying as many activities as I could, sometimes to the dismay of my professors, from rowing in crew and Dragon Boat teams, to building robots that play soccer. When it came time to choose a research topic I had a very difficult time settling on a single project. I was naturally drawn to the search for Exoplanets, which was at that time and probably still is, ranked as the sexiest topic in Astronomy. However, following the sage advice of Bob Noyse and Dimitar Sasselov, I decided to start with something easier and more of a “sure thing” – finding eclipsing binary stars. This topic was intended to be a stepping stone, to get my feet wet, however the more I learned about eclipsing binaries, the more interested I got. The two most attractive aspects of this field were the fact that the necessary observational data were already available from the OGLE team and others, and the fact that even a quick perusal through this data reveals strange and curious variable stars that no one had ever studied before.

My first attempts at automatic clustering and classification the OGLE data were seen as “butterfly collecting,” since I had no well-defined scientific goal in mind. However, the idea of automated searches showed great promise, and I was advised to identify specific types of targets with well established scientific motivations. This revised approach led me to the starting point of this thesis, the development of DEBiL. With the completion of the DEBiL pipeline in 2004, I was intently

thinking of how to leverage DEBiL’s capabilities in order to gain access to the absolute physical properties of binaries. The solution to this came to me during the 205th meeting of the American Astronomical Society in San Diego. This idea was implemented to form MECI-express, and later incrementally refined to form MECI. The implementation of MECI was very exciting, since I saw it as my most significant, entirely original, scientific contribution; and indeed much of this thesis centers around it. I would soon realize, however, that to confirm the accuracy of the DEBiL/MECI pipeline I would need to make direct observations, but because the OGLE targets I was studying at the time were so dim, they would be very difficult to follow-up. That predicament would be solved with the arrival of Dave Charbonneau, who brought with him the TrES dataset of comparably bright stars.

Even before Dave’s arrival to the CfA, I heard many impressive stories from senior graduate students who remembered him as a Harvard grad. Indeed, he is one of the most charismatic professors I have ever met, and has a real skill for explaining intricate ideas in a clear and simple way. Needless to say, I was thrilled when he accepted me as an advisee. The following years would be quite transformative. With Dave’s guidance, I learned to switch from a mostly engineering-oriented mindset to one that is more centered on addressing the scientific questions at hand. Thus even though I continue to enjoy building things that work, I learned to construct the machinery around the research needs, and not the other way around. One can see this incremental progression throughout this thesis, and as a consequence, this dissertation will hopefully better benefit the astronomical community.

Chapter 1

Introduction

Astronomical research has traditionally been divided into two interrelated categories: Observational Astronomy, which confirms or refutes hypotheses, constrains models, and finds new empirical relations, and Theoretical Astronomy (or Astrophysics), which constructs and refines physical models, and in so doing provides direction and motivation for further observations. In recent decades, a third category has been emerging: Computational Astronomy. This category is not simply an elaboration of theoretical tools, nor is it just a larger scale approach to observational data reduction, but rather it is a methodology that promises a fundamentally new way of solving astronomical problems. In this thesis, we introduce the reader to the advances that a computational approach can achieve in the field of eclipsing binary analysis, which until recently has been considered by many to be a mature and largely solved area of research.

A binary star system consists of two stars that orbit one another. When the orbital plane of such a binary is nearly parallel to an observer's line of sight (i.e.

with an inclination of $i \simeq 90^\circ$), the binary components will be seen periodically eclipsing one another. If such a system is fortuitously so aligned with respect to Earth, it is termed an eclipsing binary (EB). The probability that an observed binary will be seen eclipsing is on the order of 1 in a 100, however this fraction varies by as much as an order of magnitude in different regions of the sky (Devor 2005; Devor et al. 2008). The observed fraction, however, is biased downwards by the fact that many EBs have very long orbital periods or shallow eclipses, making them difficult to identify. The most direct way to identify EBs is by compiling series of multi-epoch photometric observations of stars, thus monitoring how their brightness changes as a function of time. Such monitoring is often done for large fields on the sky, thereby photometrically capturing many thousands of stars simultaneously. These time series are called light curves (LCs), and since for EBs they typically repeat themselves with a fixed period, they are usually shown folded modulo their respective periods. Such folded LCs are called phased LCs, and by convention, their time-axes are labels in units of their period. Binaries can also be identified through their motion in the sky (astrometric binaries) and through the doppler shift of their spectra (spectroscopic binaries). Both these techniques can be used to identify binaries that are not eclipsing, however, applying them to observe large numbers of stars is technically very challenging. Furthermore, despite recent advances in measuring additional properties of stars that do not eclipse [e.g., Perrin (2003); Zucker & Alexander (2007); Zucker et al. (2007)], EBs remain unique in that they enable the accurate measurement of both the masses and radii of a large number of stars.

EBs are generally divided into three classes according to the shape of their

LC: Algol-type, β Lyrae-type, and W Ursae Majoris-type variables. Algol-type variables (EA) are EBs whose brightness remains almost constant between eclipses. In this type of EB, the eclipse duration is a small fraction of the binary's orbital period, indicating that the binary components are detached from one another. In contrast, β Lyrae-type variables¹ vary their brightness continuously between eclipses, indicating that their components are sufficiently close to bring about significant tidal distortions. In extreme cases, an evolving component will fill its Roche Lobe and then spill over. Such binaries that undergo one-way mass transfer are called semi-detached. However, like Algol-type variables, the eclipses of these variables do not typically have the same depth and shape. Finally, W Ursae Majoris-type variables (EW) are similar to β Lyrae variables in that their brightness varies continuously, however the eclipses of these variables are nearly identical, indicating that the components have similar temperatures. This is often due to the fact that the components are in contact and have a common envelope. In this thesis, we limit ourselves to Algol-type variables, as the other two classes involve far more complex models, and therefore require significantly more computational resources for their study.

Because we are able to accurately measure the absolute properties of the EB components (i.e. their mass, radii, luminosity, etc.), they have become critical tools for the study of star formation, stellar structure, stellar evolution, and stellar dynamics. Furthermore, EBs have been used as standard candles (Stebbing 1910; Paczynski 1997) to both determine the size and structure of the Galaxy, as well

¹The accepted symbol for this class is EB, however we will be using this symbol throughout this thesis as an acronym for “eclipsing binary”.

as to constrain the cosmological distance ladder (Bonanos et al. 2006). Ongoing work will likely help resolve current uncertainties regarding binary formation and parameter distribution (Duquennoy & Mayor 1991), and may also improve our understanding of Type Ia supernovae (Iben & Tutukov 1984). However, despite their great importance, only a small fraction of the observable EBs have been identified, and only a comparably small number of these systems have been analyzed.

In this thesis, we demonstrate how one can greatly increase the speed and efficiency of EB analysis by constructing automated pipelines. Such pipelines will ultimately become necessary to take advantage of the exponentially growing number of photometric LCs being made available (Szalay & Gray 2001). We hope to show here that not only can this be achieved without excessive human effort and computational resources, but also that the derived data contain a wealth of scientifically interesting information, which can and should be used to solve open questions in astronomy and to facilitate novel insights.

1.1 A Brief Historical Overview of Eclipsing

Binary Analysis

The first person to record an eclipse of a binary was Geminiano Montanari, who noted a minimum in the brightness of Algol (β Persei) on November 8, 1670, however, the variability of Algol is likely to have been noticed far earlier than that².

²For a more comprehensive survey of the history of binary star observations, see Aitken (1964) and Kopal (1990).

Nevertheless, it was not until 1783 when the British amateur astronomer John Goodricke first noticed that Algol’s minima were periodic and suggested that Algol was being eclipsed by a large opaque body. The Royal Society of London found this report to be of such importance that they awarded Goodricke their highest award, the Copley Medal. However, it would take over a century before the first systematic efforts to quantify the photometric brightness of variable stars were made, first by eye and later using photosensitive devices, which allowed significant progress in modeling such variable stars. One of the most notable successes during this period was that of Stebbing (1910), who used a Selenium detector to discover Algol’s secondary eclipse, thereby confirming that it was an EB whose secondary component was simply a dimmer star. Soon after, Henry Norris Russell developed more generalized analytical tools for modeling such EBs (Russell 1912a,b). Russell, together with his student Harlow Shapley, then built upon this work to include the effects of stellar limb darkening (Russell & Shapley 1912a,b). During the decades that followed, an increasing number of theoreticians continued this work and constructed models that include star spots and surface inhomogeneities, stellar non-sphericity due to tidal distortions, gravity darkening, mutual reflections, gravitational perturbation by additional stellar components, relativistic effects, and others. Accounting for these effects required increasingly sophisticated mathematical techniques, as well as tedious numerical calculation and the construction of many lookup tables. These efforts culminated in the definitive work done by the Czech-born astronomer Zdeněk Kopal, beginning in the 1930s and continuing throughout the following 60 years [see e.g., Kopal (1959)].

Soon after the arrival of the first programmable computers, researchers began

writing codes that generate EB LCs, as well as routines that fit the model parameters so that the generated LC will match the observational data (see §1.2). With the growing availability and speed of computers, research efforts slowly shifted from idealized models that can be calculated using only paper-and-pencil arithmetic, to more complex models that require iterative numerical computations. The first widely accepted code of this kind was WD, originally developed by Wilson & Devinney (1971), and named for its authors. This code has been incrementally improved and built upon numerous times [e.g., Wilson (1994); Prša & Zwitter (2005)] and is generally considered the most comprehensive EB modeling code available today. Shortly thereafter, based on the Nelson & Davis (1972) model, the EBOP (Eclipsing Binary Orbit Program) code was released (Etzel 1981; Popper & Etzel 1981). EBOP has also been continuously improved, and now contains elaborate methods for parameter uncertainty estimation (Southworth et al. 2004a,b, 2005).

Today, much of the computational effort has been redirected from creating ever more comprehensive binary models that attempt to include every possible phenomenon to more simplified, faster codes that are more robust and can reliably analyze large datasets of LCs with minimal human intervention. Wyithe & Wilson (2001, 2002) produced the first such code based on WD. Soon afterwards, Tamuz et al. (2006) repeated this effort, building upon the EBOP code and designated the end product EBAS (Eclipsing Binary Automated Solver). Included among these is the DEBiL (Detached Eclipsing Binary Light curve) fitter code (Devor 2004, 2005). DEBiL was the starting point of this thesis, and was developed from the ground up to be simpler and more robust than any of the previous codes, thus enabling it to systematically analyze the largest LC datasets available, with

essentially no need for human intervention at all. In the upcoming chapters of this thesis we will describe DEBiL, as well as how it can be used to extract scientifically interesting information out of the vast photometric datasets available today.

1.2 A Primer on Parameter Extraction

It is important to underline the difference between the analytic parameter extraction and the numerical/iterative methodology that superseded it. The analytic approach attempts to measure specific geometric features of the LC, such as primary and secondary eclipse depths and durations, ingress and egress slopes, and times of the center of the eclipses, and uses these results to directly estimate the physical attributes of the binary system. In contrast, numerical methods use analytic extractions as an initial parameter guess, but then perturb these parameters through many iterations, generating and comparing each LC with the observed data. Though the LC generators are the most conspicuous part of these codes and are often used as benchmarks, the success of the parameter fitting code may in fact be more dependent on having a reliable optimization algorithm. These optimization algorithms direct the parameter perturbations based on previous results, and strive to converge the model LC to match the observations.

In order to run an optimization algorithm, one must first define an optimization statistic that describes, in a single real value, how well the model LC fits the observations. Thus, given an observed LC, this statistic simply becomes a function of the model parameters. It is convenient to visualize this statistic as a contour plot over the parameter space, where by convention, a lower value indicates a better

model fit. By far the most accepted statistic for this purpose is the χ^2 statistic, which is defined as:

$$\chi^2 = \sum_i (x_{model,i} - x_{obs,i})^2 / \sigma_{obs,i}^2 , \quad (1.1)$$

where x_{obs} indicates the value of observations made, σ_{obs} indicates their respective uncertainties, and x_{model} indicates the model's predicted values during the time of the observations. However, many other statistics have been suggested, including the ‘scatter score’ (Devor 2005), which is based upon the correlation between neighboring residuals, and the ‘alarm statistic’ described by Tamuz et al. (2006), which is based upon the distribution of positive and negative residual runs.

The choice of optimization algorithms is, however, far more complex than the choice of statistic. This is because optimization algorithms have subtle underlying behaviors that might make them successful at solving one problem, but perform poorly with another. Optimization algorithms generally fall into one of three categories: (1) Steepest Descent algorithms [e.g., Nelder (1965); Press et al. (1992)], also known as “greedy” optimization algorithms, which perturb the model in the way that will bring about the maximum improvement at each iteration. These algorithms generally converge to a solution very quickly, however they will often settle in a local minimum instead of the global minimum. This is especially troublesome since highly non-linear, high dimension parameter spaces such as these, have a large, if not infinite, number of local minima. Therefore, Steepest Descent algorithms are highly sensitive to the initial guess and require very close supervision by an expert user to make sure that they converge to a physically realistic result. We note that, in

principle, due to observational noise, instrumental systematics, and imperfections in the model, the global minimum may not exactly point to the true physical solution. However, with the absence of any additional information, the global minimum is the point that is most likely to be the true solution. (2) Genetic algorithms (Holland 1975) are inspired by biological evolution through natural selection. They attempt to reduce the sensitivity of the initial parameter choice by initiating many searches in parallel from randomized starting points. Searches that are in an unpromising region of the parameter space (i.e. represent poor model fits) are rapidly terminated, whereas those in more promising regions are allowed to multiply. The progeny are usually created by averaging a number of successful parameter space points, and adding small random variances (mutations) that place them in new locations. Genetic algorithms have the advantage of being easily parallelizable and therefore well suited for multi-CPU computers, however despite a number of attempts to introduce them [e.g., Charbonneau (1995); Metcalfe (1999)] they have not yet been widely adopted by the astronomical community. (3) Steepest descent with Simulated Annealing (Kirkpatrick et al. 1983; Press et al. 1992) includes a critical improvement over the earlier described Steepest Descent algorithm, in that with varying probabilities, it makes “leaps of faith” in directions that may initially worsen the model fit, but enable searching regions of the parameter space that would otherwise be cordoned off. Such “leaps of faith” are usually performed liberally in early iterations, and become increasingly conservative in later iterations, thus becoming more like the simple Steepest Descent algorithms. These “leaps of faith” have the effect of smoothing small scale bumps in the contours of the parameter space. At early iterations the search is guided into large-scale depressions, and only

later is influenced by the smaller-scale divots at the bottom of the depression. In this thesis, we adopted this third approach, and implemented it with an extremely fast and simple LC generator (see §1.3) that is built directly into the optimization code, so as to achieve maximum efficiency. The optimization algorithm can thus afford to scour many regions of the parameter space in a large number of iterations (up to 10^4), while requiring only modest computational resources.

Finally, once the algorithm converges and produces a model that fits the observed LC, one must estimate the resulting parameter uncertainties. Traditional analytic methods, such as analysis of variance (ANOVA), estimate the uncertainty from the local curvature or width of the minimum. However, such formal uncertainties will almost always underestimate the parameter errors, sometimes by several orders of magnitude, since as mentioned earlier, the rough small-scale terrain around the minimum will usually have far steeper slopes than the large-scale structure of the parameter space. To remedy this problem, the formal uncertainty is often multiplied by an empirical “fudge factor”, however, a far more rigorous solution is to repeat the fit many times using Bootstrapping or Monte Carlo simulations (Press et al. 1992; Southworth et al. 2005) and then assess the distribution of the resulting solutions. Bootstrapping repeats the fitting procedure with randomized subsets (i.e. resampling) of the observational data, whereas Monte Carlo randomizes the initial guesses and parameter perturbations. These methods have been shown to return far more robust estimations of the uncertainties and can indicate correlations and degeneracies between the parameters. Furthermore, unlike most analytic methods, these randomized estimators do not assume that the errors have normal distributions (i.e. white noise). While Bootstrapping methods are generally simpler to implement,

they have a tendency to generate overly optimistic uncertainty estimates, and thus have fallen out of favor, being replaced by Monte Carlo methods. In this thesis, we use an empirical multiplier to determine the parameter uncertainties at the initial pipeline phase, when modeling very large numbers of EBs. Then, once a smaller and more manageable group of systems has been selected for follow-up, we refine the uncertainty estimates using Monte Carlo simulations.

1.3 A Simple Binary Light Curve Generator

Over the past century EB models and LC generation codes have become increasingly sophisticated and complex (see §1.1). In this thesis, however, we chose to adopt an extremely simple model, which can be rapidly calculated, and optimized over many iterations without requiring large computational resources (see §1.2). This approach is the basis of the Detached Eclipsing Binary Light curve (DEBiL) fitter code, whose implementation is described in detail in the first chapter of this thesis. The model we use consists of two limb darkened spherical stars orbiting in a Newtonian orbit and thus describes a perfectly detached binary. Obviously, a perfectly detached system cannot exist, since all binary components will produce some small amount of tidal distortion on their sibling component. However, in photometric surveys with durations of more than a few months, such as the ones used in this thesis, we find that the majority of the EB LCs can be successfully fit with the DEBiL model. The non-detached systems, which either have very short-periods (typically $\lesssim 1$ day) or contain evolved components, are identified, and then either removed from the pipeline or are tagged as systems with unreliable parameters.

Since it is a central component of this thesis, we provide here a first-principle derivation of the underlying DEBiL equations. We begin with the equation of motion of a Newtonian 2-body system (Kepler's equation) on a Cartesian plane:

$$x = \cos E - e \quad (1.2)$$

$$y = (1 - e^2)^{1/2} \sin E , \quad (1.3)$$

where E is the eccentric anomaly, and e is the binary's eccentricity. The origin marks the system's center of mass (i.e. the focus of the ellipse), and the unit distance is defined as the sum of the binary components' semi-major axes (a). We then calculate the system's eccentric anomaly at any given time (t) using:

$$E - e \sin E = 2\pi (t - t_0) / P , \quad (1.4)$$

where t_0 is the epoch of periastron, and P is the system's orbital period. Though the value of the eccentric anomaly cannot be calculated directly, it can be estimated numerically to a sufficient degree of precision in only a few iterations. Next, we rotate the coordinate system by the argument of perihelion (ω):

$$x' = x \cos \omega - y \sin \omega \quad (1.5)$$

$$y' = x \sin \omega + y \cos \omega , \quad (1.6)$$

and finally tilt the plane by a given inclination angle (i):

$$x'' = x' \quad (1.7)$$

$$y'' = y' \cos i . \quad (1.8)$$

After modest algebraic manipulations, we then arrive at a formula describing the projected distance (D) between the stellar components' centers:

$$\begin{aligned} D^2 &= (x'')^2 + (y'')^2 = \\ &= (1 - e \cos E)^2 - \left[(\cos E - e) \sin \omega + (1 - e^2)^{1/2} \sin E \cos \omega \right]^2 \sin^2 i . \end{aligned} \quad (1.9)$$

We use this projected distance to calculate the unit area flux received from the eclipsed (back) component. For this to be done accurately, we must know the limb darkening function of the binary stellar components. We adopted the quadratic law approximation (Claret 2003) as it allows for faster computation:

$$I(\cos \theta) = I_0 \left[1 - \tilde{a}(1 - \cos \theta) - \tilde{b}(1 - \cos \theta)^2 \right] , \quad (1.10)$$

where θ is the angle between the line of sight and the emergent flux, I_0 is the flux at the center of the stellar disk, and \tilde{a} , \tilde{b} are the quadratic law coefficients of the given star. We next observe the geometry of the stellar disks during eclipse. All the points at a radius of r will emit a uniform flux per unit area of:

$$I_{bk}(r) = I \left(\sqrt{1 - (r/r_{bk})^2} \right) , \quad (1.11)$$

where r_{bk} is the radius of the eclipsed (back) star. Furthermore, the exposed (i.e. non-eclipsed) points at a radius of r form an angle equal to:

$$\alpha(r) = 2 \arccos \left[\frac{r_{fr}^2 - D^2 - r^2}{2Dr} \right] , \quad (1.12)$$

where r_{fr} is the radius of the eclipsing (front) star. We remind the readers that our unit distance was defined earlier as the binary's semi-major axis (a), therefore all the radii parameters indicated here are in fact fractional radii. Finally, we are able to integrate the flux emitted from the exposed portion of the eclipsed stellar disk. However, the binary may be in one of six orientations (see Figures 1.1 and 1.2), where each orientation will result in a slightly different integration expression:

$$(a) \quad F_{bk} = 2\pi \int_0^{r_{bk}} r I_{bk}(r) dr \quad (1.13)$$

$$(b) \quad F_{bk} = 2\pi \int_0^{D-r_{fr}} r I_{bk}(r) dr + \int_{D-r_{fr}}^{r_{bk}} r I_{bk}(r) \alpha(r) dr \quad (1.14)$$

$$(c) \quad F_{bk} = \int_{r_{fr}-D}^{r_{bk}} r I_{bk}(r) \alpha(r) dr \quad (1.15)$$

$$(d) \quad F_{bk} = 0 \quad (1.16)$$

$$(e) \quad F_{bk} = 2\pi \int_0^{D-r_{fr}} r I_{bk}(r) dr + \int_{D-r_{fr}}^{D+r_{fr}} r I_{bk}(r) \alpha(r) dr + 2\pi \int_{D+r_{fr}}^{r_{bk}} r I_{bk}(r) dr \quad (1.17)$$

$$(f) \quad F_{bk} = \int_{r_{fr}-D}^{r_{fr}+D} r I_{bk}(r) \alpha(r) dr + 2\pi \int_{D+r_{fr}}^{r_{bk}} r I_{bk}(r) dr . \quad (1.18)$$

Because we chose to use a quadratic limb darkening law, the integrals not involving $\alpha(r)$ can be solved analytically. The remaining integrals are be solved numerically, however this typically requires only a few iterations, since their associated functions are comparably smooth. We note that Mandel & Agol (2002)

solved these integrals using complete elliptical integrals of the third kind, however the added complexity of this approach is only justified when one must generate LCs with very high precision. Finally, we integrate the flux of the eclipsing star (F_{fr}) and sum the results to form the total expected flux from the entire binary systems (F_{binary}):

$$I_{fr}(r) = I \left(\sqrt{1 - (r/r_{fr})^2} \right) \quad (1.19)$$

$$F_{fr} = 2\pi \int_0^{r_{fr}} r I_{fr}(r) dr \quad (1.20)$$

$$F_{binary} = F_{fr} + F_{bk} . \quad (1.21)$$

Note that the values of both F_{fr} and case (a) of F_{bk} need only be evaluated once. These parameters will then swap, as each component assumes the role of the eclipsing star and then the eclipsed star, in the course of each orbital rotation.

1.4 Chapter Summaries

This thesis contains seven chapters. These chapters are chronological, closely following the actual development of the pipeline, so that each chapter builds upon the results of the previous ones. The first chapter is this introduction, which attempts to provide the reader with both the historical and computational context that lead to the research done in this thesis. **Chapter 2** describes the Detached Eclipsing Binary Light-curve (DEBiL) fitter and how it can be used. DEBiL was developed from the ground up with the intention of robustly processing large datasets of noisy LCs, which contain both EB and non-EB systems. We demonstrate how

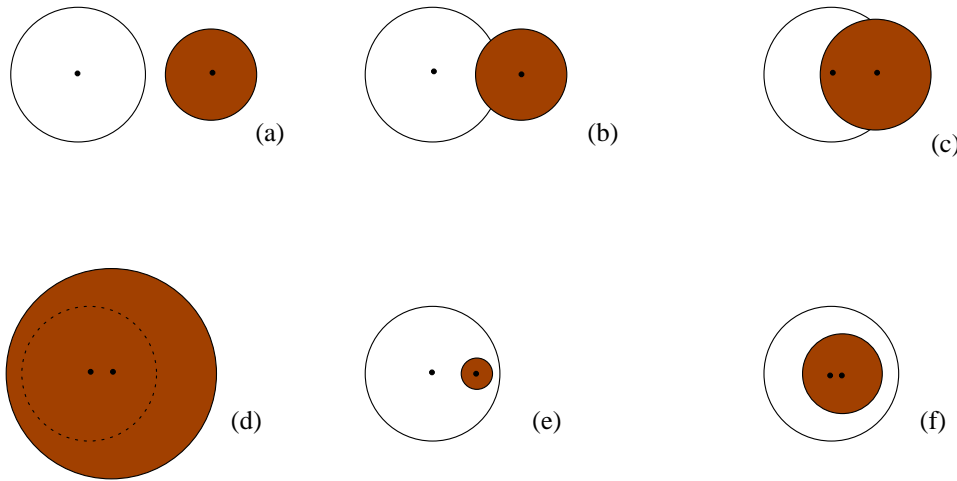


Fig. 1.1.— The six classes of geometric alinement of the binary components' disks: (a) no intersection, (b) partial intersection, where the front component is not over the back component's center, (c) partial intersection, where the front component is over the back component's center, (d) the back component is completely eclipsed by front component, (e) the front component is entirely within the disk of the back component, but it is not over the back component's center, and (f) the front component is entirely within the disk of the back component, and it covers the back component's center.

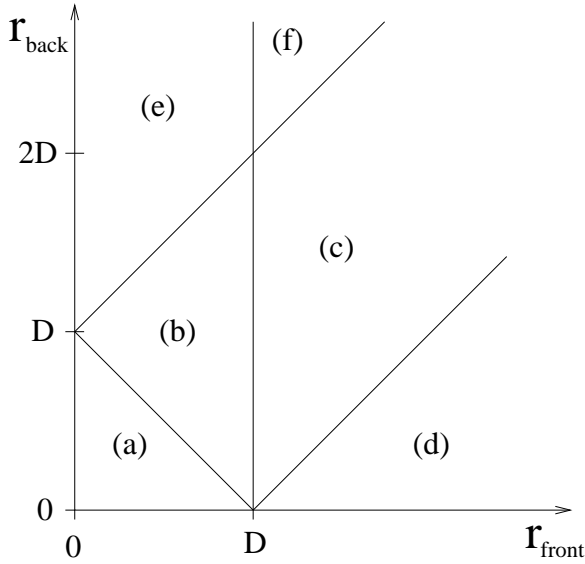


Fig. 1.2.— This chart classifies which alignment class (see Figure 1.1) a binary would belong to at some moment, given the radii of its components ($r_{fr,bk}$) and the distance between its components' centers (D). This classification proves that there are no additional alignment classes.

DEBiL successfully reproduces the model parameters of both previously published and simulated LCs. We then proceed to use DEBiL to process over 10^4 OGLE II LCs, thus creating the largest database of EB solutions to date. In **Chapter 3** we sketch our first efforts at building upon DEBiL in a fundamentally novel way, by incorporating our theoretical understanding of stellar structure and evolution. We thus constrain the models to physically realistic stars, and by doing so greatly reduce the parameter space that needs to be searched. Furthermore, abnormal systems, such as binaries that underwent mass transfer, can be identified by their poor model fits. We describe two competing approaches to the implementation of our mass determination algorithm. One is based on isochrone tables [we used Baraffe et al. (1998); Yi et al. (2001)] and is designated the Method for Eclipsing Component Identification (MECI). The other approach is based on the empirical properties of stellar spectral classes [we used Cox (2000)] and is far simpler and faster but more crude than MECI, thus we call it MECI-express³. **Chapter 4** describes our further development and testing of MECI. We verify that MECI can indeed be used to reliably determine the masses of both binary components using only photometric data, and thus can be a powerful tool in analyzing large LC datasets. We then use it to identify rare and interesting systems for follow-up. In **Chapter 5** we develop a pipeline for rapid EB LC analysis, which incorporates both DEBiL and MECI. We then use this pipeline to analyze all the LCs within 10 fields of the TrES survey, thus identifying 773 EBs and determining the absolute properties of most of them. In this single effort, we were able to significantly increase the number of EBs

³This approach was developed first but was later given this name to make clear its standing in relation to MECI.

with known absolute properties, perhaps doubling their number. Furthermore, the fact that these systems were discovered and analyzed systematically, enables us to make meaningful statistical inferences regarding the distribution of stellar properties and their evolution. We then categorized these systems, and point out groups of interesting candidates: eccentric systems, low-mass systems, and abnormal systems. In **Chapter 6** we chose one particularly promising long-period low-mass candidate, T-Lyr1-17236 and further analyzed the system using additional photometric and spectroscopic observations. These observations confirm the MECI results, making this system the longest period confirmed low-mass EB currently known, by a factor of three. As such, this system is a valuable test case for the magnetic disruption hypothesis (Ribas 2006; Torres et al. 2006), which is used to explain the disparity between theoretical and observational mass-radius relations for stars at the bottom of the main-sequence. Finally, in **Chapter 7** we present preliminary work on nine additional low-mass EB candidates. Unfortunately, we do not have sufficient observations to accurately determine all their absolute properties, however, in many cases we were able to provide strong constraints on their component masses. Furthermore, we present two EBs with interesting additional properties. One has large O-C eclipse timing variations, and the other exhibits pulsations with a period of 1.9 hours. We would like these targets to be available to the community, so that with additional observations, their properties can become better determined, and thus their physics will be better understood.

Chapter 2

Solutions for 10,000 Eclipsing Binaries in the Bulge Fields of OGLE II Using DEBiL

J. Devor 2005, *The Astrophysical Journal*, **628**, 411–425

Abstract

We have developed a fully-automated pipeline for systematically identifying and analyzing eclipsing binaries within large datasets of light curves. The pipeline is made up of multiple tiers that subject the light curves to increasing levels of scrutiny. After each tier, light curves that did not conform to a given criteria were filtered out of the pipeline, reducing the load on the following, more computationally intensive tiers. As a central component of the pipeline, we created the fully automated

Detached Eclipsing Binary Light curve fitter (DEBiL), which rapidly fits large numbers of light curves to a simple model. Using the results of DEBiL, light curves of interest can be flagged for follow-up analysis. As a test case, we analyzed the 218,699 light curves within the bulge fields of the OGLE II survey and produced 10,862 model fits¹. We point out a small number of extreme examples as well as unexpected structure found in several of the population distributions. We expect this approach to become increasingly important as light curve datasets continue growing in both size and number.

2.1 Introduction

Light curves of eclipsing binary star systems provide the only known direct method for measuring the radii of stars without having to resolve their stellar disk. These measurements are needed for better constraining stellar models. This is especially important for such cases as low-mass dwarfs, giants, pre-main-sequence stars, and stars with non-solar compositions, for which we currently have a remarkably small number of well-studied examples. Other important benefits of locating binary systems include more accurate calibration of the local distance ladder (Paczynski 1997; Kaluzny et al. 1998), constraining the low-mass IMF, and discovering new extrasolar planets². In order to obtain measurements of the stars' radii and masses,

¹The list of OGLE II bulge fields model solutions, as well as the latest version of the DEBiL source code are available online at: <http://cfa-www.harvard.edu/~jdevor/DEBiL.html>

²Although there are additional complications, extrasolar planets can be seen as the limiting case where one of the binary components has zero brightness.

one needs to incorporate both the light curve (photometric observations) and radial velocities (spectroscopic observations) of the system. Since making large-scale spectroscopic surveys is significantly more difficult than making photometric surveys, it is far more efficient to begin with a photometric survey and later follow-up with spectroscopic observation only on systems of interest.

During the past decade, there have been numerous light curve surveys [e.g., OGLE: Udalski et al. (1994); EROS: Beaulieu et al. (1995); DUO: Alard & Guibert (1997); MACHO: Alcock et al. (1998)] that take advantage of advances in photometric analysis, such as difference image analysis (Crotts 1992; Phillips & Davis 1995; Alard & Lupton 1998). The original goal of many of these surveys was not to search for eclipsing binaries, but rather to search for gravitational microlensing events (Paczynski 1986). Fortunately, the data derived from these surveys are ideal for eclipsing binary searches as well. More recently, there have also been mounting efforts to create automated light curve surveys [e.g., ROTSE: Akerlof et al. (2000); HAT: Bakos et al. (2004) ; TrES: Alonso et al. (2004)] using small robotic telescopes for extrasolar planet searches. The upcoming large synoptic surveys [e.g., Pan-STARRS: Kaiser et al. (2002); LSST: Tyson (2002)], spurred by the decadal survey of the National Academy of Sciences, are expected to dwarf all the surveys that precede them. Put together, these surveys provide an exponentially growing quantity of photometric data (Szalay & Gray 2001), with a growing fraction becoming publicly available.

2.2 Motivation

For over 30 years many codes have been developed with the aim of fitting increasingly complex models to eclipsing binary light curves [e.g., Wilson & Devinney (1971); Nelson & Davis (1972); Wilson (1979); Etzel (1981)]. These codes have had great success at accurately modeling the observed data, but also require a substantial learning curve to fully master their operation. The result is that up till now there is no comprehensive catalog of reliable elements for eclipsing binaries (Cox 2000).

In order to take full advantage of the large-scale survey datasets, one must change the traditional approach of manual light curve analysis. The traditional method of painstakingly fitting models one by one is inherently limited by the requirement of human guidance. Ideally, fitting programs should be both physically accurate and fully automated. Many have cautioned against full automation (Popper 1981; Etzel 1991; Wilson 1994) since it is surprisingly difficult, without the aid of a human eye, to recognize when a fit is “good.” In addition, it is essentially impossible to resolve certain parameter degeneracies without a priori knowledge and extensive user experience. Despite these challenges, there have been a small number of pioneering attempts at such automated programs (Wyithe & Wilson 2001, 2002). However, the large numerical requirements of these programs make it computationally expensive to perform full fits (i.e., without having some parameters set to a constant) of large-scale datasets. Moore’s law, which stated in effect that CPU speed doubles every 18 months, cannot in itself solve this problem, since the quantity of data to be analyzed is also growing at a similar exponential rate (Szalay & Gray 2001). Instead, we advocate replacing the approach of using

monolithic automated fitting programs with a multi-tiered pipeline (see Figure 2.1). In such a pipeline, a given light curve is piped through a set of programs that analyze it with increasing scrutiny at each tier. Light curves that are poorly fit or do not comply with set criteria are filtered out of the pipeline, thus passing a far smaller number of candidates on to the following, more computationally demanding tier. Such a pipeline, coupled with efficient analysis programs, can increase the effective speed of fitting models by a few orders of magnitude compared to monolithic fitting programs. This approach makes it practical to perform full fits of the largest light curve datasets, with only moderate computational resources. Using a single-CPU SUN UltraSPARC 5 workstation (333 MHz), the average processing time of our pipeline was \sim 1 minute per light curve, where each light curve typically contains a few hundred photometric observations³. We must emphasize that even at these speeds, we still need a few CPU-months to fully process an OGLE-like survey containing 10^5 light curves. In about a decade, the large synoptic surveys are slated to create datasets that are more than 4 orders of magnitude larger than that (Tyson 2002).

The Detached Eclipsing Binary Light curve fitter (DEBiL) is a program we created to serve as an intermediate tier for such a multi-tiered pipeline. DEBiL is a fully automated program for fitting eclipsing binary light curves, designed to rapidly fit a large dataset of light curves in an effort to locate a small subset that match given criteria. The matched light curves can then be more carefully analyzed using traditional fitters. Conversely, one can use DEBiL to filter out the eclipsing binary

³The processing time scales linearly with the average number of observations in the light curves.

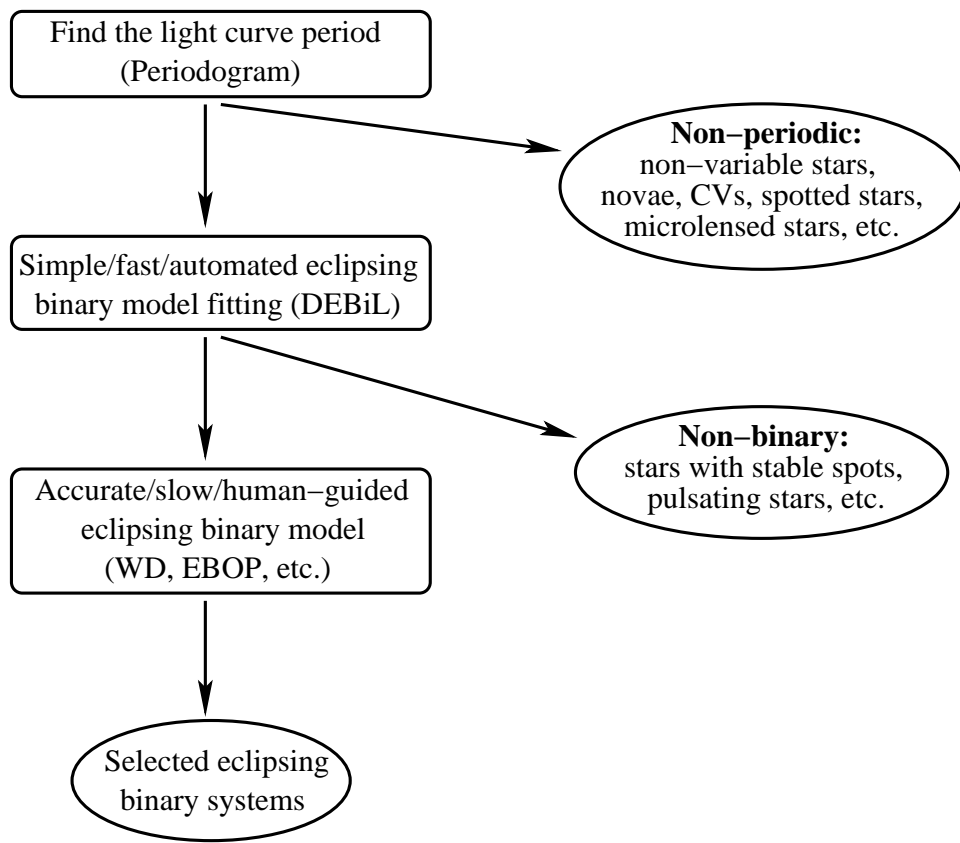


Fig. 2.1.— Diagram of a multi-tiered model-fitting pipeline.

systems in order to study other periodic systems (e.g., spotted or pulsating stars).

In order to achieve speed and reliable automation, DEBiL employs a simple model of a perfectly detached binary system: limb darkened spherical stars with no reflections or third light, in a classical 2-body orbit. Given the system's period and quadratic limb darkening coefficients (the default is solar limb darkening), the DEBiL fitter will fit the following eight parameters:

- Radius of primary star
- Radius of secondary star
- Brightness of primary star
- Brightness of secondary star
- Orbital eccentricity
- Orbital inclination
- Epoch of periastron
- Argument of periastron

Since we do not have an absolute length-scale, we measure both stars' radii as a fraction of the sum of their orbital semimajor axes (a).

This simple model allows the use of a nimble convergence algorithm that is comprised of many thousands of small steps that scour a large portion of the problem's phase space. Admittedly, this model can only give a crude approximation for semidetached and contact binaries, but it can easily identify such cases and can flag them for an external fitting procedure. In addition to pipeline filtration, DEBiL

can also provide an initial starting guess for these external fitters, a task that usually has to be performed manually.

2.3 Method

This section describes our implementation of a multi-tiered light curve-fitting pipeline. We fine-tuned and tested our design using light curves from the bulge fields of the second phase Optical Gravitational Lensing Experiment [OGLE II ; Udalski et al. (1997); Wozniak et al. (2002)]. Our resulting pipeline consists of the following six steps:

First tier: Periodogram

- (1) Find the light curve period
- (2) Filter out non-periodic light curves

Second tier: DEBiL

- (3) Find an “initial guess” for the eclipsing binary model parameters
- (4) Filter out non-eclipsing systems (i.e. pulsating stars)
- (5) Numerically fit the parameters of a detached eclipsing binary model
- (6) Filter out unsuccessful fits

For OGLE II data, we found that about half of the total CPU-time was spent on step (1) and about half on step (5). The remaining steps required an insignificant amount of CPU-time. Note that step (5), which typically takes more than 10 times

longer to run than step (1), was only run on less than 10% of the light curves. By filtering out more than 90% of the light curves at earlier steps, the pipeline was able to run \sim 10 times faster than it would have been able to otherwise. Both steps (1) and (5) can themselves be speeded up, but at a price of lowering their reliability and accuracy. The third tier, in which the light curves of interest are fitted using physically accurate models, is dependent on the research question being pursued and will not be further discussed here.

2.3.1 The First Tier – Finding the Period

Step (1) is performed using an “off-the-shelf” period search technique. All the periodogram algorithms that we have tested give comparable results, and we adopted an analysis of variance (Schwarzenberg-Czerny 1989, 1996) as it appears to do a good job of handling the aliasing in OGLE light curves. In our implementation, we scanned periods from 0.1 days up until the full duration of the light curve (\sim 1000 days for OGLE II). We then selected the period that minimizes the variance around a second order polynomial fit within eight phase bins. Aliases pose a serious problem for period searches since they can prevent the detection of weak periodicities, or periods that are close to an alias. The “raw” period distribution of the OGLE II light curves showed aliases with a typical widths ranging from 0.001 days for the shortest periods, and up to 0.04 days for longest periods. We suppressed the 12 strongest aliases, over which the results were dominated by false positives, and had the period finder return the next best period. Fewer than 1% of the true light curve periods are expected to have been affected by this alias suppression. Finally, once a

period was located, rational multiples of it, with numerators and denominators of 1 through 19 were also tested to see whether they provided better periods.

Step (2) filters out all the light curves that are not periodic. The analysis of variance from step (1) provides us with a measure of “scatter” in a light curve, after being folded into a given period. Ideally, when the period is correct, the folded data are neatly arranged, with minimal scatter due to noise. In contrast, when the light curve is folded into an incorrect period, the data are randomized and the scatter is increased. In order to quantify this, we measure the amount of scatter in each of the tested periods, and calculate the number of sigmas the minimum scatter is from the mean scatter. We call this quantity the “periodic strength score”. In an attempt to minimize the number of non-eclipsing binaries that continue to the next step, while maximizing the number of eclipsing binaries that pass through, we chose a minimum periodic strength score cutoff of 6.5. In addition to this, we set a requirement that the variables’ period be no longer than 200 days, which guarantees at least four foldings. These two criteria filtered out approximately 90% of all the light curves in the OGLE II dataset.

In order to test the effectiveness of these filtration criteria, we measured the filtration rates for field 33, a typical OGLE II bulge field (see Figure 2.2). We then repeated this measurement for a range of periodicity strength cutoffs (the 200-day criterion remained unchanged). For periodicity strength cutoffs up to 4, there is a sharp reduction in the number of systems, as non-variable light curves are filtered out. Users should be aware that constant light curves can be well-fit by degenerate DEBiL models. By filtering out systems with such low periodicity strength we correctly remove these systems, and in so doing noticeably lower the total number

of well-fitted systems. Raising the filtration cutoff, up until about 6.5, will continue reducing the filter-through rate, but with only a small impact on the number of well-fit systems. Further raising the cutoff will again reduce the number of fitted systems, this time removing good systems. We can conclude from this test that the optimal periodicity strength cutoff is between 4 and 6.5, so that non-variable systems are mostly filtered out while eclipsing binaries are mostly filtered through. Since the filter-through rate monotonically decreases as the cutoff is raised, the pipeline becomes significantly more computationally efficient at the high end of this range, thus bringing us to our cutoff choice of 6.5. Users with more computing power at their disposal may consider lowering the cutoff to the lower end of this range. In so doing they slightly reduce the risk of filtering out eclipsing binaries, at the price of significantly lowering the pipeline computational efficiency.

2.3.2 The Second Tier – DEBiL Fitter

Steps (3) through (5) are performed within the DEBiL program. Step (3) provides an “initial guess” for the model parameters. It identifies and measures the phase, depth and width of the two flux dips that occur in each orbit. Using a set of equations that are based on simplified analytic solutions for detached binary systems (Danby 1964; Mallén-Ornelas et al. 2003; Seager & Mallén-Ornelas 2003), DEBiL produces a starting point for the fitting optimization procedure. Step (4) filters out light curves with out-of-bound parameters, so as to protect the following step. In practice this step is remarkably lax. It typically filters out only a small fraction of the light curves that pass through it, but those that are filtered out are almost

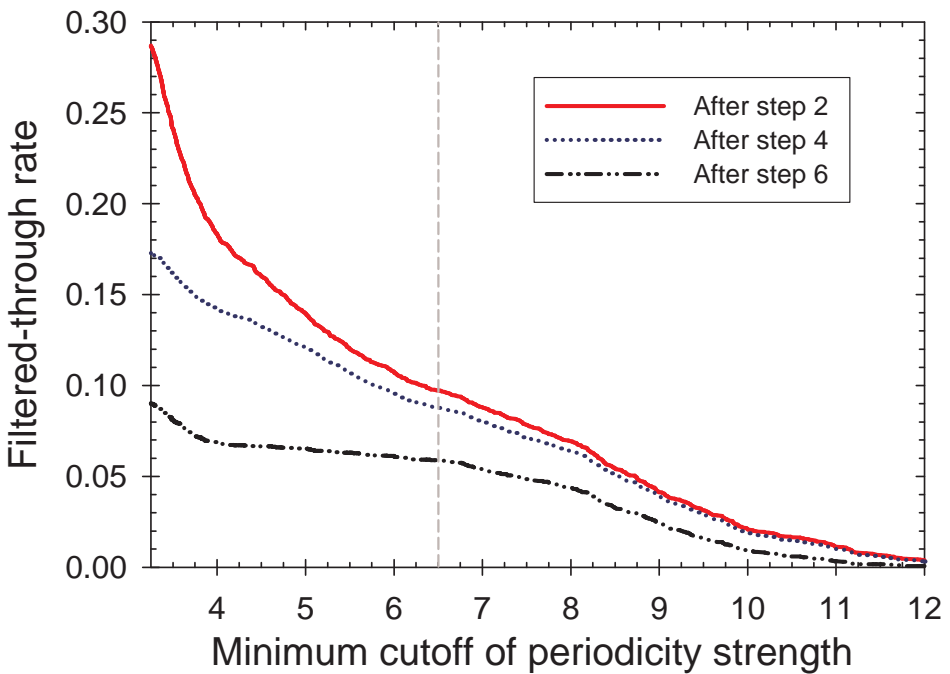


Fig. 2.2.— The pipeline filtration fractions of the variables within bulge field 33 of OGLE II ($N=4526$), with varying periodicity strength cutoffs. The vertical dashed line indicates the chosen cutoff for our pipeline (> 6.5).

certain not to be eclipsing binaries. Step (5) fits each light curve to the 8-parameter DEBiL model (see §2.2), fine-tunes it, and estimates its parameter uncertainties. This step starts with the light curve that would have been seen with the “initial guess” parameters. It then systematically varies the parameters according to an optimization algorithm, so as to minimize the square of the residuals in an attempt to converge to the best fit. The optimization algorithm chosen for the DEBiL fitter is the downhill simplex method combined with simulated annealing (Nelder 1965; Kirkpatrick et al. 1983; Vanderbilt & Louie 1983; Otten & van Ginneken 1989; Press et al. 1992). This algorithm was selected for its simplicity, speed, and relatively long history of reliably solving similar problems, which involve locating a global minimum in a high-dimensional parameter space. Other methods that were considered are gradient-based (Press et al. 1992) and genetic algorithms (Holland 1975; Charbonneau 1995). Gradient-based (steepest descent) algorithms can converge very quickly to a local minimum, but are not designed for finding the global minimum. In addition, the difficulty in calculating the gradient of non-analytic function slows these algorithms considerably and causes them to be less robust. Genetic algorithms provide a promising new approach for locating global minima, with the unique advantage of being parallelizable. Unfortunately, their implementations are more complicated, while not having a significant advantage in speed or reliability over the downhill simplex method.

Determining a convergence threshold at which to stop optimization algorithms is known to be a difficult problem (Charbonneau 1995). This is because the convergence process of these algorithms will go through fits and stops. The length of the “stops,” whereby the convergence does not significantly improve, becomes

longer with time, ultimately approaching infinity. Since there is no known way to generally predict these fits and stops, we chose simply to have the algorithm always run for 10,000 iterations (this choice can be adjusted at the command line). This number was found to be adequate for OGLE light curves (see §2.4), with larger numbers not showing a significant improvement in the convergence. Using a constant number of iterations has the significant benefit of enabling the user to make accurate predictions of the total computing time that will be required. At the end of the 10,000 iterations, the best solution encountered so far is further fine-tuned, so as to guarantee that it is very close to the bottom of the current minimum. In our implementation we make sure every parameter is within 0.1% of the minimum (p_{min}).

Finally, DEBiL attempts to estimate the uncertainties of the fitted parameters. This is done by perturbing each parameter by a small amount (Δp) and measuring how sensitive the model’s reduced chi square (χ^2_ν) is to that parameter. In our implementation we set the perturbation to be 0.5% of p_{min} . At each parameter perturbation measurement, the remaining parameters are re-fine-tuned⁴, so as to take into account the parameters’ covariances. We then use a second order Taylor expansion to derive the second derivative of χ^2_ν at the minimum, which is used to extrapolate the local shape of the χ^2_ν -surface:

⁴We limited the number of iterations for this task, so that it will not become a computational bottleneck. But since the perturbations are small, we could use a greedy fitting algorithm, for which this is rarely a problem.

$$\chi_{\nu}^2(p_{min} + \Delta p) \simeq \chi_{\nu}^2(p_{min}) + \frac{1}{2} \cdot \frac{\partial^2 \chi_{\nu}^2}{\partial p_{min}^2} \cdot (\Delta p)^2 \quad (2.1)$$

We chose to employ a non-standard definition for the DEBiL parameter uncertainties, which seems to describe the errors of all the fitted parameters (see Figure 2.3) far better than the standard definition (Press et al. 1992). In the standard definition, the uncertainty of a parameter is equal to the size of the perturbation from the parameter’s best-fit value, which will raise χ_{ν}^2 by $1/\nu$, while fitting the remaining parameters. The reasoning behind this definition implicitly assumes that χ_{ν}^2 is a smooth function. But in fact the χ_{ν}^2 -surface of this problem is jagged with numerous local minima. These minima will fool the best attempts at converging to the global minimum and cause the parameter errors to be far larger than the standard uncertainty estimate would have us believe. For this reason we adopted a non-standard empirical definition for the parameter uncertainties (ε_p). In our variant, the uncertainty of a parameter is equal to the size of the perturbation from the parameter’s best-fit value, which will *double* χ_{ν}^2 , while fitting the remaining parameters:

$$\chi_{\nu}^2(p_{min} + \varepsilon_p) = 2\chi_{\nu}^2(p_{min}) \quad (2.2)$$

This definition assigns larger uncertainties to more poorly-fit models. In addition, it is insensitive to systematic over- or under-estimated photometric uncertainties, which are all too common in many light curve surveys. Using the previous two equations, we can estimate ε_p as:

$$\varepsilon_p \simeq \Delta p \cdot \sqrt{\frac{\chi_\nu^2(p_{min})}{\chi_\nu^2(p_{min} + \Delta p) - \chi_\nu^2(p_{min})}} \quad (2.3)$$

Note that the standard uncertainty is approximately: $\varepsilon_p / \sqrt{\chi^2}$, so users can easily convert to it, if so desired.

Step (6) is the final gatekeeper of our pipeline. It evaluates the model solutions and filters out all but the “good” models according to some predefined criteria. DEBiL users are expected to configure this step so as to fit the particular needs of their research. To this end, DEBiL provides a number of auxiliary tests designed to quantify how well the model fits the data. The reduced chi-squared and fitness score values measure the overall quality of the fit, while the scatter score and waviness values measure local systematic departures of the model from the data (see appendix A).

Additional filtering criteria are usually needed in order to remove non-eclipsing-binary light curves that have either (a) have overestimated uncertainties that produce low reduced chi-squared results, or (b) look deceptively similar to eclipsing binary light curves. Filtration criteria should be placed with great care in order to minimize filtering out “good” light curves. In order to handle overestimated uncertainties (a), one can filter out models with low fitness scores. Handling non-eclipsing-binary light curves that look like binary light curves (b) is considerably more difficult. Many of these problematic light curves are created by pulsating stars (e.g., RR-Lyrae type C), which have sinusoidal light curves that resemble those of contact binaries. To this end, DEBiL also provides the reduced chi-squared of a best-fit sinusoidal function of each light curve. If this value is similar or lower than the model’s reduced

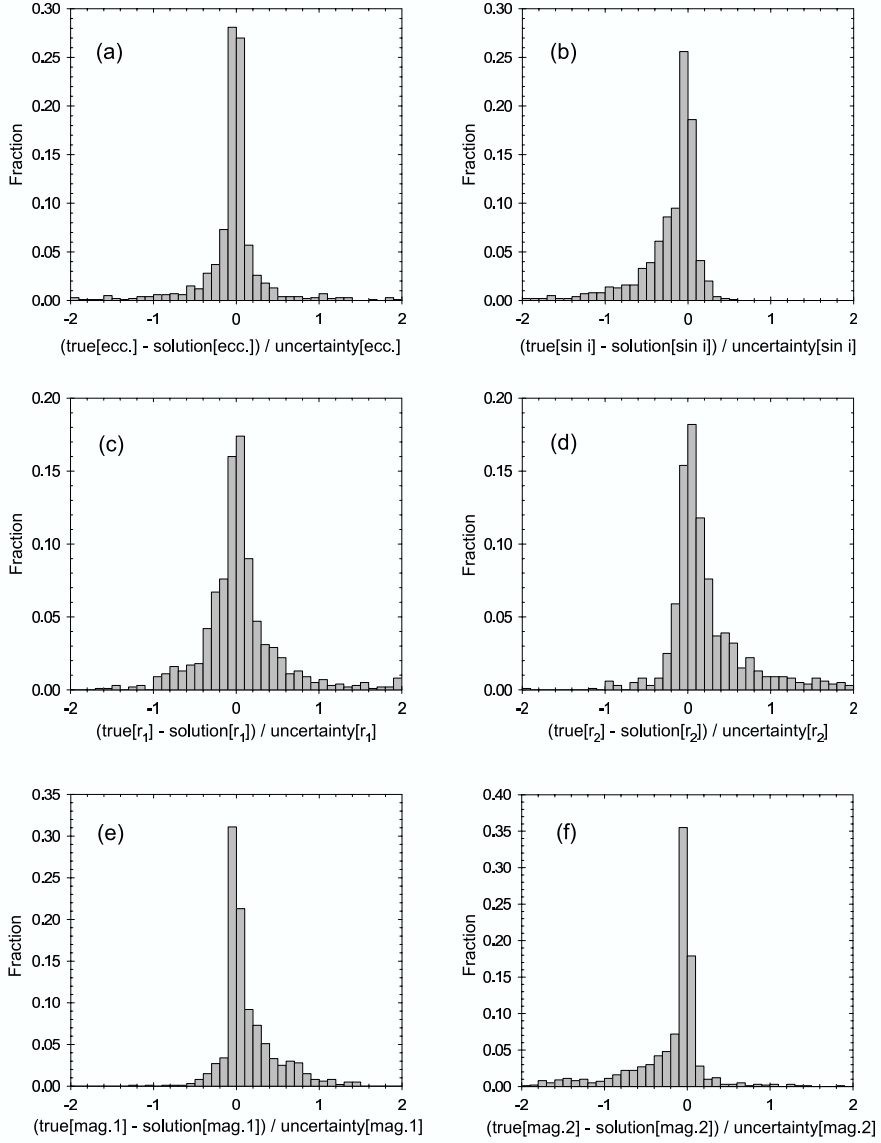


Fig. 2.3.— Histograms of the error distribution in DEBiL fitted parameters. This plot was created by fitting 1000 simulated eclipsing light curves with 5% Gaussian photometric noise. The fitting error of each parameter was normalized by its estimated uncertainty (as defined in §2.3.2). The distributions seen here are not Gaussian, but rather have a slender peak, and long tails (i.e. large kurtosis). The distributions also have varying degrees of skewness, which is discussed in §2.3.3.

chi-squared, then is it likely that the light curve indeed belongs to a pulsating star.

2.3.3 Limitations

In the previous subsection we discussed the considerable difficulties in finding the global minimum in the jagged structure of the χ^2_ν -surface. At this point we must further add, that since the data are noisy and the model is imperfect, the true solution might not be at the global minimum. For the lack of better information, we can only use the global minimum as the point in parameter space that is the most *likely* to be the true solution.

Another source of errors are systematic fitting biases, which must especially be taken into account when making detailed population studies. Two main sources of these biases are imperfect models and asymmetric χ^2_ν -minima. Almost all models are imperfect, but when effects not included in the model become significant, the optimization algorithm will often try to compensate for this by erroneously skewing some of the parameters within the model. An example of this is seen in semidetached binaries. The tidal distortions of these stars are not modeled by DEBiL, so as a result DEBiL will compensate for this by overestimating their radii. Most model imperfections are flagged by a large reduced chi-squared. Surprisingly, for tidal distortions, the reduced chi-squared is not significantly increased. For this reason we provide a “detached system” criterion that will be described in §2.5. The effects of asymmetric χ^2_ν -minima are more subtle. In such cases a perturbation to one side of a χ^2_ν -minimum raises χ^2_ν less than a perturbation to the other side. Thus random noise in the data will cause the parameters to be systematically shifted more often in the

former direction than in the latter. We believe that these biases, which are universal to all fitting programs, can be corrected after the fact. We chose not to do this in order to avoid having to insert any fudge factors into DEBiL. But we acknowledge that this may be necessary in order to extend the regimes in which DEBiL is reliable without significantly reducing its speed.

Possibly the most problematic fitting errors are those that are caused by mistaken light curve periods. For eclipsing binaries with strong periodicity scores, the main cause of this is the confusion between two types of light curves: (a) light curves with very similar and equally-spaced eclipses, and (b) light curves with an undetected eclipse. Both these types of light curves will appear to have a single eclipse in their phased light curve. Light curves with similar eclipses (a) will cause the period finder to return a period that is half the correct value⁵, folding the primary and secondary eclipse over one another. In contrast to this, light curves with an undetected eclipse (b), either because it's hidden within the noise or because it's in a phase coverage gap, will have the correct period. Because the undetected eclipse is necessary for determining a number of the fitting parameter, we are not able to model this type of light curve. Fortunately, light curves with similar eclipses (a) can be easily modeled by simply doubling their period. Since we can not generally distinguish between these two types of light curves, the DEBiL fitter treats all the single-eclipse light curves as type (a), doubling their period and fitting them as best it can. Whenever such a period-doubling occurs, DEBiL inserts a warning message into the log file. These light curves should be used with increased scrutiny. This

⁵Strictly speaking, this is not an error on the part of the period finder, since it is in fact returning the best period from its standpoint.

problem is further compounded in surveys such as the OGLE II bulge fields, which consist of many non-eclipsing-binary variables. As mentioned in §2.3.2, some of these systems look deceptively similar to eclipsing binaries. Since their brightness oscillation typically consists of a single minima, they too will have their period doubled. In conclusion, unless the systems with doubled periods are filtered out, there will be an erroneous excess of light curves with similar primary and secondary eclipses. In turn, this will manifests itself in an excess of model solutions with stars of approximately equal surface brightness.

Even though our discussion of possible causes and remedies for the limitations stems from our experience with one particular pipeline, many of these points are also likely to apply to other similar pipelines and fitting procedures.

2.4 Tests

In order to test the DEBiL fitter, we ran it both on simulated light curves and on published, fully analyzed, observed light curves (Lacy et al. 2000, 2002, 2003). Figure 2.3 shows the results of fitting 1000 simulated light curves, with 5% Gaussian photometric noise. Figure 2.4 provides a more detailed look at the fits to 50 simulated light curves, with 1% Gaussian photometric noise, giving results comparable to those of Wyithe & Wilson (2001). Not surprisingly, when less noise was inserted into the light curve, the fitter estimated considerably smaller uncertainties.

While the simulated light curves are easy to produce and have known parameter values, observed light curves are the only ones that can provide a true reality check.

To this end, we also reanalyze three published light curves (see Figure 2.5):

- Table 2.1: FS Monocerotis (Lacy et al. 2000)
- Table 2.2: WW Camelopardalis (Lacy et al. 2002), and
- Table 2.3: BP Vulpeculae (Lacy et al. 2003).

We present here a comparison between the aforementioned published photometric fits, using the Nelson-Davis-Etzel model implemented by EBOP (Etzel 1981; Popper & Etzel 1981) and the DEBiL fits. For all three cases, we used the V -band observational data and set DEBiL's limb darkening quadratic coefficients to the solar V -band values (Claret 2003). We found that when applying the physically correct limb darkening coefficients, the improvements in the best-fit model were negligible compared to the uncertainties. For this reason, we chose to use solar limb darkening coefficients throughout this project.

2.5 Results

We used the aforementioned pipeline to identify and analyze the eclipsing binary systems within the bulge fields of OGLE II (Udalski et al. 1997; Wozniak et al. 2002). The final result of our pipeline contained only about 5% of the total number of light curves we started with. The filtration process progressed as follows:

- Total number of OGLE II (bulge fields) variables: 218,699
- After step (2), with strong periodicity and periods of 0.1-200 days: 19,264

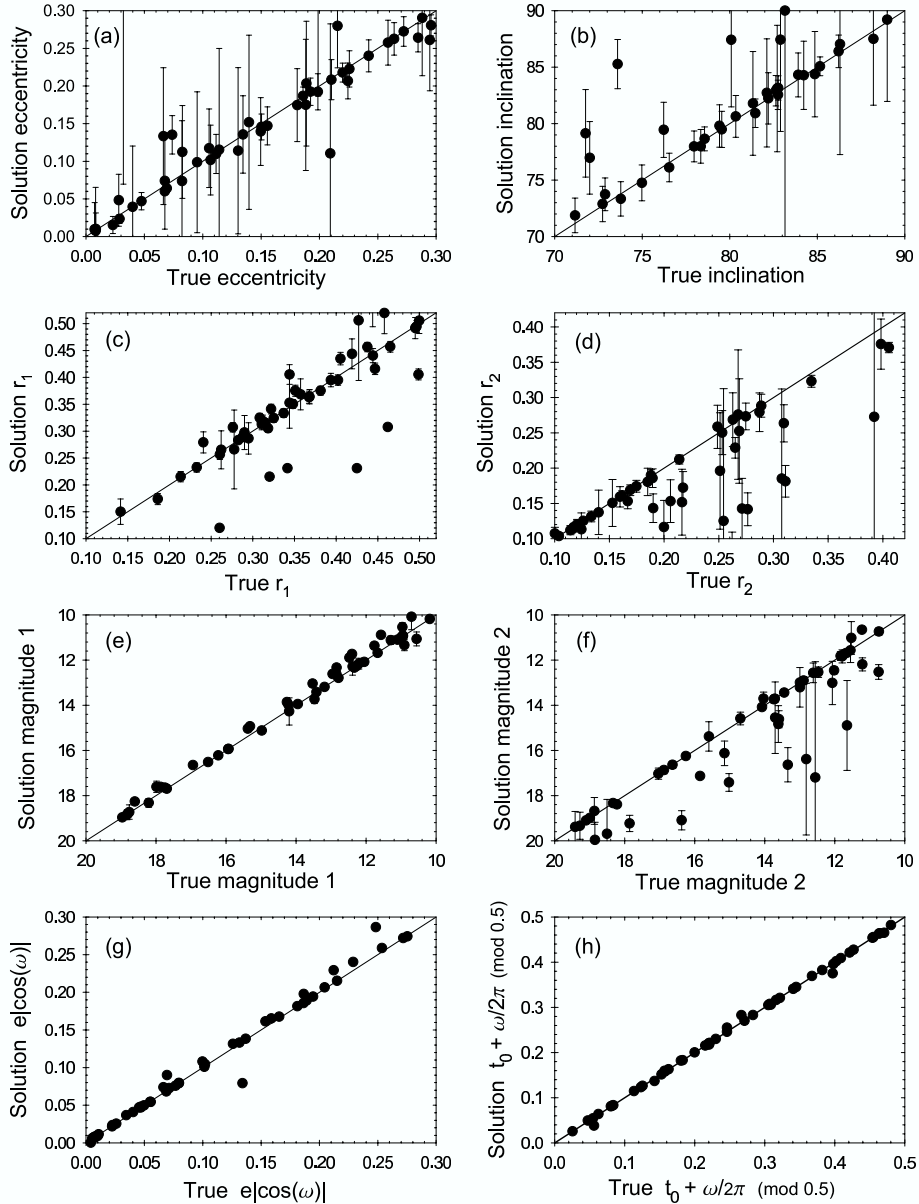


Fig. 2.4.— The fitted solutions versus the true solution in 50 simulated eclipsing binary light curves with Gaussian photometric noise of 1%. We simulated a uniform distribution of parameters, with the only requirement being that both eclipse dips were detectable through the noise. Panels (a) through (f) show the fits of DEBiL model parameters with their uncertainties, as defined in §2.3.2. Panels (g) and (h) combine parameters so that they describe prominent features of the light curve (respectively, the separation and offset of the⁴⁰ eclipse centers). In these combination, the parameter errors largely cancel out, so that the formal uncertainties should not be

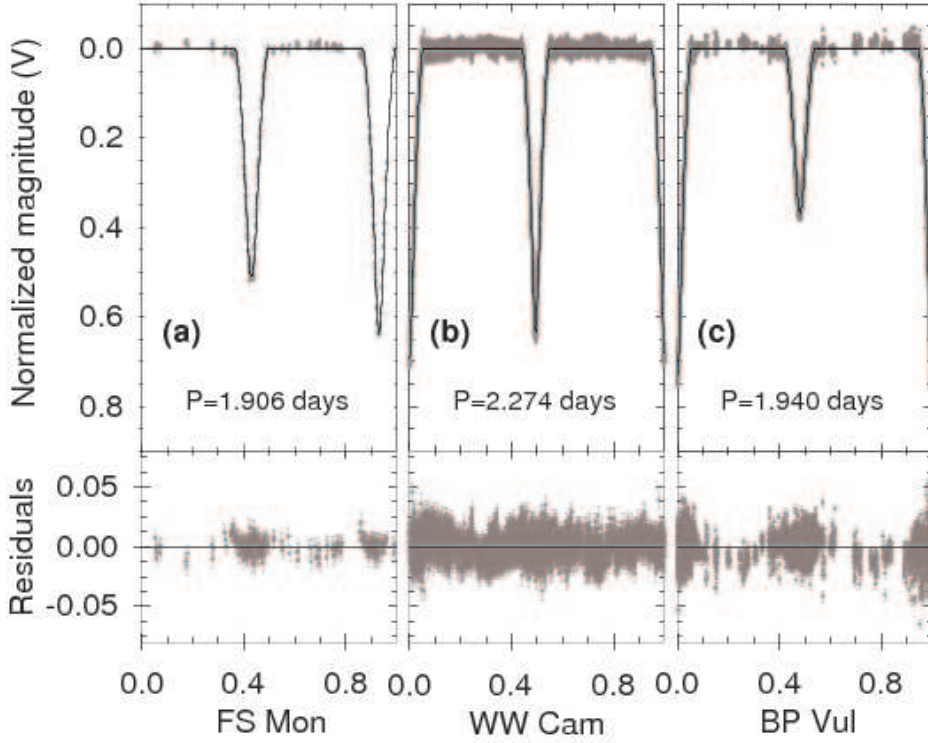


Fig. 2.5.— The phased light curves with the DEBiL model best fit (solid line) and its residuals, for the eclipsing binary systems: (a) FS Monocerotis; (b) WW Camelopardalis; (c) BP Vulpeculae.

Table 2.1. FS Monocerotis ($N = 249$)

Parameters	Symbol	(Lacy et al. 2000)	DEBiL best fit	Relative error
Radius of primary (larger) star	R_1/a	0.2188 ± 0.0005	0.222 ± 0.003	1.3 %
Radius of secondary (smaller) star	R_2/a	0.173 ± 0.003	0.179 ± 0.006	3.5 %
Surface brightness ratio	J_s	0.903 ± 0.003	0.916 ± 0.05	1.5 %
Orbital inclination	i	87.48 ± 0.08	87.86 ± 0.015	0.4 %
Eccentricity	e	0.0 (fixed)	0.001 ± 0.01	

Table 2.2. WW Camelopardalis (N = 5759)

Parameters	Symbol	(Lacy et al. 2002)	DEBiL best fit	Relative error
Radius of primary (larger) star	R_1/a	0.168 ± 0.0013	0.169 ± 0.018	0.5 %
Radius of secondary (smaller) star	R_2/a	0.159 ± 0.016	0.165 ± 0.014	3.4 %
Surface brightness ratio	J_s	0.950 ± 0.003	0.949 ± 0.08	0.1 %
Orbital inclination	i	88.29 ± 0.06	88.35 ± 0.03	0.1 %
Eccentricity	e	0.0099 ± 0.0007	0.01 ± 0.05	

Table 2.3. BP Vulpeculae (N = 5236)

Parameters	Symbol	(Lacy et al. 2003)	DEBiL best fit	Relative error
Radius of primary (larger) star	R_1/a	0.1899 ± 0.0008	0.190 ± 0.006	0.1 %
Radius of secondary (smaller) star	R_2/a	0.161 ± 0.009	0.166 ± 0.009	3.1 %
Surface brightness ratio	J_s	0.624 ± 0.0013	0.614 ± 0.08	1.5 %
Orbital inclination	i	86.71 ± 0.09	86.50 ± 0.012	0.2 %
Eccentricity	e	0.0355 ± 0.0005	0.04 ± 0.03	

- After step (4), the output of the DEBiL program: 17,767
- After step (6), with acceptable fits to binary models ($\chi^2_\nu < 4$): 10,862

Most of the fits that reach step (6) can be considered successful (see Figure 2.6).

It is then up to the user to choose criteria for light curves that are of interest, and to define a threshold for the quality of the fits. In our pipeline we chose a very liberal quality threshold ($\chi^2_\nu < 4$), so as to allow through light curves with photometric uncertainties that are too small (a common occurrence), and to leave users with a large amount of flexibility in their further filtrations. We list the first 15 DEBiL fits that passed through step (6) in table 2.4. Figure 2.7 shows another sampling of models, with their corresponding phased light curves. The complete dataset of OGLE II bulge models, both plotted and in machine readable form, is available online.

Since the filter at step (6) may not be stringent enough for many application, we also provide our results after each of two further levels of filtration:

- Non-pulsating (fitness score > 0.9 ; non-sinusoidal light curves): 8,471
- Detached systems (both stars are within their Roche limit): 3,170

For non-sinusoidal light curves, we require that the DEBiL fit have a smaller reduced chi square than the best-fit sinusoidal model. For the Roche limit calculation, we assumed an early main-sequence mass-radius power law relation: $R \propto M^{0.652}$ (Gorda & Svechnikov 1998) and set it in a third order approximation of the Roche radius (de Loore & Doom 1992). The resulting approximations are:

$$R_{Roche,1}/a \simeq 0.37771 + 0.31054x + 0.04324x^2 + 0.08208x^3 \quad (2.4)$$

$$R_{Roche,2}/a \simeq \begin{cases} 0.37710 - 0.32684x - 0.01882x^2 - 0.023812x^3, & \text{if } x \geq 0.65 \\ 0.37771 - 0.31054x + 0.04324x^2 - 0.08208x^3, & \text{otherwise} \end{cases} \quad (2.5)$$

Where $x \equiv \log(R_1/R_2)$, assuming $R_1 \geq R_2$.

In order to better interpret the data derived by the DEBiL pipeline, we combined it with color ($V - I$) and magnitude information (Udalski et al. 2002), as well as an extinction map of the galactic bulge (Sumi 2004). Thus for each eclipsing system, we also have its extinction corrected combined I -band magnitude and V-I color. Since many of the stars in the bulge fields are not in the galactic bulge but rather in the foreground, it is likely they will be overcorrected, making them too blue and too bright. These stars can be seen in both the color-magnitude diagram (see Figure 2.8) and in the color-density diagram (see Figure 2.9). With this qualification in mind, the color-density diagram provides a distance independent tool for identifying star types. Because the measured values result from a combination of the two stars in the binary, the values are not expected to precisely match either one of the stars in a binary. Remarkably, using the maximum density measure instead of the mean density (appendix B) this problem seems to be considerably lessened.

2.5.1 Population Distributions

Due to the limitations of the OGLE observations, analysis and subsequent filtrations, there are a myriad of complex selection effects that need to be accounted for. For this reason, we hesitate to make any definite population statements in this paper,

Table 2.4. Selected parameters from the DEBiL dataset of eclipsing binary systems
in the galactic bulge.

Field	Object	Period	e	R_1/a	R_2/a	I_1 [mag.]	I_2 [mag.]	$\sin(i)$	t_0 ^a	ω [deg.]	χ^2_ν	Corrected I [mag.] ^b	Corrected V-I [mag.] ^{b,c}
1	39	129.656	0.074	0.773	0.118	13.56	17.21	0.9208	0.665	256.0	1.13	12.81	1.93
	45	0.55677	0.025	0.589	0.386	17.36	18.20	0.9979	0.724	271.4	1.06	16.21	-1000 ^d
	53	2.52158	0.099	0.412	0.103	12.20	16.15	1.0000	0.418	91.4	3.07	11.38	0.18
	108	1.53232	0.005	0.516	0.301	16.80	19.12	0.9143	0.497	254.1	0.93	15.84	0.48
	112	0.35658	0.000	0.514	0.486	17.90	17.87	0.9763	0.429	40.6	1.56	16.36	0.65
	155	0.96092	0.014	0.683	0.303	16.15	17.84	0.9203	0.199	294.5	1.12	15.10	0.45
	183	0.57793	0.009	0.555	0.338	17.99	20.03	0.9828	0.055	56.4	1.29	17.14	0.41
	201	0.67241	0.101	0.509	0.246	17.26	20.08	0.9971	0.473	264.3	0.87	16.44	0.32
	202	4.51345	0.174	0.309	0.206	17.58	17.08	0.9968	0.035	270.9	2.68	15.82	0.64
	215	0.48925	0.000	0.770	0.230	15.93	18.62	0.9212	0.870	150.5	1.54	15.06	0.20
	221	0.45013	0.004	0.558	0.434	18.23	18.87	0.9332	0.107	100.7	0.92	16.92	0.58

Note. — This table is published in its entirety in the electronic edition of the *Astrophysical Journal*.

^aPhased epoch of periastron: heliocentric Julian date, minus 2450000.0, folded by the period.

^bExtinction corrected using the Sumi (2004) extinction map of the galactic bulge.

^cThe combined binary color was taken from (Udalski et al. 2002).

^dThe “-1000” values indicate missing magnitude or color data.

although there are a number of suggestive clusterings and trends that merit further scrutiny.

When considering the distribution of $r_{1,2} \equiv R_{1,2}/a$ for eclipsing binary systems, one would expect a comparably smooth distribution as determined by the binary star IMF, binary orbit dynamics and observational/detection selection effects. This distribution can be best seen in a radius-radius plot (see Figure 2.10). This plot has a few features that merit discussion. One feature is that the number of systems rapidly dwindles as their radii become smaller. This should not be surprising, as selection effects dominate the expected number of observed systems for small radii (this point will be elaborated at the end of this subsection). A second, far more surprising feature, is the appearance of three clusterings: along the contact limit, around $(r_1 = 0.33, r_2 = 0.23)$, and around $(r_1 = 0.15, r_2 = 0.09)$. These three clusterings are most likely artificial, caused by two technical limitations that are discussed in §2.3.3. The first two clusterings were likely formed when many of the semidetached systems that populated the region between the clusterings, were swept into the contact limit, because their radii were overestimated. The third clustering, although less pronounced, seems to echo the structure of the second clustering, only with about half its radii. This hints at the possibility that the periods of some of these systems were doubled when they should not have been, probably because of an undetected eclipse. It is worth mentioning that both the second and third clusterings are centered at a significant distance from $r_1 = r_2$, which is where the clusters would have been located, if r_1 and r_2 had been independent variables.

Perhaps even more surprising is the period distribution (see Figure 2.11). Using only the default filters of our pipeline, this distribution is bimodal, peaking

at approximately 1 and 100 days, and with a desert around a 20-day period. To understand this phenomenon one should look at the scatter plots of figure 2.12. In this figure we can see that long-period binaries (period > 20 days) are significantly redder than average and have low eccentricities. This is possibly due to red giants, which cannot be in short-period systems. This possibility is problematic since it contradicts the unimodal results of previous period distribution studies (Farinella et al. 1979; Antonello et al. 1980; Duquennoy & Mayor 1991). In addition, figure 2.11 shows that with additional filtrations, the grouping of systems around the 100-day period is greatly reduced. All this leads us to conclude that the \sim 100 day period peak is probably erroneous, created by a population contamination of pulsating stars, probably mostly semi-regulars, which can easily be confused with contact binaries. A similar phenomenon is seen in the spike in the number of systems around a period of 0.6 days. This increase is probably also due to pulsating stars, only this time they are likely RR-Lyrae type variables. They too were largely filtered out using the techniques described in the previous section.

Finally, we unraveled the geometric selection effects by weighting each eclipsing light curve by the inverse of the probability of observing it as eclipsing. For example, if with a random orientation there is a 1% chance of a given binary system being seen as eclipsing, we will give it a weight of 100. In this way we tabulated each observed occurrence as representing 100 such binary systems, the remaining of which exist but are not seen eclipsing and so are not included in our sample of variable stars. A binary system with a circular orbit ($e = 0$) will eclipse when its inclination angle (i) obeys: $\cos(i) < (R_1 + R_2)/a$. If the orbital orientations are randomly distributed, then the inclination angles are distributed as: $p(i) \propto |\sin(i)|$. Therefore,

the probability that such a binary system will eclipse becomes:

$$p_{\text{eclipse}}(R_{1,2}/a, e = 0) = \frac{R_1 + R_2}{a} \quad (2.6)$$

The probability of eccentric systems ($e > 0$) eclipsing is more difficult to calculate. We used a Monte-Carlo approach to calculate a 1000×1000 $[(R_1 + R_2)/a, e]$ probability table, which was then used to interpolate the probability of each fitted light curve. When applying this correction for the geometric selection effect (see Figure 2.13) we see that, as expected, it primarily effects the detached binaries. The period (P) distribution of detached systems, both before (p_{eclipse}) and after (p_{all}) the geometric correction are remarkably similar, and can both be well fit to a log-normal distribution:

$$p_{\text{eclipse,all}}(P) = \frac{1}{\sqrt{2\pi}\sigma P} \exp\left(-\frac{\ln^2(P/P_0)}{2\sigma^2}\right) \quad (2.7)$$

Before the geometric correction (p_{eclipse}), we get a fit of $P_0 = 1.83 \pm 0.01$ days and $\sigma = 0.593 \pm 0.005$ ($r^2 \simeq 0.9926$). After the correction (p_{all}), we get a fit of $P_0 = 2.06 \pm 0.01$ days and $\sigma = 0.621 \pm 0.005$ ($r^2 \simeq 0.9928$). Such log-normal distributions are generally indicative of many independent multiplicative processes taking place, possibly both in the formation of binary systems as well as in their observational/detection selection effects.

One should be very careful when using this method to calculate the total number of binaries. Simply comparing the number of binaries before and after the geometric correction will result in the conclusion that we are observing as eclipsing

binaries about half of the total number of binaries. However, this fraction should in fact be smaller than that, since we cannot detect eclipsing binaries with periods longer than a few hundred days with the OGLE II survey.

2.5.2 Extreme Systems

In the previous subsection we considered the way large sets of eclipsing systems are distributed. Now we will consider individual systems. As examples we chose to locate extreme binary systems, systems with a parameter well outside the normal range. For this to be done properly, we need to take great care in avoiding the pitfalls that arise from parameter estimation errors, both systematic and non-systematic. One pitfall is that some of the extreme systems may have large systematic errors since they will contain additional phenomena that the fitted model neglects. Another, perhaps more problematic pitfall, is that we will retrieve non-extreme systems with large errors that happen to shift the parameter in question beyond our filtering criterion threshold. Some examples of possible sources of large errors are inaccuracies in the correction for dust reddening (see the beginning of this section) and difficulties in the estimation of the argument of periastron, which directly affects the determination of binary's orbital eccentricity (Etzel 1991). Because of these pitfalls, we expect that the human eye will be required as the final decision maker for this task in the foreseeable future.

We present candidates of the most extreme eclipsing systems within the OGLE II bulge field dataset in five categories (table 2.5). We chose examples for which we were comparably confident, though we would need to follow them up with

spectroscopic measurements to be certain of their designations.

In the case of the high-density, low-density, and blue systems the measured value of the characteristic is a weighted mean of the two stars in the binary system. The weighting of the high- and low-density systems is described in appendix B. The weighting of the blue systems is determined, approximately, by the bolometric luminosity of each of the stars in the binary system.

2.6 Conclusions

We present a new multi-tiered method for systematically analyzing eclipsing binary systems within large-scale light curve surveys. In order to implement this method, we have developed the DEBiL fitter, a program designed to rapidly fit a large number of light curves to a simplified detached eclipsing binary model. Using the results of DEBiL one can select small subsets of light curves for further follow-up. Applying this approach, we have analyzed 218,699 light curves from the bulge fields of OGLE II, resulting in 10,862 model fits. From these fits we identified unexpected patterns in their parameter distribution. These patterns are likely caused by selection effects and/or biases in the fitting program. The DEBiL model was designed to fit only fully detached systems, so users should use fits of semidetached and contact binary systems with caution. One can probably find corrections for the parameters of these systems, although it is best to refit them using more complex models, which also take into account mutual reflection and tidal effects. Even so, the DEBiL fitted parameters will likely prove useful for quickly previewing large datasets, classification, fitting detached systems, and providing an initial guess for

Table 2.5. Extreme eclipsing binary system candidates

Category	Field	Object	Period	e	R_1/a	R_2/a	I_1 [mag.]	I_2 [mag.]	χ^2_ν	$\bar{\rho}$	ρ_{\max}	Corrected I [mag.]	Corrected V-I [mag.]
High density	21	5952	1.468	0.001	0.137	0.039	15.21	17.78	1.30	3.372	153.6	14.26	0.48
High density	23	1774	0.505	0.018	0.245	0.162	16.91	17.41	3.17	3.925	17.45	14.87	-1000
Low density	3	8264	151.026	0.023	0.487	0.228	17.39	18.95	2.53	0.000007	0.00007	15.46	1.33
Low density	21	2568	186.496	0.265	0.472	0.127	15.28	18.18	1.82	0.000005	0.00026	14.47	1.04
High eccentricity	2	547	2.419	0.231	0.211	0.077	12.12	14.66	1.89	0.330	7.049	11.47	-0.37
High eccentricity	38	4059	2.449	0.454	0.288	0.179	17.81	20.65	1.61	0.107	0.553	16.94	0.68
Blue	21	3797	2.653	0.003	0.193	0.104	12.33	14.35	3.03	0.322	2.373	11.48	-0.37
Blue	30	1778	6.442	0.084	0.089	0.028	12.81	15.53	2.39	0.627	21.37	11.81	-0.52
Short period	18	3424	0.179	0.119	0.670	0.211	16.73	19.28	2.10	1.895	62.905	15.53	0.13
Short period ^e	46	797	0.198	0.072	0.444	0.426	16.67	16.60	2.80	2.913	6.208	14.87	1.36
Short period	49	538	0.228	0.008	0.728	0.264	16.09	18.35	1.07	0.904	19.929	15.03	0.31
Short period	42	2087	0.233	0.021	0.568	0.336	17.94	19.40	1.27	1.580	9.242	16.68	0.85

^eAfter finding this candidate using our pipeline, we identified it as the eclipsing binary BW3 V38, which was discovered and extensively studied by Maceroni & Rucinski (1997). For consistency, we listed the DEBiL fitted parameters, though their accuracy is considerably worse than what is currently available in the literature (Maceroni & Montalbán 2004). Specifically, the DEBiL fits for the binary components' radii are overestimated by $\sim 25\%$ due to their tidal distortions (see §2.3.3).

more complex model fitters.

Acknowledgments

We would like to thank Robert Noyes, Krzysztof Stanek, Dimitar Sasselov and Guillermo Torres for many useful discussions and critiques. In addition we would like to thank Takahiro Sumi and the OGLE collaboration for providing us with the data used in this paper. Finally, we would like to thank Lisa Bergman for both her editorial help and utmost support throughout this project. This work was supported in part by NASA grants NAG5-10854 and NNG04GN74G.

2.7 Appendix - Statistical Tests

2.7.1 Fitness Score

One of the problems with using the reduced chi-squared test is that the light curve uncertainties may be systematically overestimated (underestimated), causing the reduced chi-squared to be too small (large). An easy way to get around this problem is by comparing the reduced chi-squared of the DEBiL model being considered, with the reduced chi-squared of an alternative model. We used two simple alternative models:

- A constant, set to the average amplitude of the data.
- A smoothed spline, derived from a second order polynomial fit within a sliding

kernel⁶ over the phased light curve.

The constant model should have a larger reduced chi-squared than the best-fit model, while the spline model should usually have a smaller reduced chi-squared. In a way similar to an F-test, we define the fitness score as:

$$\text{Fitness Score} \equiv \frac{\chi_{\nu}^2(\text{const}) - \chi_{\nu}^2(\text{DEBiL})}{\chi_{\nu}^2(\text{const}) - \chi_{\nu}^2(\text{spline})} \quad (2.8)$$

This definition is useful since gross over- or underestimates of the uncertainties will largely cancel out. Light curves that reach step 6 will mostly have fitness scores between 0 and 1. If the reduced chi-squared of the DEBiL model equals the constant model's reduced chi-squared, the fitness score will be 0, and if it equals the spline model's reduced chi-squared, the fitness score will be 1. The fact that most of the DEBiL models have fitness scores close to 1, and sometimes even surpassing it (see Figure 2.6), provides a validation for the fitting algorithm used.

2.7.2 Scatter Score

This test quantifies the systematic scatter of data above or below the model, using the correlation between neighboring residuals. The purpose of this test is to quantify the quality of the model fit independently of the reduced chi-squared test. While the reduced chi-squared test considers the amplitude of the residuals, the scatter score

⁶In our implementation, we used a rectangular kernel whose width varies so as to cover a constant number of data points. This is needed to robustly handle sparsely sampled regions of the phased light curve.

considers their distribution. The scatter score is defined after folding the n data points into a phase curve:

$$\text{Scatter Score} \equiv \frac{\Delta X_n \cdot \Delta X_1 + \sum_{i=2}^n \Delta X_{i-1} \cdot \Delta X_i}{\sum_{i=1}^n \Delta X_i^2} = \frac{\langle \Delta X_{i-1} \cdot \Delta X_i \rangle}{\langle \Delta X_i^2 \rangle} \quad (2.9)$$

Where: $\Delta X_i \equiv X_i(\text{data}) - X_i(\text{model})$

The scatter score will always be between 1 and -1. A score close to 1 occurs when all ΔX_i are approximately equal. In practice, this represent a severe systematic error, where the model is entirely above or entirely below the data. When there is no systematic error, the data are distributed randomly around the model, generating a scatter score approaching 0. Scores close to -1, although theoretically possible when $\Delta X_i \simeq -\Delta X_{i-1}$, can be considered unphysical in that they are unlikely to occur through systematic or non-systematic errors.

2.7.3 Waviness

This is a special case of the scatter score (see previous subsection). Here, we consider only data points in the light curve's plateau (i.e. the region in the phased curve between the eclipsing dips, where both stars are fully exposed). The Waviness score is the scatter score of these data points around their median. The purpose of this test is to get a model-independent measure of irregularities in the binary brightness, out of eclipse. A large value may indicate such effects as stellar elongation, spots, or flares.

2.8 Appendix - Density Estimation

One of the most important criteria for selecting binaries for follow-up is its stellar density. Unfortunately, the parameters that can be extracted from the light curve fitting do not provide us with enough information for deducing the density of any one of the stars in the binary, but only a combined value. We define the mean density as the sum of the stars' masses divided by the sum of their volumes:

$$\bar{\rho} \equiv \frac{M_1 + M_2}{(4\pi/3)(R_1^3 + R_2^3)} = \frac{3\pi}{GP^2(r_1^3 + r_2^3)} \simeq \frac{0.01893 \text{ g cm}^{-3}}{P_{day}^2(r_1^3 + r_2^3)} \simeq \frac{0.01344 \rho_\odot}{P_{day}^2(r_1^3 + r_2^3)} \quad (2.10)$$

Where: $r_{1,2} \equiv R_{1,2}/a$, and from Kepler's law: $a^3 = G(M_1 + M_2)(P/2\pi)^2$

It should be noted here that if the stars' have very different sizes, their mean density will be dominated by the larger one, according to the weighted average:

$$\bar{\rho} = \frac{(r_1/r_2)^3 \rho_1 + \rho_2}{(r_1/r_2)^3 + 1} \quad (2.11)$$

Similarly, assuming $R_1 \geq R_2$, the maximum possible density is:

$$\rho_{\max} \equiv \frac{M_1 + M_2}{(4\pi/3)R_2^3} = \bar{\rho}(1 + (r_1/r_2)^3) \simeq \frac{0.01893 \text{ g cm}^{-3}}{P_{day}^2 r_2^3} \simeq \frac{0.01344 \rho_\odot}{P_{day}^2 r_2^3} \quad (2.12)$$

Adding the assumption that the more dense star of the binary is the less massive component, we can reduce the upper limit of its density to $\rho_{\max}/2$.

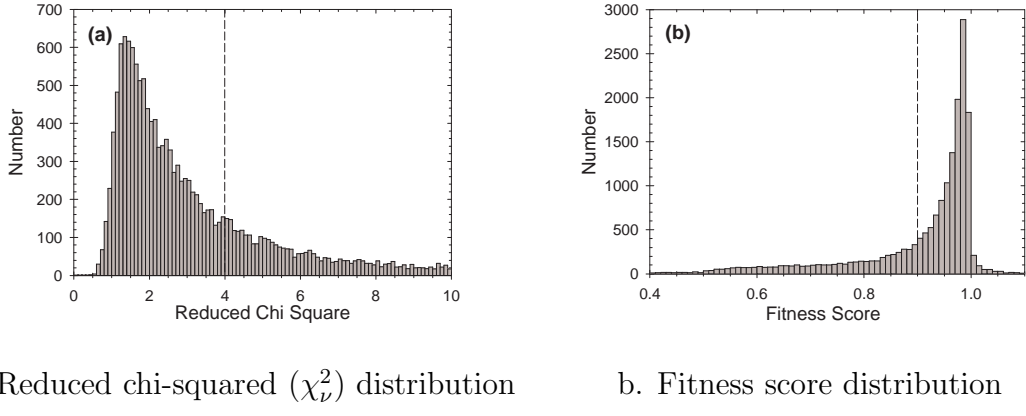


Fig. 2.6.— Results of the DEBiL model fits for OGLE II bulge (see appendix A). The vertical dashed lines mark the filtration thresholds used in our pipeline (< 4 and > 0.9 respectively). Both tests show a definite peak near 1, indicating that it is more likely that DEBiL will produce a “good” fit than a “bad” fit.

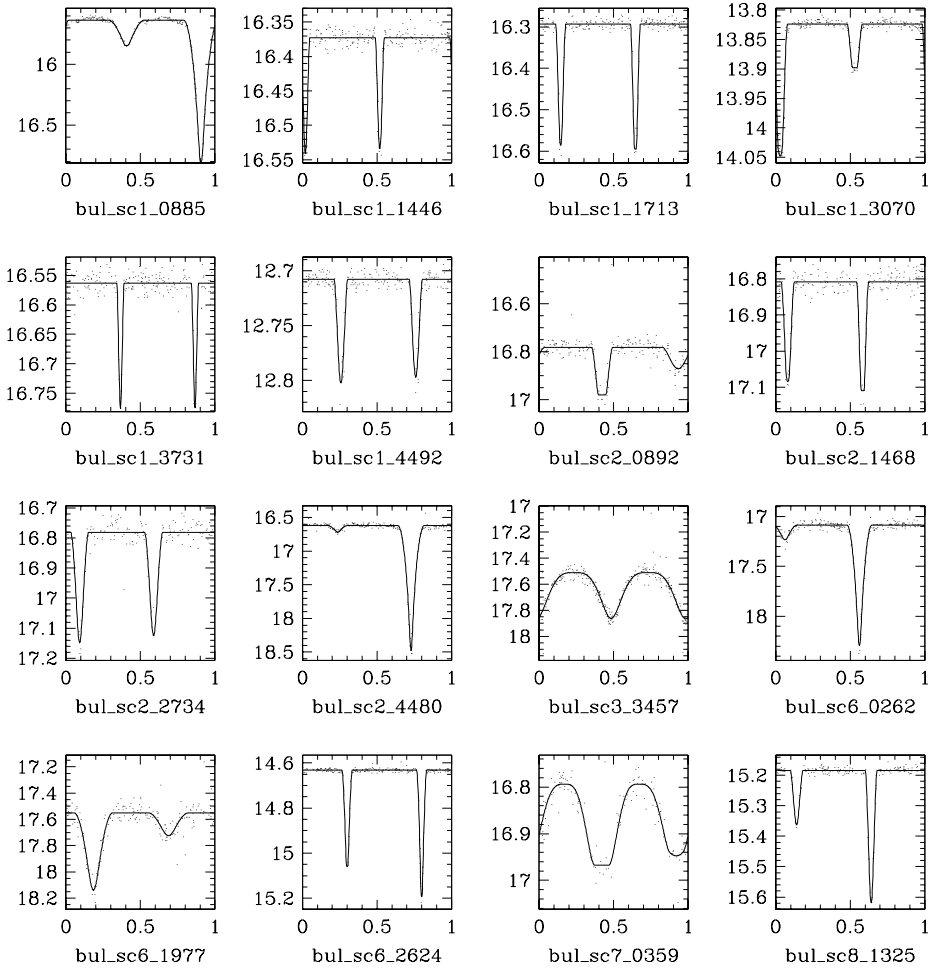


Fig. 2.7.— Selected examples of OGLE II bulge field light curves, with their DEBiL fits.

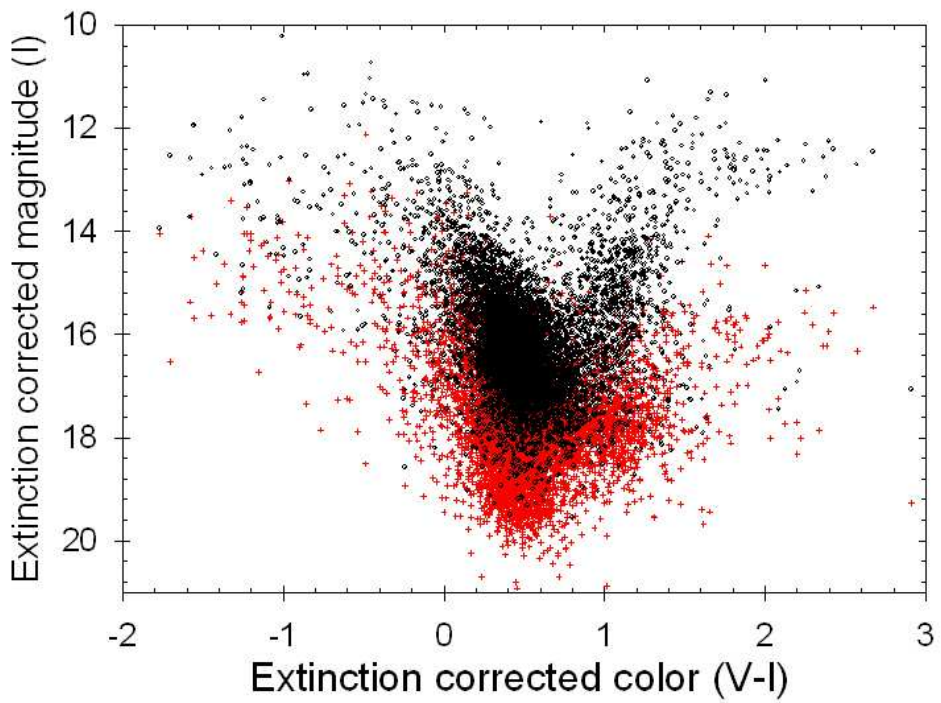


Fig. 2.8.— The color-magnitude diagram of both the primary (circles) and secondary (crosses) stars of the DEBiL models. The color of each star is the combined color of the binary, from (Udalski et al. 2002).

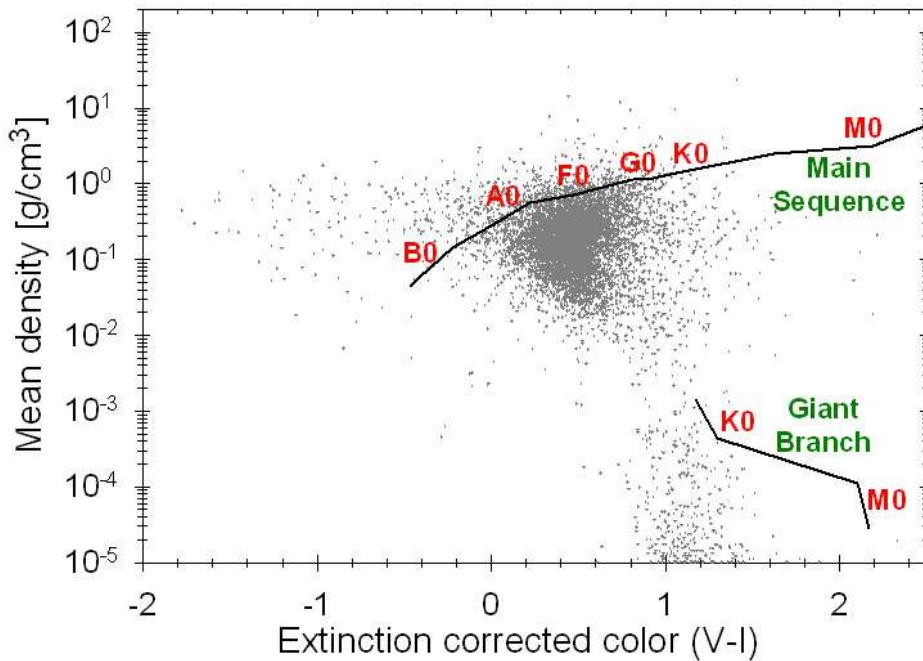


Fig. 2.9.— Color-density diagram of DEBiL models. The solid lines trace the main-sequence stars and giants (Cox 2000). Notice the strong observational selection bias for main-sequence F-type and G-type stars in the OGLE II bulge fields.

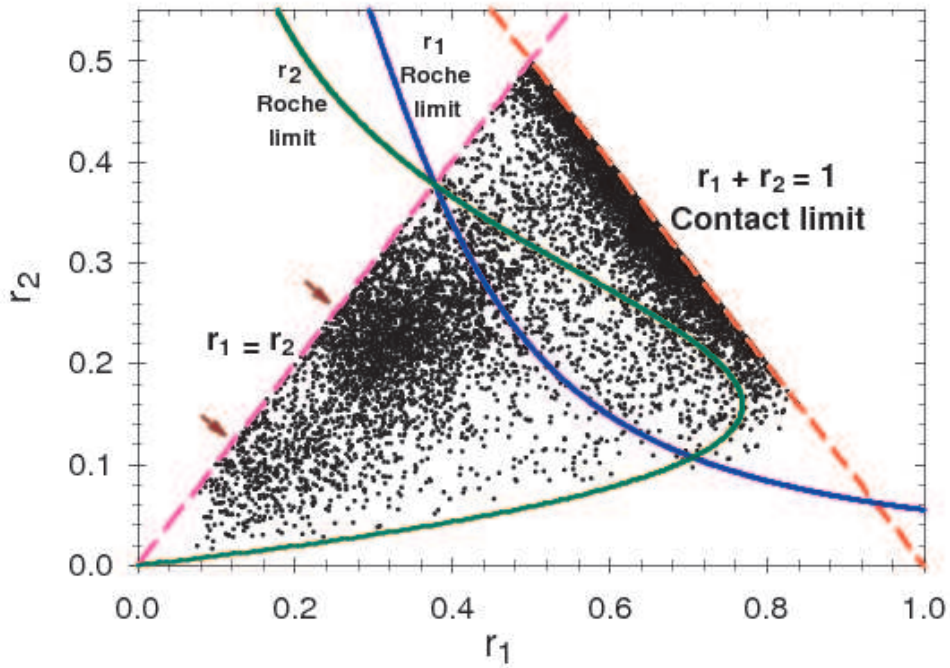


Fig. 2.10.— Radius-radius plot. The dashed lines mark the outer limit of the data. The left side is bounded by the fact that by definition: $r_1 \geq r_2$, while the right side is bounded by the physical contact limit of the stars. The two arrows mark anomalous clusterings. The two solid curves approximate the location where the primary and secondary stars reach their respective Roche limit (see Equations 2.4 & 2.5). Systems between the two solid curves are semidetached, systems to their left are detached, and systems to their right are contact or overcontact systems.

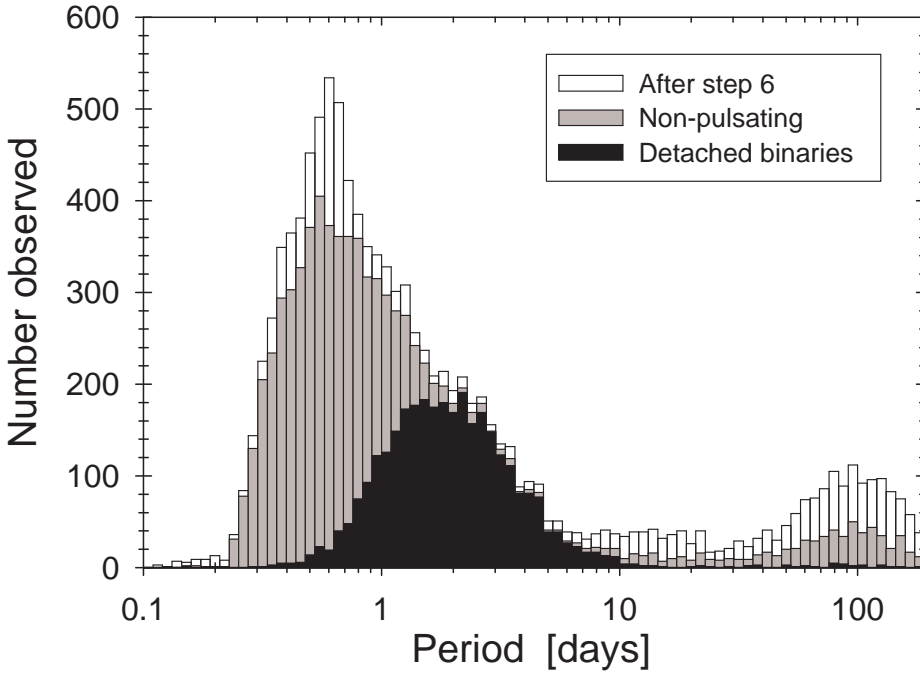


Fig. 2.11.— The period distribution of OGLE II bulge eclipsing binaries, following various stages of filtration.

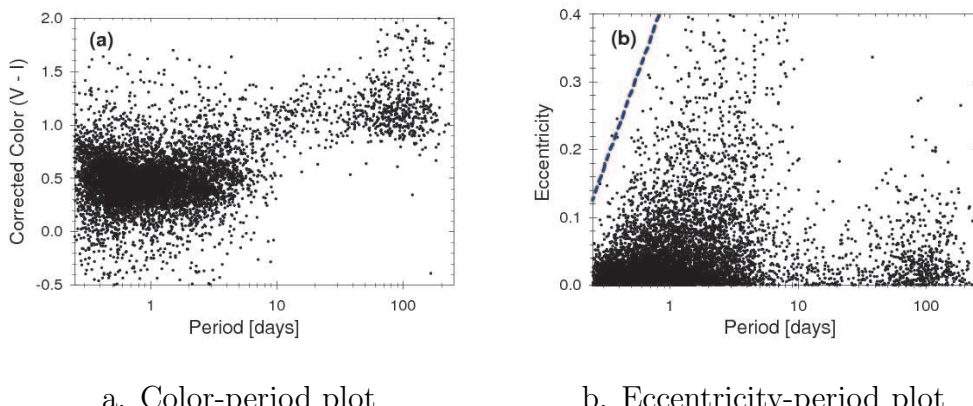


Fig. 2.12.— The relation of the binary V-I color and eccentricity to its period. The upper limit on the eccentricities of short-period binaries (dashed line) is probably due to tidal circularization.

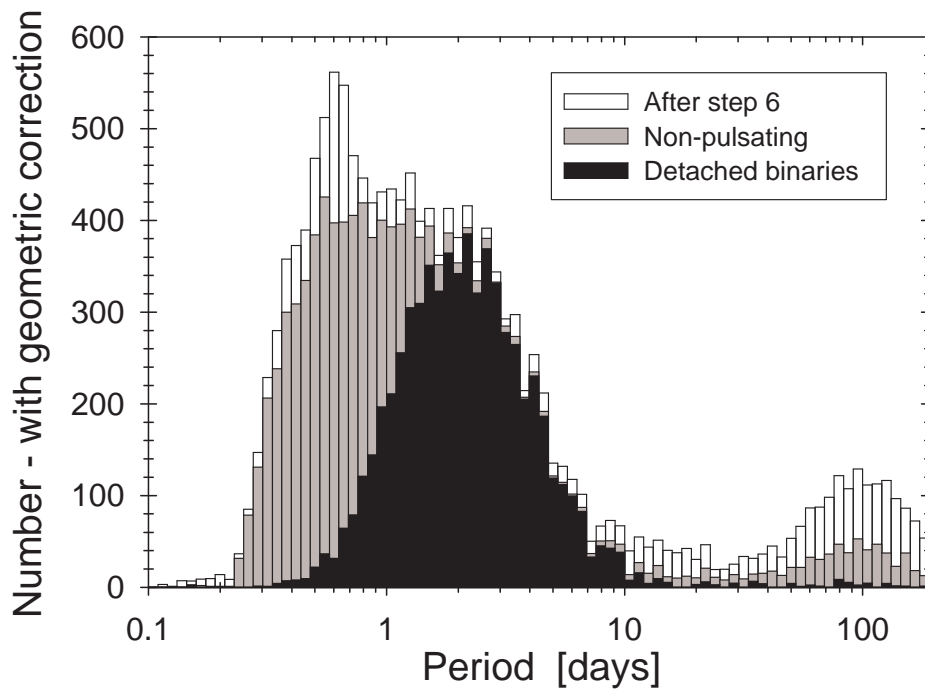


Fig. 2.13.— The period distribution of OGLE II bulge eclipsing binaries, following various stages of filtration, after correcting for their geometric selection effect.

Chapter 3

A Novel Approach to Analyzing Eclipsing Binaries in Large Photometric Datasets

J. Devor & D. Charbonneau 2006, *Astrophysics and Space Science*, **304**, 351–354

The original title of this paper was:

“A Method For Eclipsing Component Identification In Large Photometric Datasets.”

Abstract

We describe an automated method for assigning the most likely physical parameters to the components of an eclipsing binary (EB), using only its photometric light curve and combined colors. In traditional methods (e.g., WD and EBOP) one attempts

to optimize a multi-parameter model over many iterations, so as to minimize the chi-squared value. We suggest an alternative method, where one selects pairs of coeval stars from a set of theoretical stellar models, and compares their simulated light curves and combined colors with the observations. This approach greatly reduces the EB parameter space over which one needs to search, and allows one to determine the components' masses, radii and absolute magnitudes, without spectroscopic data. We have implemented this method in an automated program using published theoretical isochrones and limb darkening coefficients. Since it is easy to automate, this method lends itself to systematic analyses of datasets consisting of photometric time series of large numbers of stars, such as those produced by OGLE, MACHO, TrES, HAT, and many other surveys.

3.1 Introduction

Eclipsing double-lined spectroscopic binaries provide the only method by which both the masses and radii of stars can be estimated without having to resolve spatially the binary or rely on astrophysical assumptions. Despite the large variety of models and parameter-fitting implementations (e.g., WD and EBOP), their underlying methodology is essentially the same. Photometric data provides the light curve of the EB, and spectroscopic data provide the radial velocities of its components. The depth and shape of the light curve eclipses constrain the components' brightness and fractional radii, while the radial velocity sets the length scale of the system. In order to characterize fully the components of the binary, one needs to combine all of this information. Unfortunately, only a small fraction of all binaries eclipse, and

spectroscopy with sufficient resolution can be performed only for bright stars. The intersection of these two groups leaves a pitifully small number of stars.

In the past decade, there has been a dramatic growth in the number of stars with high-quality, multi-epoch, photometric data. This has been due to major advances in both CCD detectors and the implementation of image-difference analysis techniques (Crotts 1992; Alard & Lupton 1998; Alard 2000), which enables simultaneous photometric measurements of tens of thousands of stars in a single exposure. Today, there are many millions of light curves available from a variety of surveys, such as OGLE, Udalski et al. (1994); MACHO, Alcock et al. (1998); TrES, Alonso et al. (2004); and HAT, Bakos et al. (2004). But there has not been a corresponding growth in the quantity of spectroscopic data, nor is this likely to occur in the near future. Thus, the number of fully-characterized EBs has not grown significantly. In recent years there has been a growing effort to mine the wealth of available photometric data, by employing simplified EB models in the absence of spectroscopic observations (Wyithe & Wilson 2001, 2002; Devor 2004, 2005).

In this paper we present a novel approach, which utilizes theoretical models of stellar properties to estimate the orbital parameters as well as the masses, radii, and absolute magnitudes of the stars, while requiring *only* a photometric light curve and an estimate of the binary's combined color. This approach can be used to characterize quickly large numbers of eclipsing binaries, however it is not sufficient to improve stellar models since underlying isochrones must be assumed. We have created two implementations of this idea. The first, which we have named MECI-express, and is described in section 3.2, is a “quick and dirty” program that is designed as a simple extension to the Detached Eclipsing Binary Light curve (DEBiL) fitter (Devor 2004,

2005). The second, which we have named MECI, and is described in section 3.3, is considerably more accurate, but also more computationally demanding. The source code for both MECI-express and MECI will be provided upon request.

3.2 Express Method for Eclipsing Component Identification (MECI-express)

The primary application of MECI-express is to identify the stellar components of a given EB. It operates after a conventional EB model-fitting program has already analyzed the given EB’s light curve. In our implementation, we chose to employ DEBiL (Devor 2004, 2005) since it is simple, fast, and fully automated. The fitted parameters are the orbital period (P), the apparent magnitudes ($mag_{1,2}$), and the fractional radii ($r_{1,2}$) of the binary components. A fractional radius is defined as the radius ($R_{1,2}$) divided by the sum of the components’ semimajor axes (a). In MECI-express we iterate through a large group of MK spectral type pairings, to each of which we associate typical stellar parameters (Cox 2000). These stellar parameters are the masses ($M_{1,2}$), the radii ($R_{1,2}$), and the absolute magnitudes ($Mag_{1,2}$) of the binary components. If the assumed values of the stellar parameters match the true values, then the stellar and fitted parameters should obey to the following equations:

$$\frac{4\pi^2 R_1^3}{G(M_1 + M_2)} = P^2 r_1^3 \quad (3.1)$$

$$\frac{4\pi^2 R_2^3}{G(M_1 + M_2)} = P^2 r_2^3 \quad (3.2)$$

$$Mag_1 - Mag_2 = mag_1 - mag_2 \quad (3.3)$$

We also may have additional constraints from the observed out-of-eclipse combined colors of the system. For example, in the case of OGLE II targets, we have the estimated V-I color:

$$Mag_V - Mag_I = mag_V - mag_I \quad (3.4)$$

We assume that the color has been corrected for reddening and that no systematic errors are present, so any inequalities would be due to an incorrect choice for the component pairing. The likelihood of each pairing is assessed by calculating the difference between the left-hand-side (stellar parameters) and right-hand-side (fitted parameters) of each equation. These differences are divided by their uncertainties, and added in quadrature. The pairing with the smallest sum is deemed the most likely pairing. For each given EB light curve, MECI-express returns the list of the top ranked (most likely) binary pairings, with their corresponding sums. MECI-express can also be used to create a contour plot of the probability distribution for all pairings. We illustrate an example of individual MECI-express components in Figures 3.1.a-c, which are then combined to create the result shown in Figure 3.2.a.

3.3 Method for Eclipsing Component Identification (MECI)

MECI was developed to improve significantly upon the accuracy of MECI-express (see Table 1). This was done as follows: We replaced the use of spectral types with

the more fundamental (and continuous) quantities of mass and age. Furthermore, in MECI we assume that the two binary components are coeval, thus replacing the 2-dimensional spectral type - spectral type grid, with a 3-dimensional mass-mass-age grid. Finally, we no longer rely on parameter fits of the components' apparent magnitudes and fractional radii directly from the light curve, which are often very uncertain, nor do we assume constant limb darkening coefficients. Instead, we interpolate these values for the given mass-mass-age pairing, from precalculated tables [Yonsei-Yale isochrones (Kim et al. 2002) ; ATLAS limb darkening coefficients (Kurucz 1992), used when $T_{eff} \geq 10000K$ or $\log g \leq 3.5$; PHOENIX limb darkening coefficients (Claret 1998, 2000), used when $T_{eff} < 10000K$ and $\log g > 3.5$]. Thus, by assuming the masses ($M_{1,2}$) of the EB components and the system's age, we can look-up the radii ($R_{1,2}$), the absolute magnitudes ($Mag_{1,2}$), and the limb darkening coefficients for the binary components. We then use these values, as well as the observationally-determined period (P) and combined magnitude out of eclipse (mag_{comb}), to calculate the apparent magnitudes ($mag_{1,2}$) and fractional radii ($r_{1,2}$) of the EB components, as follows:

$$mag_1 = mag_{comb} + 2.5 \log [1 + 10^{-0.4(Mag_2 - Mag_1)}] \quad (3.5)$$

$$mag_2 = mag_1 + (Mag_2 - Mag_1) \quad (3.6)$$

$$\begin{aligned} a &= [G(M_1 + M_2)(P/2\pi)^2]^{1/3} \simeq \\ &\quad 4.206R_\odot(M_1/M_\odot + M_2/M_\odot)^{1/3} P_{day}^{2/3} \end{aligned} \quad (3.7)$$

$$r_{1,2} = R_{1,2}/a \quad (3.8)$$

Besides the epochs of eclipses, which can be determined directly from the EB

light curve, there are only two additional parameters required for us to simulate the light curves of the given pairing: the orbital eccentricity (e) and inclination (i). For binaries with short periods ($\lesssim 2$ days) and a secondary eclipse precisely half an orbit after the primary eclipse, it is reasonable to assume a circular orbit ($e = 0$). Otherwise, one should use the eccentricity derived by an EB model-fitting program (we use DEBiL). Finding the inclination robustly is more difficult. We employ a bracket search (Press et al. 1992), which returns the inclination that produces the best resulting fit.

To summarize, for every combination of component masses and system age of an EB, we can look-up, calculate, or fit all the parameters needed to simulate its light curve (P, limb darkening coefficients, $\text{mag}_{1,2}$, $r_{1,2}$, epochs of eclipses, e , i), as well as its apparent combined color. We systematically iterate through many such combinations. For each one we compare the expected light curve with the observations, and calculate the reduced chi-squared value (χ^2_ν). We also compare each observed color ($O_c \pm \epsilon_c$) with its calculated value (C_c), and combine them by defining: $score \equiv (w\chi^2_\nu + \sum_{c=1}^N [(O_c - C_c)/\epsilon_c]^2)/(w + N)$. Where w is the χ^2_ν information weighting. We use $w = 1$, and assume that the smaller the score, the more likely it is that we have chosen the correct binary pairing. One can visualize this result using a series of $score(M_1, M_2)$ contour plots, each with a constant age (e.g., Figure 3.2.b).

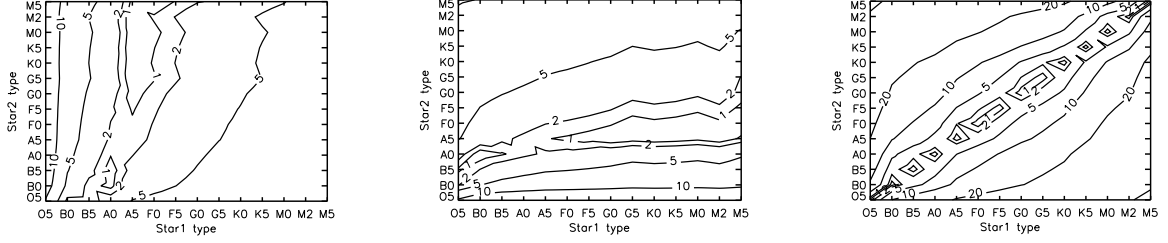
3.4 Conclusions

We have described a novel method for identifying an EB's components using only its photometric light curve and combined color. By utilizing theoretical isochrones and limb darkening coefficients, this method greatly reduces the EB parameter space over which one needs to search. This approach seeks to estimate the masses, radii and absolute magnitudes of the components, without spectroscopic data. We described two implementations of this method, MECI-express and MECI, which enable systematic analyses of datasets consisting of photometric time series of large numbers of stars, such as those produced by OGLE, MACHO, TrES, HAT, and many others. Such techniques are expected to grow in importance with the next generation surveys, such as Pan-STARRS (Kaiser et al. 2002) and LSST (Tyson 2002).

We are grateful to Guillermo Torres for many helpful conversations.

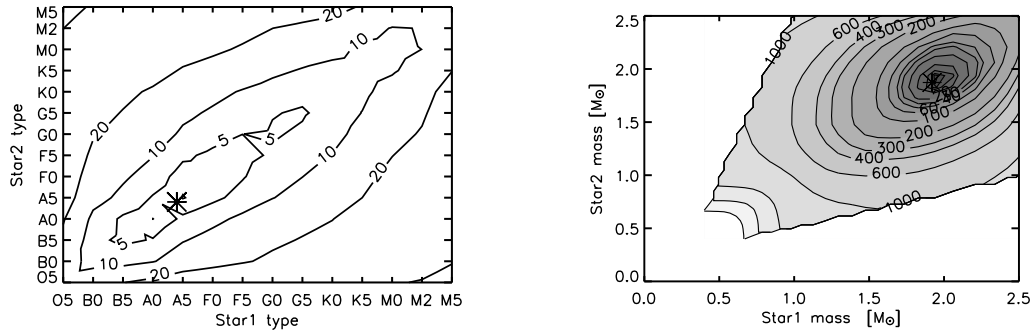
Table 3.1. A comparison of the results produced by MECI-express, MECI, and conventional analyses with their uncertainties (Lacy et al. 2000, 2002, 2003). The square brackets with numerical values indicate the deviation of our results from those of the conventional approach.

Parameter	MECI-express		MECI			Lacy et al. (2000, 2002, 2003)		
	Mass 1 [M_{\odot}]	Mass 2 [M_{\odot}]	Mass 1 [M_{\odot}]	Mass 2 [M_{\odot}]	Age [Gyr]	Mass 1 [M_{\odot}]	Mass 2 [M_{\odot}]	Age [Gyr]
FS Mon	2.9 (A0)	2.0 (A5)	1.62	1.52	1.4	1.632	1.462	1.6
	[77.7%]	[36.8%]	[0.6%]	[4.1%]	[0.2]	± 0.012	± 0.010	± 0.3
WW Cam	2.0 (A5)	2.0 (A5)	1.97	1.89	0.5	1.920	1.873	0.5
	[4.2%]	[6.8%]	[2.8%]	[1.0%]	[0.0]	± 0.013	± 0.018	± 0.1
BP Vul	2.0 (A5)	1.6 (F0)	1.77	1.48	0.7	1.737	1.408	1.0
	[15.1%]	[13.6%]	[2.1%]	[5.4%]	[0.3]	± 0.015	± 0.009	± 0.2



a. Constraints from Eq. 3.1 b. Constraints from Eq. 3.2 c. Constraints from Eq. 3.3

Fig. 3.1.— Contour plots of the absolute difference between the left-hand-side and the right-hand-side of each equation, divided by its uncertainty, as applied to the WW Camelopardalis light curve (Lacy et al. 2002). Adding these results in quadrature, produces the likelihood plot shown in Figure 3.2.a.



a. MECI-express likelihood plot b. MECI likelihood plot (age = 0.6 Gyr)

Fig. 3.2.— A comparison of the MECI-express (left) and MECI (right) likelihood contour plots for WW Camelopardalis. The value of the contours are described in the body of the text. The asterisk marks the solution of Lacy et al. (2002).

Chapter 4

MECI: A Method for Eclipsing Component Identification

J. Devor & D. Charbonneau 2006, *The Astrophysical Journal*, **653**, 647–656

Abstract

We describe an automated method for assigning the most probable physical parameters to the components of an eclipsing binary, using only its photometric light curve and combined colors. With traditional methods, one attempts to optimize a multi-parameter model over many iterations, so as to minimize the chi-squared value. We suggest an alternative method, where one selects pairs of coeval stars from a set of theoretical stellar models, and compares their simulated light curves and combined colors with the observations. This approach greatly reduces the parameter space over which one needs to search, and allows one to estimate the

components' masses, radii and absolute magnitudes, without spectroscopic data. We have implemented this method in an automated program using published theoretical isochrones and limb darkening coefficients. Since it is easy to automate, this method lends itself to systematic analyses of datasets consisting of photometric time series of large numbers of stars, such as those produced by OGLE, MACHO, TrES, HAT, and many others surveys.

4.1 Introduction

Eclipsing double-lined spectroscopic binaries provide the only method by which both the masses and radii of stars can be estimated without having to resolve the binary spatially or rely on astrophysical assumptions. Despite the large variety of models and parameter-fitting implementations [e.g., WD (Wilson & Devinney 1971) and EBOP (Etzel 1981; Popper & Etzel 1981)], their underlying methodology is essentially the same. Photometric data provide the light curve of the eclipsing binary (EB), and spectroscopic data provide the radial velocities of its components. The depth and shape of the light curve eclipses constrain the components' brightness and fractional radii, while the radial velocity sets the length scale of the system. In order to fully characterize the components of the binary, one needs to combine all of this information. Only a small fraction of all binaries eclipse, and spectra with sufficient resolution and signal-to-noise ratios can be gathered only for bright stars. The intersection of these two groups leaves a small number of stars.

Over the past decade, the number of stars with high-quality, multi-epoch, photometric data has grown dramatically due to the growing interest in finding

gravitational lensing events (Wambsganss 2006) and eclipsing extrasolar planets (Charbonneau et al. 2007). In addition, major technical improvements in both CCD detectors and implementations of image-difference analysis techniques (Crotts 1992; Alard & Lupton 1998; Alard 2000) enable simultaneous photometric measurements of tens of thousands of stars in a single exposure. Today, there are many millions of light curves available from a variety of surveys, such as OGLE (Udalski et al. 1994), MACHO (Alcock et al. 1998), TrES (Alonso et al. 2004), HAT (Bakos et al. 2004), and XO (McCullough et al. 2006). Despite the increase in photometric data, there has not been a corresponding growth in the quantity of spectroscopic data, nor is this growth likely to occur in the near future. Thus, the number of fully characterized EBs has not grown at a rate commensurate with the available photometric datasets.

In recent years, there has been a growing effort to mine the wealth of available photometric data, by employing automated pipelines that use simplified EB models in the absence of spectroscopic observations and hence without a fixed physical length scale or absolute luminosity (Wyithe & Wilson 2001, 2002; Devor 2004, 2005). In this paper, we present a method that utilizes theoretical isochrones and multi-epoch photometric observations of the binary system to estimate the physical parameters of the component stars, while still not requiring spectroscopic observations.

Our Method for Eclipsing Component Identification¹ (MECI), finds the most probable masses, radii, and absolute magnitudes of the stars. The input for MECI is an EB's photometric light curve and out-of-eclipse colors (we note that in the

¹The source code can be downloaded from: <http://cfa-www.harvard.edu/~jdevor/MECI.html>

absence of color information, the accuracy in the estimation of the stellar parameters is significantly reduced; §4.4.2). This approach can be used to quickly characterize large numbers of eclipsing binaries; however it is not sufficient to improve stellar models, since underlying isochrones must be assumed.

In a previous paper (Devor & Charbonneau 2006a), we outlined the ideas behind both MECI and a closely related, “quick and dirty” alternative, which we called “MECI-express.” Although MECI-express is much faster and easier to implement, it is also far less accurate. For this reason we will not discuss it further, and instead concentrate exclusively on MECI. We discuss its applications (§4.2), aspects of its implementation (§4.3), tests of its accuracy (§4.4), and finally summarize our findings (§4.5).

4.2 Motivation

4.2.1 Characterizing the Binary Stellar Population

First and foremost, MECI is designed as a high throughput means to systematically estimate the masses of large numbers of stars. Although the result in each system is uncertain, by statistically analyzing large catalogs, one can reduce the non-systematic errors. Much work has already been invested into characterizing binary systems through spectroscopic binary surveys (e.g., Duquennoy & Mayor 1991; Pourbaix et al. 2004), yet the limited data and their large uncertainties have led to inconsistent results (Mazeh et al. 2005). The driving questions that have spurred debate in the community include: What are the initial mass functions of the

primary and secondary components? How do they relate to the initial mass function of single stars? What is the distribution of the components' mass ratio, q , and in particular, does it peak at unity? This lack of understanding is further highlighted by the fact that most of the stars in our galaxy are members of binary systems, and that these questions have lingered for over a century. MECI may help sort this out by systematically characterizing the component stars of many EB systems.

By requiring only photometric data, a survey using MECI can study considerably fainter binary systems than spectroscopic surveys, and thus remain complete to a far larger volume. As an illustrative example, the difference image analysis of the bulge fields of OGLE II, using the Las Campanas 1.3m Warsaw telescope in a drift-scan mode (an effective exposure time of 87 seconds), attained a median noise level of 0.1 mag, for $I = 18$ binaries, even in moderately crowded fields (Wozniak 2000). In contrast to this, the CfA Digital Speedometer on the 1.5m F. L. Whipple Observatory telescope has a spectral resolution of $R \simeq 35,000$ (at 5177Å) and typically yields a radial velocity precision of 0.5 km s^{-1} , with a faint magnitude limit of $V = 13$ (Latham 1992). Although the limiting magnitudes are very much dependent on the throughput of the relevant instruments and the precision one wishes to achieve, this 5 magnitude difference for telescopes of similar aperture corresponds to a factor of 10 in distance or 1000 in volume, and illustrates the significant expansion that can be achieved by purely photometric surveys. Conversely, one can achieve the same magnitude limit with an aperture 10 times smaller. The success of this approach has been demonstrated by several automated observatories, such as TrES (Alonso et al. 2004) and HAT (Bakos et al. 2004), which each use networks of observatories with 10-cm camera lenses to monitor stars to $V \simeq 13$.

4.2.2 Identifying Low-Mass Main-Sequence EBs

One of the most compelling applications of MECI will be to quickly sort thousands of EBs present in large photometric surveys, and to subsequently select a small subset of objects from the resulting catalog for further study. In particular, lower main-sequence stars that are partially or fully convective have not been studied with a level of detail remotely approaching that of solar-type (and more massive) stars. This is particularly troubling since late-type stars are the most common in the Galaxy, and dominate its stellar mass. It has been shown that models underestimate the radii of low-mass stars by as much as 15-20% (Lacy 1977b; Torres & Ribas 2002); a significant discrepancy considering that for solar-type stars the agreement with the observations is typically within 1-2% (Andersen 1998). Similar problems exist for the effective temperatures predicted theoretically for low-mass stars. Progress in this area has been hampered by the lack of suitable M-dwarf binary systems with accurately determined stellar properties, such as mass, radius, luminosity, surface temperature, and metallicity. Detached eclipsing systems are ideal for this purpose, but only five are known among M-type stars: CM Dra (Lacy 1977a; Metcalfe et al. 1996), YY Gem (Kron 1952; Torres & Ribas 2002), CU Cnc (Delfosse et al. 1999; Ribas 2003), OGLE BW3 V38 (Maceroni & Rucinski 1997; Maceroni & Montalbán 2004), and TrES-Her0-07621 (Creevey et al. 2005). They range in mass from about $0.25 M_{\odot}$ (CM Dra) to $0.6 M_{\odot}$ (YY Gem). The number of such objects could be greatly increased by using tools such as MECI to mine the extant photometric datasets and locate these elusive low-mass systems.

4.2.3 EBs as Standard Candles

Using MECI, we are able to estimate the absolute magnitude of the binary system. This, together with its extinction-corrected out-of-eclipse apparent magnitude, allows us to then calculate the distance modulus to any given EB. The estimation of distances to EBs dates back to Stebbing (1910), and their use as distance candles in the modern astrophysical context was recently elucidated by Paczynski (1997). However, unlike these studies, MECI does not require spectroscopy and therefore is able to analyze binaries that are significantly less luminous (see §4.2.1). Although the distance estimation from MECI will be uncertain, in many cases this will still be an improvement over existing methods. For example, if there are many EBs in a stellar cluster, the distance estimate can be greatly improved by combining their results, reducing the non-systematic errors by a factor of the square root of the number of systems. Following Guinan et al. (1996), one might be able to use such clustered EB standard candles to better constrain the distance to the LMC and SMC, and thus be able to further constrain the bottom of the cosmological distance ladder. In the case of MECI, the uncertainties of each distance measurement will be considerably larger, but as suggested by T. Mazeh (2005, private communication), this will be compensated for by the far larger number of measurements that can be made (see, e.g., Figure 4.1). Another intriguing application of such EB standard candles is to map large scale structures in the Galaxy, such as the location and orientation of the Galactic bar, arms, and merger remnants [see, e.g., Vallée (2005) and references therein].

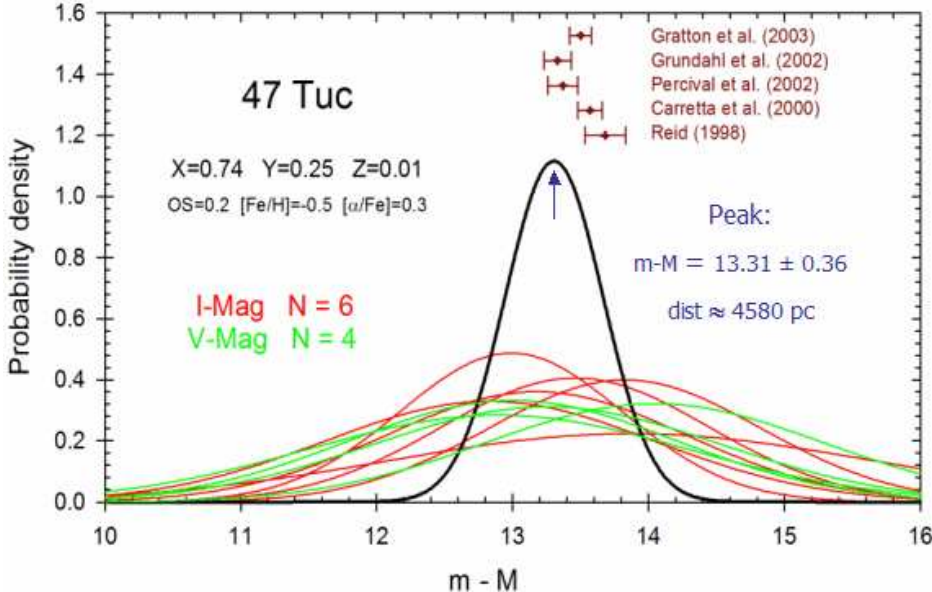


Fig. 4.1.— This figure was not originally part of this paper. We include it here since it nicely illustrates the point discussed in §4.2.3. In this figure we estimate the distance modulus of 47 Tucanae, by combining the results of ten MECI analyses of EB LCs (*I*-band or *V*-band) observed in this globular cluster (Albrow et al. 2001). We show the results of each of these MECI analyses as a Gaussian distribution. The product of these distributions produced the far narrower Gaussian distribution indicated by the arrow. The Peak of the combined result is consistent with a variety of other methods that were used to derive the distance modulus (Reid 1998; Carretta et al. 2000; Percival et al. 2002; Grundahl et al. 2002; Gratton et al. 2003).

4.3 Method

The EB component identification is performed in two stages. First the orbital parameters of the EB are estimated (§4.3.1), then the most likely stellar parameters are identified (§4.3.2). Our implementation of MECI has the option to fix the estimates of the orbital parameters, or to fine-tune them for each stellar pairing considered in the second stage. The average running time for MECI to analyze a 1000-point light curve on a single 3.4GHz Intel Xeon CPU is 0.4 minutes. If we permit fine tuning of the orbital parameters for each pairing, the running time grows to 6 minutes per light curve.

4.3.1 Stage 1: Finding the Orbital Parameters

In the first stage, we estimate the EB’s orbital parameters from its light curve. Many EBs have orbital periods of a few days or less, owing to the greater probability for such systems to present mutual eclipses, and to the limited baselines in the datasets from which they are identified. Most of these systems will have orbits that have been circularized due to tidal effects. For such circular orbits, the only parameters we seek are the orbital period, P , and epoch of periastron, t_0 . For non-circular orbits we also fit the orbital eccentricity, e , and the argument of periastron, ω . The period is determined using a periodogram, and the remaining parameters are obtained through fitting the offset, duration and time interval between the light curve’s eclipses (see below). Holding these parameters fixed at these initial estimates significantly reduces the computational requirements of MECI.

We postpone fitting the orbital inclination, i , until the second stage, since it is difficult to determine this parameter robustly without first assuming values for the stellar radii and masses. This difficulty arises because it is often difficult to distinguish a small secondary component from a large secondary component in a grazing orbit. In stage 2, additional information, such as the theoretical stellar mass-radius relation and colors are used to help resolve this degeneracy.

The procedure for fitting the aforementioned parameters from the EB light curve is a well-studied problem (Kopal 1959; Wilson & Devinney 1971; Etzel 1991). We chose to estimate the period with a variant of the analysis of variances (AOV) periodogram² by Schwarzenberg-Czerny (1989, 1996). We then use the Detached Eclipsing Binary Light curve (DEBiL) fitter³ by Devor (2004, 2005) for fitting the remaining orbital parameters. For non-circular systems, following Kopal (1959) and Kallrath & Milone (1999), we estimate the orbital eccentricity and argument of periastron from the orbital period, the duration of the eclipses, $\Theta_{1,2}$, and the time interval between the eclipse centers, Δt , as follows:

$$\omega \simeq \arctan \left[\frac{2}{\pi} \left(\frac{\Theta_1 - \Theta_2}{\Theta_1 + \Theta_2} \right) \left(\frac{\Delta t}{P} - \frac{1}{2} \right)^{-1} \right], \text{ and} \quad (4.1)$$

$$e \simeq \frac{\pi}{2 \cos \omega} \left| \frac{\Delta t}{P} - \frac{1}{2} \right|. \quad (4.2)$$

In practice, it is difficult to accurately determine the eclipse duration. We estimate this duration by first calculating the median flux outside the eclipses, then estimating the midpoints and depths of the eclipses using a spline. We then assign the duration of each eclipse to be the time elapsed from the moment at which

²The source code and running examples of both the AOV periodogram and the DEBiL fitter can be downloaded from: <http://cfa-www.harvard.edu/~jdevor/DEBiL.html>

the light curve during ingress crosses the midpoint between the out-of-eclipse and bottom-of-eclipse fluxes, until the moment at which the light curve crosses the corresponding point during egress.

4.3.2 Stage 2: Finding the Absolute Stellar Parameters

In the second stage, we estimate the EB’s absolute stellar parameters by iterating through many possible stellar pairings, simulating their expected light curves (see Figure 4.2), and finding the pairing that minimizes the χ^2_ν function (see §4.3.3). The parameters we fit are the masses of the two EB components, $M_{1,2}$, their age (the components are assumed to be coeval), and their orbital inclination, i . Optionally, we can also fine-tune the orbital parameters obtained from the first stage. This option is necessary only for binaries with eccentric orbits, since varying their inclination will affect the fit of their previously estimated orbital parameters. The flow diagram for the entire procedure is shown in Figure 4.3.

If an estimate of the out-of-eclipse combined apparent magnitude, mag_{comb} , of the EB (i.e. the light curve plateau) is available, we may also estimate the distance modulus. If mag_{comb} is not available (e.g., if the light curve has been normalized), the distance modulus cannot be evaluated unless an independent measurement of the out-of-eclipse brightness is available. In either case, this procedure does not affect our estimates of the stellar parameters.

Once we assume the masses and age of the binary components, we use pre-calculated theoretical tables to look up their absolute stellar parameters, namely their radii, $R_{1,2}$, and absolute magnitudes, $Mag_{1,2}$. We use the Yonsei-Yale isochrones

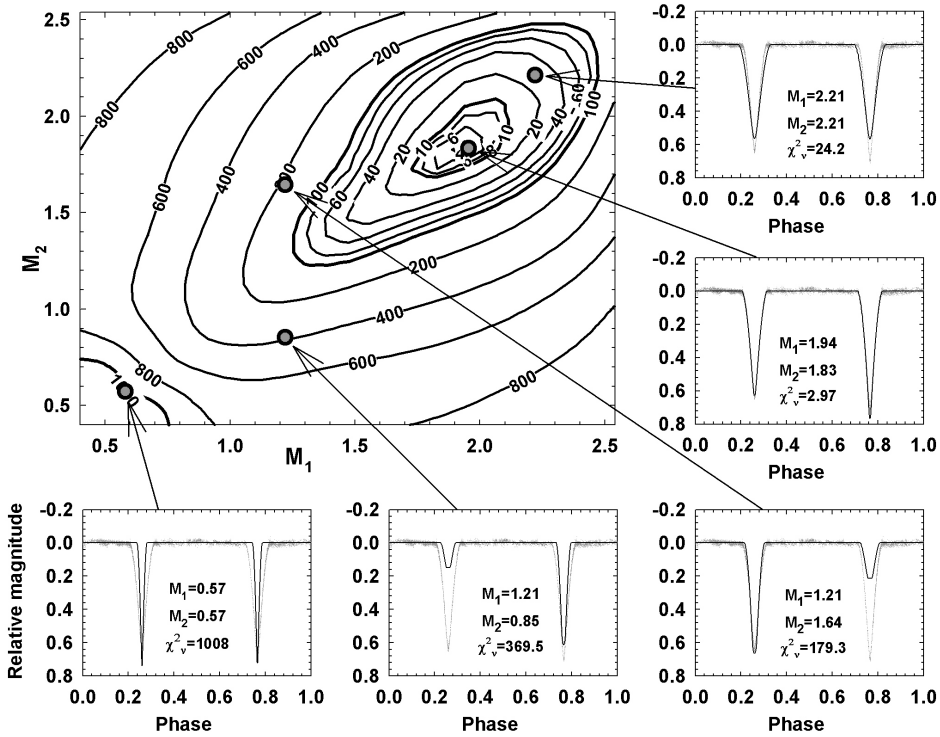


Fig. 4.2.— The large upper-left panel shows the MECI χ^2_ν surface as a function of the assumed masses (in solar units) of the component stars in the WW Camelopardalis system. The model light curve at five locations in the grid is shown in the smaller panels, overplotted on the observed light curve from Lacy et al. (2002).

of solar metallicity (Kim et al. 2002) to specify the binary components’ radii and absolute magnitudes, in a range of filters $(U, B, V, R, I)_{Cousins}$ and $(J, H, K)_{ESO}$. We note that the Yonsei-Yale isochrones do not extend below $0.4 M_\odot$. To consider stars with masses below this value we constructed tables from the isochrones of Baraffe et al. (1998), which are generally more reliable for masses below $0.75 M_\odot$.

Together with the orbital parameters (§4.3.1), we have all the information required to simulate the EB light curve. The fractional radii, $r_{1,2}$, and apparent magnitudes, $mag_{1,2}$, of the binary components, which are needed for this calculation, are calculated as follows:

$$a = [G(M_1 + M_2)(P/2\pi)^2]^{1/3} \simeq 4.206R_\odot(M_1/M_\odot + M_2/M_\odot)^{1/3}(P/day)^{2/3}, \quad (4.3)$$

$$r_{1,2} = R_{1,2}/a, \quad (4.4)$$

$$mag_1 = mag_{comb} + 2.5 \log [1 + 10^{-0.4(Mag_2 - Mag_1)}], \text{ and} \quad (4.5)$$

$$mag_2 = mag_1 + (Mag_2 - Mag_1). \quad (4.6)$$

We create model light curves using DEBiL, which has a fast light curve generator. DEBiL assumes that the EB is detached, with limb-darkened spherical components (i.e. no tidal distortions or reflections). To describe the stellar limb darkening, it employs the quadratic law (Claret et al. 1995):

$$I(\theta) = I_0 \left[1 - \tilde{a}(1 - \cos \theta) - \tilde{b}(1 - \cos \theta)^2 \right], \quad (4.7)$$

where θ is the angle between the line of sight and the emergent flux, I_0 is the flux at the center of the stellar disk, and \tilde{a} , \tilde{b} are coefficients that define the amplitude of the center-to-limb variations. We use the ATLAS (Kurucz 1992) and PHOENIX

(Claret 1998, 2000) tables to look up the quadratic limb darkening coefficients, for high-mass ($T_{eff} \geq 10000\text{K}$ or $\log g \leq 3.5$) and low-mass ($T_{eff} < 10000\text{K}$ and $\log g > 3.5$) main-sequence stars respectively.

Finally, the orbital inclination is fit at each iteration so as to make the simulated light curve most similar to the observations. For this we employed the robust “golden section” bracket search algorithm (Press et al. 1992). This inner loop dominates the computational time required. In the case of non-circular orbits, it is often necessary to iterate the estimates of the orbital parameters (e , t_0 , ω , i). When this option is enabled, MECI employs the rolling simplex algorithm (Nelder 1965; Press et al. 1992), which fits all four orbital parameters simultaneously.

4.3.3 Assessing the Likelihood of a Binary Pairing

The observational data for each EB consists of N_{lc} observed magnitudes O_i , each with an associated uncertainty ϵ_i , as well as N_{colors} out-of-eclipse colors \tilde{O}_c , each with an uncertainty $\tilde{\epsilon}_c$. Our model yields the corresponding predicted light curve magnitudes C_i and out-of-eclipse colors \tilde{C}_c . We define the goodness-of-fit function to be:

$$\chi^2_\nu = \frac{1}{w + N_{colors}} \left[\frac{w}{N_{lc}} \sum_{i=1}^{N_{lc}} \left(\frac{O_i - C_i}{\epsilon_i} \right)^2 + \sum_{c=1}^{N_{colors}} \left(\frac{\tilde{O}_c - \tilde{C}_c}{\tilde{\epsilon}_c} \right)^2 \right], \quad (4.8)$$

where w is a factor that describes the relative weights assigned to the light curve and color data (see below). The value of χ^2_ν should achieve unity if the assumed model accurately describes the data, and the errors are Gaussian-distributed and are estimated correctly.

In practice, typical light curves may have $N_{lc} > 1000$ points, whereas only

$1 \leq N_{colors} \leq 5$ might be available. We have found it necessary to select a value for w that increases the relative weight of the color information to obtain reliable results ($w < N_{lc}$). In general, the optimal value for w will depend on the accuracy of the observed colors \tilde{O}_c and the degree to which the EB light curve deviates from the assumption of two well-detached, limb-darkened spherical components. Based on the tests described in §4.4, we find that a wide range of values for w produces similar results, and that values in the range $10 \leq w \leq 100$ most accurately recover the correct values for the stellar parameters.

We identify the global minimum of χ^2_ν in three steps: First, we calculate the value of χ^2_ν at all points in a coarse $N \times N$ grid at each age slice. The N mass values are selected to be spaced from the lowest mass value present in the models to the greatest values at which the star has not yet evolved off the main-sequence. Next, we identify any local minima, and refine their values by evaluating all available intermediate mass pairings. Finally, we identify the global minimum from the previous step, and fit an elliptic paraboloid to the local χ^2_ν surface around the lowest minimum. We assign the most likely values for the stellar masses and age to be the location of the minimum of the paraboloid. The curvature of the paraboloid in each axis provides the estimates of the uncertainties in these parameters. In practice, these formal uncertainties underestimate the true uncertainties since they do not consider the systematic errors due to (1) the over-simplified EB model, (2) errors in the theoretical stellar isochrones and limb darkening coefficients, and (3) sources of non-Gaussian noise in the data.

When choosing the value of N above, we must balance computational speed considerations with the risk of missing the global minimum by under-sampling the χ^2_ν

surface. For most main-sequence EBs, the χ^2_ν surface contains only one, or at most a few local minima, and our experience is that $N = 10$ usually suffices (see §4.4.2). For systems that are either very young or in which a component has begun to evolve off the main-sequence, the χ^2_ν surface requires a much denser sampling. Evolved components, which may be present in as many as a third of the EBs of a magnitude-limited photometric survey (Alcock et al. 1997), introduce an additional challenge if their isochrones intersect other isochrones on the color-magnitude diagram. At such intersection points, stars of different masses will have approximately equal sizes and effective temperatures, creating degenerate regions on the χ^2_ν surface. This degeneracy can, in principle, be broken with sufficient color information, which will probe differences in the stars' limb darkening and absorption features, both of which vary with surface gravity.

We also note that multiple local minimum may result for light curves with very small formal uncertainties. In this case, numerical errors in the simulated light curve dominate. This problem can be mitigated by increasing the number of iterations used in fitting the orbital parameters (see §4.3.2).

4.3.4 Optimization

We implemented a number of optimizations to increase the speed of MECI. First, since each light curve is independent, we parsed the data set and ran MECI in parallel on multiple CPUs. Second, we reduced the number of operations by identifying and skipping unphysical stellar pairings. Specifically, we required $(r_1 + r_2 < 0.8)$ to preclude binaries that were not well detached. In addition, for EBs with clear

primary and secondary eclipses, we skipped high-contrast-ratio pairings for which the maximum depth of the primary eclipse, Δmag_1 , or the maximum depth of the secondary eclipse, Δmag_2 , fell below a specified threshold, $\Delta mag_{\text{cutoff}}$. In particular, we skipped over pairings for which $\min(\Delta mag_1, \Delta mag_2) \leq \Delta mag_{\text{cutoff}}$, where

$$\Delta mag_1 \simeq 2.5 \log \left[1 + \frac{(R_2/R_1)^2}{1 - (R_2/R_1)^2 + 10^{0.4(Mag1-Mag2)}} \right], \text{ and} \quad (4.9)$$

$$\Delta mag_2 = 2.5 \log [1 + 10^{0.4(Mag1-Mag2)}]. \quad (4.10)$$

These estimates assume equatorial eclipses, since we seek to evaluate the maximum possible eclipse depths. The first expression is approximate because it neglects the effects of limb darkening on the eclipse depth. In practice, the chosen value for $\Delta mag_{\text{cutoff}}$ will depend on the typical precision and cadence of the data set in question.

We note here a special case that we revisit in §4.4.3. For EB light curves with equally spaced eclipses of equal depth, we must also consider the possibility that our assumed period is double the true value, and hence the secondary eclipse is undetected. When we identified such cases, we analyzed the light curve as usual but removed the above requirement. In such cases, we can place only an upper limit on the mass of the secondary component.

4.4 Testing MECI

In order to establish the accuracy and reliability of MECI under a variety of scenarios, we conducted two distinct tests.

4.4.1 Observed Systems

The first test was to run MECI on several observed light curves of eclipsing binary systems whose stellar parameters had been precisely determined from detailed photometric and spectroscopic studies.

We examined three well-studied EBs. The first was FS Monocerotis (Lacy et al. 2000), for which we modeled the published light curve, which had $N_{lc} = 249$ data points, as well as the published $U - B$ and $B - V$ colors. The second was WW Camelopardalis (Lacy et al. 2002), for which we modeled the published light curve, which had $N_{lc} = 5759$ observations, as well as the $B - V$ color. Finally, we studied BP Vulpeculae (Lacy et al. 2003), for which we modeled the published light curve, which had $N_{lc} = 5236$ observations, as well as the $B - V$ color. All three published light curves were observed in V -band and are plotted in Figure 4.4. The colors had been corrected for reddening. The contour plots of the χ^2_ν surfaces resulting from our MECI analysis (setting the weighting $w = 10$) are shown in Figures 4.5, 4.6, and 4.7. Note that FS Mon is more tightly constrained due to its greater color information. Furthermore, the asymmetry in the BP Vul contour is due to its unequal eclipse depths. In all cases, the χ^2_ν surface has a single minimum, which is close to the published values. In Table 4.1, we tabulate the results of our analysis and compare these to the published values.

We then changed the weighting factor to $w = 100$ and repeated this procedure. The MECI results for FS Mon and BP Vul were essentially identical to our earlier findings for $w = 10$. In the case of WW Cam, the results for $w = 10$ were significantly closer to the published values. This is likely due to the fact that it is a

young system ($age = 500$ Myr), for which the brightness and radii at constant mass vary significantly. Thus, the lower light curve information weighting brought about smoother χ^2_ν contours (see §4.3.3).

4.4.2 Simulated Systems

In our second test, we produced large numbers of simulated EB light curves with various levels of injected noise, and subsequently analyzed these photometric datasets with MECI. We then compared the input and derived estimates of the stellar masses and ages in order to quantify the accuracy of the MECI analysis.

We selected the orbital and stellar parameters of each simulated EB as follows. First, we drew an age at random from a uniform probability distribution between 200 Myr and 10 Gyr. We then selected the masses of the two EB components independently from a flat distribution from $0.4M_\odot$ and the maximum mass at which stars of this age would still be located on the main-sequence. We then assigned the orbital period by drawing a number from a uniform probability distribution spanning $0 < P \leq 10$ days. Similarly, we assigned the epoch of perihelion by drawing from a uniform probability distribution spanning $0 \leq t_0 < P$, and the orbital inclination from a uniform distribution within the range that produces eclipses, $\arccos(r_1 + r_2) \leq i \leq \pi/2$. For the tests of eccentric systems, we also randomly selected an eccentricity, uniformly from $0 \leq e \leq 0.1$, and randomly selected the angle of perihelion, uniformly from $0 \leq \omega < 2\pi$. Finally, we rejected any EB system if its components were overlapping or in near contact, $r_1 + r_2 \geq 0.8$. We also filtered out EBs with undersampled eclipses, or for which one of the eclipse depths was smaller

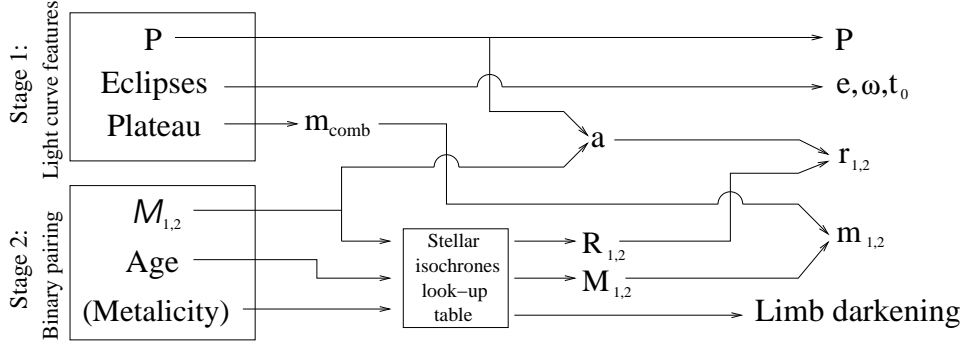


Fig. 4.3.— A flow diagram demonstrating the process by which MECI assigns the parameters to an EB based on its observed light curve. The details of stages 1 & 2 are described in §4.3.1 and §4.3.2, respectively.

Table 4.1. Accuracy of MECI parameter estimates for 3 well-studied binaries.

System	MECI ($w = 10$)			MECI ($w = 100$)			Lacy et al. (2000, 2002, 2003)		
	Mass 1 [M_\odot]	Mass 2 [M_\odot]	Age [Gyr]	Mass 1 [M_\odot]	Mass 2 [M_\odot]	Age [Gyr]	Mass 1 [M_\odot]	Mass 2 [M_\odot]	Age [Gyr]
FS Monocerotis $(N_{lc} = 249)$	1.58 [3.3%]	1.47 [0.5%]	1.6 [0.3%]	1.57 [3.6%]	1.47 [0.5%]	1.6 [0.1%]	1.632 ±0.012	1.462 ±0.010	1.6 ±0.3
WW Camelopardalis $(N_{lc} = 5759)$	1.92 [0.2%]	1.86 [0.9%]	0.5 [3%]	2.10 [9.6%]	2.02 [8.0%]	0.4 [17%]	1.920 ±0.013	1.873 ±0.018	0.5 ±0.1
BP Vulpeculae $(N_{lc} = 5236)$	1.78 [2.2%]	1.48 [5.3%]	0.7 [26%]	1.77 [1.9%]	1.48 [5.2%]	0.8 [22%]	1.737 ±0.015	1.408 ±0.009	1.0 ±0.2

Note. — The rightmost columns list the masses, ages, and errors of the component stars as determined by a combined analysis of their light curves and spectroscopic orbits (Lacy et al. 2000, 2002, 2003). The leftmost columns list the estimates of these quantities produced by MECI assuming $w = 10$, and the central columns list the estimates from MECI assuming $w = 100$. The square brackets indicate the fractional errors of the MECI results with respect to the numbers in the rightmost columns.

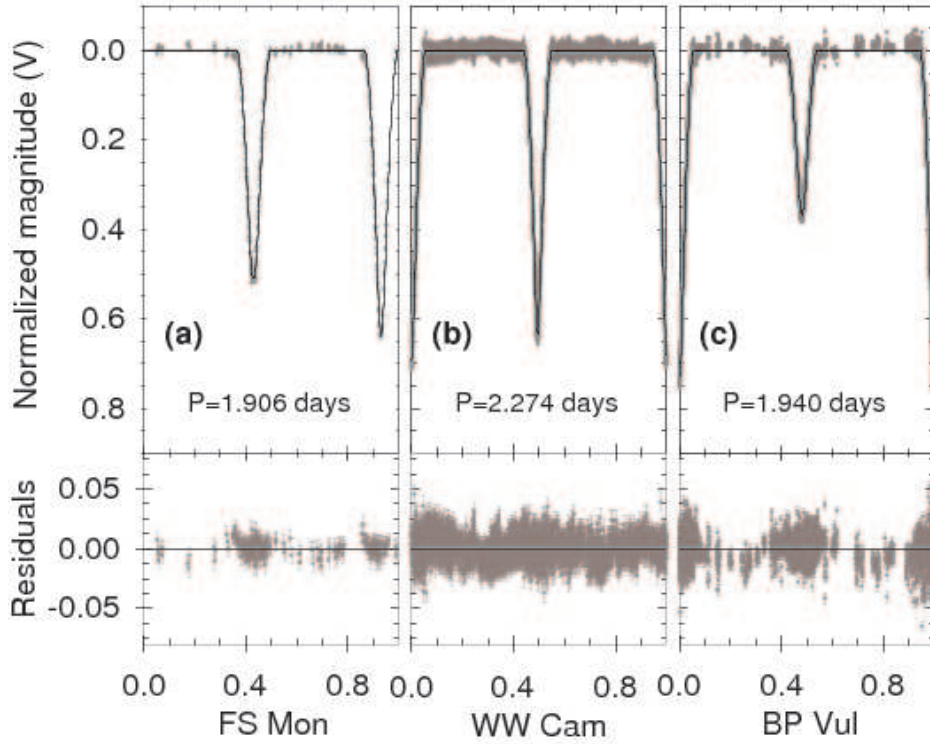


Fig. 4.4.— The observed light curves of FS Monocerotis (Lacy et al. 2000), WW Camelopardalis (Lacy et al. 2002), and BP Vulpeculae (Lacy et al. 2003), each overplotted with the best-fit model DEBiL solution used in our MECI algorithm. The masses and ages corresponding to these solutions are listed in Table 4.1. The residuals to each fit are shown in the lower panels.

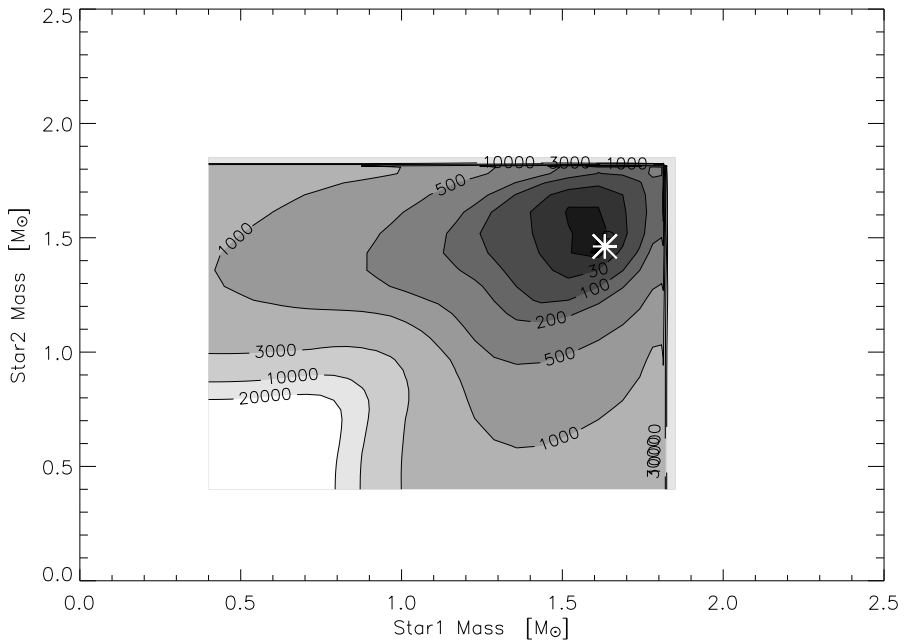


Fig. 4.5.— The MECI χ^2_ν surface to the FS Monocerotis light curve and colors (Lacy et al. 2000), assuming an age of 1.6 Gyr and fixing $w = 10$. The estimate of the stellar masses (Lacy et al. 2000) from a combined analysis of the light curve and spectroscopic observations is indicated by a white asterisk, and is near to the minimum identified by MECI. Note the erratic behavior of the contours at the upper end of the mass range, which results from the rapid evolution of stars of those masses at this age.

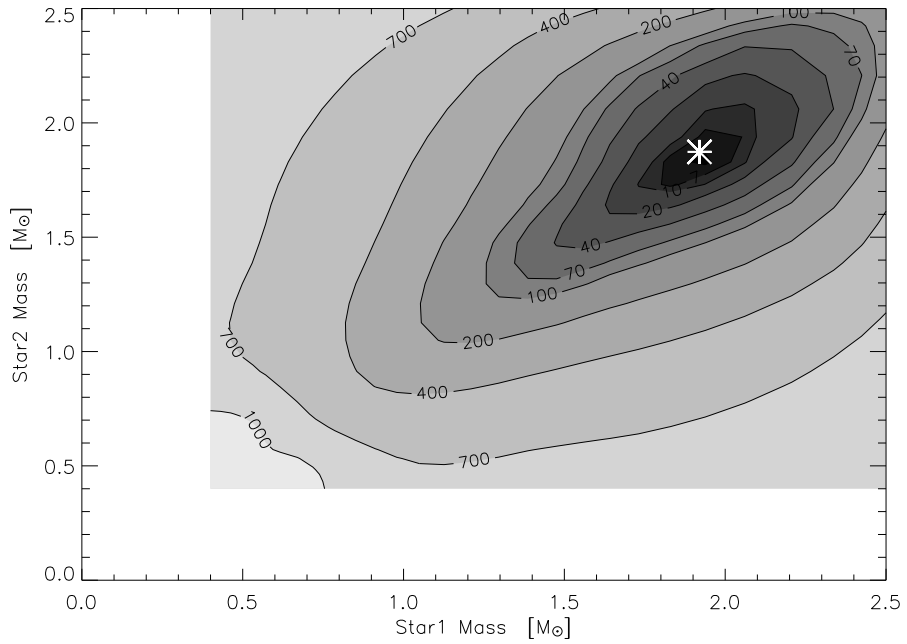


Fig. 4.6.— The MECI χ^2_ν surface to the WW Camelopardalis light curve and colors (Lacy et al. 2002), assuming an age of 0.6 Gyr and fixing $w = 10$. The estimate of the stellar masses (Lacy et al. 2002) from a combined analysis of the light curve and spectroscopic observations is indicated by a white asterisk, and is extremely close to the solution identified by MECI.

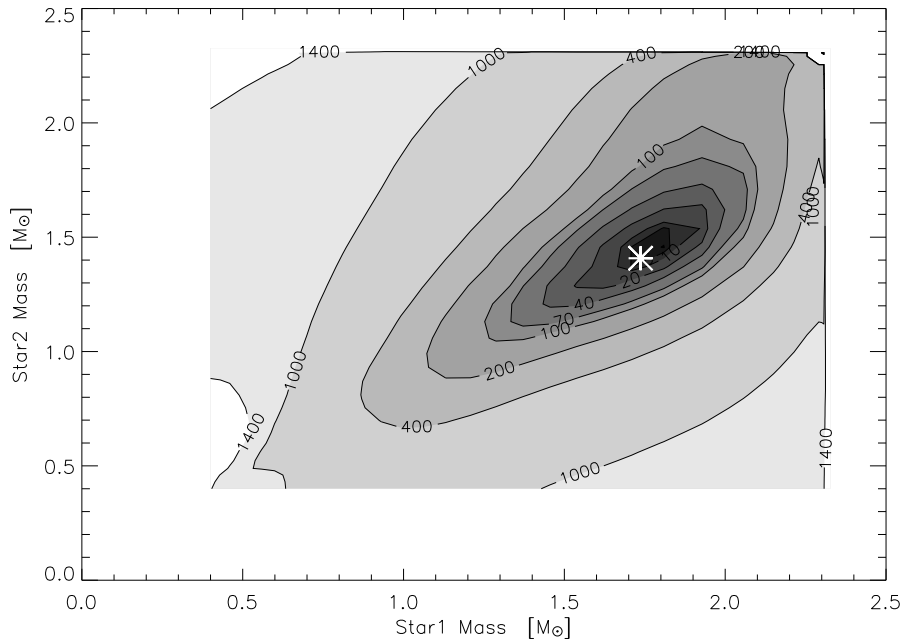


Fig. 4.7.— The MECI χ^2_ν surface to the BP Vulpeculae light curve and colors (Lacy et al. 2003), assuming an age of 0.8 Gyr and fixing $w = 10$. The estimate of the stellar masses (Lacy et al. 2003) from a combined analysis of the light curve and spectroscopic observations is indicated by a white asterisk, and is extremely close to the solution identified by MECI.

than the assumed 1σ noise level.

Each simulated light curve contained 1000 R -band data points, to which we injected Gaussian-distributed noise. When color information was required, we computed the out-of-eclipse photometric colors for each EB, and injected a 0.02 mag Gaussian-distributed error to this value. The colors we considered were $(V - I)_{Cousins}$, which is similar to the color provided by the OGLE II catalog (Wozniak et al. 2002), as well as $(J - H)_{ESO}$ and $(H - K)_{ESO}$, which are similar to the colors provided by the 2MASS catalog³ (Kleinmann et al. 1994).

We simulated 8 sets of 2500 systems each, with the sets differing in the following respects (see Table 4.2): (1) circular or eccentric orbits, (2) the number of points in the search grid, (3) the value of w , which describes the relative weight between the color and photometric data, and (4) the availability of color information.

In order to summarize the accuracy of the MECI results, we computed the quadrature sum of the relative differences between the assumed and derived values for the masses of the two components. We plot the histograms of these values in Figure 4.8. In each histogram, we identify the value encompassing the region that contains 90% of the results. We call this range the “90th percentile error”, and list it in the final column of Table 4.2.

We find that the inclusion of color information significantly improves the accuracy of the MECI results, lowering the 90th percentile error from 30% in set (A), to less than 6% in sets (B) and (C). In contrast, changing the value of w from 100

³The 2MASS catalog uses custom J, H, and K_s filters, which can be approximately converted to the ESO standard using linear transformations (Carpenter 2001).

in set (C), to 10 in set (E), results in only a modest increase of 0.8% in the size of the 90th percentile error. This indicates that the results are robust to the particular choice of w . We note, however, that a value of $w > 100$ will usually provide too little weight to the color information, which results in poorer accuracy. An extreme example of this is seen in set (A).

Similarly, MECI is not sensitive to the exact value of the search grid size. In particular, decreasing the grid size from 15×15 in set (C), to 10×10 in set (F), increases the 90th percentile error only modestly, from 5.8% to 6.1%. This stability results from the fact that the χ^2_ν function contains a broad minimum, which is well sampled even with $N = 10$ grid points. We note, however, that this is no longer the case when considering evolved star systems (e.g., §4.3.3), for which a larger number of grid points is required.

When we decreased the level of the noise injected into the photometric time series from 0.01 mag in set (C), to 0.001 mag in set (D), the 90th percentile error dropped from 5.8% to 4.0%. Surprisingly, the tail of the upper end of the error distribution extends to larger values in set (D). This appears to be due to the phenomenon discussed in §4.3.3, whereby the χ^2_ν function occasionally contains many local minima. This problem becomes acute for eccentric systems, since they have a far more complex χ^2_ν function. Decreasing their noise from 0.01 mag in set (G), to 0.001 mag in set (H), raises the 90th percentile error from 8.8% to 23%. This relatively poor performance reflects the algorithm's inability to robustly identify the global minimum under these conditions. In such cases one must increase the size of the search grid and iteratively solve for the orbital parameters of the systems, which results in a significant increase in the computational time.

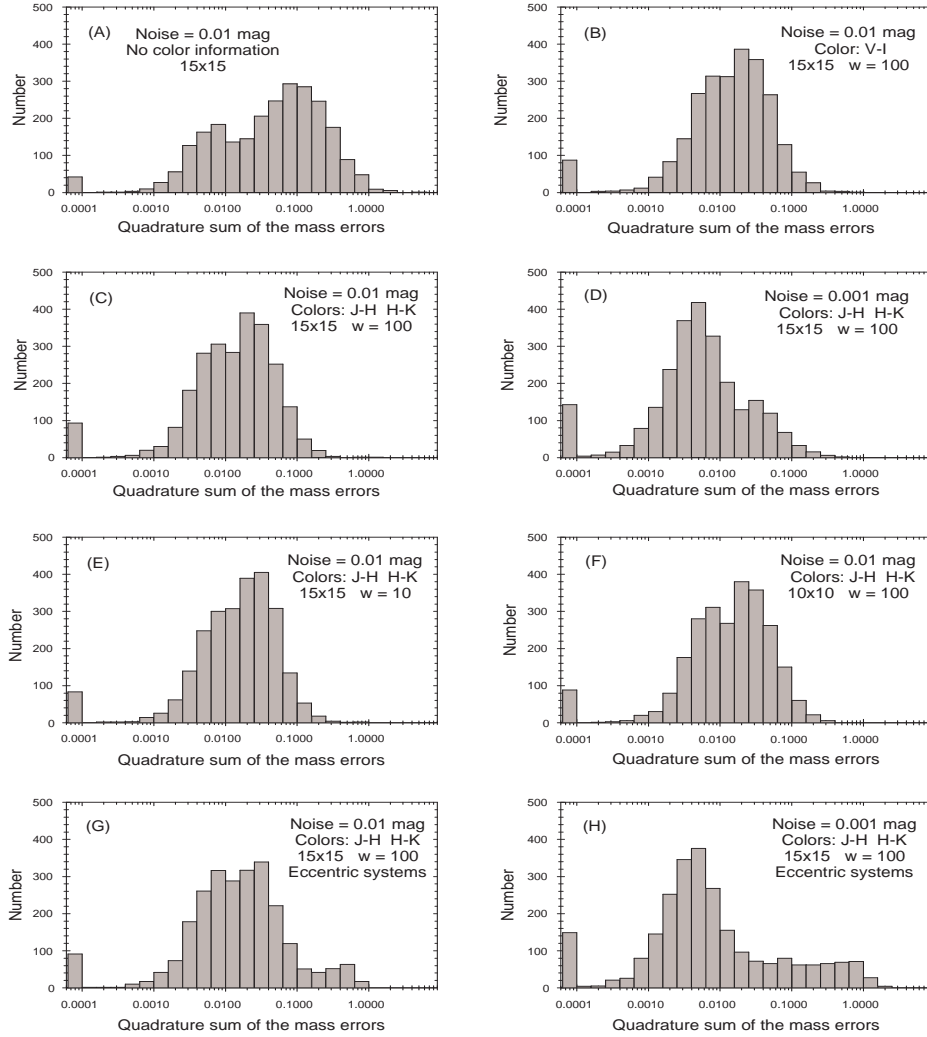


Fig. 4.8.— Histograms of the quadrature sums of the relative differences in the assumed and calculated masses for the stellar components, for each of the sets of simulated light curves described in Table 4.2. Each set contains 2500 simulated EBs as described in §4.4.2, and the key parameters of each set are listed in the upper right corner of each panel. The leftmost bin contains the sum of all results with values less than 0.0001. The ability of the method to accurately assign the masses to the component stars degrades significantly in the absence of any color information (upper left panel), but is generally robust against changes in the particular choice of w or N (see §4.4.2).

4.4.3 Limitations

A significant degeneracy results for light curves in which two distinct eclipses are not apparent. For such systems, two distinct possibilities exist, namely that either the EB consists of two twin components with an orbital period P , or that the EB consists of two stars with very disparate sizes (such that the secondary eclipse is not discernible), with an orbital period $2P$. It is often necessary to flag such systems and conduct analyses with both possible values for the orbital periods. Distinguishing which of these possibilities is the correct solution is challenging, but in some instances there are clues. One such clue is a variable light curve plateau that results from the mutual tidal distortions, which in turn might indicate the true orbital period (twice that of the observed modulation). A second possibility is a red excess in the system color indicating a low-mass secondary. Of course, follow-up spectroscopic observations can readily resolve this degeneracy, either by indicating the presence of two components of similar brightness, or through a direct determination of the orbital period.

We note that MECI employs a simplified model for the generation of the light curves (DEBiL), which can bring about additional complications when applied to systems in which our assumptions (see §4.3.2) do not hold. For example, our model ignores the effect of third light, from either a physically associated star or a chance superposition, which reduces the apparent depths of the eclipses and may contaminate the estimate of the system color. Furthermore, we have ignored reflection effects, which can raise the light curve plateau at times immediately preceding or following eclipses. Finally, tidal distortions will increase the apparent

Table 4.2. Accuracy of MECI mass estimates for simulated systems.

Set	Noise	Orbit	Search grid	Weighting	Color information	90 th percentile error
A	0.01 mag	circular	15×15	N/A	No color information	30%
B	0.01 mag	circular	15×15	$w = 100$	$(V - I)_{Cousins}$	5.9%
C	0.01 mag	circular	15×15	$w = 100$	$(J - H)_{ESO}$ and $(H - K)_{ESO}$	5.8%
D	0.001 mag	circular	15×15	$w = 100$	$(J - H)_{ESO}$ and $(H - K)_{ESO}$	4.0%
E	0.01 mag	circular	15×15	$w = 10$	$(J - H)_{ESO}$ and $(H - K)_{ESO}$	6.6%
F	0.01 mag	circular	10×10	$w = 100$	$(J - H)_{ESO}$ and $(H - K)_{ESO}$	6.1%
G	0.01 mag	eccentric	15×15	$w = 100$	$(J - H)_{ESO}$ and $(H - K)_{ESO}$	8.8%
H	0.001 mag	eccentric	15×15	$w = 100$	$(J - H)_{ESO}$ and $(H - K)_{ESO}$	23%

Note. — The parameters of the 8 distinct sets of simulated EB light curves that we generated and subsequently analyzed with MECI. The rightmost column lists the range of the quadrature sum of the fractional errors on the masses which encompasses 90% of the solutions (see Figure 4.8), which we take to be indicative of the accuracy of MECI under the specified conditions.

system brightness at orbital quadrature, which can serve to increase the apparent depth of the eclipses. In order for MECI to be able to properly handle these cases, its light curve generator must be replaced with a more sophisticated one (e.g., WD or EBOP), which will likely make MECI significantly more computationally expensive.

4.5 Conclusions

We have described a method for identifying an EB's components using only its photometric light curve and combined colors. By utilizing theoretical isochrones and limb darkening coefficients, this method greatly reduces the EB parameter space over which one needs to search. Using this approach, we can quickly estimate the masses, radii and absolute magnitudes of the components, without spectroscopic data. We described an implementation of this method, which enables the systematic analyses of datasets consisting of photometric time series of large numbers of stars, such as those produced by OGLE, MACHO, TrES, HAT, and many others. Such techniques are expected to grow in importance with the next generation surveys, such as Pan-STARRS (Kaiser et al. 2002) and LSST (Tyson 2002). In a future publication, we shall describe a specific application of these codes, namely to search for low-mass eclipsing binaries in the TrES dataset.

Acknowledgments

We would like to thank Guillermo Torres and Tsevi Mazeh for many useful discussions, and we would like to thank Sarah Dykstra for her editorial assistance.

Chapter 5

Identification, Classifications, and Absolute Properties of 773 Eclipsing Binaries Found in the TrES Survey

J. Devor, D. Charbonneau, F. T. O'Donovan, G. Mandushev, & G. Torres 2008,
The Astronomical Journal, **135**, 850–877

Abstract

In recent years, we have witnessed an explosion of photometric time-series data, collected for the purpose of finding a small number of rare sources, such as transiting

extrasolar planets and gravitational microlenses. Once combed, these data are often set aside, and are not further searched for the many other variable sources that they undoubtedly contain. To this end, we describe a pipeline that is designed to systematically analyze such data, while requiring minimal user interaction. We ran our pipeline on a subset of the Trans-Atlantic Exoplanet Survey dataset, and used it to identify and model 773 eclipsing binary systems. For each system we conducted a joint analysis of its light curve, colors, and theoretical isochrones. This analysis provided us with estimates of the binary’s absolute physical properties, including the masses and ages of their stellar components, as well as their physical separations and distances. We identified three types of eclipsing binaries that are of particular interest and merit further observations. The first category includes 11 low-mass candidates, which may assist current efforts to explain the discrepancies between the observation and the models of stars at the bottom of the main-sequence. The other two categories include 34 binaries with eccentric orbits, and 20 binaries with abnormal light curves. Finally, this uniform catalog enabled us to identify a number of relations that provide further constraints on binary population models and tidal circularization theory.

5.1 Introduction

Since the mid-1990s, there has been an explosion of large-scale photometric variability surveys. The search for gravitational microlensing events, which were predicted by Paczynski (1986), motivated the first wave of surveys [e.g., OGLE: Udalski et al. (1994); EROS: Beaulieu et al. (1995); DUO: Alard & Guibert (1997);

MACHO: Alcock et al. (1998)]. Encouraged by their success, additional surveys, searching for gamma-ray bursts [e.g., ROTSE: Akerlof et al. (2000)] and general photometric variabilities [e.g., ASAS: Pojmanski (1997)] soon followed.

Shortly thereafter, with the discovery of the first transiting extrasolar planet (Charbonneau et al. 2000; Henry et al. 2000; Mazeh et al. 2000), a second wave of photometric surveys ensued [e.g., OGLE-III: Udalski (2003); TrES: Alonso et al. (2004); HAT: Bakos et al. (2004); SuperWASP: Christian et al. (2006); XO: McCullough et al. (2006); for a review, see Charbonneau et al. (2007)]. Each of these projects involved intensive efforts to locate a few proverbial “needles” hidden in a very large data haystack. With few exceptions, once the needles were found, thus fulfilling the survey’s original purpose, the many gigabytes of photometric light curves (LCs) collected were not made use of in any other way. In this paper, we demonstrate how one can extract a great deal more information from these survey datasets, with comparably little additional effort, using automated pipelines. To this end, we have made all the software tools described in this paper freely available (see web links listed in §5.2), and they are designed to be used with any LC dataset.

In the upcoming decade, a third wave of ultra-large ground-based synoptic surveys [e.g., Pan-STARRS: Kaiser et al. (2002); LSST: Tyson (2002)], and ultra-sensitive space-based surveys [e.g., KEPLER: Borucki et al. (1997); COROT: Baglin & The COROT Team (1998); GAIA: Gilmore et al. (1998)] are expected to come online. These surveys are designed to produce photometric datasets that will dwarf all preceding efforts. To make any efficient use of such large quantities of data, it will become imperative to have in place a large infrastructure of automated pipelines for performing even the most casual data mining query.

In this paper, we focus exclusively on the identification and analysis of eclipsing binary (EB) systems. EBs provide favorable targets, as they are abundant and can be well modeled using existing modeling programs [e.g., WD: Wilson & Devinney (1971); EBOP: Popper & Etzel (1981)]. Once modeled, EBs can provide a wealth of useful astrophysical information, including constraints on binary component mass distributions, mass-radius-luminosity relations, and theories describing tidal circularization and synchronization. These findings, in turn, will likely have a direct impact on our understanding of star formation, stellar structure, and stellar dynamics. These physical distributions of close binaries may even help solve open questions relating to the progenitors of Type Ia supernovae (Iben & Tutukov 1984). In addition to these, EBs can be used as tools; both as distance indicators (Stebbing 1910; Paczynski 1997) and as sensitive detectors for tertiary companions via eclipse timing (Deeg et al. 2000; Holman & Murray 2005; Agol et al. 2005).

In order to transform such large quantities of data into useful information, one must construct a robust and computationally efficient automated pipeline. Each step along the pipeline will either measure some property of the LC, or filter out LCs that do not belong, so as to reduce the congestion in the following, more computationally intensive steps. One can achieve substantial gains in speed by dividing the data into subsets, and processing them in parallel on multiple CPUs. The bottlenecks of the analysis are the steps that require user interaction. In our pipeline, we reduce user interaction to essentially yes/no decisions regarding the success of the EB models, and eliminate any need for interaction in all but two stages. We feel that this level of interaction provides good quality control, while minimizing its detrimental subjective effects.

The data that we analyzed originate from ten fields of the Trans-atlantic Exoplanet Survey [TrES ; Alonso et al. (2004)]. Alonso et al. (2004). TrES employs a network of three automated telescopes to survey $6^\circ \times 6^\circ$ fields of view. To avoid potential systematic noise, we used the data from only one telescope, Sleuth, located at the Palomar Observatory in Southern California (O'Donovan et al. 2004). This telescope has a 10 cm physical aperture and a photometric aperture of radius of 30''. The number of LCs in each field ranges from 10,405 to 26,495 (see Table 5.1), for a total of 185,445 LCs. The LCs consist of \sim 2000 *r*-band photometric measurements at a 9 minute cadence. These measurements were created by binning the image-subtraction results of five consecutive 90 second observations, thus improving their non-systematic photometric noise. As a result \sim 16% of the LCs have an RMS $< 1\%$, and \sim 38% of the LCs have an RMS $< 2\%$ (see Table 5.2). The calibration of TrES images, identification of stars therein, extraction, and decorrelation of the LCs is described elsewhere (Dunham et al. 2004; Mandushev et al. 2005; O'Donovan et al. 2006, 2007). TrES is currently an active survey that is continuously observing new fields, though for this paper we have limited ourselves to these ten fields.

5.2 Method

The pipeline we have developed is an extended version of the pipeline described by Devor (2005). At the heart of this analysis lie two computational routines that we have described in earlier papers: the Detached Eclipsing Binary Light curve fitter¹

¹The DEBiL source code, utilities, and running example files are available online at:
<http://www.cfa.harvard.edu/~jdevor/DEBiL.html>.

Table 5.1. Observational parameters of the TrES fields

Field	Constellation	α (J2000) ^a	δ (J2000)	Galactic coordinates (l,b)	Starting epoch (HJD)	Ending epoch (HJD)	Duration (days)
And0	Andromeda	01 09 30.1255	+47 14 30.453	(126.11, -015.52)	2452878.9	2452934.9	56.0
Cas0	Cassiopeia	00 39 09.8941	+49 21 16.519	(120.88, -013.47)	2453250.8	2453304.6	53.8
CrB0	Corona Borealis	16 01 02.6616	+33 18 12.634	(053.49, +048.92)	2453493.8	2453536.8	43.0
Cyg1	Cygnus	20 01 21.5633	+50 06 16.902	(084.49, +010.28)	2453170.7	2453250.0	79.3
Dra0	Draco	16 45 17.8177	+56 46 54.686	(085.68, +039.53)	2453093.8	2453163.0	69.2
Her0	Hercules	16 49 14.2185	+45 58 59.963	(071.61, +039.96)	2452769.9	2452822.0	52.1
Lyr1	Lyra	19 01 26.3713	+46 56 05.325	(077.15, +017.86)	2453541.8	2453616.7	74.9
Per1	Perseus	03 41 07.8581	+37 34 48.712	(156.37, -014.04)	2453312.8	2453402.8	90.0
Tau0	Taurus	04 20 21.2157	+27 21 02.713	(169.83, -015.94)	2453702.7	2453770.9	68.2
UMa0	Ursa Major	09 52 06.3560	+54 03 51.596	(160.87, +047.70)	2453402.9	2453487.8	84.9

^aICRS 2000.0 coordinates of the guide star, which is located at the center of the field of view.

Table 5.2. The number of sources and yield of the TrES fields

Field	Number of LCs	Number of observations in each LC	Fraction RMS < 1%	Fraction RMS < 2%	Found EBs	EB discovery yield
And0	26495	2357	16.5%	40.4%	111	0.42%
Cas0	22615	2069	11.0%	38.2%	119	0.53%
CrB0	18954	1287	11.0%	22.4%	28	0.15%
Cyg1	17439	3256	30.3%	65.7%	125	0.72%
Dra0	15227	2000	11.8%	26.4%	42	0.28%
Her0	15916	974	16.8%	35.0%	28	0.18%
Lyr1	22964	2815	19.4%	49.0%	135	0.59%
Per1	20988	1647	15.9%	38.4%	93	0.44%
Tau0	14442	1171	13.1%	32.5%	68	0.47%
UMa0	10405	1343	13.6%	29.5%	24	0.23%

[DEBiL ; Devor (2005)], and the Method for Eclipsing Component Identification² [MECI ; Devor & Charbonneau (2006a,b)]. DEBiL fits each LC to a *geometric* model of a detached EB (steps 3 and 5 below). This model consists of two luminous, limb-darkened spheres that orbit in a Newtonian two-body orbit. MECI restricts the DEBiL fit along theoretical isochrones, and is thus able to create a *physical* model of each EB (step 9). This second model describes the masses and absolute magnitudes of the EB's stellar components, which are then used to determine the EB's distance and absolute separation.

The pipeline consists of ten steps. We elaborate on each of these steps below.

1. Determine the period.
2. If a distinct secondary eclipse is not observed, add an entry with twice the period.
3. Fit the orbital parameters with DEBiL.
4. Fine-tune the period using eclipse timing.
5. Refine the orbital parameters with DEBiL using the revised period.
6. Remove contaminated LCs.
7. Visually assess the quality of the EB models.
8. Match the LC sources with external databases.

²The MECI source code and running examples are available online at:
<http://www.cfa.harvard.edu/~jdevor/MECI.html>.

9. Estimate the absolute physical properties of the binary components using MECI.

10. Classify the resulting systems using both automatic and manual criteria.

We use the same filtering criteria as described in Devor (2005), both for removing LCs that are not periodic (step 1) and then for removing non-EB LCs (step 3). Together, these automated filters remove approximately 97% of the input LCs. In addition to these filters, we perform stringent manual inspections (steps 7 and 10) whereby we removed all the LCs we were not confident were EBs. These inspections ultimately removed approximately 86% of the remaining LCs. Thus only 1 out of every 240 input LCs, were included in the final catalog.

In step 1, we use both the Box-fitting Least Squares (BLS) period finder (Kovács et al. 2002), and a version of the analysis of variances (AoV) period finder (Schwarzenberg-Czerny 1989, 1996) to identify the periodic LCs within the dataset and to measure their periods. In our AoV implementation, we scan periods from 0.1 days up to the duration of each LC. We then select the period that minimizes the variance of a linear fit within eight phase bins. We remove all systems with weak periodicities [see Devor (2005) for details], and with one exception (T-Lyr1-14413), all the systems whose optimal period is found to be longer than half their LC duration. In this way we are able to filter out many of the non-periodic variables.

The AoV algorithm is most effective in identifying the periods of LCs with long duration features, such as semi-detached EBs and pulsating stars. The BLS algorithm, in contrast, is effective at identifying periodic systems whose features span only a brief portion of the period, such as detached EBs and transiting planets

(see Figure 5.1). However, the BLS algorithm is easily fooled by outlier data points, identifying them as short duration features. For this reason, the BLS algorithm has a significantly higher rate of false positives than AoV, especially for long periods, which have only a few cycles over the duration of the observations. Therefore, we limit the search range of the BLS algorithm to periods shorter than 12 days, although as Figure 5.1 illustrates, its efficiency at locating EBs rapidly declines at periods greater than 10 days.

In step 2, we address the ambiguity between EBs with identical components in a circular orbit, and EBs with extremely disparate components. The phased LC of EBs with identical components contains two identical eclipses, whereas the phased LC of EBs with disparate components will have a secondary eclipse below the photometric noise level. These two cases are degenerate, since doubling the period of a disparate system will result in an LC that looks like an equal-component system. In the pipeline, we handle this problem by doubling such entries; one with the period found in step (1), and another with twice that period. Both of these entries proceed through the pipeline independently. In many cases, after additional processing by the following steps, one of these entries will emerge as being far less likely than the other (see Appendix 5.5), at which point it is removed. But in cases where photometry alone cannot determine which is correct, one needs to perform spectroscopic follow-up to break the ambiguity. In particular, a double-lined spectrum would support the equal-component hypothesis.

Step 3 is performed using DEBiL, which fits the fractional radii ($r_{1,2}$) and observed magnitudes ($mag_{1,2}$) of the EB's stellar components, their orbital inclination (i) and eccentricity (e), and their epoch (t_0) and argument of periastron (ω). DEBiL

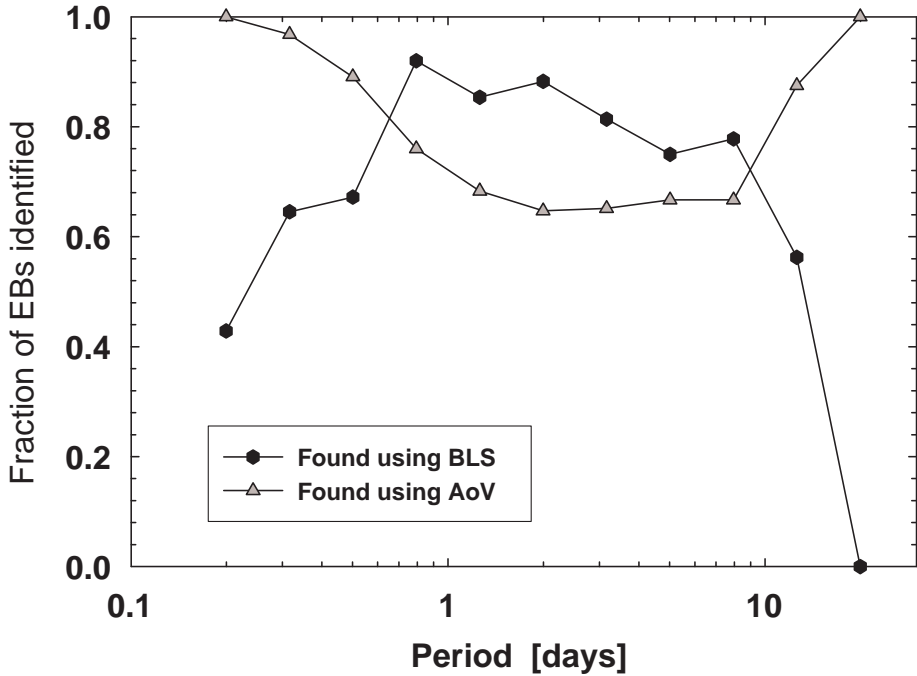


Fig. 5.1.— The fraction of the EBs in the final catalog found using the BLS algorithm and the AoV algorithm. The number of EBs in each bin is shown in Figure 5.8. The BLS method excelled at identifying EBs with short-duration eclipses (compared to the orbital period), which predominately occur at periods > 0.75 days. The AoV method fared better with EBs that have long-duration eclipses, which predominately occur in sub-day periods. The AoV method also does well with EBs with period longer than 10 days, which may be dominated by giant-giant binaries (Derekas et al. 2007), and so also have broad eclipses. This plot demonstrates the importance of using multiple independent methods of identifying EB, otherwise the results will have a significant selection effect that may bias any statistical results.

first produces an initial guess for these parameters, and then iteratively improves the fit using the downhill simplex method (Nelder 1965) with simulated annealing (Kirkpatrick et al. 1983; Press et al. 1992).

In step 4, we fine-tune the period (P) using a method based on eclipse timing³, which we describe below. In order to produce an accurate EB model in step 9, it is necessary to know the system’s period with greater accuracy than that produced in step 1. If we neglect to fine-tune the period, the eclipses may be out of phase with respect to one another, and so the phased eclipses will appear broadened. Our timing method employs the DEBiL model produced in step (3), and uses it to find the difference between the observed and calculated ($O - C$) eclipse epochs. This is done by minimizing the chi-squared fit of the model to the data points in each eclipse, while varying only the model’s epoch of periastron. When the period estimate is off by a small quantity (ΔP), the $O - C$ difference increases by ΔP each period. This change in the $O - C$ over time can be measured from the slope of the linear regression, which is expected to equal $\Delta P/P$. Thus measuring such an $O - C$ slope will yield the desired period correction (see Figure 5.2).

If the EB has an eccentric orbit, the primary and secondary eclipse will separate on the $O - C$ plot, and form two parallel lines with a vertical offset of Δt (see Figure 5.3). We measure this offset and use it as a sensitive method to detect orbital eccentricities. In particular, the value of Δt constrains $e \cos \omega$, which in turn provides a lower limit for the system’s eccentricity (Tsesevich 1973):

³The source code and running examples are available online at
<http://www.cfa.harvard.edu/~jdevor/Timing.html>.

$$e \cos \omega \simeq \frac{\pi}{2} \frac{\Delta t}{P} . \quad (5.1)$$

This formula assumes an orbital inclination of $i = 90^\circ$, making it a good approximation for eclipsing binaries. We use this method, in combination with DEBiL, to identify the eccentric EBs in the catalog (see Table 5.3). However, in cases where the eclipse timing measures $|e \cos \omega| < 0.005$, or when the eccentricity is consistent with zero, we assume that the EB is non-eccentric, and model it using a circular orbit. We further discuss the physics of these systems in §5.3.2.

Step 5 is identical to step 3, except that it uses the revised period from step 4. This step provides an improved fit to the LCs, as evidenced by an improved chi-squared value in over 70% of the cases.

In step 6, we locate and remove non-EB sources that seem to be periodic due to photometric contamination by true EBs. Such contaminations result from overlapping point spread functions (PSF) that cause each source to partially blend into the other. These cases can be easily identified with a program that scans through pairs of targets⁴, and selects those that both have similar periods (see description below) and are separated by an angle that is smaller than twice the PSF. We found 14 such pairs, all of which were separated by less than $41''$, which is well within twice the TrES PSF ($60''$), while the remaining pairs with similar periods were separated by over $450''$. Upon inspection, all 14 of the pairs we found had

⁴We ran a brute force scan, which required $O(N^2)$ iterations. But by employing a data structure that can restrict the scan to nearby pairs, it is possible to perform this scan in only $O(N)$ iterations, assuming that such pairs are rare.

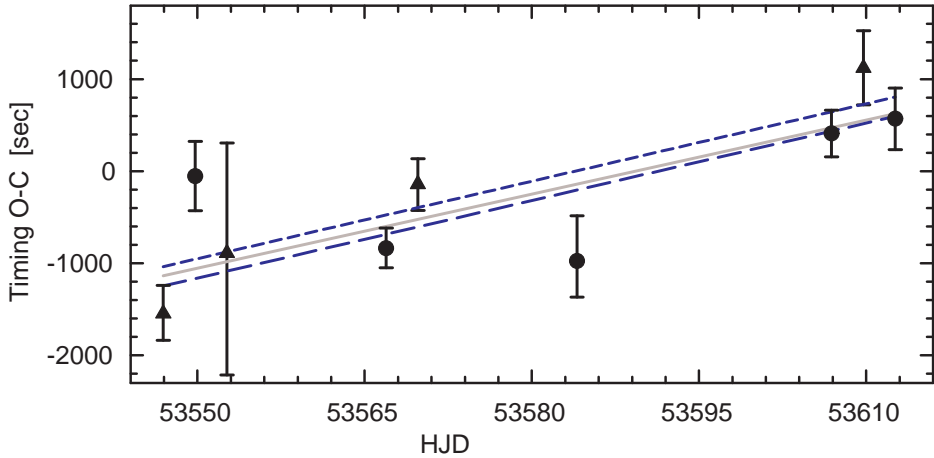


Fig. 5.2.— An eclipse timing plot produced in step 4, showing the $O - C$ residuals of the primary eclipses (circles) and the secondary eclipses (triangles). Here, T-Lyr1-14962 is shown with an assumed period of 5.710660 *days*, as measured with an AoV periodogram. The slope of the residuals indicates that the assumed period is inaccurate. The gray solid line is predicted by the best circular-orbit model, whereas the dashed lines are predicted by the best eccentric-orbit model (compare to Figure 5.3). After correction, we get a fine-tuned period of 5.712516 *days*. This 0.03% correction is small but significant in that without having had this correction, the eclipses would have smeared out and widened.

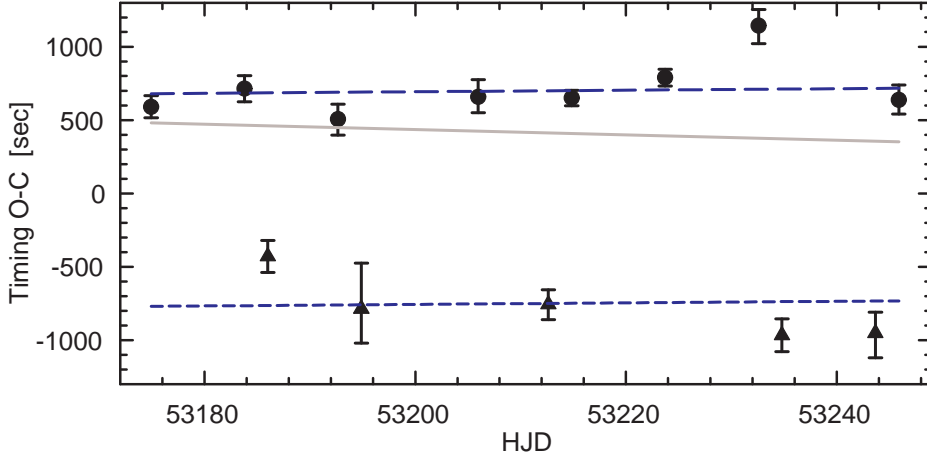


Fig. 5.3.— An eclipse timing plot for T-Cyg1-01373, with an assumed period of 4.436013 *days*. In contrast to Figure 5.2, the slope here is consistent with zero, thus indicating that the period does not need to be fine-tuned. However, the $O - C$ offset between the primary (circles) and secondary (triangle) eclipses is significant (1449 *seconds*), indicating that this EB has an eccentric orbit. The reduced chi-squared of the best circular-orbit model (gray solid line) is $\chi^2_\nu = 12.9$, while the reduced chi-squared of the best eccentric-orbit model (dashed lines) is $\chi^2_\nu = 0.95$. Applying the $O - C$ timing offset to equation 5.1 provides a lower limit to the binary’s orbital eccentricity: $e \geq |e \cos \omega| \simeq 0.00594$.

similar eclipse shapes, indicating that we had no false positives. Between each pair, we identify the LC with shallower eclipses (in magnitudes) as being contaminated and remove it from the catalog.

We define periods as being similar if the difference between them is smaller than their combined uncertainty. We estimate the period uncertainty using the relation: $\varepsilon_P \propto P^2/T$, where T is the time interval between the initial and the final observations. One arrives at this relation by noticing that when phasing the LC, the effect of any perturbation from the true period will grow linearly with the number of periods in the LC (see step 4). This amplified effect will become evident once it reaches some fraction of the period itself, in other words, when $\varepsilon_P(T/P) \propto P$. A typical TrES LC with a revised period will have a proportionality constant of approximately 1/1000. In order to avoid missing contaminated pairs (false negatives), we adopt in this step the extremely liberal proportionality constant of unity.

In step 7, we conduct a visual inspection of all the LC fits. Most EBs were successfully modeled and were included into the catalog as is. About 1% of the LCs analyzed had misidentified periods, as a result of failures of the period-finding method of step 1. In most of these cases, the period finder indicated either a harmonic of the true period or a rational multiple of a solar or sidereal day. In such cases, we use an interactive periodogram⁵ to find the correct period and then reprocess the LCs through the pipeline. Some entries were misidentified at step 2 as being ambiguous, even though they have a detectable secondary eclipse or have

⁵LC, created by Grzegorz Pojmanski.

slightly unequal eclipses. In these cases, the erroneous doubled entry was removed. Lastly, some of the EBs were not fit sufficiently well with DEBiL in step 5. These cases were typically due to clustered outlier data points, systematic noise, or severe activity of a stellar component (e.g., flares or spots), which caused DEBiL to produce erroneous initial model parameters. These cases were typically handled by having DEBiL produce the initial model parameters from a more smoothed version of the LC.

In step 8, we match each system, through its coordinates, with the corresponding source in the Two Micron All Sky Survey catalog [2MASS ; (Skrutskie et al. 2006)]. This was done to obtain both accurate target positions and observational magnitudes. These magnitude measurements are then used to derive the colors of each EB, which are incorporated into the MECI analysis, as well as to estimate the EB's distance modulus (step 9). To this end, 2MASS provides a unique combination of high astrometric accuracy ($\sim 0.1''$) together with high photometric accuracy (~ 0.015 mag) at multiple near-infrared bands, all while maintaining a decent spacial resolution ($\sim 3''$). By employing these near-infrared bands, we both inherently reduce the detrimental effects of stellar reddening, and are able to correct for much of the remaining extinction by fitting for the Galactic interstellar absorption.

In order to use the measurements from the 2MASS custom J , H , and K_s filters, we converted them to the equivalent ESO-filter values so that they could be compared to the isochrone table values used in the MECI analysis. This conversion was done using approximate linear transformations (Carpenter 2001). However, the colors of three EBs (T-And0-10336, T-Cyg1-02304, and T-Per1-05205) were so anomalous that they did not permit a reasonable model solution; thus, we chose not

to include any color information in their MECI analyses.

In addition to its brightness, we also look up each EB’s proper motion. Although proper motion is not required for any of the pipeline analyses, it provides a useful verification for low-mass candidates (see §5.3.1). These systems are expected to have large proper motions, since they must be nearby to be observable in this magnitude-limited survey. The most extreme such case in the catalog is CM Draconis (T-Dra0-01363), which has a proper motion of over 1300 mas yr^{-1} (Salim & Gould 2003), and is probably the lowest mass system in our catalog. To this end, we match each system to the Second U.S. Naval Observatory CCD Astrograph Catalog [UCAC release 2.4 ; Zacharias et al. (2004)]. When there is no match with UCAC, we use the more comprehensive but less accurate U.S. Naval Observatory photographic sky survey [USNO-B release 1.0 ; Monet et al. (2003)]. These matches are made using the more accurate aforementioned adopted 2MASS coordinates. However, because of their increased observational depth, and the fact that some high-proper motion targets are expected to have moved multiple arcseconds in the intervening decades, we chose to match each target to the brightest (*R*-band) source within $7.5''$. It should be noted that the position of CM Draconis shifted by more than $22''$ and had to be matched manually, though 90% of the matches were separated by less than $0.6''$, and 98% were separated by less than $2''$ (see Figure 5.4).

The proper motions garnered from these databases can be combined with distance estimates (D), to calculate the absolute transverse velocity (v_{tr}) of a given EB:

$$v_{tr} \simeq 4.741 \text{ km s}^{-1} \left(\frac{PM}{1 \text{ mas yr}^{-1}} \right) \left(\frac{D}{1 \text{ kpc}} \right), \quad (5.2)$$

where PM is the system's angular proper motion. In the catalog we list the right ascension and declination components (PM_α and PM_δ , respectively), so as to allow one to compute the system's direction of motion in the sky. The value of PM can be computed from its components, using: $PM^2 = PM_\delta^2 + PM_\alpha^2 \cos^2 \delta$, where δ is the system's declination. When applying this formula, one should be aware that the $\cos \delta$ coefficient is generally folded into PM_α . We follow this convention as well in our catalog.

Finally, we incorporate the USNO-B photographic B - and R -magnitude measurements into our catalog to provide a rough estimate of the optical brightness of each target. USNO-B lists two independent measurements in each of these filter; however, in some cases one or both of these measurements failed. When both measurements are available, we average them for improved accuracy. However, each measurement has a large photometric uncertainty of ~ 0.3 mag; thus, even these averaged values will have errors that are over an order of magnitude larger than the photometric measurements of 2MASS. For this reason, and because of the increased effect of stellar reddening, we chose not to incorporate these data into the MECI analysis. However, USNO-B's high spacial resolution ($\sim 1''$) enabled us to detect many sources that blended with our targets in the TrES exposures. By summing the R -band fluxes of all the USNO-B sources within $30''$ of each target, we estimated the fraction of third-light included in each LC (see Figure 5.5). Note that this measure provides only a lower bound to the true third-light fraction, as some EBs are

expected to have additional close hierarchical components that would not be resolved by USNO-B. For most of the catalog targets, the third-light flux fraction was found to be small (<10%). We therefore conclude that stellar blending will usually have only a minor effect on the MECI analysis results; however, users should be aware of the potential biases in the calculated properties of highly blended targets. Though it was not applied to this catalog, in principle, given a third-light flux fraction at a well-determined LC phase, one could correct for the effects of blending.

In step 9, we analyze the LCs with MECI. We refer the reader to the full description of this method in Devor & Charbonneau (2006a,b), and provide here only a brief outline. Given an observed EB LC and out-of-eclipse colors, MECI will iterate through a range of values for the EB age and the masses of its two components. By looking up their radii and luminosities in theoretical isochrone tables, MECI simulates the expected LC and combined colors, and selects the model that best matches the observations, as measured by the chi-squared statistic. Or, more concisely, MECI searches the (M_1, M_2, age) -parameter space for the chi-squared global minimum of each EB. Figures 5.6 and 5.7 show constant-age slices through such a parameter space. Once found, the curvature of the global minimum along the parameter space axes is used to determine the uncertainties of the corresponding parameters.

The MECI analysis makes two important assumptions. The first is that EB stellar components are coeval, which has been shown to generally hold for close binaries (Claret & Willems 2002). When this assumption is violated, MECI will often not be able to find an EB model that successfully reproduces the LC eclipses. Such systems, which may be of interest in their own right, make up $\sim 3\%$ of the

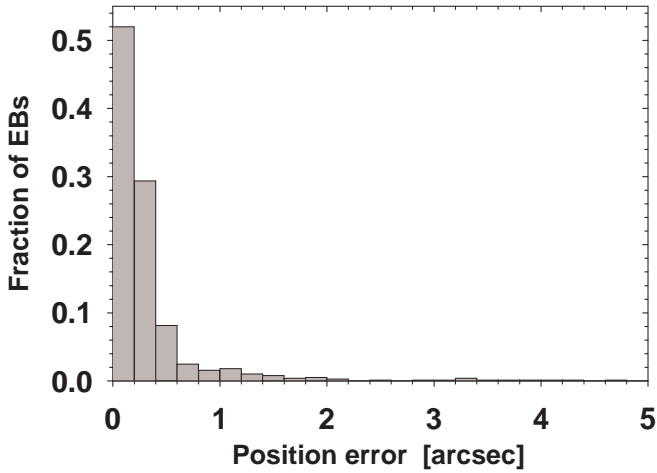


Fig. 5.4.— The distribution of the catalog position errors when matching targets to the proper motion databases. In some cases, the position errors are dominated by the motion of the EB during the intervening years.

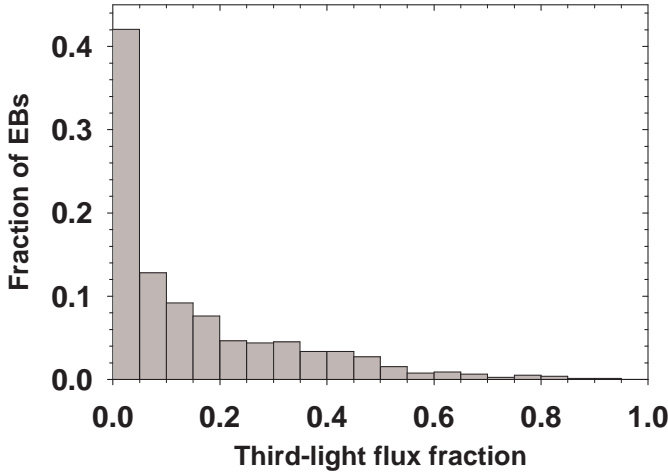


Fig. 5.5.— The distribution of the *R*-band third-light flux fraction in the catalog LCs. This fraction was calculated by summing the fluxes of all the USNO-B sources within $30''$ of the target, excluding the target, and dividing this value by the total flux within $30''$, including the target. The resulting fraction ranges from 0 to 1.

catalog and are further discussed later in this section. The second assumption is that there is no significant reddening, or third-light blended into the observations (i.e. from a photometric binary or hierarchical triple). Such blending in the LC will make the eclipses shallower, which produces an effect very similar to that of the EB having a grazing orbit. Thus, it will cause the measured orbital inclination to be erroneous, although it should rarely otherwise affect the results of the MECI analysis significantly. However, the MECI analysis is sensitive to color biases caused by stellar reddening and blending.

We reduce both these biases by incorporating 2MASS colors (see step 8), which are both less suspectable to reddening than optical colors, and suffer from significantly less blending than TrES, as the radius of the 2MASS photometric aperture is \sim 20 times smaller than that of TrES. We then attempt to further mitigate this problem by analyzing each EB twice, using different relative LC/color information weighting values [see Devor & Charbonneau (2006b) for further details]. We first run MECI with the default weighting value ($w = 10$), and then run MECI again with an increased LC weighting ($w = 100$) thereby decreasing the relative color weighting. Finally, we adopt the solution that has a smaller reduced chi-squared. Typically, the results of the two MECI analyses are very similar, indicating that the observed colors are consistent with those predicted by the theoretical isochrones. In such cases, the color information provides an important constraint, which significantly reduces the parameter uncertainties. However, when there is a significant color bias, the default model will not fit the observed data as well as the model that uses a reduced weighting of the color information. In such a case, the reduced color information model, which has a smaller chi-squared, is

adopted. Following this procedure, we find that in $\sim 9\%$ of our EBs, the reduced color information model provided a better fit, indicating that while significant color-bias is uncommon, it is a source of error that should not be ignored.

By default, we had MECI use the Yonsei-Yale (Yi et al. 2001; Kim et al. 2002) isochrone tables of solar metallicity stars. Although they successfully describe stars in a wide range of masses, these tables become increasingly inaccurate for low-mass stars, as the stars become increasingly convective. For this reason we re-analyze EBs for which both components were found to have masses below $0.75M_{\odot}$, using instead the Baraffe et al. (1998) isochrone tables, assuming a convective mixing length equal to the pressure scale height. Our EB models also take into account the effects of the limb darkening of each of the stellar components. To this end, we employ the ATLAS (Kurucz 1992) and PHOENIX (Claret 1998, 2000) tables of quadratic limb darkening coefficients.

As previously mentioned, once we know the absolute properties of an EB system, we are able to estimate its distance (Stebbing 1910; Paczynski 1997), and thus such systems can be considered standard candles. We use the extinction coefficients of Cox (2000), assuming the standard Galactic ISM optical parameter, $R_V = 3.1$, to create the following system:

$$mag_J - Mag_J = \Delta Mag + 0.282 \cdot A(V) \quad (5.3)$$

$$mag_H - Mag_H = \Delta Mag + 0.176 \cdot A(V) \quad (5.4)$$

$$mag_K - Mag_K = \Delta Mag + 0.108 \cdot A(V) \quad (5.5)$$

Where ΔMag is the extinction-corrected distance modulus, and $A(V)$ is the $V - mag$ absorption due to Galactic interstellar extinction. The estimated distance can then be solved using: $D = 10pc \cdot 10^{\Delta Mag/5}$. Because we have three equations for only two unknowns, we adopt the solution that minimizes the sum of the squares of the residuals. In some cases we remove one of the bands as being an outlier (i.e. if it would have resulted in a negative absorption), after which we are still able to solve the systems. But in cases where we need to remove two bands, we set $A(V) = 0$ in order to solve for the distance modulus. Although this method has a typical uncertainty of 10% to 20%, it can be applied to EBs that are far more distant and dim than are accessible in other methods, such as parallax measurement. It can be used to map broad features of the Galaxy, and identify binaries that are in the Galactic halo. This method can also be applied to a clustered group of EBs, whereby averaging their distances will reduce the distance uncertainty to the cluster as the inverse square root of the number of EBs measured.

In step 10, we perform a final quality check for the EB model fits, and classify them into seven groups.

- I. Eccentric: EBs with unequally-spaced eclipses
- II. Circular: EBs with equally-spaced but distinct eclipses
- III. Ambiguous-unequal: EBs with undetected secondary eclipses
- IV. Ambiguous-equal: EB with equally-spaced and indistinguishable eclipses
- V. Inverted: detached EBs that are not successfully modeled by MECI
- VI. Roche-lobe-filling: non-detached EBs that are filling at least one Roche-lobe

VII. Abnormal: EBs with atypical out-of-eclipse distortions

We list the model parameters for the EBs of groups I-IV in the electronic version of this catalog (see full description in Appendix 5.6). The EBs of groups V-VII could not be well modeled by MECI; therefore, we list only their coordinates and periods, so that they can be followed up.

Figure 5.8 illustrates the period distribution of these groups. Note, however, that both the orbital geometry of EBs (eclipse probability $\propto P^{-2/3}$), and the limited duration of the TrES survey data (≤ 90 days ; varies from field to field ; see Table 5.1), act to suppress the detection of binaries with longer periods. An added complication for single-telescope surveys is that about half of the EBs with periods close to an integer number of days will not be detectable, as they eclipse only during the daytime. This EB distribution is consistent with the far deeper OGLE II field catalog (Devor 2005), where the long tail of Roche-lobe-filling systems has recently been explained by Derekas et al. (2007) as being the result of a strong selection toward detecting eclipsing giant stars.

Group [I] contains the eccentric EBs identified in step (4) as having centers of eclipse that are separated by a duration significantly different from half an orbital period (see Figures 5.9- 5.11). This criterion is sufficient for demonstrating eccentricity, but not necessary, since we miss systems for which $\cos \omega \simeq 0$ (see equation 5.1). Fortunately, we are able to detect eccentricities in well-detached EBs with $|e \cos \omega| \geq 0.005$, using eclipse timing. Therefore, assuming that ω is uniformly distributed, we are approximately 67% complete for $e = 0.01$, and over 92% complete for $e = 0.04$. In principle, it would be possible to be 100% complete for these systems

by measuring the differences in their eclipse durations; however, this measurement is known to be unreliable (Etzel 1991) and so would likely contaminate this group with false positives. Group [II] consists of all circular-orbit EBs that were successfully fit by a single MECI model (see Figure 5.12).

EBs with only one detectable eclipse can potentially be modeled in two alternative ways⁶. One way is to assume very unequal stellar components, which have a very shallow undetected secondary eclipse (group [III]). Since we cannot estimate the eccentricity of such systems, we assume that they have circular orbits. The other way is to assume that the period at hand is twice the correct value, and that the components are nearly equal (group [IV]). The entries of such ambiguous LCs were doubled in step (2), so that these two solutions would be independently processed through the pipeline (see Figure 5.13). Therefore, these two groups have a one-to-one correspondence between them, although only one entry of each pair can be correct. Resolving this ambiguity may not always be possible without spectroscopic data. In some cases, we were able to resolve this ambiguity using either a morphological or a physical approach. The morphological approach consists of manually examining the LCs of group [IV] for any asymmetries in the two eclipses (e.g., width, depth, or shape), or in the two plateaux between the eclipses (e.g., perturbations due to tidal effects, reflections, or the “O’Connell effect”). The

⁶There is in fact a third possibility. A highly eccentric binary could be oriented in such a way that one component is eclipsed near its periastron, while its orbital plain is not sufficiently inclined to produce a second eclipse near its apoastron. For example, when $\cos \omega \simeq 0$ and $\cos i \simeq r_1 + r_2$. This possibility, however, is expected to be very rare, especially in datasets such as this one that contain very few binaries with large eccentricities.

physical approach consists of applying our understanding of stellar evolution in order to exclude entries that cannot be explained through any coeval star pairing (see Appendix 5.5). Either way, once one of the two models has been eliminated, the other model is moved into group [II] and is adopted as a non-ambiguous solution. It is interesting to note that when analyzing the two models with MECI, the equal-component solution (group [IV]) has masses approximately equal to the primary component of the unequal-component solution (group [III]). The mass of the unequal-component solution's secondary component will typically be the smallest value listed in the isochrone table, as this configuration will produce the least detectable secondary eclipse.

Group [V] consists of detached EBs that cannot be modeled by two coeval stellar components. As mentioned earlier, we can reject the single-eclipse solution for EBs with sufficiently deep eclipses (see Appendix 5.5). This argument can be further extended to cases where we can detect both eclipses in the LC, but where one is far shallower than the other. In some cases, no two coeval main-sequence components will reproduce such an LC, but unlike the previous case, since both eclipses are seen, we cannot conclude that the period needs to be doubled. Such systems are likely to have had mass transfer from a sub-giant component onto a main-sequence component through Roche-lobe overflow, to the point where currently the main-sequence component has become significantly more massive and brighter than it was originally (Crawford 1955). This process will cause the components to effectively behave as non-coeval stars, even though they have in fact the same chronological age. In extreme cases, the originally lower-mass main-sequence component can become more massive than the sub-giant, and thus swap their

original primary/secondary designations, so that the main-sequence component is now the primary component. We call such systems “inverted” EBs, and place them into group [V] (see Figure 5.14). This phenomenon is often referred to in the literature as the “Algol paradox,” though we chose not to adopt this term so as to avoid confusing it with the term “Algol-type EB” (EA), which is defined by the General Catalogue of Variable Stars [GCVS ; (Kukarkin 1948; Samus 2006)] as being the class of all well-detached EBs.

Group [VI] contains the EBs that have at least one component filling its Roche-lobe (see Figure 5.15). Such system cannot be well fit by either DEBiL or MECI since they assume that the binary components are detached, and so neglect tidal and rotational distortions, gravity darkening, and reflection effects. These systems must be separated from the rest of the catalog since their resulting best-fit models will be poor and therefore their evaluated physical attributes will likely be erroneous. In a similar fashion to Tamuz et al. (2006), we detect these systems automatically by applying the Eggleton (1983) approximation for the Roche-lobe radius, and place in group [VI] all the systems for which at least one of the EB components has filled its Roche-lobe (see Figure 5.16), that is, if either one of the following two inequalities occurs:

$$r_1 > \frac{0.49 q^{-2/3}}{0.6 q^{-2/3} + \ln(1 + q^{-1/3})} \quad \text{or} \quad (5.6)$$

$$r_2 > \frac{0.49 q^{2/3}}{0.6 q^{2/3} + \ln(1 + q^{1/3})}, \quad (5.7)$$

where $q = M_2/M_1$ is the EB components’ mass ratio. Since we expect non-detached EBs to be biased toward evolving, higher-mass stellar components, we

estimated q using the early-type mass-radius power law relation found in binaries (Gorda & Svechnikov 1998): $q \simeq (r_2/r_1)^{1.534}$. Although in principle, we could have estimated q directly from the EB component masses resulting from the MECI analysis, we chose not to, since as stated above, the analysis of such systems is inaccurate. The analytic approximation we used, though crude, proved to be remarkably robust, as we found only five false negatives and no false positives when visually inspecting the LCs. We found many more false positives/negatives when using the alarm criteria suggested by Devor (2005) or Mazeh et al. (2006), both of which attempt to identify bad model fits by evaluating the temporal correlations of the model’s residuals.

Finally, group [VII] contains systems visually identified as EBs (i.e. having LCs with periodic flux dips), yet having atypical LC perturbations that indicate the existence of additional physical phenomena (see Figures 5.17 and 5.18). For lack of a better descriptor, we call such systems “abnormal” (see further information in §5.3.3). This group is different from the previous six in that we cannot automate their classification, and their selection is thus inherently subjective. In 15 of the 20 systems, we were able to approximately model the LCs, and included them in one of the aforementioned groups. In these cases, users should be aware that these models may be biased by the phenomenon that brought about their LC distortion.

5.3 Results

We identified and classified a total of 773 EBs⁷. These systems consisted of 734 EBs with circular orbits, 34 detached EBs with eccentric orbits (group [I] ; Table 5.3), and 5 unclassified abnormal EBs (group [VII] ; Table 5.4). We marked 15 of the detached EBs with circular orbits as also being abnormal. Of the 734 EBs with circular orbits, we classify 290 as unambiguous detached EBs (group [II] ; Table 5.5), 103 as ambiguous detached EBs, for which we could not determine photometrically if they consisted of equal or disparate components (groups [III] and [IV] ; Table 5.6), 23 as inverted EBs (group [V] ; Table 5.7), and 318 as non-detached (group [VI] ; Table 5.8). With the exception of the abnormal EBs, which were selected by eye, we use an automated method to classify each of these groups (see §5.2 for details). Our mass estimates for the primary and secondary components are plotted in Figure 5.19.

The EB discovery yield (the fraction of LCs found to be EBs), varies greatly from field to field, ranging from 0.72% for Cygnus, to 0.15% for Corona Borealis (see Table 5.2). This variation is strongly correlated with Galactic latitude, where fields near the Galactic plane have larger discovery yields than those that are farther from it (see Figure 5.20). This effect is likely due to the fact that fields closer to the Galactic plane contain a higher fraction of early-type stars. These early-type stars are both physically larger, making them more likely to be eclipsed, and are more luminous, which causes them to produce brighter and less noisy LCs, thereby

⁷The observed LCs, fitted models, and model residuals of each of these EBs are shown at <http://www.cfa.harvard.edu/~jdevor/Catalog.html>.

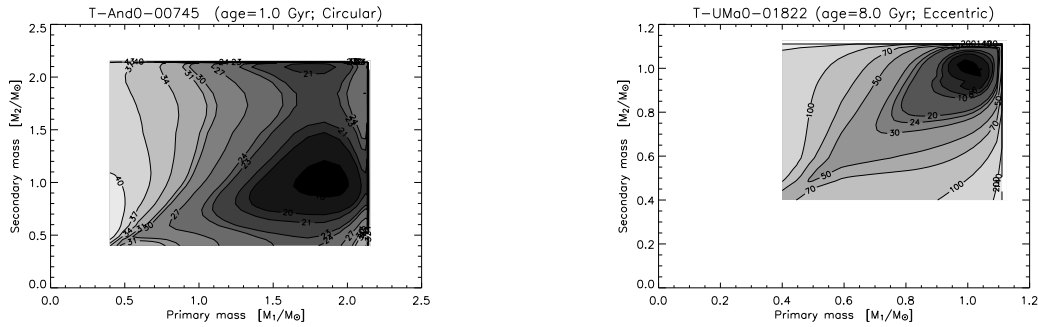
enabling the detection of EBs with shallower eclipses. Furthermore, much of the residual scatter can be attributed to the variation in the observed duration of each field (see Table 5.1). That is, we find additional EBs, with longer periods, in fields that were observed for a longer duration.

Currently, 88 of the cataloged EBs (11%) appear in either the International Variable Star Index⁸ (VSX), or in the SIMBAD⁹ astronomical database (Table 5.9). However, only 49 systems (6%) have been identified as being variable. Not surprisingly, with few exceptions, these targets were among the brightest sources of the catalog. Using only photometry, it is often notoriously difficult to distinguish non-detached EBs from pulsating variables that vary sinusoidally in time, such as type-C RR Lyrae. Furthermore, unevenly spotted stars may also cause false positive identifications, especially in surveys with shorter durations. Ultimately, spectroscopic follow-up will always be necessary to confirm the identification of such variables.

We highlight three groups of EBs as potentially having special importance as test beds for current theory. For more accurate properties, these EBs will likely need to be followed-up both photometrically and spectroscopically. The brightness of these EBs will considerably facilitate their follow-up.

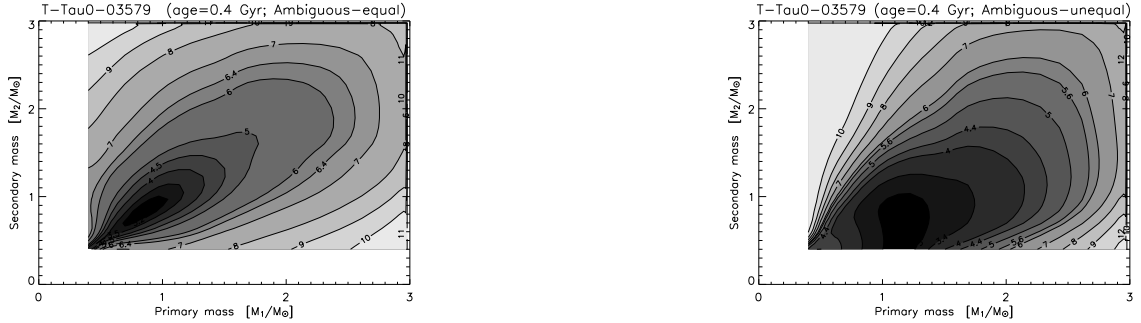
⁸Maintained by the American Association of Variable Star Observers (AAVSO).

⁹Maintained by the Centre de Données astronomiques de Strasbourg (CDS).



a. T-And0-00745: A circular-orbit EB b. T-UMa0-01822: An eccentric-orbit EB

Fig. 5.6.— MECI likelihood contour plots of a typical circular-orbit EB and a typical eccentric-orbit EB. There is no significant difference in the way MECI handles these cases, and both usually have a single contour minimum. The plots shown here have the ages set to the values that produced the lowest MECI minima.



a. T-Tau0-03579: Assuming equal components b. T-Tau0-03579: Assuming unequal components

Fig. 5.7.— MECI likelihood contour plots of a typical ambiguous EB (T-Tau0-03579). These plots show the effect of assuming that the binary components are equal (left) or unequal (right). Note that the equal-component solution will have a nearly symmetric contour around the diagonal, while the unequal-component solution can provide only an upper limit to the secondary component's mass, in this case $M_2 \lesssim 1 M_\odot$. The plots shown here have the ages set to the values that produced the lowest MECI minima.

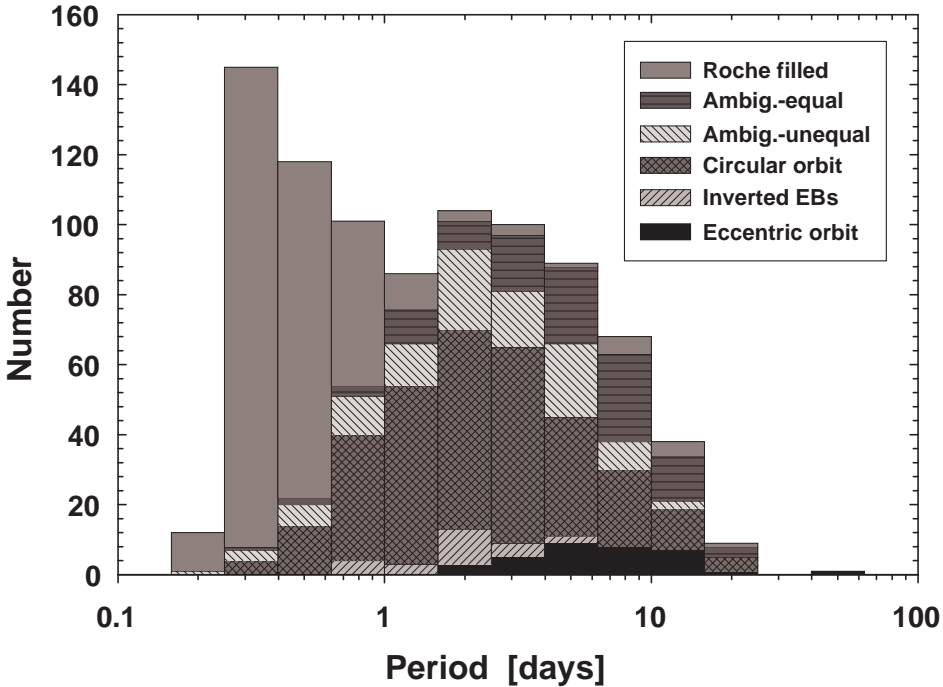


Fig. 5.8.— The EB orbital period distribution within the catalog. Each bin is subdivided to show the number of binaries belonging to each of the classification groups described in §5.2. We do not include here five unclassified abnormal systems (see Table 5.4). The remaining abnormal systems were all classified as having circular orbits (group [II]) and are included with them. Note that the ambiguous-equal and ambiguous-unequal entries represent the same stars, with entries in the former group having double the period of the latter. Note also how the Roche-lobe-filling EBs dominate the sub-day bins, and have a long tail stretching well above 10 day periods. Furthermore, the circular-orbit EBs have a period distribution peak of at ~ 2 days, while the eccentric orbit EBs peak at ~ 5 days. This is likely due to the orbital circularization that occurs preferentially in short-period systems (see also Figures 5.22 and 5.23).

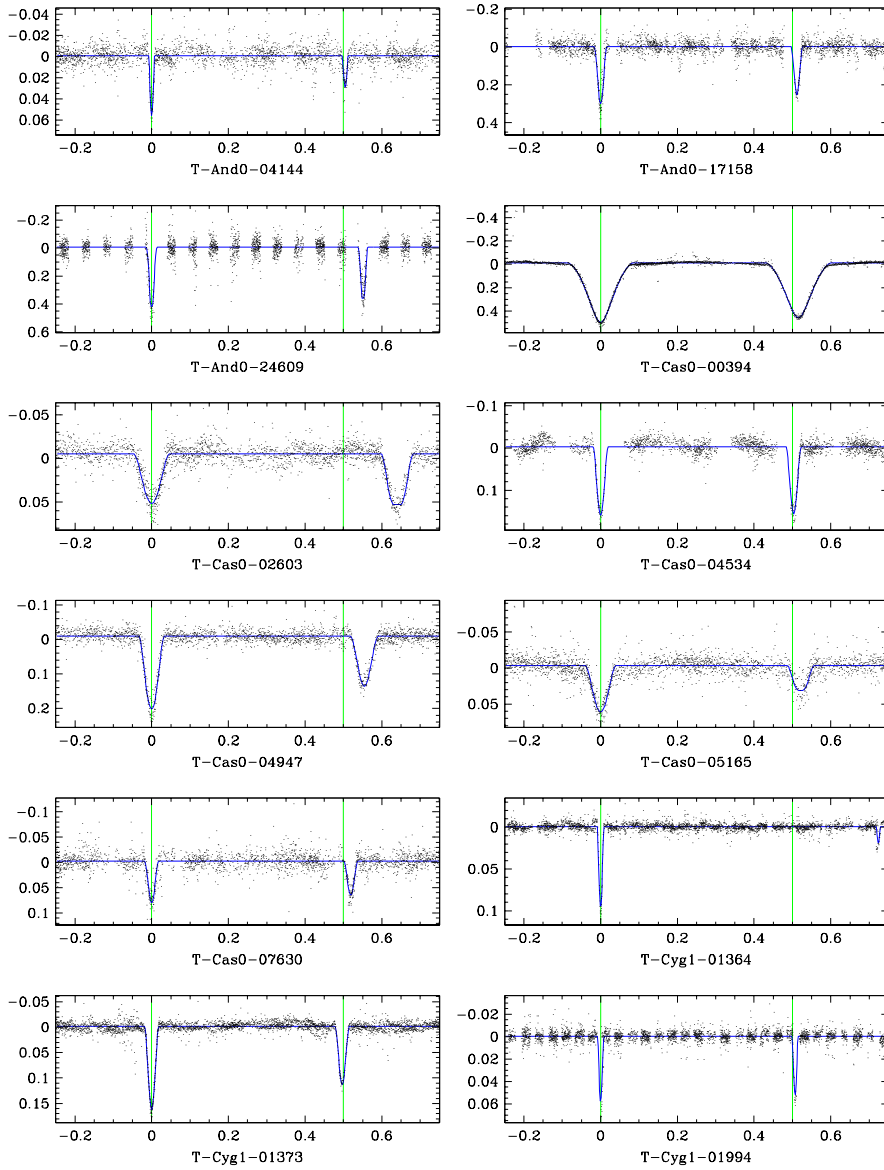


Fig. 5.9.— Eccentric EBs (panel 1). Note how the secondary eclipse is not at phase 0.5, as it would be in circular orbit EBs.

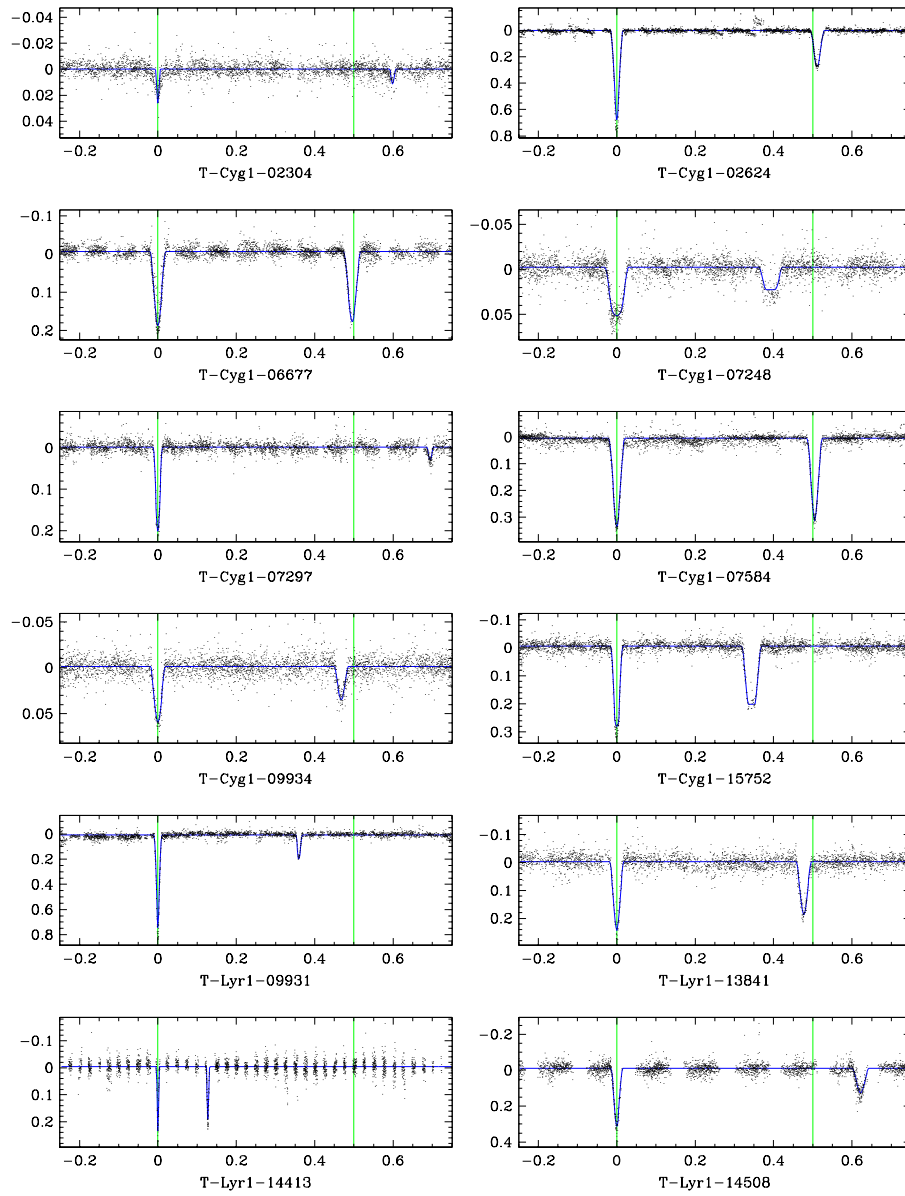


Fig. 5.10.— Eccentric EBs (panel 2).

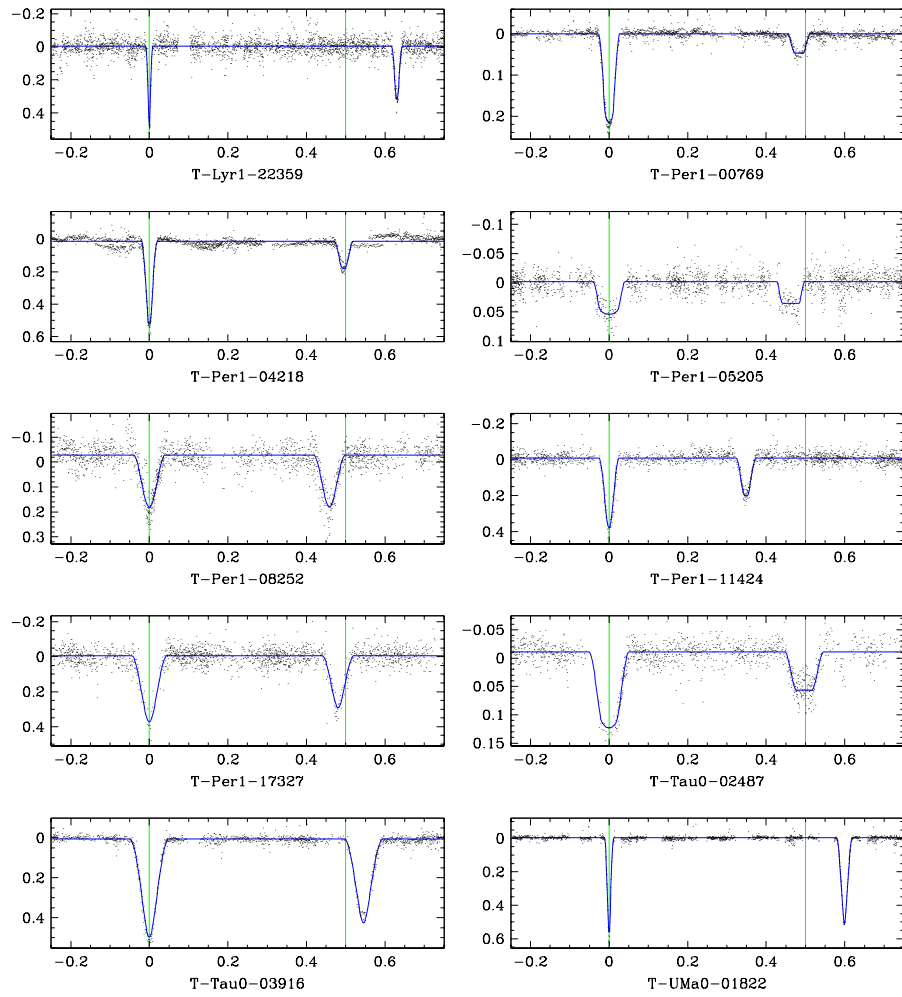


Fig. 5.11.— Eccentric EBs (panel 3).

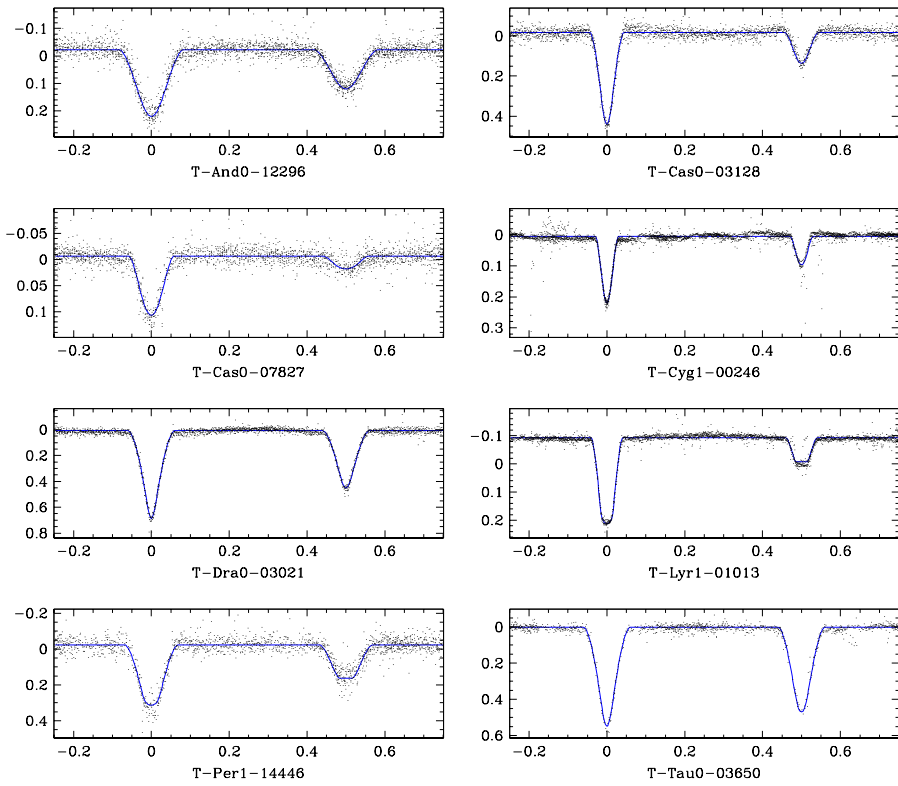


Fig. 5.12.— Examples of unambiguous EBs with circular orbits, with their best-fit MECI models (solid line).

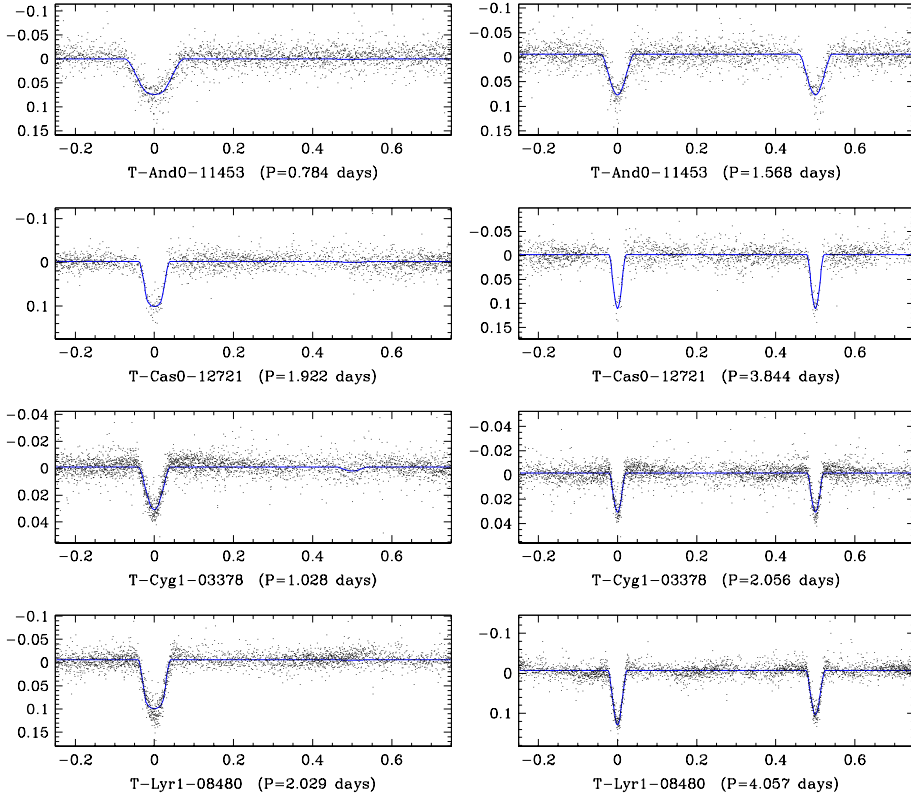


Fig. 5.13.— Examples of ambiguous EBs. Left column: assuming very unequal components. Right column: assuming approximately equal components with double the period.

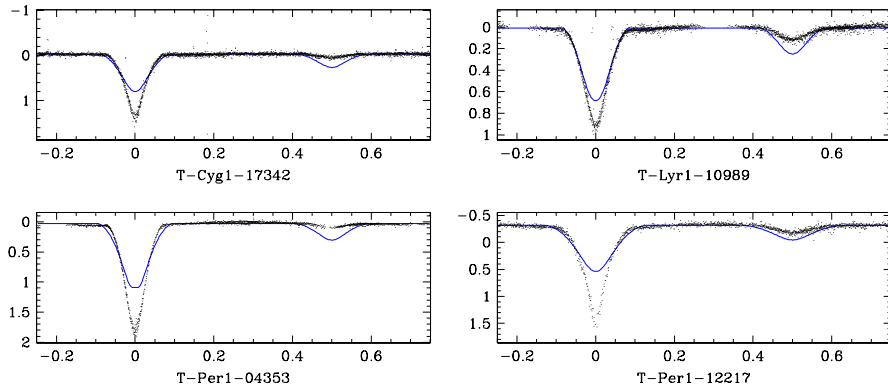


Fig. 5.14.— Examples of EBs classified as inverted EBs. We included the unsuccessful best-fit MECI model (solid curve) as an approximate reference to illustrate the LC of a corresponding binary that has had no mass transfer. Note how the model LC is unable to achieve a sufficiently deep primary eclipse, while producing a secondary eclipse that is too deep.

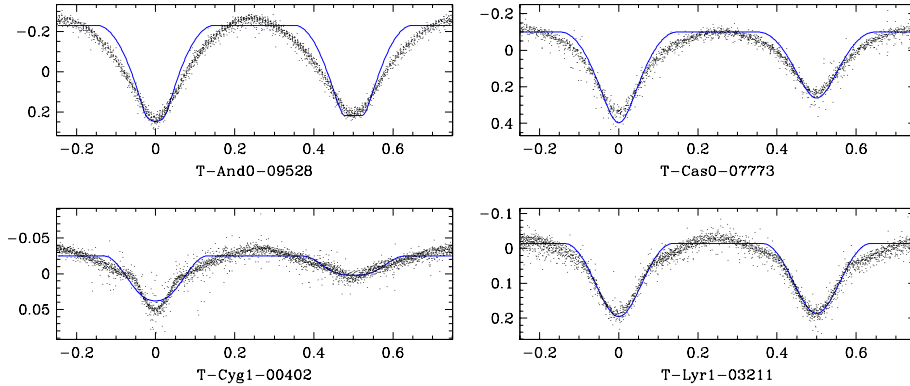


Fig. 5.15.— Examples of EBs that are assumed to have filled at least one of their Roche-lobes. We included, for illustration purposes only, their best-fit MECI models (solid line). These models were not adopted since they neglect tidal distortions, reflections, and gravity- darkening effects, and so produce a poor fit to the data.

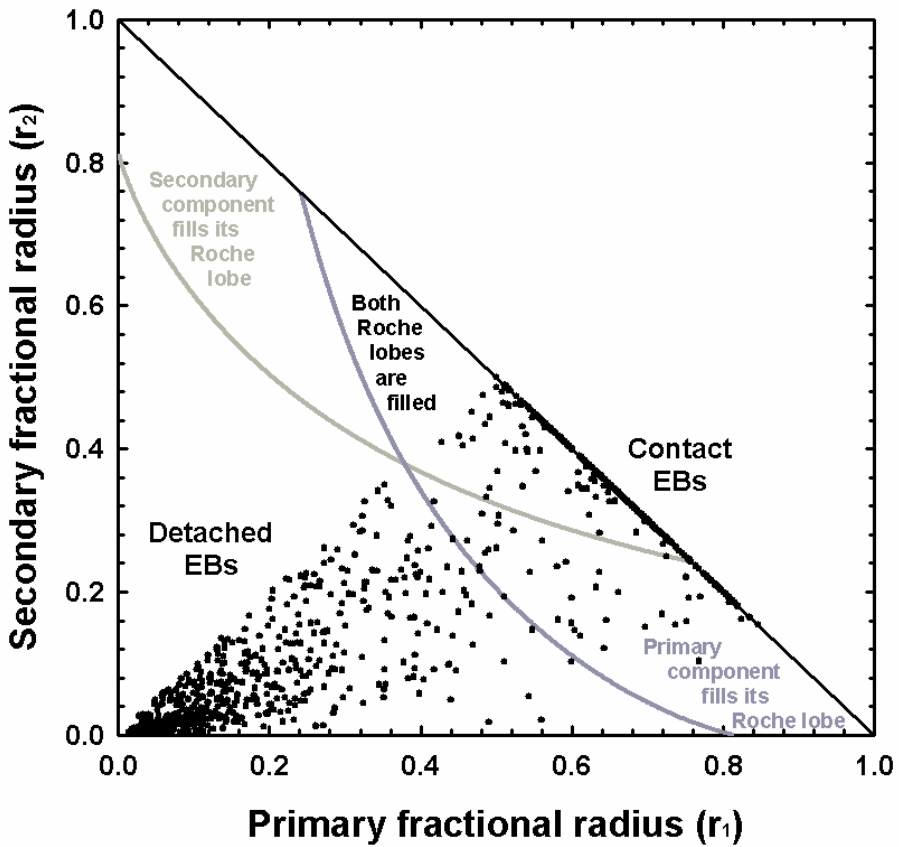


Fig. 5.16.— The criterion applied in equations 5.6 and 5.7 to determine whether one or both the EB components have filled their Roche-lobe, and thus need to be placed into group [VI]. This categorization is similar to the one performed for the OGLE II dataset in §2.5 (see Figure 2.10), although the threshold criteria here are slightly revised.

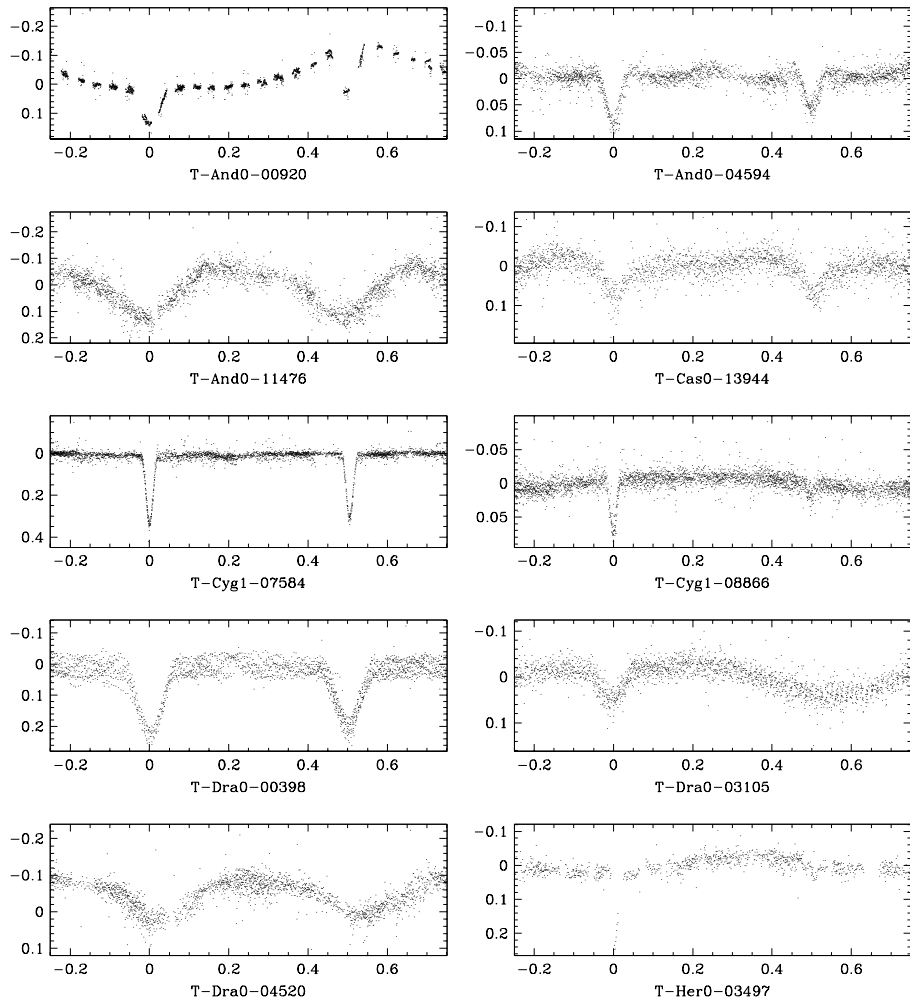


Fig. 5.17.— LCs of abnormal EBs (panel 1).

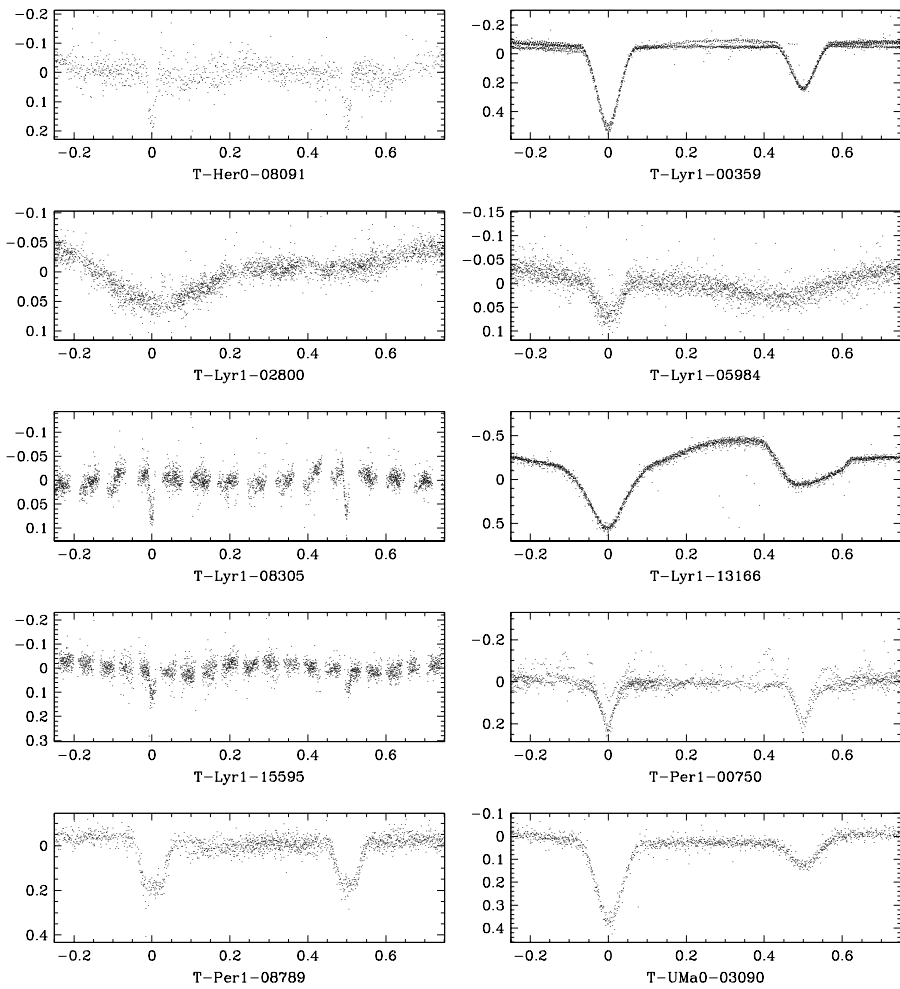


Fig. 5.18.— LCs of abnormal EBs (panel 2).

Table 5.3. Eccentric EBs

Object	α (J2000)	δ (J2000)	Period [days] ^a	$ e \cos \omega _{timing}$ ^b	$ e \cos \omega _{adopted}$ ^c	e^d	M_1/M_\odot	M_2/M_\odot	age [Gyr]	t_{circ} [Gyr] ^e
T-And0-04144	01 17 35.247	49 46 16.97	7.869	0.0072	0.0068	$0.14^{+0.08}_{-0.08}$	0.84 (-1) ^f	0.54 (-1)	10.0 (-3)	140
T-And0-17158	01 10 09.143	48 18 19.68	11.415	0.0182	0.0180	$0.038^{+0.12}_{-0.02}$	1.03 (-1)	0.92 (-1)	10.0 (-3)	370
T-And0-24609	00 58 29.826	49 25 08.88	17.997	0.0794	0.0799	$0.10^{+0.10}_{-0.02}$	1.22 ± 0.10	1.10 ± 0.30	5.4 ± 12.0	6400
T-Cas0-00394	00 32 51.608	49 19 39.36	1.746	0.0235	0.0242	$0.024^{+0.03}_{-0.001}$	1.46 ± 0.01	1.44 ± 0.01	3.4 ± 0.3	260
T-Cas0-02603	00 47 08.610	50 37 19.32	2.217	0.2098	0.2143	$0.25^{+0.14}_{-0.04}$	1.25 ± 0.01	0.75 ± 0.04	5.4 ± 5.0	0.26
T-Cas0-04534	00 31 04.585	51 52 10.88	6.909	0.0057	0.0048	$0.014^{+0.03}_{-0.01}$	1.17 ± 0.04	0.96 ± 0.15	6.4 ± 6.9	29
T-Cas0-04947	00 47 10.336	50 45 12.36	3.285	0.0845	0.0845	$0.10^{+0.04}_{-0.02}$	1.04 (-1)	0.86 (-1)	10.0 (-3)	0.53
T-Cas0-05165	00 43 59.256	51 14 00.07	2.359	0.0311	0.0327	$0.15^{+0.08}_{-0.08}$	1.50 ± 0.21	0.76 ± 0.17	2.7 ± 2.9	0.34
T-Cas0-07630	00 37 23.347	47 19 20.68	5.869	0.0200	0.0298	$0.038^{+0.15}_{-0.008}$	1.15 ± 0.12	0.87 ± 0.34	5.9 ± 9.7	13
T-Cyg1-01364	20 09 38.211	49 05 08.02	12.233	N/A	0.3254	$0.53^{+0.04}_{-0.04}$	1.03 ± 0.18	0.50 ± 0.09	0.4 ± 1.2	1100
T-Cyg1-01373	19 55 44.105	52 13 34.61	4.436	0.0059	0.0054	$0.010^{+0.02}_{-0.005}$	0.97 (-1)	0.82 (-1)	10.0 (-3)	3.0
T-Cyg1-01994	20 03 03.111	52 42 04.17	14.482	N/A	0.0107	$0.15^{+0.15}_{-0.14}$	1.80 (-1)	1.06 (-1)	0.20 (-2)	2300
T-Cyg1-02304	20 02 04.388	47 34 14.75	5.596	0.1549	0.1529	$0.23^{+0.10}_{-0.08}$	2.20 ± 1.28	0.72 ± 0.41	0.7 ± 4.8	46
T-Cyg1-02624	19 59 25.926	52 23 59.91	11.608	0.0172	0.0172	$0.068^{+0.03}_{-0.03}$	2.11 ± 0.05	1.52 ± 0.03	0.3 ± 0.1	10^7
T-Cyg1-06677	20 07 25.526	52 22 00.54	6.512	0.0077	0.0069	$0.062^{+0.03}_{-0.03}$	1.54 ± 0.20	1.31 ± 0.22	1.6 ± 1.9	10^6
T-Cyg1-07248	19 54 45.937	50 24 05.32	6.058	0.1674	0.1681	$0.17^{+0.07}_{-0.001}$	1.68 ± 0.01	0.87 ± 0.20	2.0 ± 2.1	33
T-Cyg1-07297	20 10 46.910	49 09 29.42	11.613	0.3019	0.3010	$0.38^{+0.08}_{-0.08}$	0.97 (-1)	0.55 (-1)	10.0 (-3)	830
T-Cyg1-07584	19 58 58.012	47 38 19.26	4.925	0.0074	0.0074	$0.022^{+0.08}_{-0.01}$	0.94 (-1)	0.90 (-1)	10.0 (-3)	4.7
T-Cyg1-09934	20 10 44.209	51 07 51.77	4.549	0.0505	0.0501	$0.11^{+0.06}_{-0.06}$	1.35 ± 0.64	0.94 ± 0.41	3.5 ± 5.6	5.6
T-Cyg1-15752	20 13 52.454	50 52 23.12	9.372	0.2402	0.2402	$0.35^{+0.05}_{-0.05}$	1.31 ± 0.04	1.05 ± 0.11	3.6 ± 4.9	230
T-Lyr1-09931	18 59 08.441	48 36 00.04	11.632	0.2207	0.2209	$0.25^{+0.04}_{-0.03}$	0.91 ± 0.09	0.67 ± 0.08	2.7 ± 3.3	730
T-Lyr1-13841	19 06 26.558	48 28 47.04	6.640	0.0362	0.0362	$0.075^{+0.11}_{-0.04}$	1.01 ± 0.27	1.01 ± 0.24	8.7 ± 13.1	19
T-Lyr1-14413	19 03 41.143	47 36 55.78	39.861	0.5922	0.6240	$0.64^{+0.006}_{-0.006}$	1.08 ± 0.34	0.96 ± 0.26	6.4 ± 18.9	10^5
T-Lyr1-14508	18 57 40.271	48 40 51.28	8.050	0.1861	0.1862	$0.31^{+0.16}_{-0.12}$	1.34 ± 0.28	1.20 ± 0.78	2.9 ± 8.4	220
T-Lyr1-22359	19 10 54.290	49 26 06.95	12.319	0.1990	0.1984	$0.33^{+0.05}_{-0.05}$	0.97 ± 0.48	0.97 ± 0.46	6.9 ± 29.3	550
T-Per1-00769	03 31 43.915	36 31 52.36	3.648	0.0248	0.0263	$0.055^{+0.05}_{-0.03}$	1.06 ± 0.01	0.65 ± 0.03	7.6 ± 2.1	1.4
T-Per1-04218	03 35 33.667	40 00 49.18	4.070	0.0072	0.0079	$0.10^{+0.19}_{-0.09}$	0.94 (-1)	0.72 (-1)	10.0 (-3)	2.4

Table 5.3—Continued

Object	α (J2000)	δ (J2000)	Period [days] ^a	$ e \cos \omega _{timing}$ ^b	$ e \cos \omega _{adopted}$ ^c	e ^d	M_1/M_\odot	M_2/M_\odot	age [Gyr]	t_{circ} [Gyr] ^e
T-Per1-05205	03 34 19.432	39 32 44.41	8.472	0.0558	0.0592	$0.095^{+0.11}_{-0.04}$	2.22 ± 0.01	1.17 ± 0.28	0.9 ± 1.7	210
T-Per1-08252	03 52 00.670	40 03 47.73	4.457	0.0656	0.0645	$0.063^{+0.06}_{-0.001}$	1.56 ± 0.01	1.40 ± 0.34	2.4 ± 2.5	10^5
T-Per1-11424	03 47 56.473	37 31 31.83	4.247	0.2403	0.2404	$0.24^{+0.02}_{-0.006}$	1.01 (-1)	0.82 (-1)	10.0 (-3)	2.3
T-Per1-17327	03 40 45.644	34 47 57.26	3.946	0.0332	0.0305	$0.069^{+0.25}_{-0.04}$	1.10 ± 0.02	1.09 ± 0.09	8.4 ± 16.4	1.2
T-Tau0-02487	04 21 55.933	25 35 49.28	2.826	0.0125	0.0054	$0.014^{+0.005}_{-0.005}$	1.74 ± 0.07	1.01 ± 0.08	1.6 ± 0.7	0.39
T-Tau0-03916	04 23 37.351	25 46 36.00	3.217	0.0713	0.0706	$0.071^{+0.02}_{-0.004}$	1.18 ± 0.01	1.15 ± 0.03	6.0 ± 4.4	0.56
T-UMa0-01822	09 53 37.710	52 45 44.72	9.551	0.1502	0.1503	$0.31^{+0.02}_{-0.02}$	1.01 ± 0.04	1.00 ± 0.05	8.3 ± 4.8	130

^aThe full precision of the measured period is listed in the electronic version of the catalog, together with its uncertainty and the epoch of the center of eclipse (see appendix 5.6).

^bMeasurements made using the eclipse timing of step (4). Although these values are approximations, they do not suffer from nearly as much numerical error as the DEBiL measurement, and are therefore usually accurate. “N/A” marks LCs for which there were too few eclipses to be able to apply the timing method.

^cThe adopted value is a combination of the values measured with the timing method and with DEBiL.

^dThe uncertainties of the eccentricities are non-Gaussian, since they have a strict lower bound ($e \geq |e \cos \omega|$). We truncated the quoted lower uncertainties at this value, though even at this truncated value the real uncertainty is beyond 1σ .

^eFor each EB, the circularization timescales of both components were estimated using Equation 5.10, then these values were combined as described in §5.3.2.

^fWhen the most likely model is at the edge of the parameter space, MECI is not able to bound the solution, and therefore cannot estimate the uncertainties. We mark (-3) when the upper limit was reached, (-2) when the lower limit was reached, and (-1) if one of the other parameters is at its limit.

Table 5.4. Abnormal EBs

Object	α (J2000)	δ (J2000)	Period (days)	Classified in catalog?	In SIMBAD/VSX? (see Table 5.9)	Notes
T-And0-00920	01 17 30.677	47 03 31.61	24.073	no	no	Large asymmetric reflection (0.1 mag) offset eclipse
T-And0-04594	01 16 10.713	48 52 18.97	3.910	yes	no	Spots / active
T-And0-11476	01 07 32.106	45 55 44.93	6.380	yes	no	Tilted plateaux (spots?)
T-Cas0-13944	00 29 48.990	50 49 54.06	1.739	yes	no	Irregular eclipse depths
T-Cyg1-07584	19 58 58.012	47 38 19.26	4.925	yes	no	Large persistent spot
T-Cyg1-08866	20 08 36.448	49 29 35.79	2.876	yes	no	Offset eclipse ^a
T-Dra0-00398	16 57 33.875	59 31 51.98	1.046	yes	yes	Active (has 0.2 mag fluctuations with periods of a few hours)
T-Dra0-03105	16 23 02.558	59 27 23.44	0.485	no	yes	Unequal eclipses ^b / semi-detached
T-Dra0-04520	16 49 57.960	56 26 45.56	3.113	yes	no	Tilted plateaux (spots?)
T-Her0-03497	16 52 28.391	44 51 29.63	7.853	yes	no	Unequal plateaux ^c
T-Her0-08091	16 51 52.608	47 01 47.98	2.694	yes	no	Offset eclipse
T-Lyr1-00359	19 15 33.695	44 37 01.30	1.062	yes	yes	Large recurring spots (~ 0.05 mag)
T-Lyr1-02800	19 08 18.809	47 12 48.16	4.876	no	no	Semi-detached / unequal plateaux (spots?)
T-Lyr1-05984	18 53 50.481	45 33 20.90	1.470	no	no	Unequal eclipses ^b / semi-detached
T-Lyr1-08305	18 56 43.798	48 07 02.86	14.081	yes	no	Large asymmetric reflection (0.05 mag) ; offset eclipse
T-Lyr1-13166	19 02 28.120	46 58 57.75	0.310	no	no	Unequal plateaux ; misshapen eclipse (persistent spot?)
T-Lyr1-15595	19 06 05.267	49 04 08.95	9.477	yes	no	Offset eclipse
T-Per1-00750	03 47 45.543	35 00 37.08	1.929	yes	yes	Spots / active
T-Per1-08789	03 54 33.282	39 07 41.53	2.645	yes	no	Tilted plateaux
T-UMa0-03090	10 08 52.180	52 45 52.49	0.538	yes	yes	Unequal plateaux

^aEven when the LC plateaux are not flat, due to tidal distortion or reflections, the system's mirror symmetry normally guarantees that the eclipses will occur during a plateau minimum or maximum. When, as in these cases, the eclipses are significantly offset from the plateau minima/maxima we can conclude that some mechanism, perhaps severe tidal lag, is breaking the system's symmetry.

^bMight not be an EB. This LC could be due to non-sinusoidal pulsations.

^cThe two LC plateaux between the eclipses, have a significantly different mean magnitude. This may be due to one or both components being tidally locked, and having a persistent spot or surface temperature variation at specific longitudes.

Table 5.5. Circular EBs (first 20)

Object	α (J2000)	δ (J2000)	Period [days]	M_1/M_\odot	M_2/M_\odot	age [Gyr]	Proper motion source catalog	PM_α [MAS/year]	PM_δ [MAS/year]
T-And0-00194	01 20 12.816	48 36 41.36	2.145	2.07 ± 0.02	0.97 ± 0.02	0.59 ± 0.12	UCAC	28.4	-12.2
T-And0-00459	01 11 24.845	46 57 49.44	3.655	1.20 ± 0.01	1.19 ± 0.01	5.35 ± 1.13	UCAC	-1.6	-20.6
T-And0-00745	01 03 45.076	44 50 41.14	2.851	1.86 ± 0.23	1.02 ± 0.22	1.04 ± 0.72	UCAC	-6.6	-4.8
T-And0-01461	01 06 15.353	45 08 25.66	5.613	1.47 ± 0.01	1.45 ± 0.08	2.76 ± 2.72	UCAC	-11.4	2.8
T-And0-01554	01 17 04.999	45 54 06.20	1.316	0.90 (-1) ^a	0.84 (-1)	10.00 (-3)	UCAC	-44.6	-40.8
T-And0-01597	01 10 32.071	46 49 53.18	3.503	1.55 ± 0.03	1.54 ± 0.01	2.37 ± 0.76	UCAC	2.9	-5.5
T-And0-02462	01 18 00.594	49 27 12.47	3.069	1.97 ± 0.69	1.10 ± 1.31	1.02 ± 1.58	UCAC	5.8	-1.1
T-And0-02699	01 06 44.813	47 31 08.61	1.759	1.18 ± 0.02	0.53 ± 0.07	5.21 ± 3.37	UCAC	0.2	-6.8
T-And0-02798	01 21 18.345	48 48 05.63	2.860	1.04 ± 0.10	0.65 ± 0.13	6.14 ± 9.51	UCAC	6.3	-8.1
T-And0-03526	01 20 17.451	47 39 23.32	1.536	1.04 ± 0.02	0.84 ± 0.02	6.29 ± 2.37	UCAC	17.9	-11.1
T-And0-04046	00 55 20.157	47 44 53.20	3.916	1.30 ± 0.09	1.25 ± 0.12	3.10 ± 4.31	UCAC	-3.8	-7.3
T-And0-04594	01 16 10.713	48 52 18.97	3.910	1.05 (-1)	0.82 (-1)	10.00 (-3)	UCAC	1.5	-1.9
T-And0-04829	01 15 15.228	47 45 58.97	0.678	0.99 (-1)	0.92 (-1)	10.00 (-3)	UCAC	-23.8	44.4
T-And0-05241	00 56 34.679	46 37 02.91	1.454	1.56 ± 0.01	1.47 ± 0.31	2.69 ± 7.01	UCAC	-4.5	-0.5
T-And0-05375	01 10 58.225	49 52 48.69	1.640	2.13 (-1)	1.85 (-2)	1.00 (-1)	UCAC	-6.3	0.1
T-And0-05794	01 12 11.763	47 32 30.94	1.053	2.06 ± 0.19	1.08 ± 0.54	1.08 ± 1.92	UCAC	-0.4	-1.4
T-And0-06039	01 23 37.548	48 25 37.73	4.923	1.22 ± 0.05	1.08 ± 0.31	5.33 ± 7.17	UCAC	-2.5	-5.0
T-And0-06340	01 01 55.269	49 18 38.23	5.437	1.33 (-1)	0.40 (-2)	4.00 (-1)	UCAC	0.3	-2.9
T-And0-06538	01 20 58.907	49 29 08.89	18.669	1.33 ± 0.15	0.97 ± 0.17	3.38 ± 3.45	UCAC	1.1	-6.8
T-And0-06632	01 22 36.840	47 52 53.29	1.669	1.69 ± 0.01	1.45 ± 0.24	2.21 ± 1.02	UCAC	-7.2	-7.6

^aWhen the most likely model is at the edge of the parameter space, MECI is not able to bound the solution, and therefore cannot estimate the uncertainties. We mark (-3) when the upper limit was reached, (-2) when the lower limit was reached, and (-1) if one of the other parameter is at its limit.

Table 5.6. Ambiguous EBs (first 10)

Ver.	Object	α (J2000)	δ (J2000)	Period [days]	M_1/M_\odot	M_2/M_\odot	age [Gyr]
A	T-And0-00657	01 06 06.159	47 31 59.37	6.725	2.50 (-1)	0.74 (-1)	0.20 (-2)
B	T-And0-00657	01 06 06.159	47 31 59.37	13.456	1.92 (-1) ^c	1.92 (-1)	0.20 (-2)
A	T-And0-01203	01 03 34.745	48 32 39.27	3.505	1.86 ± 0.09	0.56 ± 0.10	0.89 ± 0.83
B	T-And0-01203	01 03 34.745	48 32 39.27	7.011	1.90 ± 0.12	0.66 ± 0.19	0.80 ± 1.13
A	T-And0-06017	01 12 48.217	49 58 07.16	2.543	1.40 ± 0.35	0.52 ± 0.77	3.49 ± 4.28
B	T-And0-06017	01 12 48.217	49 58 07.16	5.085	1.18 ± 0.71	1.12 ± 0.85	3.12 ± 11.15
A	T-And0-06500	01 25 56.083	49 23 31.74	5.337	0.97 ± 0.20	0.49 ± 0.53	7.71 ± 16.33
B	T-And0-06500	01 25 56.083	49 23 31.74	10.674	1.01 ± 0.30	0.93 ± 0.45	0.74 ± 1.60
A	T-And0-06680	00 55 48.153	45 02 48.57	4.551	1.16 ± 0.04	0.51 ± 0.20	6.09 ± 8.91
B	T-And0-06680	00 55 48.153	45 02 48.57	9.104	1.16 ± 0.09	0.96 ± 0.29	6.24 ± 10.78
A	T-And0-08053	01 13 59.402	45 51 43.43	4.116	1.14 (-1)	0.40 (-2)	6.00 (-1)
B	T-And0-08053	01 13 59.402	45 51 43.43	8.231	1.09 ± 0.55	1.05 ± 0.64	3.22 ± 16.37
A	T-And0-08417	01 01 39.041	45 03 32.98	2.053	1.01 (-1)	0.47 (-1)	10.00 (-3)
B	T-And0-08417	01 01 39.041	45 03 32.98	4.106	1.01 (-1)	0.90 (-1)	10.00 (-3)
A	T-And0-09365	01 01 00.459	45 14 24.77	1.887	1.05 ± 0.03	0.43 ± 0.39	8.74 ± 16.06
B	T-And0-09365	01 01 00.459	45 14 24.77	3.774	1.05 ± 0.05	0.93 ± 0.52	9.47 ± 23.55
A	T-And0-10518	01 07 44.417	48 44 58.11	0.194	0.90 (-1)	0.40 (-2)	0.40 (-1)
B	T-And0-10518	01 07 44.417	48 44 58.11	0.387	0.45 ± 0.27	0.45 ± 0.28	0.27 ± 0.54
A	T-And0-11453	01 05 42.744	44 54 02.26	0.784	1.12 (-1)	0.40 (-2)	7.00 (-1)
B	T-And0-11453	01 05 42.744	44 54 02.26	1.568	1.02 ± 0.43	1.01 ± 0.32	8.81 ± 14.54

^AUnequal eclipse model, assuming an unseen secondary eclipse.^BEqual eclipse model, with double the period of the unequal model.

^cWhen the most likely model is at the edge of the parameter space, MECI is not able to bound the solution, and therefore cannot estimate the uncertainties. We mark (-3) when the upper limit was reached, (-2) when the lower limit was reached, and (-1) if one of the other parameter is at its limit.

Table 5.7. Inverted EBs

Object	α (J2000)	δ (J2000)	Period [days]
T-And0-13653	00 59 57.881	45 03 41.53	3.342
T-Cas0-02069	00 49 17.959	50 39 02.92	2.830
T-Cas0-03012	00 45 41.832	51 01 35.40	1.108
T-Cas0-04618	00 46 22.661	50 39 17.57	2.798
T-Cas0-07780	00 34 18.779	52 00 35.72	1.852
T-Cas0-19045	00 21 44.707	50 32 29.55	0.785
T-Cas0-19668	00 48 01.342	47 06 11.58	1.848
T-Cas0-21651	00 26 34.895	46 38 42.69	1.155
T-Cyg1-01956	19 53 29.106	47 48 49.86	2.045
T-Cyg1-02929	20 11 57.009	48 07 03.59	4.263
T-Cyg1-17342	19 49 54.197	50 53 28.08	2.220
T-Her0-05469	16 54 51.245	43 20 35.89	0.899
T-Lyr1-04431	19 12 16.047	49 42 23.58	0.903
T-Lyr1-05887	18 52 10.489	47 48 16.67	1.802
T-Lyr1-07179	18 49 14.039	45 24 38.61	1.323
T-Lyr1-10989	19 06 22.791	45 41 53.82	2.015
T-Lyr1-11067	18 52 53.489	47 51 26.58	2.241
T-Per1-04353	03 45 04.887	37 47 15.91	2.953
T-Per1-06993	03 40 59.668	39 12 35.90	2.125
T-Per1-09366	03 49 20.305	39 55 41.97	2.374
T-Per1-12217	03 28 59.454	37 37 42.14	1.690
T-Tau0-00686	04 07 13.870	29 18 32.44	5.361
T-UMa0-00127	09 38 06.716	56 01 07.32	0.687

Table 5.8. EBs that fill at least one of their Roche-lobes (first 20)

Object	α (J2000)	δ (J2000)	Period [days]
T-And0-03774	00 59 01.029	46 47 17.08	1.362
T-And0-04813	01 16 37.880	47 33 23.43	0.552
T-And0-05140	01 03 22.258	44 56 24.31	0.981
T-And0-05153	01 18 48.278	49 39 36.86	0.492
T-And0-05343	00 52 55.122	48 01 37.68	0.824
T-And0-07638	01 09 27.871	49 20 33.81	0.403
T-And0-07892	00 56 15.567	48 39 10.73	0.380
T-And0-08330	01 19 15.949	48 00 17.45	0.630
T-And0-08652	00 56 58.855	49 05 05.00	0.335
T-And0-09528	01 22 09.328	47 14 29.86	0.918
T-And0-10071	01 14 50.412	49 17 46.28	0.387
T-And0-10206	00 55 55.724	49 49 46.56	0.859
T-And0-10511	01 19 16.430	47 07 46.27	0.563
T-And0-10722	01 04 03.859	48 37 13.04	1.062
T-And0-11354	01 18 05.168	46 10 14.66	0.331
T-And0-11476	01 07 32.106	45 55 44.93	6.380
T-And0-11599	01 09 28.113	46 18 24.85	0.280
T-And0-11617	01 07 28.020	45 22 40.35	0.503
T-And0-12453	01 17 12.316	46 42 35.43	0.448
T-And0-12769	00 52 58.164	44 44 11.26	0.325

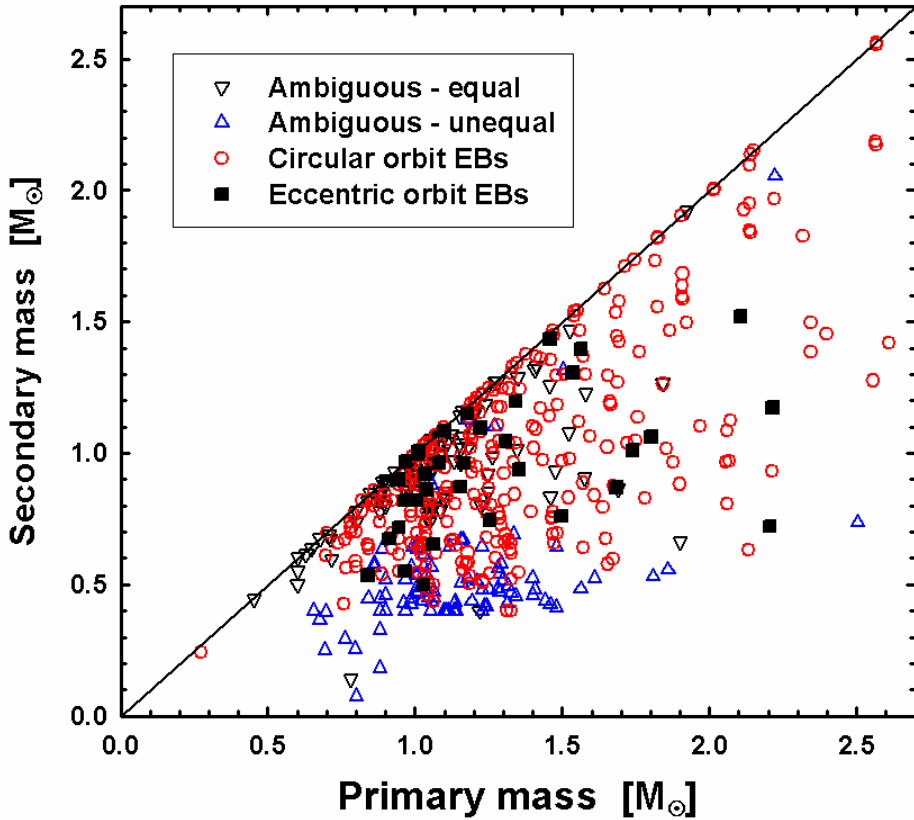


Fig. 5.19.— The mass-mass relation for the detached EBs of the TrES dataset. Each category is represented by a different symbol. Note that the ambiguous EBs are plotted twice, where only one of the solutions can be correct. Note also that the equal-component solutions are clustered along the diagonal, while the unequal-component solutions with $M_1 > 0.75 M_\odot$ are clustered along the minimum available mass of the Yonsei-Yale isochrones ($0.4 M_\odot$). Some of the ambiguous solutions deviate from these clusters due to poor constraints on the secondary eclipse, which brings about a large uncertainty. Finally, note the sparsity of EBs populating the low-mass corner of this plot ($M_{1,2} < 0.75 M_\odot$). These systems, whose importance is outlined in §5.3.1, were modeled using the Baraffe isochrones. CM Draconis (T-Dra0-01363) clearly sets itself apart, being the lowest-mass binary in the catalog (circle at bottom left).

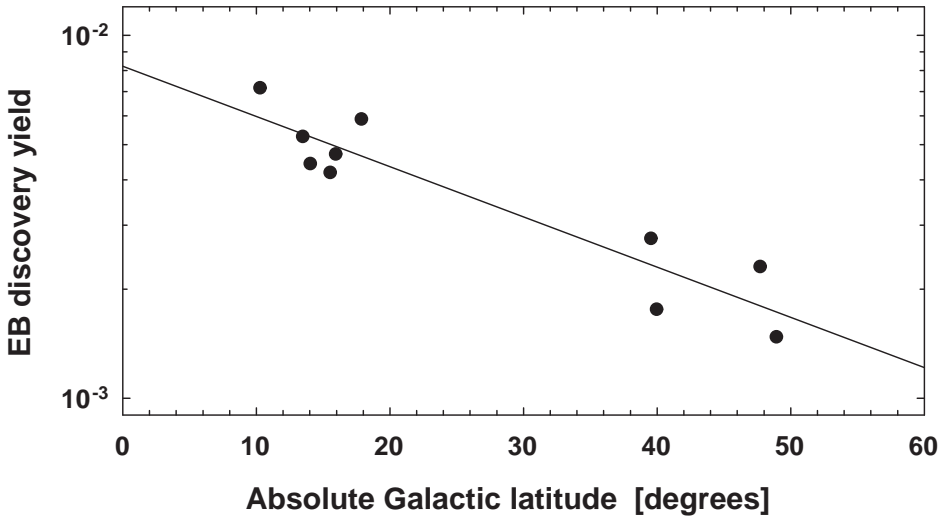


Fig. 5.20.— The relation between the EB discovery yield (the fraction of LCs found to be EBs) and the absolute value of the Galactic latitude, or $|b|$, for the ten TrES fields used in this catalog (see Tables 5.1 and 5.2). The solid line is the linear regression of the log of the EB discovery yield ($r^2 = 0.867$). Some of the residual scatter can be explained as being due to differences in the duration of observations in each field. By including the duration in a bi-linear regression, we get a substantially improved fit ($r^2 = 0.911$).

Table 5.9. EBs that appear in either the VSX or the SIMBAD databases

Category	Object	α (J2000)	δ (J2000)	Spectral type	Classification	Identifiers
Circular	T-And0-00194	01 20 12.816	48 36 41.36	A5	Star	BD+47 378 ; GSC 03269-00662 ; SAO 37126 ; AG+48 143 PPM 43886 ; TYC 3269-662-1
Circular	T-And0-00459	01 11 24.845	46 57 49.44	F8	EB of Algol type	CO And ; GSC 03268-00398 ; TYC 3268-398-1 ; BD+46 281 ; BV 74
Ambiguous	T-And0-00657	01 06 06.159	47 31 59.37	K0	Star	BD+46 254 ; GSC 03267-01349 ; TYC 3267-1349-1 ; AG+47 120 ; PPM 43637
Circular	T-And0-00745	01 03 45.076	44 50 41.14		Star	TYC 2811-470-1 ; GSC 02811-00470
Ambiguous	T-And0-01203	01 03 34.745	48 32 39.27		Star	TYC 3267-1176-1 ; GSC 03267-01176
Circular	T-And0-04046	00 55 20.157	47 44 53.20		Star	GPM 13.833991+47.748193
Roche-fill	T-And0-05153	01 18 48.278	49 39 36.86		EB of W UMa type	QW And
Roche-fill	T-And0-05343	00 52 55.122	48 01 37.68		Star	GPM 13.232700+48.019757
Roche-fill	T-And0-07892	00 56 15.567	48 39 10.73		EB	NSVS 3757820
Circular	T-And0-23792	00 54 09.254	47 45 19.91		Star	GPM 13.538629+47.755510
Roche-fill	T-Cas0-00170	00 53 37.847	48 43 33.83		Star	TYC 3266-195-1 ; GSC 03266-00195
Eccentric	T-Cas0-00394	00 32 51.608	49 19 39.36	B3	EB of β Lyr type	V381 Cas ; BD+48 162 ; BV 179
Roche-fill	T-Cas0-00430	00 40 06.247	50 14 15.64	K4	EB of W UMa type	V523 Cas ; GSC 03257-00167 ; WR 16 ; CSV 5867 1RXS J004005.0+501414 ; TYC 3257-167-1
Circular	T-Cas0-00640	00 47 06.277	48 31 13.14		Star	TYC 3266-765-1 ; GSC 03266-00765
Circular	T-Cas0-00792	00 48 26.554	51 35 02.52		Star	TYC 3274-664-1 ; GSC 03274-00664
Roche-fill	T-Cas0-02013	00 40 46.427	46 56 57.41		Star	TYC 3253-1767-1 ; GSC 03253-01767
Inverted	T-Cas0-02069	00 49 17.959	50 39 02.92		EB	V385 Cas
Roche-fill	T-Cas0-08802	00 51 32.351	47 16 42.57		Star	GPM 12.884787+47.278540
Roche-fill	T-CrB0-00654	16 00 14.507	35 12 31.56		EB of W UMa type	AS CrB ; GSC 02579-01125 ; NSVS 7847829 ROTSE1 J160014.54+351228.4
Roche-fill	T-CrB0-00705	15 55 51.838	33 11 00.39		EB of W UMa type	ROTSE1 J155551.87+331100.5
Roche-fill	T-CrB0-01589	16 10 09.313	35 57 30.57		Variable of δ Sct type	ROTSE1 J161009.33+355730.8
Roche-fill	T-CrB0-01605	16 00 58.472	34 18 54.34		EB of W UMa or RR Lyr-C	NSVS 7848126 ; ROTSE1 J160058.45+341854.5
Roche-fill	T-CrB0-04254	16 09 19.589	35 32 11.48		EB of W UMa type	ROTSE1 J160919.62+353210.8
Circular	T-Cyg1-00246	19 44 01.777	50 13 57.42		Star	TYC 3565-643-1 ; GSC 03565-00643

Table 5.9—Continued

Category	Object	α (J2000)	δ (J2000)	Spectral type	Classification	Identifiers
Roche-fill	T-Cyg1-00402	19 54 39.939	50 36 41.91		Star	TYC 3566-606-1 ; GSC 03566-00606
Ambiguous	T-Cyg1-01385	20 15 21.936	48 17 14.14		Star	TYC 3576-2035-1 ; GSC 03576-02035
Circular	T-Cyg1-01627	19 45 20.426	51 35 07.22		Star	TYC 3569-1752-1 ; GSC 03569-01752
Roche-fill	T-Cyg1-04652	20 07 07.305	50 34 01.34		EB of W UMa type	GSC 03567-01035
Roche-fill	T-Cyg1-04852	19 51 59.208	50 05 29.61		EB of W UMa type	NSVS 5645908
Circular	T-Cyg1-09274	20 16 06.814	51 56 26.07		EB of W UMa type	V1189 Cyg ; CSV 8488 ; GSC 03584-01600 ; SON 7885
Roche-fill	T-Cyg1-11279	19 59 53.377	49 23 27.86		X-ray source	1RXS J195954.0+492318
Roche-fill	T-Cyg1-12518	19 58 15.339	48 32 15.79		Variable star	Mis V1132
Roche-fill	T-Cyg1-14514	19 48 05.077	52 51 16.25		EB of W UMa or RR Lyr-C	V997 Cyg ; GSC 03935-02233 ; ROTSE1 J194804.79+525117.6 ; SON 7839
Ambiguous	T-Dra0-00240	17 03 52.919	57 21 55.54		Star	TYC 3894-898-1 ; GSC 03894-00898
Ambiguous	T-Dra0-00358	16 45 38.339	54 31 32.02		Star	TYC 3879-2689-1 ; GSC 03879-02689
Circular	T-Dra0-00398	16 57 33.875	59 31 51.98		EB of Algol type/X-ray source	RX J1657.5+5931 ; 1RXS J165733.5+593156 VSX J165733.8+593151 ; GSC 03898-00272
Roche-fill	T-Dra0-00405	16 27 49.103	58 50 23.30		Star	TYC 3884-1488-1 ; GSC 03884-01488
Roche-fill	T-Dra0-00959	16 27 44.159	56 45 59.30		EB of W UMa type/X-ray source	NSVS 2827877 ; 1RXS J162743.9+564557
Circular	T-Dra0-01363	16 34 20.417	57 09 48.95	M4.5V	EB of BY Dra type	CM Dra ; CSI+57-16335 1 ; LSPM J1634+5709 ; G 225-67 ; G 226-16 IDS 16326+5721 A ; [RHG95] 2616 ; SBC7 580 ; CCDM J16343+5710A GJ 630.1 A ; LP 101-15 ; IDS 16325+5721 A ; [GKL99] 324 ; LHS 421 2MASS J16342040+5709439 ; CCABS 108 ; CABS 134 ; GEN# +9.80225067
					High proper-motion Star	RX J1634.3+5709 ; 1RXH J163421.2+570941 ; 1RXS J163421.2+570933 PM 16335+5715 ; USNO 168 ; USNO-B1.0 1471-00307615 ; NLTT 43148
Roche-fill	T-Dra0-01346	16 52 12.345	57 43 31.70		EB of Algol type	BPS BS 16080-0095 ; VSX J165212.3+574331 ; GSC 03885-00583
Roche-fill	T-Dra0-02224	16 30 01.408	54 45 55.80		Star	BPS BS 16084-0159
Circular	T-Dra0-03021	17 01 03.618	55 14 54.70		EB of Algol type	VSX J170103.5+551455 ; GSC 03890-01216
Abnormal	T-Dra0-03105	16 23 02.558	59 27 23.44		X-ray source	1RXS J162303.6+592717
Roche-fill	T-Dra0-05259	16 41 48.751	56 22 34.40		EB of W UMa type	VSX J164148.7+562234 ; GSC 03882-02264 ; USNO-B1.0 1463-0278621
Ambiguous	T-Her0-00274	17 00 51.150	45 25 35.94		Star	TYC 3501-2245-1 ; GSC 03501-02245

Table 5.9—Continued

Category	Object	α (J2000)	δ (J2000)	Spectral type	Classification	Identifiers
Roche-fill	T-Her0-01086	16 48 15.539	44 44 28.73		EB of W UMa type	GSC 03082-00896 ; NSVS 5252572 ; 1RXS J164817.3+444430
Roche-fill	T-Her0-03579	16 35 47.390	45 24 58.19		EB of W UMa type	GSC 03499-01631
Inverted	T-Her0-05469	16 54 51.245	43 20 35.89		EB	V747 Her ; SVS 2066
Circular	T-Lyrl-00359	19 15 33.695	44 37 01.30	G0V	EB	V2277 Cyg ; GSC 03133-01149 ; ROTSE1 J191533.92+443704.9
					X-ray source	BD+44 3087 ; ILF1+44 155 ; 1RXS J191533.7+443704
Circular	T-Lyrl-00687	18 55 27.911	47 13 41.76		Star	TYC 3544-1392-1 ; GSC 03544-01392
Circular	T-Lyrl-01013	18 55 03.963	47 49 08.39		Star	TYC 3544-2565-1 ; GSC 03544-02565
Circular	T-Lyrl-01439	19 06 13.439	46 57 26.42		Star	TYC 3545-2716-1 ; GSC 03545-02716
Circular	T-Lyrl-02109	18 57 35.415	45 07 44.10		Cepheid variable star	ROTSE1 J185735.99+450752.5
Roche-fill	T-Lyrl-02166	19 05 07.448	46 15 07.51		X-ray source	1RXS J190504.8+461512
Roche-fill	T-Lyrl-03173	18 59 45.531	47 20 07.34		EB of W UMa type	ROTSE1 J185945.43+472007.0
Roche-fill	T-Lyrl-03211	18 45 56.939	47 19 09.54		EB of W UMa type/X-ray source	ROTSE1 J184556.86+471914.4 ; 1RXS J184557.9+471906
Roche-fill	T-Lyrl-03270	18 57 33.098	48 05 22.49		EB of W UMa type	ROTSE1 J185733.12+480522.5
Roche-fill	T-Lyrl-03783	18 50 12.684	45 35 44.05		Star	GPM 282.552858+45.595521
Inverted	T-Lyrl-04431	19 12 16.047	49 42 23.58		EB of Algol type	NSV 11822 ; GSC 03550-01770 ; NSVS 5578839 ; SON 9371
Roche-fill	T-Lyrl-05706	18 47 57.211	44 38 11.30		EB of W UMa type	ROTSE1 J184757.18+443810.8
Inverted	T-Lyrl-05887	18 52 10.489	47 48 16.67		EB of Algol type	WX Dra ; AN 24.1925
Roche-fill	T-Lyrl-06583	18 52 26.837	44 55 20.86		EB	ROTSE1 J185226.53+445527.8
Inverted	T-Lyrl-07179	18 49 14.039	45 24 38.61		Star	GPM 282.308454+45.410868
Roche-fill	T-Lyrl-08406	18 50 06.942	45 41 05.95		Star	GPM 282.528833+45.685035
Roche-fill	T-Lyrl-10276	18 46 55.088	45 00 52.27		EB of W UMa type	V596 Lyr ; GPM 281.729421+45.014635 ; GSC 03540-00085
						ROTSE1 J184654.98+450054.7
Inverted	T-Lyrl-10989	19 06 22.791	45 41 53.82		EB of Algol type	V512 Lyr ; SON 10931
Roche-fill	T-Lyrl-11226	18 45 21.748	45 53 28.79		EB of W UMa type or δ Sct	V594 Lyr ; GPM 281.340617+45.891326 ; GSC 03540-01842
						ROTSE1 J184522.47+455321.0
Roche-fill	T-Lyrl-12772	18 52 25.096	44 55 40.23		EB of W UMa type	ROTSE1 J185226.53+445527.8
Abnormal	T-Lyrl-13166	19 02 28.120	46 58 57.75	F9V	EB	V361 Lyr ; SON 9349

5.3.1 Low-Mass EBs

The first group consists of 11 low-mass EB candidates, including 10 newly discovered EBs with either K or M-dwarf stellar components. Our criteria for selecting these binaries were that they be well-detached, and that both components have estimated masses below $0.75M_{\odot}$ (see Table 5.10 and Figure 5.21). Currently, only seven such detached low-mass EBs have been confirmed [YY Gem: (Kron 1952; Torres & Ribas 2002); CM Dra: (Lacy 1977a; Metcalfe et al. 1996); CU Cnc: (Delfosse et al. 1999; Ribas 2003); T-Her0-07621: (Creevey et al. 2005); GU Boo: (López-Morales & Ribas 2005); NSVS01031772: (López-Morales et al. 2006); and UNSW-TR-2: (Young et al. 2006)].

Despite a great deal of work that has been done to understand the structure of low-mass stars [e.g., Chabrier & Baraffe (2000)], models continue to underestimate their radii by as much as 15% (Lacy 1977b; Torres & Ribas 2002; Creevey et al. 2005; Ribas 2006), a significant discrepancy considering that for solar-type stars the agreement with the observations is typically within 1 – 2% (Andersen 1991, 1998). In recent years, an intriguing hypothesis has been put forward that strong magnetic fields may have bloated these stars through chromospheric activity (Ribas 2006; Torres et al. 2006; López-Morales 2007; Chabrier et al. 2007). Furthermore, Torres et al. (2006) find that such bloating occurs even for stars with nearly a solar mass, and suggest that this effect may also be due to magnetically induced convective disruption. In either case, these radius discrepancies should diminish for widely separated binaries with long periods, as they become non-synchronous and thus rotate slower, which according to dynamo theory would reduce the strength of

Table 5.9—Continued

Category	Object	α (J2000)	δ (J2000)	Spectral type	Classification	Identifiers
Roche-fill	T-Per1-00328	03 41 57.108	39 07 29.60	G5	EB of Algol type	HD 275743 ; BD+38 787 ; GSC 02863-00755 ; TYC 2863-755-1
Circular	T-Per1-00459	03 34 57.745	39 33 18.70	G5	Star	HD 275547 ; GSC 02866-01995 ; TYC 2866-1995-1
Circular	T-Per1-00750	03 47 45.543	35 00 37.08		Double or multiple star	TYC 2364-2327-1 ; GSC 02364-02327 ; CCDM J03478+3501BC ADS 2771 BC ; BD+34 732B ; CSI+34 732 2 ; NSV 1302
Roche-fill	T-Per1-00974	03 34 43.738	38 40 22.22	A	Star	HD 275481
Circular	T-Per1-01218	03 42 33.165	39 06 03.63	A	EB	HU Per ; HD 275742 ; SVS 922
Roche-fill	T-Per1-01482	03 48 45.999	35 14 10.05	F0	Star	HD 279025
Circular	T-Per1-02597	03 44 32.202	39 59 34.94	K4V	T Tau type Star	[LH98] 94 ; 1RXS J034432.1+395937 ; 1SWASP J034433.95+395948.0
Inverted	T-Per1-04353	03 45 04.887	37 47 15.91		EB of Algol type	HV Per ; SVS 368 ; P 107
Roche-fill	T-Tau0-00397	04 30 09.466	25 32 27.05	A3	EB of β Lyr type	GW Tau ; SVS 1421 ; HD 283709 ; ASAS 043009+2532.4
Inverted	T-Tau0-00686	04 07 13.870	29 18 32.44		EB of Algol type	IL Tau ; SON 9543
Roche-fill	T-Tau0-00781	04 12 51.218	24 41 44.26	G9	Eruptive/T Tau-type Star	V1198 Tau ; NPM2+24.0013 ; 1RXS J041250.9+244201 GSC 01819-00498 ; RX J0412.8+2442 ; [WKS96] 14
Roche-fill	T-Tau0-01262	04 16 28.109	28 07 35.81	K7V	Variable Star of Orion Type	V1068 Tau ; EM StHA 25 ; JH 165 ; EM LkCa 4 HBC 370 ; ASAS 041628+2807.6
Roche-fill	T-Tau0-01715	04 19 26.260	28 26 14.30	K7V	T Tau-type Star/X-ray source	V819 Tau ; HBC 378 ; NAME WK X-Ray 1 ; 1E 0416.3+2830 IRAS C04162+2819 ; TAP 27 ; [MWF83] P1 ; WK81 1 1RXS J041926.1+282612 ; X 04163+283
Roche-fill	T-Tau0-06463	04 07 27.415	27 51 06.36		EB of W UMa type	V1022 Tau ; HV 6199 ; NSV 1464
Inverted	T-UMa0-00127	09 38 06.716	56 01 07.32	A2V	EB of Algol type	VV UMa ; GEN# +0.05601395 ; HIP 47279 ; TYC 3810-1290-1 GSC 03810-01290 ; SBC7 384 ; GCRV 6211 ; BD+56 1395 HIC 47279 ; SVS 770 ; AAVSO 0931+56
Circular	T-UMa0-00222	10 07 18.023	56 12 37.12	A0	Star	HD 237866 ; GSC 03818-00504 ; SAO 27524 ; AG+56 778 ; HIC 49581 BD+56 1432 ; HIP 49581 ; YZ 56 6209 ; TYC 3818-504-1
Roche-fill	T-UMa0-01701	10 03 02.856	55 47 53.34		X-ray source	RX J100303.4+554752 ; [PTV98] H22 ; [PTV98] P29
Circular	T-UMa0-03090	10 08 52.180	52 45 52.49	K2e	Star	GSC 03815-01151 ; RIXOS 229-302 ; RX J100851.6+524553
Roche-fill	T-UMa0-03108	10 04 16.780	54 12 02.83		EB of W UMa type	NSVS 2532137

their magnetic fields.

Unfortunately, the small number of well-characterized low-mass EBs makes it difficult to provide strong observational constraints to theory. Despite the fact that such stars make up the majority of the Galactic stellar population, their intrinsic faintness renders them extremely rare objects in magnitude-limited surveys. In addition, once found, their low flux severely limits the ability to observe their spectra with both sufficiently high resolution and a high signal-to-noise ratio. To this end, the fact that the TrES survey was made with small-aperture telescopes is a great advantage, as any low-mass EB candidate found is guaranteed to be bright, and thus requires only moderate-aperture telescopes for their follow-up. Thus we propose multi-epoch spectroscopic study of the systems listed here, in order to confirm their low mass and to estimate their physical properties with an accuracy sufficient to test models of stellar structure. Moreover, two of our candidates (T-Cyg1-12664 and T-Cas0-10450), if they are in fact ambiguous-equal (group [IV]), have periods greater than 8 days, making them prime targets for testing the aforementioned magnetic-bloating hypothesis.

5.3.2 Eccentric EBs

The second group of EBs consists of 34 binaries with eccentric orbits (see Table 5.3, and Figures 5.9-5.11). We were able to reliably measure values of $|e \cos \omega|$ as low as ~ 0.005 by using the eclipse timing technique (see §5.2 and Figure 5.3). Since this measure provides a lower limit to the eccentricity, it is well suited to identify eccentric EBs, even though the actual value of the eccentricity may be uncertain.

Table 5.10. Low-mass EB candidates ($M_{1,2} < 0.75M_{\odot}$; sorted by mass)

Category	Object	α (J2000)	δ (J2000)	Period [days]	M_1/M_{\odot}	M_2/M_{\odot}	age [Gyr]	Proper motion source catalog ^a	PM_{α} mas/year	PM_{δ} mas/year
Circular	T-Dra0-01363 ^b	16 34 20.417	57 09 48.95	1.268	0.27 ± 0.02	0.24 ± 0.03	1.6 ± 1.6	Salim & Gould (2003)	-1121	1186
AmbigEq ^c	T-And0-10518	01 07 44.417	48 44 58.11	0.387	0.45 ± 0.27	0.45 ± 0.28	0.3 ± 0.5	UCAC	2.7	-2.0
AmbigEq	T-Cyg1-12664	19 51 39.824	48 19 55.38	8.257	0.50 ± 0.20	0.48 ± 0.19	0.3 ± 0.4	USNO-B	-18	-6
AmbigEq	T-CrB0-14232	16 10 22.495	33 57 52.33	0.971	0.60 ± 0.24	0.55 ± 0.29	4.4 ± 8.8	UCAC	-15.2	-24.2
AmbigEq	T-CrB0-14543	15 57 45.926	33 56 07.28	1.506	$0.60 (-1)^d$	$0.60 (-1)$	$0.2 (-2)$	UCAC	-13.9	13.3
Circular	T-Per1-13685	03 53 51.217	37 03 16.73	0.384	$0.60 (-1)$	$0.50 (-1)$	$10.0 (-3)$	UCAC	-24.1	-15.9
AmbigEq	T-CrB0-10759	15 52 18.455	30 35 32.13	1.901	0.63 ± 0.24	0.62 ± 0.21	7.3 ± 49.6	UCAC	3.6	-19.4
AmbigEq	T-UMa0-08238	10 09 25.384	53 57 01.31	1.250	0.69 ± 0.54	0.61 ± 0.51	4.1 ± 15.0	USNO-B	6	-4
AmbigEq	T-Cas0-10450	00 29 16.288	50 27 38.58	8.656	0.71 ± 0.21	0.67 ± 0.20	0.3 ± 0.4	UCAC	-3.1	-4.2
AmbigEq	T-Dra0-07116	17 02 53.025	55 07 47.44	1.369	0.71 ± 0.22	0.69 ± 0.22	2.1 ± 3.6	USNO-B	-2	-16
Circular	T-Tau0-04859	04 08 11.608	24 51 10.18	3.068	0.74 ± 0.10	0.66 ± 0.10	8.8 ± 14.8	UCAC	3.4	-8.0

^aWhere possible, we used the more accurate UCAC catalog, otherwise we reverted to the USNO-B catalog. Since they are dim and nearby, we expect most of the low-mass binaries to have comparably large proper motions.

^bThis binary is CM Draconis, which has been extensively studied and found to have a masses of $M_1 = 0.2307 \pm 0.0010M_{\odot}$ and $M_2 = 0.2136 \pm 0.0010M_{\odot}$ (Lacy 1977a; Metcalfe et al. 1996). For consistency, we listed the MECI results, which are off by less than $0.04M_{\odot}$ ($\sim 1.5\sigma$). We also adopted an alternate proper motion estimate, as its USNO-B values seems to be erroneous, probably due to its very high angular velocity.

^cFor clarity we list for the ambiguous systems, only the solution with approximately equal components. But it is likely that at least a few of the ambiguous systems may be unequal, with half the period. Such cases can be identified as single-line spectroscopic binaries, with the secondary component being no larger than a few $0.1M_{\odot}$.

^dWhen the most likely model is at the edge of the parameter space, MECI is not able to bound the solution, and therefore cannot estimate the uncertainties. We mark (-3) when the upper limit was reached, (-2) when the lower limit was reached, and (-1) if one of the other parameter is at its limit.

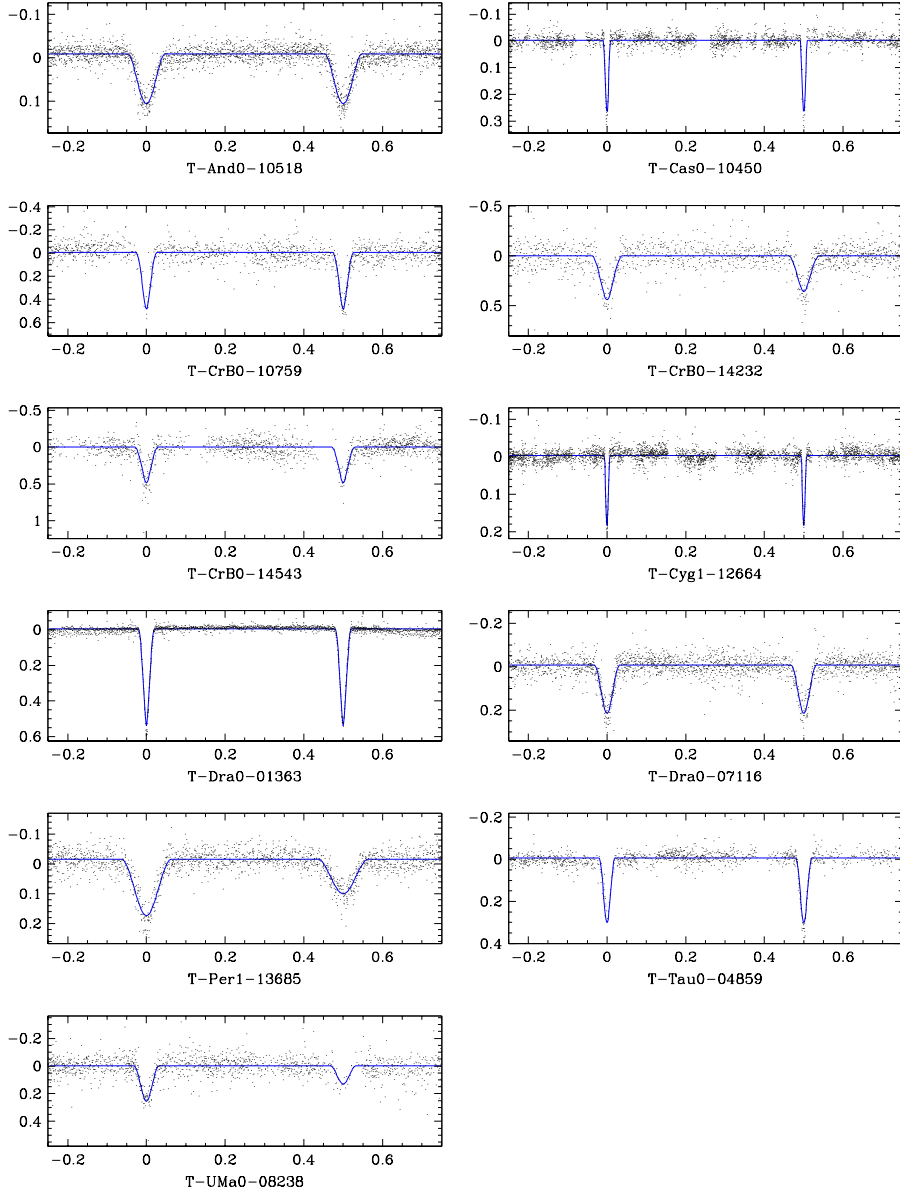


Fig. 5.21.— Low-mass candidates ($M_1 < 0.75 M_\odot$), with their best-fit MECI models (solid line).

As mentioned earlier, in an effort to avoid false-positives, we do not include in this group EBs whose eclipse timing measures $|e \cos \omega| < 0.005$, or EBs with an eccentricity consistent with zero.

Our interest in these eccentric binaries stems from their potential to constrain tidal circularization theory (Darwin 1879). This theory describes how the eccentricity of a binary orbit decays over time due to tidal dissipation, with a characteristic timescale (t_{circ}) that is a function of the components' stellar structure and orbital separation. As long as the components' stellar structure remains unchanged, the orbital eccentricity is expected to decay approximately exponentially over time [$e \propto \exp(-t/t_{circ})$]. However, once the components evolve off the main-sequence, this timescale may vary considerably (Zahn & Bouchet 1989). Thus, to understand the circularization history of binaries with circularization timescales similar to or larger than their evolutionary timescales, one must integrate over the evolutionary tracks of both stellar components.

Three alternative tidal dissipation mechanisms have been proposed: dynamical tides (Zahn 1975, 1977), equilibrium tides (Zahn 1977; Hut 1981), and hydrodynamics (Tassoul 1988). Despite its long period of development, the inherent difficulty of observing tidal dissipation has prevented definitive conclusions. Zahn & Bouchet (1989) add a further complication by maintaining that most of the orbital circularization process takes place at the beginning of the Hayashi phase, and that the eccentricity of a binary should then remain nearly constant throughout its lifetime on the main-sequence.

Observational tests of these tidal circularization theories, whereby t_{circ} is

measured statistically in coeval stellar populations, have so far proved inconclusive. North & Zahn (2003) found that short-period binaries in both the Large and Small Magellanic Clouds seem to have been circularized in agreement with the theory of dynamical tides. However, Meibom & Mathieu (2005) show that, with the exception of the Hyades, the stars in the clusters that they observed were considerably more circularized than any of the known dissipation mechanisms would predict. Furthermore, they find with a high degree of certainty, that older clusters are more circularized than younger ones, thereby contradicting the Hayashi phase circularization model.

Encouraged by the statistical effect of circularization that can be seen in our catalog (Figure 5.22), we further estimated t_{circ} for each of the eccentric systems as follows. Zahn (1977, 1978) provides an estimate for the orbital circularization timescale due to turbulent dissipation in stars possessing a convective envelope, assuming that corotation has been achieved:

$$t_{circ} = \frac{1}{21q(1+q)k_2} \left(\frac{MR^2}{L} \right)^{1/3} \left(\frac{a}{R} \right)^8 \quad (5.8)$$

where M, R, L are the star's mass, radius, and luminosity, and k_2 is the apsidal motion constant of the star, which is determined by its internal structure and dynamics.

More massive stars, which do not have a convective envelope but rather develop a radiative envelope, are thought to circularize their orbit using radiative damping (Zahn 1975; Claret & Cunha 1997). This is a far slower mechanism, whose circularization timescale can be estimated by:

$$t_{circ} = \frac{2}{21q(1+q)^{11/6}E_2} \left(\frac{R^3}{GM}\right)^{1/2} \left(\frac{a}{R}\right)^{21/2} \quad (5.9)$$

where E_2 is the tidal torque constant of the star, and G is the universal gravitational constant. We can greatly simplify these expressions by applying Kepler's law [$a^3 = GM(1+q)(P/2\pi)^2$], and adopt the Cox (2000) power law approximations for the main-sequence mass-radius and mass-luminosity relations. For the convective envelope case, we adopt the late-type mass-radius relation ($M < 1.3M_\odot$), and for the radiative envelope case we adopt the early-type mass-radius relation ($M \geq 1.3M_\odot$), thus arriving at:

$$t_{circ} \simeq \begin{cases} 0.53 \text{Myr} (k_2/0.005)^{-1} q^{-1} (1+q)^{5/3} (P/\text{day})^{16/3} (M/M_\odot)^{-4.99}, & M < 1.3M_\odot \\ 1370 \text{Myr} (E_2/10^{-8})^{-1} q^{-1} (1+q)^{5/3} (P/\text{day})^7 (M/M_\odot)^{-2.76}, & M \geq 1.3M_\odot \end{cases} \quad (5.10)$$

Determining the values of k_2 and E_2 is the most difficult part of this exercise, since their values are a function of the detailed structure and dynamics of the given star, which in turn changes significantly as the star evolves (Claret & Cunha 1997; Claret & Willems 2002). In our calculation, we estimate these values by interpolating published theoretical tables [k_2 : Zahn (1994), E_2 : Zahn (1975); Claret & Cunha (1997)]. Since both stellar components contribute to the circularization process, the combined circularization timescale becomes $t_{circ} = 1/(t_{circ,1}^{-1} + t_{circ,2}^{-1})$, where the subscripts 1 and 2 refer to the primary and secondary binary components (Claret & Cunha 1997). In Table 5.3, we list the combined circularization timescale for each of the eccentric EBs we identify.

The value of t_{circ} for most of the eccentric systems (21 of 34) is larger than the

Hubble time, indicating that no significant circularization is expected to have taken place since they settled on the main-sequence. About a quarter of the eccentric systems (8 of 34) have a t_{circ} smaller than the Hubble time but larger than 1 *Gyr*. While circularization is underway, the fact that they are still eccentric is consistent with theoretical expectations. The remaining systems (5 of 34) all have $t_{circ} < 1 \text{ Gyr}$, have periods less than 3.3 days, and unless they are extremely young, require an explanation for their eccentric orbits. Two of these EBs (T-Tau0-02487 and T-Tau0-03916) are located near the star-forming regions of Taurus, supporting the hypothesis that they are indeed young. However, this hypothesis does not seem to be adequate for T-Cas0-02603, which has a period of only 2.2 days and $t_{circ} \simeq 0.26 \text{ Gyr}$, while possessing a large eccentricity of $e \simeq 0.25$. An alternative explanation is that some of these binaries were once further apart, having larger orbital periods, and thus larger circularization timescales. These systems may have been involved in a comparably recent interaction with a third star (a collision or near miss), or have been influenced by repeated resonant perturbations of a tertiary companion.

Finally, we would like to draw the reader's attention to our shortest-period eccentric EB, T-Cas0-00394, whose period is a mere 1.7 days. Notably, this system is entirely consistent with theory, since its mass falls in a precarious gap, where the stellar envelopes of its components are no longer convective, yet their radiative envelopes are not sufficiently extended to produce significant tidal drag (see Figure 5.23).

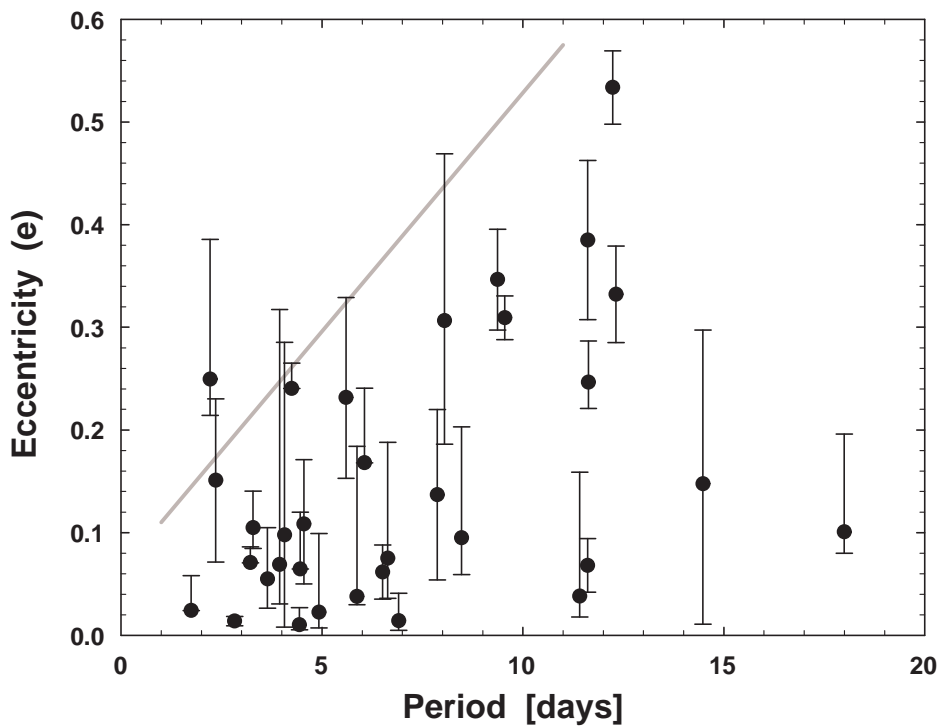


Fig. 5.22.— The period-eccentricity relation. The lower ends of the error bars were truncated, where needed, by the measured lower limit, $|e \cos \omega|$. Note the lack of eccentric short-period systems. The diagonal line is provided to guide the eye.

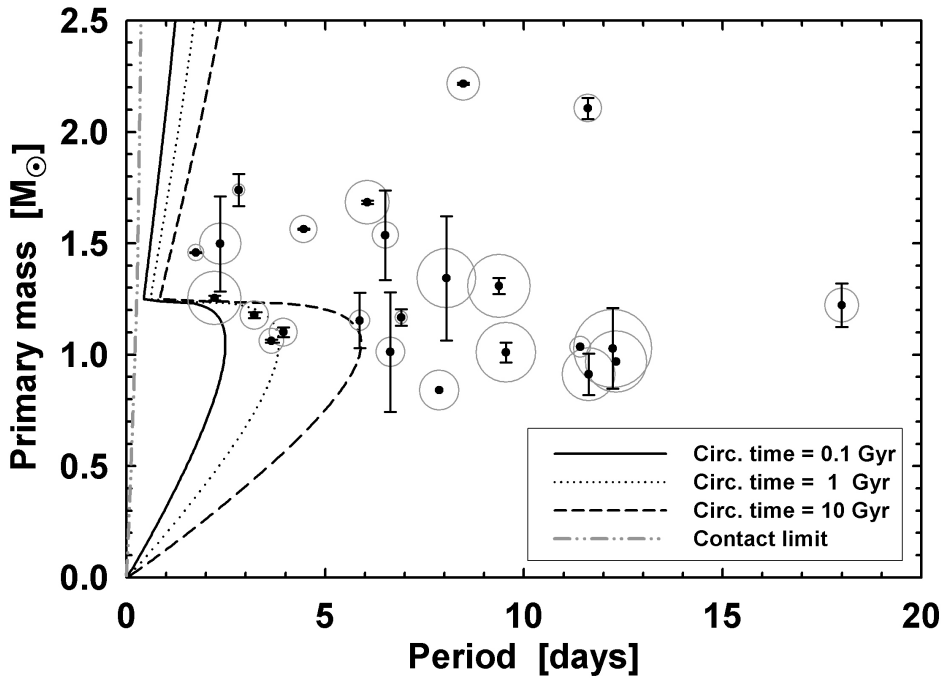


Fig. 5.23.— The period-primary mass relation for eccentric EBs. We included all systems with well-determined masses. The area of the gray circles is proportional to the EB's eccentricity. All the curves are theoretical boundaries, assuming that the binary components are both on the main-sequence and have equal masses ($q = 1$). The left-most dot-dash line demarcates the binary contact limit, and the remaining curves mark systems with increasing circularization time (see equation 5.10). Note the abrupt increase in the circularization time for systems more massive than $\sim 1.25 M_{\odot}$, at which point the stellar convective envelope becomes radiative, and thus far less efficient at tidal dissipation.

5.3.3 Abnormal EBs

The third group of EBs consists of 20 abnormal systems (see Table 5.4, and Figures 5.17 and 5.18). While possessing the distinctive characteristics of EBs, these LCs stood out during manual inspection for a variety of reasons. These systems underline the difficulty of fully automating any LC pipeline, as any such system will inevitably need to recognize atypical EBs that were not encountered before.

The LCs we listed can be loosely classified into groups according to the way they deviate from a simple EB model. A few cases exhibited pulsation-like fluctuations that were not synchronized with the EB period (shorter-period: T-Dra0-00398, longer-period: T-Lyr1-00359, T-Per1-00750). These fluctuations may be due either to the activity of an EB component, or to a third star whose light is blended with the binary. In principle, one can identify the active star by examining the amplitude of the fluctuations during the eclipses. If the fluctuations originate from one of the components, their observed amplitude will be reduced when the component is being eclipsed. In such a case, if the fluctuations are due to pulsations, they can further provide independent constraints to the stellar properties through astro-seismological models (Mkrtichian et al. 2004). To identify such fluctuating EBs one must subtract the fitted EB model from the LC, and evaluate the residuals [e.g., Pilecki & Szczygiel (2007)]. When the fluctuation period is fixed, one can simply search the residual LC using a periodogram, as was done in step (1) of our pipeline (see §5.2). However, when the fluctuation period varies (i.e. non-coherent), as in the aforementioned LCs, one must employ alternative methods, since simply phasing their LC will not produce any discernable structure. For LCs with long-period

fluctuations, one can directly search the residuals for time dependencies, while for LCs with short-period fluctuations one can search the residuals for non-Gaussian distributions. However, in practice these measurements will likely not be robust, as there are many instrumental effects that can produce false positives. Thus, we employ a search for auto-correlations in the residual time series, which overcomes most instrumental effects, while providing a reliable indicator for many types of pseudo-periodic fluctuations.

The remaining systems had LC distortions that appear to be synchronized with the orbital period. The source of these fluctuations is likely due to long-lasting surface inhomogeneities on one or both of the rotationally synchronized components. When the LC has brief periodic episodes of darkening (T-And0-11476, T-Cas0-13944, T-Cyg1-07584, T-Dra0-04520), they can usually be explained as stable star spots, but brief periodic episodes of brightening (T-And0-04594, T-Her0-08091), which may indicate the presence of stable hot-spots, are more difficult to interpret. This phenomenon is especially puzzling in the aforementioned two cases, in which the brightening episodes are briefer than one would expect from a persistent surface feature and repeat at the middle of both plateaux.

When the two plateaux of an LC are not flat, they are usually symmetric about the center of the eclipses. This is due to the physical mirror symmetry about the line intersecting the binary components' centers. When the axis of symmetry does not coincide with the center of eclipse (T-And0-00920, T-Cyg1-08866, T-Dra0-03105, T-Lyr1-07584, T-Lyr1-15595), a phenomenon we term "eclipse offset," we conclude that this symmetry must somehow be broken. This may occur if the EB components are not rotationally synchronized, or have a substantial tidal lag. Another form of

this asymmetry can appear as an amplitude difference between the two LC plateaux (T-Her0-03497, T-Lyr1-13166, T-Per1-08789, T-UMa0-03090). This phenomenon, which was originally called the “periastron effect” and has since been renamed the “O’Connell effect,” has been known for over a century, and has been extensively studied [e.g., O’Connell (1951); Milone (1986)]. Classical hypotheses suggest an uneven distribution of circumstellar material orbiting with the binary (Struve 1948) or surrounding the stars (Mergenthaler 1950), either of which could induce a preferential H^- absorption on one side. Binnendijk (1960) was the first of many to suggest that this asymmetry is due to subluminous regions of the stellar surface (i.e. star spots). However, this explanation also requires the stars to be rotationally synchronized, and for the spots to be stable over the duration of the observations. Alternative models abound, including a hot spot on one side of a component brought about through mass transfer from the other component, persistent star spots created by an off-axis magnetic field, and circumstellar material being captured by the components and heating one side of both stars (Liu & Yang 2003). As with many phenomena that have multiple possible models, the true answer may involve a combination of a number of these mechanisms, and will likely vary from system to system (Davidge & Milone 1984).

Finally, a few particularly unusual LCs (T-Dra0-03105, T-Lyr1-05984) display a very large difference between their eclipse durations. Although a moderate difference could be explained by an eccentric orbit, such extreme eccentricities in systems with such short orbital periods (0.5 and 1.5 days) are highly unlikely.

5.4 Conclusions

We presented a catalog of 773 eclipsing binaries found in ten fields of the TrES survey, identified and analyzed using an automated pipeline. We described the pipeline we used to identify and model them. The pipeline was designed to be mostly automated, with manual inspections taking place only once the vast majority of non-EB LCs had been automatically filtered out. At the final stage of the pipeline, we classified the EBs into seven groups: eccentric, circular, ambiguous-equal, ambiguous-unequal, inverted, Roche-lobe-filling, and abnormal. The former four groups were all successfully modeled with our model fitting program. However, the latter three groups possessed significant additional physical phenomena (tidal distortions, mass-transfer, and surface activity), which did not conform to the simple detached-EB model we employed.

We highlighted three groups of binaries, which may be of particular interest and warrant follow-up observations. These groups are: low-mass EBs, EBs with eccentric orbits, and abnormal EBs. The low-mass EBs (both components $< 0.75 M_{\odot}$) allow one to probe the mass-radius relation at the bottom of the main-sequence. Only seven such EBs have previously been confirmed, and the physical properties of many of them are inconsistent with current theoretical models. Our group of ten new candidates will likely provide considerable additional constraints to the models, and the discovery of two long-period systems could help confirm a recent hypothesis that this inconsistency is due to stellar magnetic activity. The eccentric-orbit EBs may help confirm and constrain tidal circularization theory, as many of them have comparably short circularization timescales. We demonstrated that, as one would

predict from the theory, the shortest-period systems fall within a narrow range of masses, in which their stellar envelopes cease to be convective yet their envelopes are not extended enough to produce significant tidal drag. The abnormal EBs seem to show a plethora of effects that are indicative of asymmetries, stellar activity, persistent hot and cold spots, and a host of other physical phenomena. Some of these systems may require dedicated study to be properly understood.

In the future, as LC datasets continue to grow, it will become increasingly necessary to use such automated pipelines to identify rare and interesting targets. Such systematic searches promise a wealth of data that can be used to test and constrain theories in regions of their parameter space that were previously inaccessible. Furthermore, even once the physics of “vanilla” systems has been solved, more complex cases will emerge to challenge us to achieve a better understanding of how stars form, evolve, and interact.

Acknowledgments

We would like to thank Tsevi Mazeh for many useful discussions, as well as Søren Meibom for his repeated help. We would also like to thank Sarah Dykstra for her continuous support throughout the preparation of this paper. We are grateful to the staff of the Palomar Observatory for their assistance in operating the Sleuth instrument, and we acknowledge support from NASA through grant NNG05GJ29G issued through the Origins of Solar Systems Program. This research has made use of NASA’s Astrophysics Data System Bibliographic Services, the SIMBAD database, operated at CDS, Strasbourg, and the VSX database, which was created

by Christopher Watson for the AAVSO. This publication also utilizes data products from 2MASS, which is a joint project of the University of Massachusetts and the Infrared Processing and Analysis Center/California Institute of Technology, funded by NASA and NSF. Finally, we would like to thank the anonymous referee for very insightful comments and suggestions, which significantly improved this manuscript.

5.5 Appendix - Rejecting Single-Eclipse EB Models

An EB LC comprising a deep eclipse and a very shallow eclipse, can occur in one of two ways. Either the secondary component is luminous but extremely small (e.g., a white dwarf observed in UV), thus producing a shallow primary eclipse, or the secondary component is comparably large but extremely dim, thus producing a shallow secondary eclipse. The first case, though possible [e.g., Maxted et al. (2004)], is extremely rare, and will have a signature “flat bottom” to the eclipse. We have not encountered such an LC in our dataset. The second case will have a rounded eclipse bottom, due to the primary component’s limb darkening. Assuming this latter contingency, in which the secondary component is dark in comparison to the primary component, we can place a lower bound on its radius (R_2):

$$R_2 \geq R_1 \sqrt{1 - 10^{-0.4\Delta mag_1}} , \quad (5.11)$$

where R_1 is the radius of the primary component, and Δmag_1 is the magnitude depth of the primary eclipse. Thus, if the eclipse is very deep, the size of the

secondary component must approach the size of the primary component. However, coeval short-period detached EBs with components of similar sizes yet disparate luminosities are expected to be very rare, assuming that they follow normal stellar evolution. Therefore, if only one eclipse is detected, and it is both rounded and sufficiently deep, we may conclude that this configuration entry is likely to be incorrect, and that the correct configuration has double the orbital period and produces two equal eclipses. Only when we cannot apply such a period-doubling solution (i.e. when the secondary eclipse is detectable), do we resort to questioning our assumption of normal stellar evolution (see classification group V, described in §5.2).

5.6 Appendix - Description of the Catalog Fields

Due to the large size of the catalog, we were only able to list small excerpts of it in the body of this paper. Readers interested in viewing the catalog in its entirety can download it electronically. Note that although the catalog lists 773 unique systems, each of the 103 ambiguous EBs appears in both possible configurations (see §5.2), raising the total number of catalog entries to 876. Below, we briefly describe the catalog's 38 columns. The column units, if any, are listed in square brackets.

1. *Category*— the EB's classification (see §5.2).
2. *Binary name*— the EB's designation, which is composed of its TrES field (see Table 5.1) and index.
3. α — the EB's right ascension (J2000).

4. δ – the EB’s declination (J2000).
5. *Period* [days]– the EB’s orbital period.
6. *Period uncertainty* [days] – the uncertainty in the EB’s orbital period.
7. $Mass_1 [M_\odot]$ – the mass of the EB’s primary (more massive) component.
8. $Mass_1 \text{ uncertainty } [M_\odot]$ – the uncertainty in the primary component’s mass.
9. $Mass_2 [M_\odot]$ – the mass of the EB’s secondary (less massive) component.
10. $Mass_2 \text{ uncertainty } [M_\odot]$ – the uncertainty in the secondary component’s mass.
11. *Age* [Gyr] – the age of the EB (assumed to be coeval).
12. *Age uncertainty* [Gyr] – the uncertainty in the EB’s age.
13. *Score*– a weighted reduced χ^2 of the MECI model fit [see Devor & Charbonneau (2006b) for further details].
14. *Isochrone source*– isochrone tables used [Y2: Kim et al. (2002), or Baraffe: Baraffe et al. (1998)].
15. *Color weighting*– the relative weight (w) of the LC fit, compared to the color fit [see Devor & Charbonneau (2006b) for further details].
16. *PM source*– the database that provided the proper motion measurement [UCAC: Zacharias et al. (2004), USNO-B: Monet et al. (2003), or Salim03: Salim & Gould (2003)].
17. $PM_\alpha [\text{mas yr}^{-1}]$ – the right ascension component of the EB’s proper motion.

18. PM_δ [mas yr $^{-1}$] – the declination component of the EB’s proper motion.
19. *Location error* [arcsec]– the distance between our listed location (columns 3 and 4) and the location listed by the proper motion database.
20. mag_B – the USNO-B *B*-band observational magnitude of the EB (average of both magnitude measurements, if available).
21. mag_R – the USNO-B *R*-band observational magnitude of the EB (average of both magnitude measurements, if available).
22. *Third – light fraction*– the fraction of third-light flux (*R*-band) blended into the LC (i.e. the flux within 30”, excluding the target, divided by the total flux within 30”).
23. mag_J – the 2MASS observational *J*-band magnitude of the EB, converted to ESO *J*-band.
24. mag_H – the 2MASS observational *H*-band magnitude of the EB, converted to ESO *H*-band.
25. mag_K – the 2MASS observational K_s -band magnitude of the EB, converted to ESO *K*-band.
26. Mag_J – the absolute ESO *J*-band magnitude of the EB listed in the isochrone tables.
27. Mag_H – the absolute ESO *H*-band magnitude of the EB listed in the isochrone tables.

28. Mag_K — the absolute ESO K -band magnitude of the EB listed in the isochrone tables.
29. $Distance$ [pc]— the distance to the EB, as calculated from the extinction-corrected distance modulus.
30. $A(V)$ — the EB’s V-mag absorption due to Galactic interstellar extinction (assuming $R_V = 3.1$).
31. $\sin(i)$ — the sine of the EB’s orbital inclination.
32. $|e \cos(\omega)|$ — a robust lower limit for the EB’s eccentricity (see equation 5.1).
33. $Eccentricity$ — the orbital eccentricity of the EB.
34. $Eccentricity\ uncertainty$ — the uncertainty in the orbital eccentricity of the EB.
35. Δmag_1 — the r -band primary (deeper) eclipse depth in magnitudes.
36. $Epoch_1$ — the Heliocentric Julian date (HJD) at the center of a primary eclipse, minus 2,400,000.
37. Δmag_2 — the r -band secondary (shallower) eclipse depth in magnitudes.
38. $Epoch_2$ — the Heliocentric Julian date (HJD) at the center of a secondary eclipse, minus 2,400,000.

Note that the values of the uncertainties (columns 6, 8 10, 12, and 34), were calculated by measuring the curvature of the parameter space χ^2 contour, near its minimum. This method implicitly assumes a Gaussian distribution of the parameter

likelihood. If the likelihood distribution not Gaussian, but rather has a flattened (boxy) distribution, then the computed uncertainty becomes large. In extreme cases, the estimated formal uncertainty can be larger than the measurement itself.

Chapter 6

T-Lyr1-17236: A Long-Period Low-Mass Eclipsing Binary

J. Devor, D. Charbonneau, G. Torres, C. H. Blake, R. J. White, M. Rabus,
F. T. O'Donovan, G. Mandushev, G. Á. Bakos, G. Fűrész, & A. Szentgyorgyi

The Astrophysical Journal, **687**, 1253–1263

Abstract

We describe the discovery of a $0.68+0.52\,M_{\odot}$ eclipsing binary (EB) with an 8.4-day orbital period, found through a systematic search of 10 fields of the Trans-atlantic Exoplanet Survey (TrES). Such long-period low-mass EBs constitute critical test cases for resolving the long standing discrepancy between the theoretical and observational mass-radius relations at the bottom of the main-sequence. It has been suggested that this discrepancy may be related to strong stellar magnetic fields,

which are not properly accounted for in current theoretical models. All previously well-characterized low-mass main-sequence EBs have periods of a few days or less, and their components are therefore expected to be rotating rapidly as a result of tidal synchronization, thus generating strong magnetic fields. In contrast, the binary system described here has a period that is more than 3 times longer than previously characterized low-mass main-sequence EBs, and its components rotate relatively slowly. It is therefore expected to have a weaker magnetic field and to better match the assumptions of theoretical stellar models. Our follow-up observations of this EB yield preliminary stellar properties that suggest it is indeed consistent with current models. If further observations confirm a low level of activity in this system, these determinations would provide support for the hypothesis that the mass-radius discrepancy is at least partly due to magnetic activity.

6.1 Introduction

Despite a great deal of work that has been done to understand the structure of low-mass ($< 0.8 M_{\odot}$) main-sequence stars (e.g., Chabrier & Baraffe 2000), models continue to underestimate their radii by as much as 15% (Lacy 1977b; Torres & Ribas 2002; Ribas 2006). This is a significant discrepancy, considering that for solar-type stars the agreement with the observations is typically within 1%–2% (Andersen 1991, 1998). In recent years an intriguing hypothesis has been put forward, suggesting that strong magnetic fields may have bloated these stars, either through chromospheric activity (e.g., Ribas 2006; Torres et al. 2006; López-Morales 2007; Chabrier et al. 2007) or through magnetically induced convective disruption (Torres et al. 2006).

Such strong magnetic fields are expected to be formed by the dynamo mechanism of rapidly rotating stars.¹ To test this hypothesis, one needs to measure both the masses and radii of low-mass stars, which thus far can be done most accurately with eclipsing binary (EB) systems. However, all well characterized low-mass main-sequence EBs have orbital periods shorter than 3 days (see Table 6.1) and are therefore expected to have synchronization timescales shorter than ~ 100 Myr (Zahn 1977, 1994, see Figure 6.1 and further description in § 6.6). As a result of these short periods and synchronization timescales, the rotations of these binary components are expected to have accelerated to the point that they now match the rapid angular velocity of their orbits. With such rapid rotations, these binary components could have a wide range of dynamo-induced magnetic field strengths. To better constrain current stellar models, we set out to find systems with slowly rotating components. Such systems would presumably have comparably weak magnetic fields, thus being more consistent with the model assumptions. Furthermore, by comparing the mass-radius relations of binary components with well-determined levels of magnetic activity, one could test various magnetic disruption models.

We note here that in addition to EB analysis, long-baseline optical interferometry has also been used recently to measure the radii of nearby low-mass stars (Lane et al. 2001; Ségransan et al. 2003; Berger et al. 2006). While these stars are single and are therefore expected to rotate slowly, their masses can only be estimated through

¹Dynamo theory predicts that this mechanism operates only in partially convective stars. However, the strong magnetic activity observed in fully convective low-mass stars indicates that they also possess a mechanism for generating strong magnetic fields (see Browning & Basri 2007, and references therein).

empirical mass-luminosity relations or other indirect methods. Those determinations are thus less fundamental, in a sense, and arguably of lesser value for accurately constraining stellar models and testing the magnetic disruption hypothesis.

6.2 Initial Photometric Observations

T-Lyr1-17236 was first identified as a likely low-mass EB candidate in the Devor et al. (2008) catalog, following a systematic analysis of the light curves (LCs) within 10 fields of the Trans-atlantic Exoplanet Survey (TrES; Alonso et al. 2004). TrES employs a network of three automated telescopes to survey $6^\circ \times 6^\circ$ fields of view. To avoid potential systematic noise, we performed our initial search using data from only one telescope, Sleuth, located at the Palomar Observatory in Southern California (O'Donovan et al. 2004), and we combined additional data at subsequent follow-up stages. Sleuth has a 10-cm physical aperture and a photometric aperture radius of $30''$. The number of LCs in each field ranges from 10,405 to 26,495, for a total of 185,445 LCs. The LCs consist of \sim 2000 Sloan *r*-band photometric measurements binned to a 9-minute cadence. The calibration of the TrES images, the identification of stars therein, and the extraction and decorrelation of the LCs are described elsewhere (Dunham et al. 2004; Mandushev et al. 2005; O'Donovan et al. 2006, 2007).

An automated pipeline was used to identify and characterize the EBs among the TrES LCs. This pipeline has been described in detail in a previous paper (Devor et al. 2008). At the heart of this analysis lie two computational tools:

Table 6.1. Periods of Well-characterized Main-Sequence EBs with Both Component Masses below $0.8 M_{\odot}$

Name	Period (days)	Citation
OGLE BW5 V38 ^a	0.198	Maceroni & Montalbán (2004)
RR Cae ^b	0.304	Maxted et al. (2007)
NSVS01031772	0.368	López-Morales et al. (2006)
SDSS-MEB-1	0.407	Blake et al. (2007)
GU Boo	0.489	López-Morales & Ribas (2005)
2MASS J04463285+1901432	0.619	Hebb et al. (2006)
YY Gem	0.814	Kron (1952); Torres & Ribas (2002)
T-Her0-07621	1.121	Creevey et al. (2005)
CM Dra	1.268	Lacy (1977a); Metcalfe et al. (1996)
UNSW-TR-2	2.117	Young et al. (2006)
2MASS J01542930+0053266	2.639	Becker et al. (2008)
CU Cnc	2.771	Delfosse et al. (1999); Ribas (2003)

^aThis binary might not be detached, as its components seem to be undergoing significant mutual heating and tidal interactions due to their proximity ($a = 1.355 \pm 0.066 R_{\odot}$).

^bThis is an unusual case of an EB containing a white dwarf (primary) and an M dwarf (secondary). As such, the primary component is likely to have transferred mass to the secondary component, and perhaps even enveloped it during the red giant phase of its evolution.

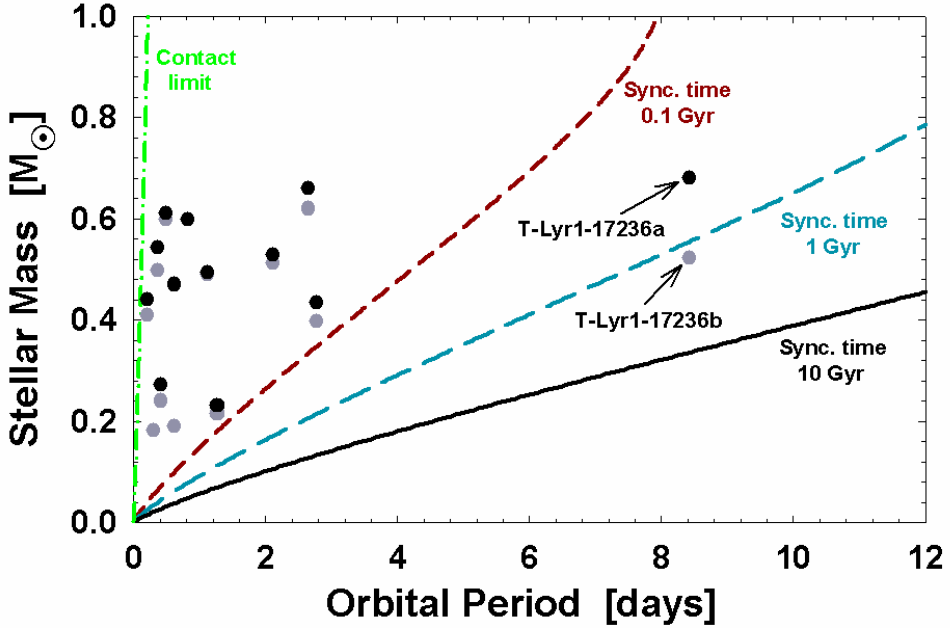


Fig. 6.1.— The predicted synchronization timescales due to turbulent dissipation (Zahn 1977, 1994) for well characterized low-mass EBs from Table 6.1. The lines trace constant synchronization timescales of binary components for which $q = 1$ (see §6.6 for further details on this calculation). The black circles indicate primary components and the gray circles indicate secondary components. Note that in some cases the primary and secondary symbols nearly overlap.

the Detached Eclipsing Binary Light curve fitter² (DEBiL; Devor 2005), and the Method for Eclipsing Component Identification³ (MECI; Devor & Charbonneau 2006a,b). DEBiL fits each LC to a *geometric* model of a detached EB that consists of two luminous, limb-darkened spheres that describe a Newtonian two-body orbit. MECI then incorporated some of the DEBiL results, and together with 2MASS color information (Skrutskie et al. 2006), refit each LC to a *physical* model that is constrained by the solar metallicity Yonsei-Yale theoretical isochrones (Yi et al. 2001; Kim et al. 2002). Thus, using only photometric data, the DEBiL/MECI pipeline provided initial estimates of the absolute physical properties of each EB. These estimates were then used to locate promising candidates for follow-up.

Using this pipeline a total of 773 EBs were identified within the TrES dataset. Of these, 427 EBs were both detached and had small out-of-eclipse distortions, thereby enabling the DEBiL/MECI pipeline to estimate their component masses. These results, together with many other properties, are listed for each EB in an online catalog⁴ (Devor et al. 2008). Of these characterized EBs, we then identified a handful of promising long-period low-mass candidates and chose one, T-Lyr1-17236 ($\alpha_{2000.0} = 19^h 07^m 16.621^s$, $\delta_{2000.0} = +46^\circ 39' 53.21''$, $P = 8.429441 \pm 0.000033$ days; see Table 6.2 for additional information), for further follow-up and analysis. As with all of our low-mass candidates, we repeated the MECI analysis using the

²The DEBiL source code, utilities, and example files are available at
<http://www.cfa.harvard.edu/~jdevor/DEBiL.html>

³The MECI source code and running examples are available at
<http://www.cfa.harvard.edu/~jdevor/MECI.html>

⁴Available at <http://www.cfa.harvard.edu/~jdevor/Catalog.html>

Baraffe et al. (1998) solar-metallicity isochrones (with a mixing-length parameter of $\alpha_{\text{ML}} = 1.0$), which are more accurate than the Yonsei-Yale isochrones in this regime. The resulting MECI mass-mass likelihood contour plot of T-Lyr1-17236 is shown in Figure 6.2. Since the MECI analysis incorporates data from theoretical stellar models, we cannot use it to constrain stellar models. Rather, once we identified the candidate, we followed it up photometrically and spectroscopically, and used only these follow-up data to derive the binary's absolute properties.

6.3 Follow-up Photometric Observations

In order to characterize T-Lyr1-17236 we combined photometric data from four telescopes: (1) Sleuth and (2) the Planet Search Survey Telescope (PSST; Dunham et al. 2004) of the TrES network, (3) the Instituto de Astrofísica de Canarias telescope (IAC80; Galan & Cobos 1987), and (4) the Hungarian Automated Telescope Network (HATNet; Bakos et al. 2004). With the exception of the IAC80, we obtained our photometric data from archived survey datasets that were intended for locating exoplanets.

As part of the TrES network (see § 6.2), Sleuth and PSST are operated similarly. However, PSST, which is located at the Lowell Observatory in Arizona, observes in the Johnson *R*-band whereas Sleuth observes in the Sloan *r*-band (see Figures 6.3 and 6.4). Furthermore, PSST has a $20''$ photometric aperture radius compared to Sleuth's $30''$ radius, which provides PSST with a higher resolving power than Sleuth. However, the smaller aperture of PSST also causes it to have noisier photometry, with an RMS of 0.031 mag for T-Lyr1-17236, compared to the Sleuth photometry,

Table 6.2. Catalog Information for T-Lyr1-17236

Source Catalog	Parameter	Value
2MASS ^a	α (J2000.0)	19 ^h 07 ^m 16.621 ^s
2MASS	δ (J2000.0)	+46°39'53.21''
USNO-B ^b	B mag	16.11 ± 0.2
GSC2.3 ^c	V mag	14.37 ± 0.28
USNO-B	R mag	14.41 ± 0.2
CMC14 ^d	r' mag	14.073 ± 0.029
2MASS	J mag	12.019 ± 0.015
2MASS	H mag	11.399 ± 0.015
2MASS	K_s mag	11.235 ± 0.015
USNO-B	μ_α (mas yr ⁻¹)	-2 ± 3
USNO-B	μ_δ (mas yr ⁻¹)	-28 ± 2
2MASS	Identification	19071662+4639532
CMC14	Identification	190716.6+463953
GSC2.3	Identification	N2EH033540
USNO-B	Identification	1366-0314305

^aTwo Micron All Sky Survey (Skrutskie et al. 2006).

^bU.S. Naval Observatory photographic sky survey (Monet et al. 2003).

^cGuide Star Catalog ver. 2.3.2 (Morrison et al. 2001).

^dCarlsberg Meridian Catalog 14 (Evans et al. 2002).

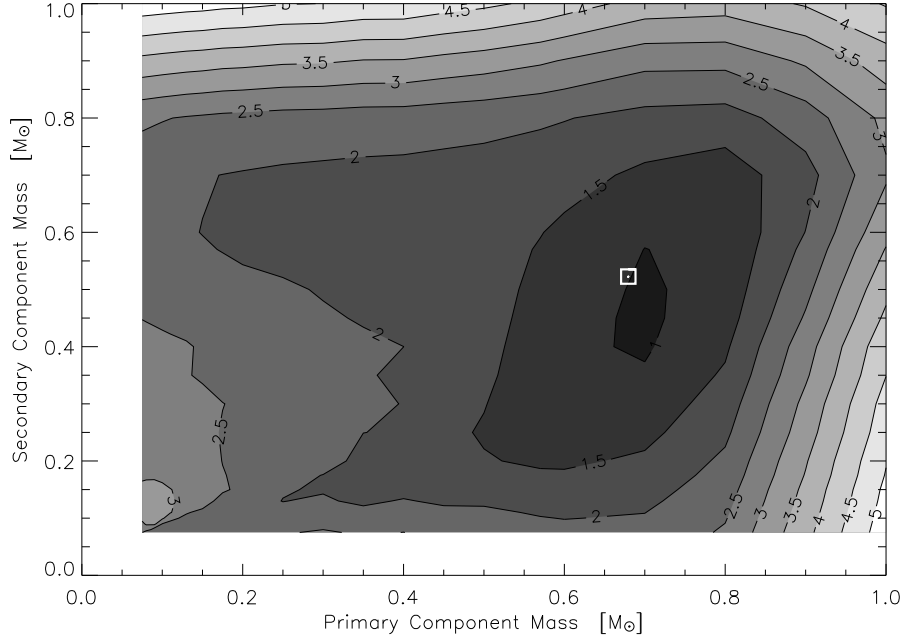


Fig. 6.2.— Mass-mass likelihood plot for T-Lyr1-17236 created with MECI, using the Baraffe et al. (1998) isochrones for an age of 2.5 Gyr. This analysis incorporated the *r*-band LC and the 2MASS colors of the target. The contour lines indicate the weighted reduced χ^2 values of each component mass pairing, using $w = 10$ (Devor & Charbonneau 2006b). The white point indicates our final mass estimate from this paper, and the white square approximates our current mass uncertainties.

which has an RMS of 0.028 mag. Though these differences are small, they would have affected our analysis. We therefore chose not to use the PSST data for fitting the photometric model, although we did use them to improve the determination of the orbital period and the epoch of eclipse (see § 6.5).

In an effort to better constrain the eclipses of T-Lyr1-17236, we obtained data from the IAC80, an 82-cm aperture telescope with a $14' \times 14'$ field of view, located at the Observatorio del Teide in the Canary Islands. We produced an *I*-band LC at a 1.3-minute cadence using the 1024×1024 -pixel Tromso CCD Photometer (TCP), resulting in 0.008 mag RMS photometry for T-Lyr1-17236. Unfortunately, we were only able to observe a primary eclipse with the IAC80. We therefore incorporated archival HATNet observations so as to provide coverage of the secondary eclipse in a similar bandpass (see Figures 6.3 and 6.5).

HATNet is a network of six 11-cm aperture, fully-automated telescopes (HATs) located at the F. L. Whipple Observatory in Arizona and the Submillimeter Array site atop Mauna Kea, Hawaii. The HATs have an $8^\circ \times 8^\circ$ field of view, a response that peaks in the *I*-band, and they operate at a 5.5-minute cadence. To reduce the photometric noise, the HAT point spread function (PSF) is broadened to an $\sim 15''$ aperture radius through microstepping (Bakos et al. 2002). Even so, the HATNet photometric RMS for T-Lyr1-17236 was comparably large, at 0.084 mag. Nevertheless, to provide more complete coverage of the primary and secondary eclipses in the *I*-band, we combined the IAC80 observations with data from HAT-7 (Whipple Observatory) and HAT-8 (Mauna Kea). Due to the very different characteristics of these two systems, however, we chose not to adopt any of the model parameters derived from these data, and we only used these results as an

independent confirmation of the Sleuth *r*-band LC analysis.

6.4 Spectroscopic Observations

T-Lyr1-17236 was observed spectroscopically with two instruments: the Near-Infrared Spectrometer (NIRSPEC; McLean et al. 1998, 2000) at the W. M. Keck Observatory in Hawaii, and the Tillinghast Reflector Echelle Spectrograph (TRES; Szentgyorgyi & Fűrész 2007), installed on the 1.5 m Tillinghast telescope at the F. L. Whipple Observatory in Arizona.

NIRSPEC was operated using a 3-pixel slit ($0.432''$) and an N7 blocking filter, thus producing a spectral resolving power of $R = \lambda/\Delta\lambda \simeq 25,000$. The duration of the exposures, which ranged from 420 to 900 seconds, was adjusted according to observing conditions. The spectra were gathered in two consecutive nods, producing a total of five NIRSPEC nod pairs. The nods of each pair were then subtracted one from the other, removing much of the sky emission. We extracted the spectra of both nods using the optimal extraction procedure outlined in Horne (1986), and then co-added the two resulting one-dimensional spectra. We calibrated the wavelengths of the resulting spectrum using its atmospheric telluric features, and then corrected for both the telluric absorption and the blaze of the spectrograph by dividing this spectrum by the spectrum of an A0V-type star (HR 5511). Finally, we cross-correlated each spectrum with the spectrum of an M0.5V template star (GJ 182). To this end, we used a single NIRSPEC order (2290–2320 nm), which is within the *K*-band, and has a scale of $0.0336 \text{ nm pixel}^{-1}$ at its center. This order covers the CO(2-0) band head, which includes a rich forest of R-branch transition

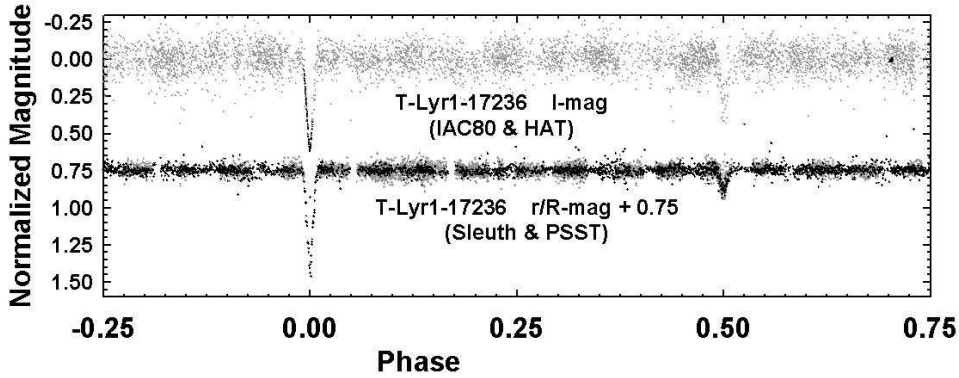


Fig. 6.3.— Phased LCs of T-Lyr1-17236. The top curve is from the IAC80 (black symbols) and HATNet (gray symbols) telescopes, both of which observed in the I -band. Note the tight cluster of IAC80 observations near phase 0.7; these points determine the IAC80 LC zero point. The bottom curve is from the Sleuth (black symbols) and PSST (gray symbols) telescopes, which observe, respectively, in the r -band and R -band. The secondary eclipse is about twice as deep in the I -band as it is in the r - or R -bands, indicating that the secondary component is significantly redder and therefore cooler than the primary.

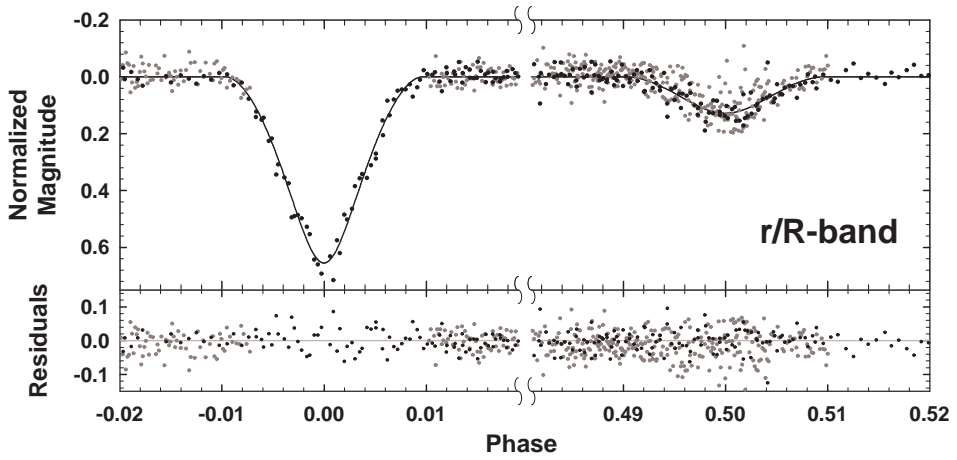


Fig. 6.4.— Enlargement of the eclipse phases in the LC of T-Lyr1-17236, as recorded by the Sleuth (black symbols) and PSST (gray symbols) telescopes (r -band and R -band, respectively). The solid line shows the best-fit JKTEBOP model, for which the residuals are displayed at the bottom.

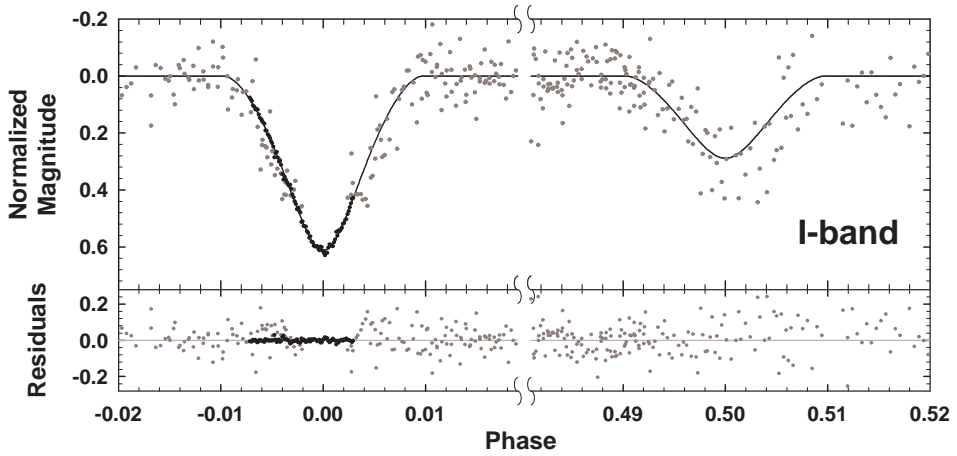


Fig. 6.5.— Enlargement of the eclipse phases in the LC of T-Lyr1-17236, as recorded by the IAC80 (black symbols) and the HATNet (gray symbols) telescopes (I -band). The solid line shows the best-fit JKTEBOP model, for which the residuals are displayed at the bottom.

lines, as well as many telluric absorption features due to methane in the Earth’s atmosphere. The advantages offered by this spectral region and the details of the instrument setup are described in Blake et al. (2008).

TRES is a high-resolution fiber-fed optical echelle spectrograph designed to cover a large range of wavelengths (390–934 nm) in 51 orders. We employed the medium-size fiber (2.3'') so as to cover the full stellar PSF, while providing a spectral resolving power of $R \simeq 47,000$. Following each of our three 900–1000 second exposures, the TRES data were read from a 4638×1090 -pixel CCD, which we set to a 2×2 binning mode for a more rapid read-out. We then used a dedicated IRAF toolset to process and extract 51 spectral orders simultaneously, ultimately producing 2319 data points along each order. The IRAF processing of the TRES data involved merging the mosaic FITS files, removing cosmic ray hits, flattening fringing effects, and then extracting the orders. We wavelength-calibrated the TRES spectra using Thorium-Argon (ThAr) exposures, and then corrected the telluric absorption and spectroscopic blazing by dividing each spectrum by a TRES spectrum of a rapidly-rotating B0IV-type star (HR 264). Though TRES produces 51 spectral orders, we used only 4 of them, covering wavelengths of 665–720 nm (similar to the *R*-band), and with a post-binning scale of ~ 0.0065 nm pixel $^{-1}$. These orders contain a diverse array of absorption features, including those of TiO, Fe I, Ca I, Ni I, and Cr I. We limited ourselves to these orders because at shorter wavelengths there was insufficient flux from our red target, while at longer wavelengths the spectra were dominated by telluric absorption features, produced largely by terrestrial O₂ and H₂O. We cross-correlated these four orders with the corresponding orders of an M1.5V template star (GJ 15A, also known as GX And A) and averaged their

cross-correlation functions. We repeated this final calculation using the Zucker (2003) maximum-likelihood method, which reproduced our results to within a fraction of their uncertainties, although with slightly larger errors.⁵

In total, we produced five radial velocity (RV) measurements of each component with NIRSPEC and three with TRES. In all cases we were able to measure the RVs of both binary components by employing a cross-correlation method that transforms the spectra to Fourier-space using the Lomb-Scargle algorithm (Press et al. 1992). This method allowed us to cross-correlate spectra with arbitrary sampling, without having to interpolate or resample them onto an equidistant grid. We then multiplied the Fourier-transformed target and template spectra, inverse-Fourier-transformed the product, and normalized it. Since the resulting two peaks in the cross-correlation functions were always well separated, we were able to fit each with a parabola, and thus measure their offsets and widths. The uncertainties of these RVs are somewhat difficult to determine with our procedures, but tests indicate that they are approximately 1.0 and 1.4 km s⁻¹ for the primary and secondary in our NIRSPEC spectra, and about 0.5 and 1.2 km s⁻¹ in our TRES spectra. These internal errors are adopted below in the spectroscopic analysis, but they have relatively little effect on the results. Finally, the RVs were transformed to the barycentric frame, and the TRES RV measurements were further offset by -2.82 km s^{-1} in order to place them on the same reference frame as the NIRSPEC measurements, which were obtained

⁵The Zucker (2003) method is more accurate than simple cross-correlation averaging for large N . However, because it takes the absolute value of the correlation, it loses some information and effectively increases the noise baseline. This increased noise will negate its advantage when combining a small number of correlations, as is the case in our TRES analysis ($N = 4$).

with a different template (GJ 182). This offset was determined by including it as an additional free parameter in the Keplerian RV model (see § 6.5). Once the offset was determined, we held its value fixed in all subsequent analyses. The final velocities are listed in Table 6.3 and include this offset. Note that these listed RVs are all relative to GJ 182, for which Montes et al. (2001) have measured the value $+32.4 \pm 1.0 \text{ km s}^{-1}$.

6.5 Orbital Analysis

We began our analysis by determining the orbital period (P) and the epoch of primary eclipse (t_0) and constraining the eccentricity (e) of T-Lyr1-17236 through eclipse timing. The times of eclipse determined from our photometric observations are listed in Table 6.4. Since our data span 3.5 years, we were able to determine the period to an accuracy of 3 seconds (see Table 6.5). To estimate the binary's eccentricity, we first measured the observed minus calculated ($O-C$) timing difference between the primary and secondary eclipses in all available LCs, which provided an upper bound of $|e \cos \omega| \lesssim 0.0008$, where ω is the argument of periastron (see Figure 6.6). Though ω and e cannot be determined separately in this way, this result indicates that the orbit of T-Lyr1-17236 is likely to be circular or very nearly so. This conclusion is further supported by a weaker upper limit of $|e \sin \omega| \lesssim 0.06$, obtained through preliminary LC model fitting (see below). Theoretical estimates (Zahn 1977, 1978, 1994) of this binary suggest a circularization timescale of $t_{\text{circ}} \simeq 390 \text{ Gyr}$ (see also Devor et al. 2008). Being many times the age of the binary, this long timescale suggests that T-Lyr1-17236 formed in a circular orbit. However, this

timescale value is an instantaneous estimate for the current epoch, and is likely to have been significantly different in the past (see Zahn & Bouchet 1989; Mazeh 2008, and references therein). Therefore, it is quite possible that the binary circularized while it was in the pre-main-sequence; however, to the extent that this theory is correct, it is unlikely to have circularized once it settled on the main-sequence.

A Keplerian model was fit to the RVs to determine the elements of the spectroscopic orbit of T-Lyr1-17236. We assumed the eccentricity to be zero based on the evidence above and the lack of any indications to the contrary from preliminary spectroscopic solutions. The period and t_0 were held fixed at the values determined above. We solved simultaneously for the velocity semi-amplitudes of the components ($K_{A,B}$) and the RV of their center of mass (V_γ). The results are shown graphically in Figure 6.7, and the elements are listed in Table 6.6. The minimum masses $M_{A,B} \sin^3 i$ are formally determined to better than 2%. However, because of the small number of observations ($N = 8$), the possibility of systematic errors cannot be ruled out and further observations are encouraged to confirm the accuracy of these results.

We then proceeded to find the remaining photometric parameters of T-Lyr1-17236. To this end, we analyzed the Sleuth r -band LC using JKTEBOP (Southworth et al. 2004a,b), a LC modeling program based on the EBOP light curve generator (Nelson & Davis 1972; Etzel 1981; Popper & Etzel 1981). We assumed a circular orbit, as before, a mass ratio of $q = 0.7692$ from the spectroscopic model, and the period determined above. We solved simultaneously for the orbital inclination (i), the fractional radii ($r_{A,B}$), the central surface brightness ratio of the secondary in units of the primary (J), the time of primary eclipse (t_0), and

Table 6.3. Radial Velocity Measurements for T-Lyr1-17236 in the Barycentric Frame Relative to GJ 182

Epoch (BJD)	Primary RV (km s ⁻¹)	Secondary RV (km s ⁻¹)	Exposure Time (sec)	Template	Instrument
2,453,927.9400	-2.87	-45.24	480	GJ 182	NIRSPEC
2,453,930.9258	-68.09	38.85	900	GJ 182	NIRSPEC
2,453,946.8846	-64.26	36.53	600	GJ 182	NIRSPEC
2,453,948.9100	-43.45	7.03	420	GJ 182	NIRSPEC
2,454,312.7985	7.66	-57.68	480	GJ 182	NIRSPEC
2,454,372.6179	23.99	-80.14	900	GJ 15A	TRES
2,454,377.6382	-68.03	40.10	1000	GJ 15A	TRES
2,454,377.6624	-67.97	39.73	1000	GJ 15A	TRES

Table 6.4. Eclipse Timings Measured for T-Lyr1-17236

Eclipse Type	Epoch (HJD)	O-C (sec)	Data Source
Primary	2,453,152.96121	-299 ⁺²³² ₋₂₃₆	HATNet
Secondary	2,453,157.17593	-546 ⁺⁶⁸⁶⁸ ₋₈₄₉	HATNet
Primary	2,453,169.82009	48 ⁺¹²⁶ ₋₁₃₁	HATNet
Primary	2,453,186.67897	237 ⁺²¹⁴ ₋₂₂₁	HATNet
Secondary	2,453,190.89369	-231 ⁺⁴³¹ ₋₄₂₃	HATNet
Primary	2,453,195.10841	-333 ⁺²⁶³ ₋₂₃₈	HATNet
Secondary	2,453,207.75258	225 ⁺⁶⁴² ₋₆₄₈	HATNet
Secondary	2,453,544.93022	-452 ⁺³⁴⁶ ₋₃₃₂	Sleuth
Secondary	2,453,561.78910	312 ⁺⁹⁷ ₋₉₈	Sleuth + PSST
Secondary	2,453,578.64798	515 ⁺²⁰⁶ ₋₂₀₈	Sleuth
Primary	2,453,582.86270	159 ⁺⁹⁹ ₋₉₈	Sleuth
Primary	2,453,599.72158	94 ⁺⁶⁴ ₋₆₄	Sleuth
Secondary	2,453,603.93630	1047 ⁺⁴²⁴ ₋₃₇₁	Sleuth + PSST
Primary	2,453,616.58046	-57 ⁺¹⁷⁵ ₋₁₇₅	Sleuth
Primary	2,453,861.03425	238 ⁺²⁸⁰ ₋₂₃₃	PSST
Primary	2,454,417.37736	-1 ⁺¹⁰ ₋₁₀	IAC80

Table 6.5. Photometric Parameters of T-Lyr1-17236

Parameter	Symbol	Value
Period (days)	P	8.429441 ± 0.000033
Epoch of eclipse (HJD)	t_0	$2453700.87725 \pm 0.00041$
Primary fractional radius	r_A	0.0342 ± 0.0023
Secondary fractional radius	r_B	0.0283 ± 0.0028
Orbital inclination [deg]	i	89.02 ± 0.26
Eccentricity	e	0.0 (fixed)
Sum of fractional radii	$r_A + r_B$	0.06256 ± 0.00095
Ratio of radii (R_B/R_A)	k	0.83 ± 0.15
Light ratio (r -band)	L_B/L_A	0.173 ± 0.073
Surface brightness ratio (r -band)	J_B/J_A	0.2525 ± 0.0099

Table 6.6. Spectroscopic Parameters of T-Lyr1-17236

Parameter	Symbol	Value
Primary RV semi-amplitude (km s^{-1})	K_A	48.36 ± 0.23
Secondary RV semi-amplitude (km s^{-1})	K_B	62.86 ± 0.46
Barycentric RV, relative to GJ 182 ^a (km s^{-1})	V_γ	-21.01 ± 0.18
Binary separation with projection factor (R_\odot)	$a \sin i$	18.526 ± 0.083
Primary mass with projection factor (M_\odot)	$M_A \sin^3 i$	0.6792 ± 0.0107
Secondary mass with projection factor (M_\odot)	$M_B \sin^3 i$	0.5224 ± 0.0061
Mass ratio (M_B/M_A)	q	0.7692 ± 0.0069

^aMontes et al. (2001) list the RV of GJ 182 as $+32.4 \pm 1.0 \text{ km s}^{-1}$.

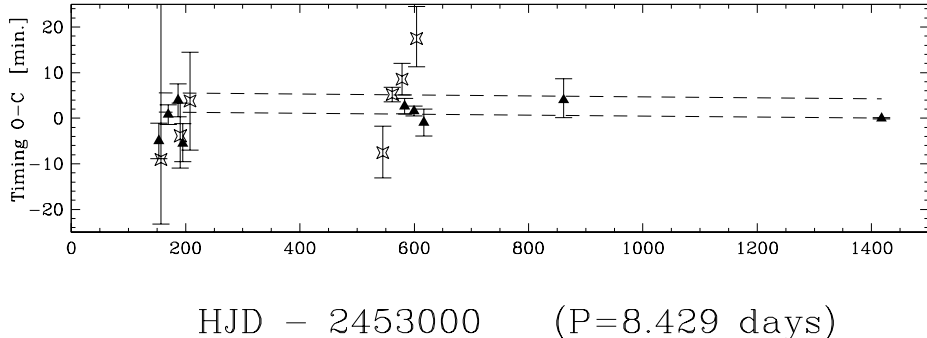


Fig. 6.6.— Eclipse timing ($O-C$) measurements of T-Lyr1-17236. The triangles indicate primary eclipses, and the four-pointed stars indicate secondary eclipses. The large error bars are generally due to eclipses that are constrained by only a few observations, or for which only the ingress or egress was observed. The cluster of points at the very left ($HJD < 2,453,300$) are measurements from HATNet, the single data point at $HJD\ 2,454,417$ is from the IAC80, and the remaining data are from Sleuth and PSST. The two parallel dashed lines indicate the expected $O-C$ location of the primary (bottom) and secondary (top) eclipses, in the best-fit eccentric model ($|e \cos \omega| \simeq 0.0005$). This eccentric model provides only a very small improvement in the fit compared to the circular model (F-test: $\chi^2_{\nu, circ}/\chi^2_{\nu, ecc} \simeq 1.29$, indicating a $p \simeq 0.33$ significance).

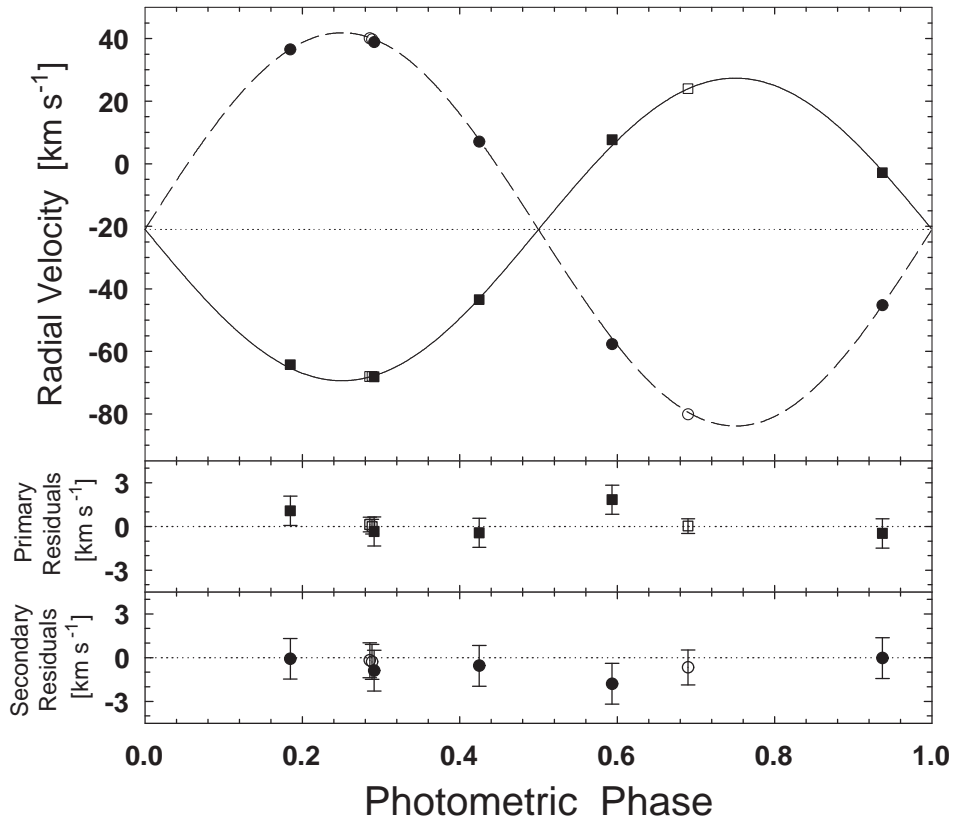


Fig. 6.7.— RV measurements of T-Lyr1-17236, relative to GJ 182, shown as a function of orbital phase. The velocities of the primary component are represented with squares, and those of the secondary with circles. The filled symbols correspond to data taken with NIRSPEC, and the open symbols represent TRES measurements. Residuals from the model fit are shown in the bottom panels for the primary and secondary components.

the out-of-eclipse magnitude (zero point). We estimated the uncertainties of the fitted parameters by evaluating the distribution generated by 1000 Monte Carlo simulations (Southworth et al. 2005).

Because of the large photometric aperture of Sleuth, the presence of significant contamination from the light of additional stars is a distinct possibility. Unfortunately, due to its degeneracy with the orbital inclination and the fractional radii, we were not able to simultaneously determine the fractional third light of the system (l_3). We therefore sequentially refit the LC model parameters with fixed fractional third-light values ranging from 0 to 0.2 (see Figure 6.8). We repeated this routine with the *I*-band IAC80/HATNet LC as well, although these results were not used because of their larger uncertainties. We obtained an external estimate of the third-light fraction affecting the Sleuth observations using the USNO-B catalog (Monet et al. 2003), which lists two dim objects within 30'' of T-Lyr1-17236 (USNO-B1.0 1366-0314297 and 1366-0314302). Assuming that these objects are completely blended into T-Lyr1-17236, we expect an *R*-band third-light fraction of $l_3 = 0.085 \pm 0.018$, and we adopted this value for the *r*-band LC. Fortunately, the fitted parameters are quite insensitive to third light, so that the uncertainty in l_3 only moderately increases their uncertainties. No objects were listed within the smaller photometric apertures of either IAC80 or HATNet, so we conclude that the *I*-band LC should have little or no third-light contamination. It is important to note that these third-light estimates assume that there are no further unresolved luminous objects that are blended with T-Lyr1-17236 (e.g., a hierarchical tertiary component). However, the divergence of the *r*-band and *I*-band solutions at higher third-light fractions (see Figure 6.8), and the deep primary eclipse in both the *r*- and

I-bands (0.649 and 0.604 mag, respectively), suggest that if such unresolved objects exist, they are unlikely to account for more than ~ 0.1 of the total flux, and therefore would not bias the fitted results beyond the current estimated uncertainties. The final results of our LC fits are given in Table 6.5.

6.6 Physical Parameters

The fundamental parameters of T-Lyr1-17236, such as their absolute masses and radii, were derived by combining the results of the spectroscopic analysis (Table 6.6) with those from the photometric analysis (Table 6.5). These and other physical properties are listed in Table 6.7. Our estimates of the primary and secondary component masses, $M_A = 0.6795 \pm 0.0107$ and $M_B = 0.5226 \pm 0.0061 M_\odot$, lead us to infer spectral types of K5V and M0V, respectively, according to empirical tables (Cox 2000). We are not able to make independent estimates of the effective temperatures of the stars from the data in hand. This could be done if, for example, we had individual color indices based on combined light values and light ratios in two different bands, but we can only derive a reliable estimate of the light ratio in the *r*-band. The comparison with stellar evolution models by Baraffe et al. (1998) in § 6.8 suggests primary and secondary component temperatures of approximately 4150 and 3700 K, respectively, although the accuracy of these values is difficult to assess.

No trigonometric parallax is available for T-Lyr1-17236. A rough distance estimate to the system may be made using the JHK_s brightness measurements in the 2MASS Catalog, collected in Table 6.2, along with estimates of the absolute

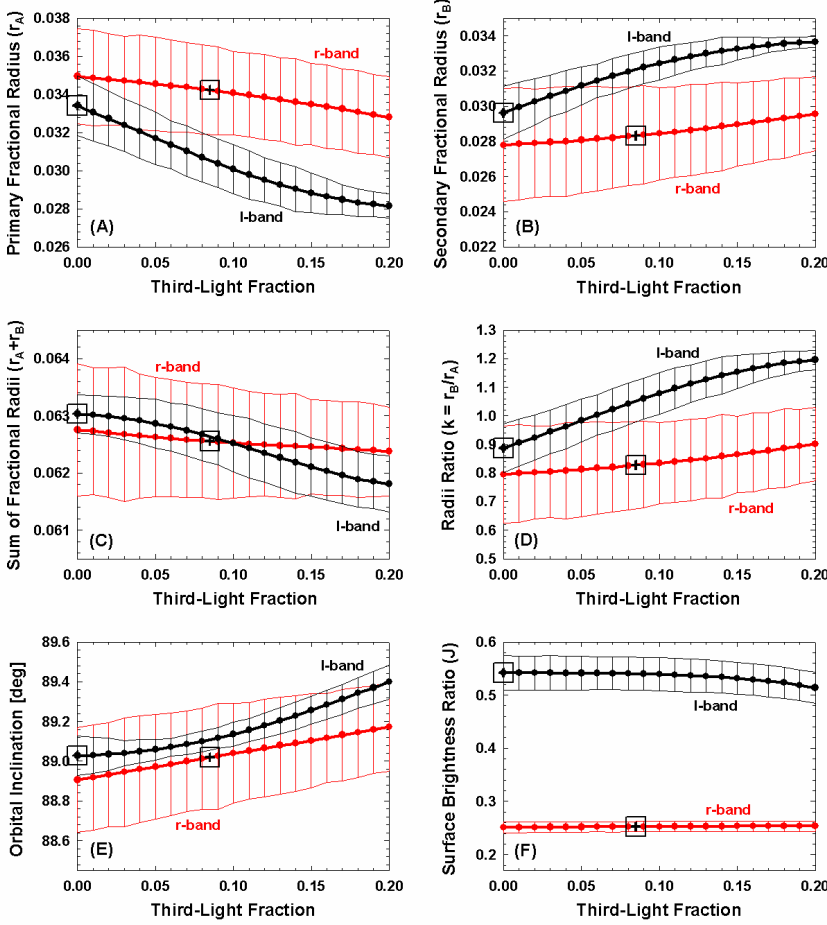


Fig. 6.8.— JKTEBOP parameter fits over a range of values for the third light fraction.

The panels show the best-fit values and uncertainties for (A) the fractional radii of the primary (r_A) and (B) secondary (r_B) components; (C) the sum of the fractional radii (r_A+r_B) and (D) the radius ratio ($k = r_B/r_A$); (E) the binary orbital inclination (i); and (F) the central surface brightness ratio (J , secondary over primary). Note that in contrast to the other panels, (F) shows distinct values for the I - and r -band LCs. This is expected, since the two components have different colors, and therefore different relative fluxes through different filters. In all cases the estimated third light fractions for the r -band and the I -band LCs are indicated by squares.

magnitudes. For these we must rely once again on models. The Galactic latitude of $+16.8^\circ$ suggests the possibility of some interstellar extinction. From the reddening maps of Schlegel et al. (1998) we infer $E(B - V) \simeq 0.07$ in the direction of the object (total reddening), which corresponds to extinctions of $A(J) \simeq 0.061$, $A(H) \simeq 0.038$, and $A(K) \simeq 0.011$, assuming $R_V = 3.1$ (Cox 2000). Under the further assumption that this extinction applies to T-Lyr1-17236, we derive a mean distance of 230 ± 20 pc, after conversion of the near-infrared magnitudes in the CIT system from the Baraffe et al. (1998) models to the 2MASS system, following Carpenter (2001). With the proper motion components from the USNO-B catalog listed in Table 6.2, the center-of-mass velocity V_γ from the spectroscopic solution corrected for the velocity of GJ 182 (Montes et al. 2001), and the distance above, we infer space velocity components in the Galactic frame of $(U,V,W) \simeq (+41,+21,+2)$ km s^{-1} , where U points in the direction of the Galactic center.

Because of the relevance of the rotational velocities of the stars for the interpretation of the chromospheric activity results of § 6.7, we have made an effort here to measure the rotational broadening of both components from the widths of the cross-correlation functions derived from our TRES spectra. We rely on the fact that to first order, the width of a cross-correlation peak is approximately equal to the quadrature sum of the line broadening of the two spectra. We began our estimation procedure by finding the effective resolution of the instrument (σ_i) in the four TRES orders we used. This was done by auto-correlating a TRES ThAr spectrum that was taken just before the second T-Lyr1-17236 observation. We found that the four orders produced peaks with an average FWHM of 8.90 ± 0.17 km s^{-1} . Thus, assuming that the intrinsic widths of the ThAr emission lines are negligible

compared to the instrumental resolution, we found that $\sigma_i = 6.29 \pm 0.12 \text{ km s}^{-1}$. This value corresponds to a spectral resolving power of $R = 47,630 \pm 930$, which is consistent with the TRES specifications. Next, we determined the intrinsic spectral line broadening of the template star, GJ 15A (σ_t). We auto-correlated the template spectrum and found that it produced peaks with an average FWHM of $9.7 \pm 1.4 \text{ km s}^{-1}$. This value should be equal to $\sqrt{2}(\sigma_i^2 + \sigma_t^2)^{1/2}$, from which we infer that $\sigma_t = 2.7 \pm 2.5 \text{ km s}^{-1}$. Note that this result is well within the upper bound provided by Delfosse et al. (1998), following their non-detection of any rotational broadening in GJ 15A. Using this information, we can now find the intrinsic spectral line broadening of the T-Lyr1-17236 components ($\sigma_{A,B}$). The average FWHM of the primary and secondary peaks, resulting from the cross-correlation of each observed spectrum of T-Lyr1-17236 against the template, were measured to be $12.6 \pm 2.0 \text{ km s}^{-1}$ and $12.0 \pm 2.4 \text{ km s}^{-1}$, respectively. These widths are expected to be equal to $[(\sigma_i^2 + \sigma_t^2) + (\sigma_i^2 + \sigma_{A,B}^2)]^{1/2}$, from which we calculate that $\sigma_A = 8.4 \pm 3.0$ and $\sigma_B = 7.6 \pm 3.8 \text{ km s}^{-1}$.

The rotational profile FWHM expected for a homogeneous stellar disk is $\sqrt{3} v \sin i_r$, where v is the star's equatorial rotational velocity, and i_r is the inclination of its rotational axis. Stellar limb darkening, however, will narrow the rotational profile, thus decreasing the observed FWHM (Gray 1992). Adopting the *R*-band PHOENIX linear limb darkening coefficients from Claret (1998), we find that the expected FWHM values for the primary and secondary components of T-Lyr1-17236 are, respectively, $1.495 v \sin i_r$ and $1.499 v \sin i_r$. Using these results we can set upper bounds to the components' $v \sin i_r$. These upper bounds represent the limiting case whereby the spectral line broadening is due entirely to stellar rotation,

and we neglect all other line broadening mechanisms, such as microturbulence and the Zeeman effect. We thus determine the maximum rotational velocities of the T-Lyr1-17236 primary and secondary components to be $v \sin i_r = 5.6 \pm 2.0$ and $5.1 \pm 2.3 \text{ km s}^{-1}$, respectively.

An estimate of the timescale for tidal synchronization of the stars' rotation with their orbital motion may be obtained from theory following Zahn (1977), and assuming simple power-law mass-radius-luminosity relations (Cox 2000). Thus, for stars less massive than $1.3 M_\odot$,

$$t_{\text{sync}} \simeq 0.00672 \text{ Myr } (k_2/0.005)^{-1} q^{-2} (1+q)^2 (P/\text{day})^4 (M/M_\odot)^{-4.82} , \quad (6.1)$$

where k_2 is determined by the structure and dynamics of the star and can be obtained by interpolating published theoretical tables (Zahn 1994). This calculation leads to timescales of $t_{\text{sync}} \simeq 0.56$ and 1.02 Gyr for the primary and secondary components of T-Lyr1-17236, respectively, which are much shorter than the circularization timescale determined in § 6.5. We note that similar to the circularization timescale, the synchronization timescales estimated above are the current instantaneous values, and are likely to have changed over time. The age of the system is undetermined (see § 6.8), but assuming its age is at least a few Gyr, as is typical for field stars, it would not be surprising if tidal forces between the components had already synchronized their rotations. This is illustrated in Figure 6.1, where T-Lyr1-17236 is shown along with the other systems in Table 6.1 and with curves representing theoretical estimates of the synchronization timescale as a function of orbital period.

If we assume that the components are indeed rotationally synchronized, we can compute their rotational velocities more accurately using $v_{A,B} = 2\pi R_{A,B}/P$. We thus

derive synchronized velocities of $(v \sin i_r)_{\text{sync}} = 3.81 \pm 0.26$ and $3.15 \pm 0.31 \text{ km s}^{-1}$ for the primary and secondary components, respectively. These values are slightly below but still consistent with the maximum rotational velocities measured above. Thus, observational evidence suggests that the stars' rotations may well be synchronized with their orbital motion, although more precise measurements would be needed to confirm this. Our conclusion from this calculation is that regardless of whether we assume that the components of T-Lyr1-17236 are synchronized, their rotational velocities do not appear to be large.

6.7 Chromospheric Activity

Our absolute mass and radius determinations for T-Lyr1-17236 offer the possibility of testing stellar evolution models in the lower main-sequence, in particular testing the idea that the discrepancies noted in § 6.1 are related to chromospheric activity and the associated magnetic fields in systems where the components are rotating relatively rapidly. Thus, establishing the level of the activity in the system presented here is of considerable importance. We have shown in § 6.6 that the relatively long period of T-Lyr1-17236 ($P \simeq 8.429441$ days) implies that even if the components are synchronized, their rotational velocities are slow, and therefore they are not expected to induce a great deal of chromospheric activity. However, demonstrating that the stars are indeed inactive requires more direct evidence, given that some stars of masses similar to these are still found to be quite active at rotation periods as long as 8 days (see, e.g., Pizzolato et al. 2003). We present here the constraints available on the surface activity of T-Lyr1-17236 from its X-ray emission, optical

variations, and spectroscopic indicators.

The present system has no entry in the *ROSAT* Faint Source Catalog (Voges et al. 1999), suggesting that the X-ray luminosity, usually associated with activity, is not strong. Examination of the original *ROSAT* archive images leads to a conservative upper limit to the X-ray flux of 6.71×10^{-14} erg cm $^{-2}$ s $^{-1}$ in the energy range 0.1–2.4 keV, and together with information from Table 6.7, we infer an upper limit for the ratio of the X-ray to bolometric luminosity of $\log L_X/L_{\text{bol}} \lesssim -3.13$. Values for the four best studied cases of CM Dra, YY Gem, CU Cnc, and GU Boo, which are all very active, are respectively -3.15 , -2.88 , -3.02 , and -2.90 (see López-Morales 2007). These are at the level of our limit or higher, although we do not consider this evidence conclusive.

There are no detectable variations in the *r*-band LC out of eclipse, within the uncertainties. Such variations would be expected from activity-related surface features showing significant contrast with the photospheres. We estimate an upper limit of ~ 0.01 mag in *r* for the night-to-night variations (see Figure 3). Because the secondary components is significantly dimmer, it has a weaker variability upper limit of ~ 0.09 mag. We note, however, that this evidence for inactivity is not conclusive either, since the observed photometric variations can depend significantly on the distribution of spots on the surface.

A number of spectroscopic activity indicators (the Ca II H and K lines, H α , etc.) should in principle allow a more direct assessment of the activity level in T-Lyr1-17236. Unfortunately, however, the quality of our spectroscopic material in the optical makes this difficult. The flux in the blue for this very red system is too

low to distinguish the Ca II H and K lines, and even at H α the noise is considerable (typical signal-to-noise ratios at this wavelength are ~ 12 pixel $^{-1}$). Two of the three TRES spectra show the H α line in absorption, and the other appears to show H α in emission. This suggests some degree of chromospheric activity, although perhaps not at such a high level as to sustain the emission at all times, as is seen in other stars. H β appears to be in absorption in all three TRES spectra.

Clearly more spectra with higher signal-to-noise ratios are needed to better characterize the level of activity, but from the sum of the evidence above it would not appear that the activity in T-Lyr1-17236 is as high as in other low-mass EBs studied previously, thus more closely aligning it with the assumptions of current standard stellar models. The system may therefore constitute a useful test case for confirming or refuting the magnetic disruption hypothesis (see § 6.1), which predicts that the absolute properties of its slowly rotating components should match the theoretical models of convective stars.

6.8 Comparison with Models and Conclusions

A comparison with solar-metallicity models by Baraffe et al. (1998) for a mixing-length parameter of $\alpha_{\text{ML}} = 1.0$ is presented in Figure 6.9. Our mass and radius determinations for T-Lyr1-17236 (see Table 6.7) are shown along with those of the low-mass systems listed in Table 6.1. The location of the models in this diagram depends only slightly on age because these stars evolve very slowly. The age of T-Lyr1-17236 is difficult to establish independently. The space motions derived in § 6.6 do not associate the system with any known moving group, and are quite typical

of the thin disk. Thus, all we can say is that it is not likely to be very old. We display in Figure 6.9 two models for ages of 1 and 10 Gyr, which likely bracket the true age of T-Lyr1-17236. Within the errors, our measurements for the two components are consistent with the models, which would in principle support the magnetic disruption hypothesis. Unfortunately, however, the uncertainties in the radius measurements ($\sim 7\%$ and $\sim 10\%$) are still large enough that our statement cannot be made more conclusive. Further follow-up observations, especially rapid-cadence and precise photometric measurements during multiple eclipses, should significantly reduce the uncertainties in the radii and thus provide far stronger constraints on the theoretical models of low-mass stars. In addition, higher quality spectroscopic observations than ours are needed to confirm that the level of chromospheric activity in the system is relatively low. If after such observations, the masses and radii of the T-Lyr1-17236 components remain consistent with the stellar models, then the magnetic disruption hypothesis will be strengthened. However, if further observations find that the components of T-Lyr1-17236 are larger than predicted by current stellar models, as is the case with most other similar systems investigated in sufficient detail, then this will provide evidence that additional mechanisms need to be included in the models of the structure of low-mass main-sequence stars (see, e.g., Chabrier et al. 2007).

It is important to note here that T-Lyr1-17236 falls within the field of view of the upcoming NASA *Kepler* mission (Borucki et al. 2003). The *Kepler* Mission will not return data for all stars within its field of view; rather, the targets will be selected by the *Kepler* team. We see at least two reasons why such monitoring of T-Lyr1-17236 would be of significant value. First, the data would greatly refine the estimates of the physical parameters of the component stars and might permit a

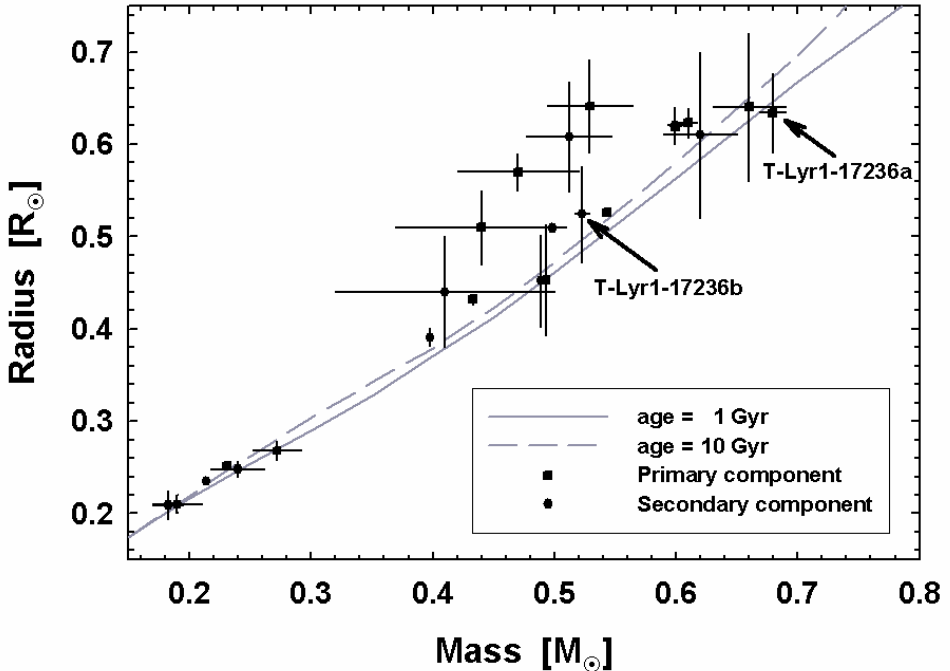


Fig. 6.9.— Mass-radius diagram for T-Lyr1-17236 and other low-mass EBs under $0.8 M_{\odot}$ from Table 6.1. Theoretical isochrones for solar metallicity from Baraffe et al. (1998) are shown for ages of 1 and 10 Gyr. The components of T-Lyr1-17236 are indicated with arrows. Most of these binary components (particularly those with smaller uncertainties) display a systematic offset in which their measured radii are larger than predicted from models.

search for their asteroseismological modes. Second, the data would enable a search for transits of exoplanets, which are expected to orbit in the same plane as that defined by the stellar orbits.

Finally, we note that our findings in this paper confirm the accuracy of the MECI algorithm (see Figure 6.2), which can be further used to find additional long-period low-mass EBs, and indeed a variety of other interesting targets. We have shown in a recent paper (Devor et al. 2008) how this can be done with comparable ease by systematically searching the ever-growing body of LC survey datasets. We hope that this new approach for locating rare EBs will motivate additional studies of these vast, largely untapped datasets, which likely harbor a wealth of information on the formation, structure, dynamics, and evolution of stars.

Acknowledgments

We would like to thank Joel Hartman and Doug Mink for their help in operating a few of the software analysis tools used for this paper, and we would like to thank Sarah Dykstra for her editorial assistance. Valeri Hambaryan provided expert assistance in examining archival *ROSAT* images of T-Lyr1-17236, for which we are grateful, and we thank the referee for a number of helpful comments that have improved the paper. G. T. acknowledges partial support from NSF grant AST-0708229 and NASA's MASSIF SIM Key Project (BLF57-04). This research has made use of NASA's Astrophysics Data System Bibliographic Services, as well as the SIMBAD database operated at CDS, Strasbourg. This publication also used data products from the Two Micron All Sky Survey, which is a joint project of the University of

Massachusetts and the Infrared Processing and Analysis Center/California Institute of Technology, and is funded by NASA and the National Science Foundation. Some of the data presented herein were obtained at the W. M. Keck Observatory, which is operated as a scientific partnership among Caltech, the University of California and NASA. The Observatory was made possible by the generous financial support of the W. M. Keck Foundation. The authors wish to recognize and acknowledge the very significant cultural role and reverence that the summit of Mauna Kea has always had within the indigenous Hawaiian community. We are most fortunate to have the opportunity to conduct observations from this mountain.

Table 6.7. System Parameters of T-Lyr1-17236

Parameter	Symbol	Component A	Component B
Mass (M_{\odot})	M	0.6795 ± 0.0107	0.5226 ± 0.0061
Radius (R_{\odot})	R	0.634 ± 0.043	0.525 ± 0.052
Log surface gravity (cgs)	$\log g$	4.666 ± 0.059	4.718 ± 0.086
Semimajor axis (10^6 km)	a	5.606 ± 0.027	7.288 ± 0.053
Maximum rotational velocity ^a (km s^{-1})	$v \sin i_r$	5.6 ± 2.0	5.1 ± 2.3
Synchronized rotational velocity ^a (km s^{-1})	$(v \sin i_r)_{\text{sync}}$	3.81 ± 0.26	3.15 ± 0.31
Absolute visual magnitude ^b (mag)	M_V	8.03	9.67
Bolometric luminosity ^b (L_{\odot})	L	0.110	0.039
Effective temperature ^b (K)	T_{eff}	4150	3700
Distance ^b (pc)	D	230 ± 20	

^aSee description in §6.6.

^bInferred using stellar evolution models by Baraffe et al. (1998) assuming solar metallicity and an age of 2.5 Gyr.

Chapter 7

Conclusions and Future Work

In this thesis, we showed how assembly line astronomical analysis can be constructed and used. This approach enabled us to produce orders of magnitude more data than traditional approaches would have, and with this dramatic increase, we entered a new regime, where problems once considered difficult become readily accessible. Such problems include constraining the orbital period distribution of various binary populations (see Figures 2.11 and 5.8), correlating the masses of the binary components (see Figure 5.19), and testing tidal circularization theory (see Figure 5.23). Furthermore, we have demonstrated that rare objects, which would once have required a serendipitous discovery, can now be found in large numbers through a systematic search. The bottlenecks of assembly line pipelines are ultimately occur with those tasks that must be performed manually. However, we have shown that with the exception of quality control, all the necessary tasks for the analysis of EBs through their photometric LCs can be fully automated.

The fastest and most efficient analysis will be of little value if its results are

not reliable. We thus spent considerable effort demonstrating how each part of our pipeline, namely DEBiL and MECI, are robust and provide realistic uncertainty estimates. Though in themselves they are not as accurate as the best manual methods, when high accuracy measurements are required, one can follow-up the pipeline results with additional observations, and manually fine-tune the fitted EB model. This way we are able to combine both the high-throughput capability of an automated pipeline with the precision of the traditional approach.

T-Lyr1-17236 was a case in point; this long-period EB was identified by our pipeline in a systematic search of the TrES dataset as containing two low-mass components (see Chapter 5). It was then followed-up photometrically and spectroscopically (see Table 7.1), and then reanalyzed manually (see Chapter 6). The follow-up analysis confirmed the original results and greatly improved the accuracy of its parameters, thus establishing T-Lyr1-17236 as the longest-period low-mass EB known to date. In addition to T-Lyr1-17236, our pipeline identified 11 additional low-mass candidates (see Table 5.10), which is remarkable considering that there are only 12 well characterized main-sequence low-mass EBs currently known (see Table 6.1). Of our 11 candidates, only one system, T-Dra0-01363, more commonly known as CM Draconis, was previously known, and was indeed found to be a low-mass EB ($0.23 + 0.21 M_{\odot}$) through the extensive work of Lacy (1977a) and the further parameter refinements of Metcalfe et al. (1996). We followed-up five of the ten remaining candidates, as well as four additional low-mass candidates with RV measurements (see Tables 7.1 and 7.10). Although our results are preliminary, we were able to confirm the low-mass status of all the binary candidate with at least three RV measurements (see §7.1). The candidates with fewer than three RV

measurements have very uncertain masses, but are all consistent with being low-mass (see §7.2).

Considering that they relied only on photometric data, the results of the MECI analyses were remarkably consistent with the RV follow-up results. However, we did find a tendency for the MECI analysis to overestimate the masses of our low-mass binaries. This bias is probably largely due to the fact that for masses in this range, the stellar models that MECI incorporates systematically underestimate the radii of stars. Thus, after inferring a given EB’s fractional radii from its measured eclipse duration, these stellar models will match it to a mass value that is too large. Once these theoretical models are further refined, the MECI analysis should become more accurate.

Though most of the work in this thesis centered on modeling EB LCs and fitting their parameters, one can reverse this approach and search for LCs that do not conform to the given model. For example, in Chapter 5 we located a group of EBs that were flagged by our pipeline, because they could not be successfully modeled by MECI due to their very disparate eclipse depths (see Table 5.7 and Figure 5.14). We thus suggested that effectively these systems may not be coeval, as is assumed by MECI, and that this phenomenon may have come about through an earlier epoch of mass transfer. Another group that we identified in Chapter 5 included EBs that have large periodic perturbations in their LCs (see Table 5.4, and Figures 5.17 and 5.18). Some of these perturbations may be due to persistent star spots or other large surface inhomogeneities, however, some perturbations may require more exotic explanations. We thus conclude that adding an “other” category is advisable for any automated pipeline. This category may at first receive a large number of rejected

cases, however, once these systems are better understood, they can be further classified until the full taxonomy of the observed population is revealed. One should be aware, though, that even with a complete classification of all the LCs there will inevitably be subtle phenomena that will be overlooked. As an illustration of this point, we describe two maverick LCs that would not have been found using our pipeline alone, but rather required a combination of pipeline results coupled with a dedicated search. The first, T-Cas0-07656, described in section §7.3, is an EB that contains a pulsating component. The second, T-Cyg1-03378, described in section §7.4, is an EB with large sinusoidal eclipse timing variations. These two binaries, as well as the aforementioned low-mass EBs candidates, merit further observation and investigation. We sincerely hope that others will further pursue these systems and continue the work begun here.

7.1 Low-Mass Candidates with At Least Three RV Measurements

Subsequent to the development of our pipeline, we identified a number of low-mass candidates for further follow-up. From late 2005 until mid 2007, these candidates were observed periodically using the Near-Infrared Spectrometer [NIRSPEC ; McLean et al. (1998, 2000)] at the W. M. Keck Observatory in Mauna Kea, Hawaii. Then, in late 2007 they were further observed with the Tillinghast Reflector Echelle Spectrograph [TRES ; Szentgyorgyi & Fűrész (2007)], installed on the 1.5-meter Tillinghast telescope at the F. L. Whipple Observatory in Arizona. These spectra

were processed and analyzed using the procedure described in Chapter 6, and converted into RV values. We preferred to make the spectral observations near the EB's quadrature (i.e., at a phase of 1/4 or 3/4) for two related reasons. Firstly, since during this time each measurement best constrains the RV model, and secondly, since at this time the spectral lines of the two components are maximally separated. The latter reason becomes critical when the components' respective absorption lines overlap, thus lowering the accuracy of our measurement technique, which simply fits the absorption line profiles to parabolas. Specifically, such an overlap would bias the centroid of the two absorption lines towards one another. One must pay close attention to this issue when analyzing short-period systems (e.g., T-Tau0-07388; see §7.1.4), which rotate rapidly and thus have highly broadened absorption features. Unfortunately, in many cases we had to compromise and make our observations far from quadrature. However, we were careful, at the very least, to avoid making spectral observations during an eclipse, as the partial occultation of a spinning star can create a significant bias to its RV measurements, in what is known as the Rossiter-McLaughlin effect (Rossiter 1924; McLaughlin 1924). To this end we may estimate the full duration of an EB's eclipse using:

$$\Delta t_{\text{eclipse}} = \frac{P}{\pi} \arcsin(r_1 + r_2) , \quad (7.1)$$

where P is the binary's orbital period and $r_{1,2}$ are its fraction radii.

In the following subsections, we describe what we know about each of these EBs, and illustrate their phased LC, their phased RV measurements, and the results of their MECI analysis (see Chapter 4). In all cases we modeled these data with

circular orbits, since both the RV data and the photometric LC were found to be consistent with having no eccentricity. When modeling these data, we did not distinguish between the sources of the RV data (i.e. NIRSPEC and TRES), however, we did weight the RV measurements according to their estimated uncertainties.

By convention, a positive RV value indicates that the object is receding from the observer. Thus, for a normal main-sequence binary, we expect the primary component to have a negative acceleration immediately after the primary eclipse (phase 0), as it moves out from behind the eclipsing secondary component and then curves towards the observer. Since the epoch of eclipse (t_0) and orbital period (P) of the binary are typically well constrained by its LC, we adopted an RV model with only three free parameters: the primary and secondary RV amplitudes ($K_{A,B}$), and the barycentric RV (V_γ). We were able to fit this model confidently when we had at least three double-lined RV measurements, or six observables. Binaries with fewer than three RV measurements could not be robustly modeled this way, but were rather fit to a simplified model (see §7.2). The component RV amplitudes were then used to compute the binary components' masses ($M_{A,B}$), and the sum of their semimajor axes (a), also known as the binary separation. To this end we used the following equations [see, e.g., Batten (1973)]:

$$\begin{aligned} a \sin i &= P(K_A + K_B)(1 - e^2)^{1/2}/2\pi \simeq \\ &\simeq 0.01977 R_\odot P_d(k_A + k_B)(1 - e^2)^{1/2}, \text{ and} \end{aligned} \quad (7.2)$$

$$\begin{aligned} M_{A,B} \sin^3 i &= PK_{B,A}(K_A + K_B)^2(1 - e^2)^{3/2}/2\pi G \simeq \\ &\simeq 1.0361 \cdot 10^{-7} M_\odot P_d k_{B,A}(k_A + k_B)^2(1 - e^2)^{3/2}, \end{aligned} \quad (7.3)$$

where for convenience, we define the unitless parameters: $P_d \equiv P/\text{day}$, and $k_{A,B} \equiv K_{A,B}/\text{km s}^{-1}$. Note that since we assume that the orbits are circular, we fix the eccentricity to $e = 0$. The RV projection factor ($\sin i$) can, in principle, be estimated using second order relativistic effects in ultra-high precision spectroscopy (Zucker & Alexander 2007). However, since our binaries eclipse, we were able to easily derive the projection factor by modeling the photometric LC and fitting for the orbital inclination (i). To this end, we used the DEBiL parameter fit, which was able to provide a comparably accurate estimate, as detached EBs inherently constrain the projection factor to be within a small interval immediately below unity.

When estimating the uncertainties of $a \sin i$ and $M_{A,B} \sin^3 i$, we took into account both the primary and secondary RV amplitude uncertainties, and the asymmetric uncertainty of the period. In the cases we will describe here, the RV measurements were often obtained a few years after those of the photometric LC data. Therefore, even small errors in the orbital period produce significant shifts in the RV model phase due to the long extrapolation, and can thus produce a noticeable error in the measured RV amplitudes. We next estimated each binary component's spectral classification using its derived mass and empirical tables of the properties of a range of MK spectral type stars (Cox 2000). Finally, we compared these results with those produced through the MECI analysis (using $w = 100$) and plotted each binary LC with the LC model of its most likely MECI model. Because the MECI model has only three free parameters (the binary's age and the masses of its two components), it will often produce a LC fit that is worse than the fit that DEBiL or EBOP would produce. However, since MECI is constrained to use only the parameters of physically realistic main-sequence stars, if it is unable to

successfully fit a given LC, we will have a strong indication that either one of our assumptions is erroneous or that additional effects must be considered.

Table 7.1. Measured radial velocities for EBs with at least three RV measurements

Target	Epoch (HJD)	Primary RV [km s ⁻¹]	Secondary RV [km s ⁻¹]	Template	Instrument	Comments
T-CrB0-10759	2,453,930.816114	47.20 ± 2.0	-99.10 ± 2.0	GJ 182	NIRSPEC	
	2,454,104.167015	50.53 ± 2.0	-110.11 ± 2.0	GJ 182	NIRSPEC	
	2,454,311.845306	-60.30 ± 2.0	7.93 ± 2.0	GJ 182	NIRSPEC	
T-Cyg1-12664	2,454,311.884551	34.51 ± 3.0	-82.48 ± 10.0	GJ 182	NIRSPEC	
–	2,454,373.642658	28.13 ± 2.0	...	GX And A	TRES	offset to match GJ 182
–	2,454,373.655263	28.21 ± 2.0	...	GX And A	TRES	offset to match GJ 182
–	2,454,373.667080	29.14 ± 2.0	...	GX And A	TRES	offset to match GJ 182
–	2,454,377.686427	23.47 ± 2.0	...	GX And A	TRES	offset to match GJ 182
–	2,454,377.678074	24.12 ± 2.0	...	GX And A	TRES	offset to match GJ 182
–	2,454,377.710062	24.45 ± 2.0	...	GX And A	TRES	offset to match GJ 182
T-Tau0-04859	2,453,928.118216	100.17 ± 7.0	-27.30 ± 3.0	GJ 182	NIRSPEC	
	2,454,024.132604	-21.76 ± 8.0	100.89 ± 3.0	GJ 182	NIRSPEC	
	2,454,100.852420	-28.44 ± 3.0	108.01 ± 3.0	GJ 182	NIRSPEC	
	2,454,103.952431	-31.36 ± 3.0	108.93 ± 5.0	GJ 182	NIRSPEC	
	2,454,377.920886	21.90 ± 3.0	52.11 ± 3.0	HD 3651	TRES	offset to match GJ 182
	2,454,377.932704	23.37 ± 3.0	50.61 ± 3.0	HD 3651	TRES	offset to match GJ 182
	2,454,377.944544	25.18 ± 3.0	48.33 ± 3.0	HD 3651	TRES	offset to match GJ 182
T-Tau0-07388	2,453,931.117781	-37.68 ± 25.0	2.32 ± 25.0	GJ 182	NIRSPEC	merged peaks- not used
	2,454,100.866271	113.33 ± 5.0	-150.85 ± 5.0	GJ 182	NIRSPEC	
	2,454,102.971832	-103.01 ± 25.0	144.20 ± 25.0	GJ 182	NIRSPEC	uncertain
	2,454,377.992485	86.42 ± 5.0	-118.18 ± 10.0	GX And A	TRES	offset to match GJ 182
	2,454,378.001999	92.89 ± 5.0	-128.20 ± 10.0	GX And A	TRES	offset to match GJ 182
	2,454,378.011501	98.18 ± 5.0	-143.22 ± 10.0	GX And A	TRES	offset to match GJ 182
	2,454,378.021119	100.66 ± 5.0	-136.24 ± 7.5	GX And A	TRES	offset to match GJ 182
	2,454,378.030923	107.53 ± 5.0	-157.77 ± 7.5	GX And A	TRES	offset to match GJ 182

7.1.1 T-CrB0-10759

The nearly equal eclipses of this binary indicate that the components have similar effective temperatures, and are thus likely to have similar masses. This conclusion is in agreement with the fact that the components also show similar RV amplitudes. The double-line spectra of this binary eliminate the possibility that the orbital period is half the stated value and that the secondary component is dark. We thus conclude that this binary is comprised of $0.60+0.58 M_{\odot}$ components ($K7 + K8$), in remarkable agreement with the results of its MECI analysis.

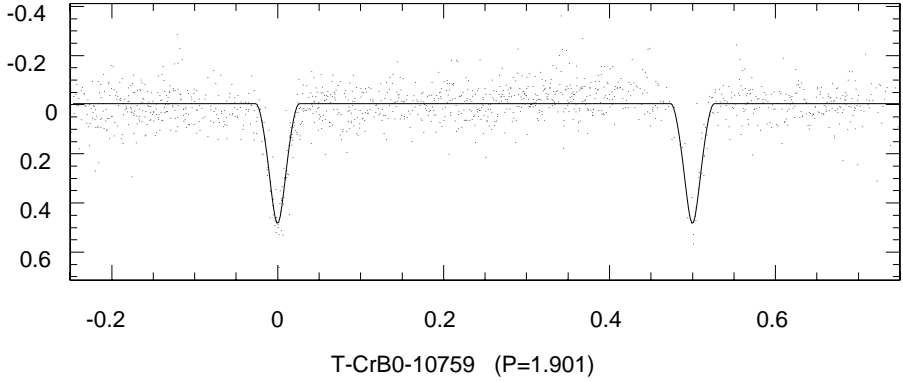


Fig. 7.1.— The phased TrES light curve (r -band), with the best-fit MECI model (solid line).

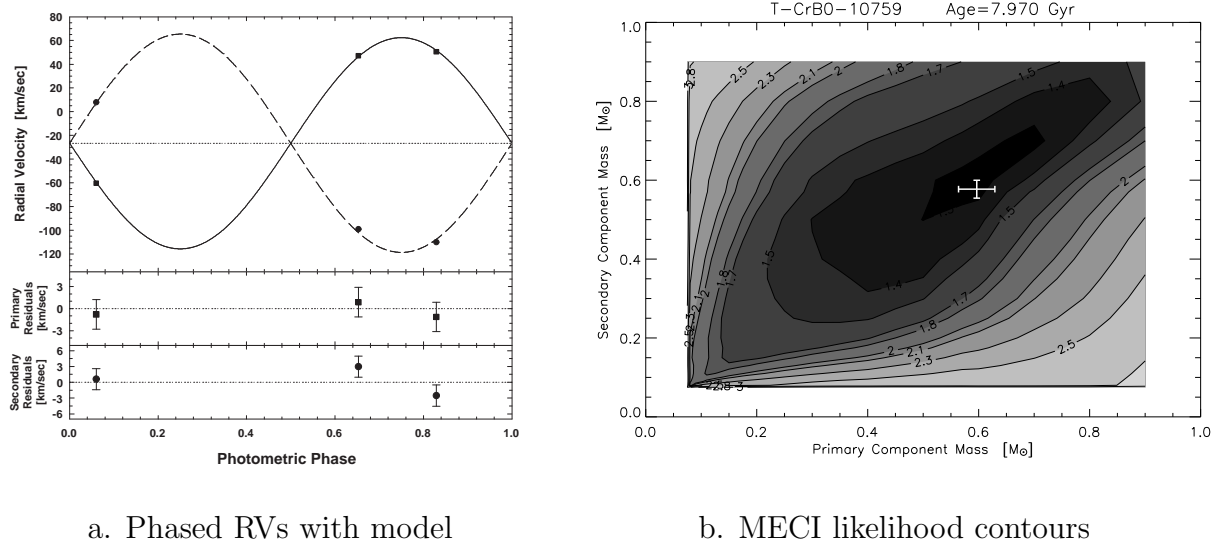


Fig. 7.2.— The phased RVs of T-CrB0-10759 are shown with the best-fit circular orbit model. The square symbols indicate the primary component's RVs and the solid line illustrate their fitted model, while the circular symbols indicate the secondary component RVs and the dashed line illustrates their fitted model. The MECI likelihood contours are compared with the RV solution (error bars).

Table 7.2. Catalog information of T-CrB0-10759

Parameter	Value
α (J2000)	15:52:18.455
δ (J2000)	30:35:32.13
USNO-B ^a B -mag	17.495 ± 0.2
GSC2.3 ^b V -mag	15.67 ± 0.30
USNO-B R -mag	15.185 ± 0.2
CMC14 ^c r' -mag	15.543 ± 0.021
2MASS ^d J -mag	13.049 ± 0.015
2MASS H -mag	12.388 ± 0.015
2MASS K_s -mag	12.160 ± 0.015
UCAC ^e μ_α [mas yr $^{-1}$]	3.6 ± 5.4
UCAC μ_δ [mas yr $^{-1}$]	-19.4 ± 5.3
TrES third light ^f [R -mag]	0.028 ± 0.006

^aU.S. Naval Observatory photographic sky survey
(Monet et al. 2003).

^bGuide Star Catalog, version 2.3.2 (Morrison et al. 2001).

^cCarlsberg Meridian Catalog 14 (Evans et al. 2002).

^dTwo Micron All Sky Survey catalog (Skrutskie et al. 2006).

^eThe Second U.S. Naval Observatory CCD Astrograph Catalog (Zacharias et al. 2004).

^fThe fraction of blended light in the TrES LC from resolved USNO-B sources within 30" of the target.

Table 7.3. Binary parameters of T-CrB0-10759

Parameter	Symbol	Value
Orbital Period [days]	P	$1.901274^{+0.000012}_{-0.000014}$
Epoch of eclipse [HJD]	t_0	$2453515.09699 \pm 0.00064$
Number of light curve data points	N_{LC}	1287
Number of RV data points	N_{RV}	3
MECI analysis primary mass [M_\odot]	M_A^{MECI}	0.61 ± 0.30
MECI analysis secondary mass [M_\odot]	M_B^{MECI}	0.60 ± 0.25
MECI analysis binary age [Gyr]	T^{MECI}	7.4 ± 58
Primary RV amplitude [km s^{-1}]	K_A	89.08 ± 0.92
Secondary RV amplitude [km s^{-1}]	K_B	92.06 ± 2.22
Barycenteric RV, relative to GJ 182 [km s^{-1}]	V_γ	-26.65 ± 0.78
DEBiL estimate of the projection factor	$\sin i$	0.9991 ± 0.0070
Combined semimajor axis with projection factor [R_\odot]	$a \sin i$	$6.809^{+0.040}_{-0.042}$
Primary mass with projection factor [M_\odot]	$M_A \sin^3 i$	$0.595^{+0.030}_{-0.030}$
Secondary mass with projection factor [M_\odot]	$M_B \sin^3 i$	$0.576^{+0.019}_{-0.019}$

7.1.2 T-Cyg1-12664

This binary was originally thought to have an 8.2-day orbital period, with two equal eclipses and therefore equal components, because all of the eclipses observed in its TrES (*r*-band) LC are similar. However, we subsequently observed it to have six single-lined TRES spectra (*R*-band), and one double-lined NIRSPEC spectrum (*K*-band) in which the secondary component is very weak. We therefore revised our model for this EB to one with a 4.1-day orbital period with an unobserved secondary eclipse, indicating that the secondary component is far dimmer and cooler than the primary component. Furthermore, the fact that the secondary component is unobserved in the optical, but is observed in the near infrared, supports the assertion that it is very red, and thus likely to be a cool low-mass star. Since we only have a single RV measurement for the secondary component, the primary component's mass remains uncertain, nevertheless we estimate that this binary is comprised of $0.62+0.32 M_{\odot}$ components (*K6 + M3*), which are smaller than those predicted by its MECI analysis. As with T-Lyr1-17236, the comparably long orbital period of this EB may make it a good test case for the magnetic disruption hypothesis (see Chapter 6). The fact that the MECI analysis overestimated the components' masses might be due to them having bloated radii, which could then be explained through magnetic disruption. Finally, also like T-Lyr1-17236 (see §6.8), this EB falls within the field of view of the upcoming NASA *Kepler* mission. If it is observed with this mission, both eclipses would be easily detected and the high-precision LC would allow for strong constraints on the fractional radii of both binary components.

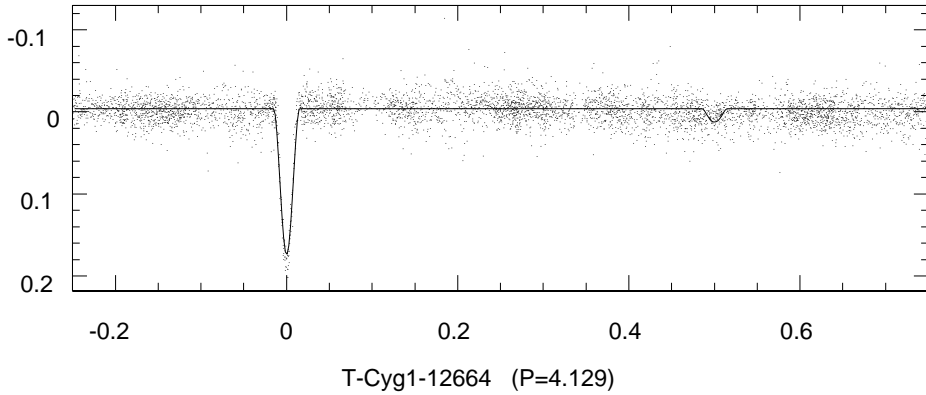
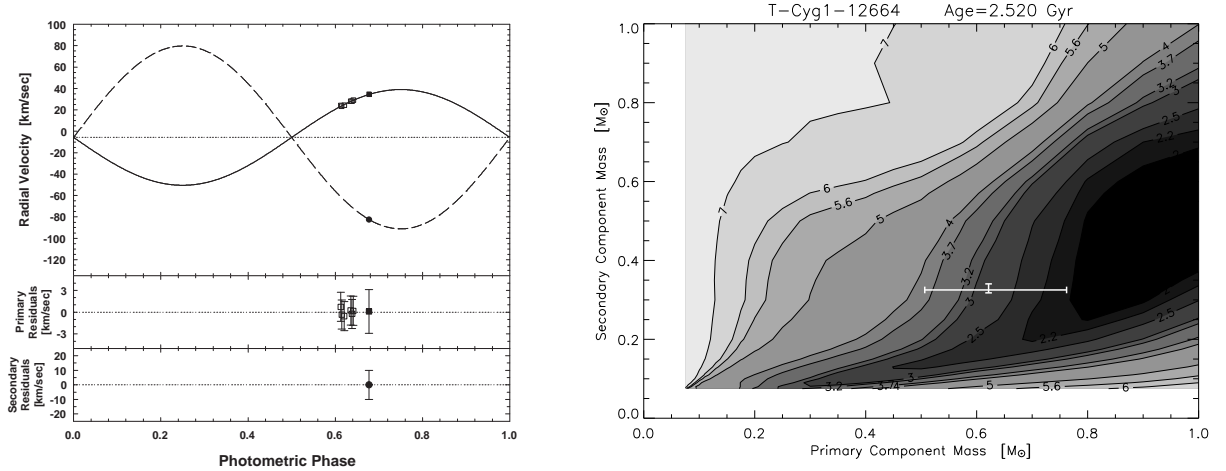


Fig. 7.3.— The phased TrES light curve (r -band), with the best-fit MECI model (solid line).



a. Phased RVs with model

b. MECI likelihood contours

Fig. 7.4.— The phased RVs of T-Cyg1-12664 are shown with the best-fit circular orbit model. The filled symbols indicate NIRSPEC measurements, while the unfilled symbols indicate TRES measurements. The square symbols indicate the primary component's RVs and the solid line is their fitted model, while the circular symbols indicate the secondary component RVs and the dashed line is their fitted model. The MECI likelihood contours are compared with the RV solution (error bars).

Table 7.4. Catalog information of T-Cyg1-12664

Parameter	Value
α (J2000)	19:51:39.824
δ (J2000)	48:19:55.38
USNO-B B -mag	14.240 \pm 0.2
GSC2.3 V -mag	13.11 \pm 0.30
USNO-B R -mag	13.315 \pm 0.2
CMC14 r' -mag	13.024 \pm 0.035
2MASS J -mag	11.911 \pm 0.015
2MASS H -mag	11.582 \pm 0.015
2MASS K_s -mag	11.529 \pm 0.015
USNO-B μ_α [mas yr $^{-1}$]	-18 \pm 6
USNO-B μ_δ [mas yr $^{-1}$]	-6 \pm 2
TrES third light [R -mag]	0.177 \pm 0.034

Table 7.5. Binary parameters of T-Cyg1-12664

Parameter	Symbol	Value
Orbital Period [days]	P	4.128751 \pm 0.000032
Epoch of eclipse [HJD]	t_0	2453210.84051 \pm 0.00020
Number of light curve data points	N_{LC}	5280
Number of RV data points	N_{RV}	7
MECI analysis primary mass [M_\odot]	M_A^{MECI}	0.91 \pm 0.27
MECI analysis secondary mass [M_\odot]	M_B^{MECI}	0.41 \pm 0.38
MECI analysis binary age [Gyr]	T^{MECI}	2.4 \pm 2.4
Primary RV amplitude [km s $^{-1}$]	K_A	44.73 \pm 0.23
Secondary RV amplitude [km s $^{-1}$]	K_B	-85.48 \pm 1.04
Barycenteric RV, relative to GJ 182 [km s $^{-1}$]	V_γ	-5.72 \pm 0.13
DEBiL estimate of the projection factor	$\sin i$	0.9992 \pm 0.0028
Combined semimajor axis with projection factor [R_\odot]	$a \sin i$	10.63 $^{+0.49}_{-0.39}$
Primary mass with projection factor [M_\odot]	$M_A \sin^3 i$	0.620 $^{+0.140}_{-0.115}$
Secondary mass with projection factor [M_\odot]	$M_B \sin^3 i$	0.324 $^{+0.015}_{-0.007}$

7.1.3 T-Tau0-04859

This system exhibits clearly disparate eclipses, which eliminates the possibility that the secondary component is unseen. Furthermore, the RV measurements indicate that the components are similar yet not equal, having masses of $0.66+0.62 M_{\odot}$ ($K5 + K6$). Though these mass estimates are in agreement with those derived from its MECI analysis, MECI was not able to reproduce the large depth of the EB's primary eclipse (~ 0.45 mag in r -band) together with the significantly shallower secondary eclipse (~ 0.2 mag in r -band). As mentioned earlier, one explanation for such a phenomenon is that the binary components are effectively not coeval, bringing about a larger than expected difference in their surface temperatures. However, it is unlikely that a K -dwarf binary such as this would be old enough to have evolved off the main-sequence, and therefore it is improbable that its components underwent mass transfer. An alternative explanation for this phenomenon is that this binary is very young, and has therefore not yet reached the main-sequence isochrones used by MECI. This latter hypothesis is strengthened by the fact that this candidate resides in the Taurus field, which is known to harbor many young stars; however, the fact that the eclipse durations are comparably short, significantly constrains the size of the components, and therefore limits how young they could be.

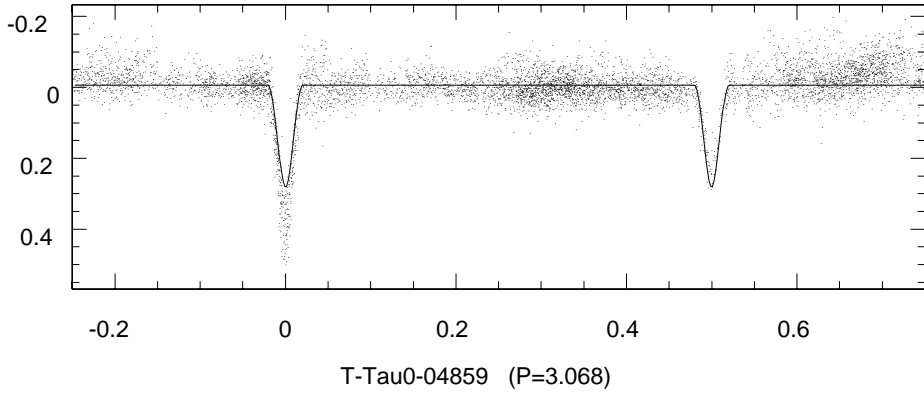
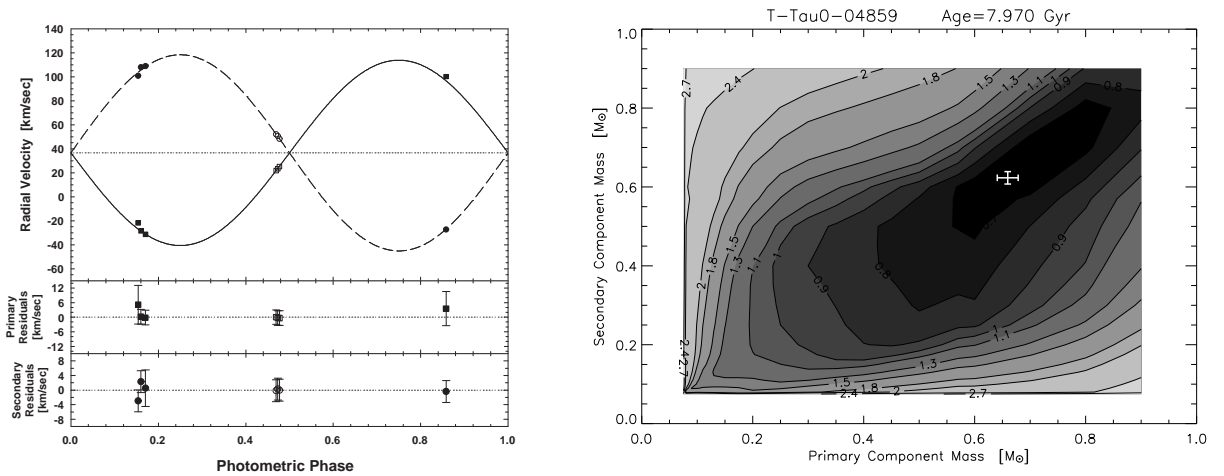


Fig. 7.5.— The phased TrES light curve (r -band), with the best-fit MECI model (solid line).



a. Phased RVs with model

b. MECI likelihood contours

Fig. 7.6.— The phased RVs of T-Tau0-04859 are shown with the best-fit circular orbit model. The filled symbols indicate a NIRSPEC measurements, while the unfilled symbols indicate TRES measurements. The square symbols indicate the primary component's RVs and the solid line is their fitted model, while the circular symbols indicate the secondary component RVs and the dashed line is their fitted model. The MECI likelihood contours are compared with the RV solution (error bars).

Table 7.6. Catalog information of T-Tau0-04859

Parameter	Value
α (J2000)	04:08:11.608
δ (J2000)	24:51:10.18
USNO-B B -mag	15.520 \pm 0.2
GSC2.3 V -mag	14.05 \pm 0.23
USNO-B R -mag	13.495 \pm 0.2
CMC14 r' -mag	13.748 \pm 0.022
2MASS J -mag	11.748 \pm 0.015
2MASS H -mag	11.064 \pm 0.015
2MASS K_s -mag	10.869 \pm 0.015
UCAC μ_α [mas yr $^{-1}$]	3.4 \pm 5.2
UCAC μ_δ [mas yr $^{-1}$]	-7.7 \pm 5.2
TrES third light [R -mag]	0.004 \pm 0.001

Table 7.7. Binary parameters of T-Tau0-04859

Parameter	Symbol	Value
Orbital Period [days]	P	$3.068000^{+0.000027}_{-0.000028}$
Epoch of eclipse [HJD]	t_0	2453738.33643 \pm 0.00031
Number of light curve data points	N_{LC}	6729
Number of RV data points	N_{RV}	7
MECI analysis primary mass [M_\odot]	M_A^{MECI}	0.73 \pm 0.24
MECI analysis secondary mass [M_\odot]	M_B^{MECI}	0.67 \pm 0.24
MECI analysis binary age [Gyr]	T^{MECI}	8.3 \pm 14.7
Primary RV amplitude [km s $^{-1}$]	K_A	77.21 \pm 0.77
Secondary RV amplitude [km s $^{-1}$]	K_B	81.73 \pm 1.01
Barycenteric RV, relative to GJ 182 [km s $^{-1}$]	V_γ	36.63 \pm 0.37
DEBiL estimate of the projection factor	$\sin i$	0.9984 \pm 0.0031
Combined semimajor axis with projection factor [R_\odot]	$a \sin i$	$9.642^{+0.047}_{-0.047}$
Primary mass with projection factor [M_\odot]	$M_A \sin^3 i$	$0.656^{+0.018}_{-0.018}$
Secondary mass with projection factor [M_\odot]	$M_B \sin^3 i$	$0.620^{+0.015}_{-0.015}$

7.1.4 T-Tau0-07388

Like T-Tau0-04859, this binary also clearly exhibits disparate eclipses, which eliminates the possibility that the secondary component is unseen. However, unlike T-Tau0-04859, the RV measurements of this binary indicate that the components of this binary are significantly different, having masses of $0.65+0.47 M_{\odot}$ ($K6 + M1$). The MECI analysis significantly overestimated these component masses, which suggests that the components are larger than predicted by stellar models. Such a size increase could be explained through the magnetic disruption hypothesis (see Chapter 6), since this binary has a short 0.6-day orbital period, making it likely that both these components are spinning rapidly and producing strong magnetic fields. However, another explanation for the components' large radii is that they are young and still in the process of forming. As with T-Tau0-04859, this latter explanation is supported by the fact that this binary resides in the Taurus field, which is known to contain star forming regions. Lastly, we note that the LC plateaux are of unequal brightness, thus indicating an “O’Connell effect” (see §5.3.3). Specifically, the out-of-eclipse r -band brightness of the binary is ~ 0.05 mag dimmer after the primary eclipse than it was before the eclipse, perhaps indicating a persistent off-axis hot spot (e.g., reflection) or cold spot (e.g., gravity darkening) on one of the components.

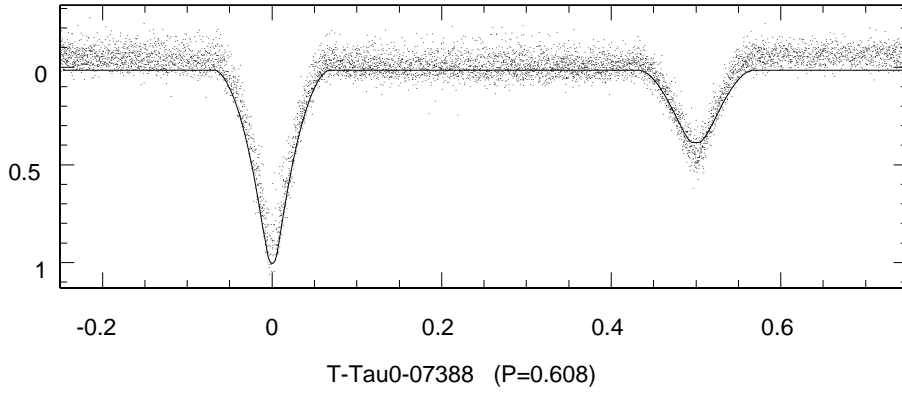


Fig. 7.7.— The phased TrES light curve (r -band), with the best-fit MECI model (solid line).

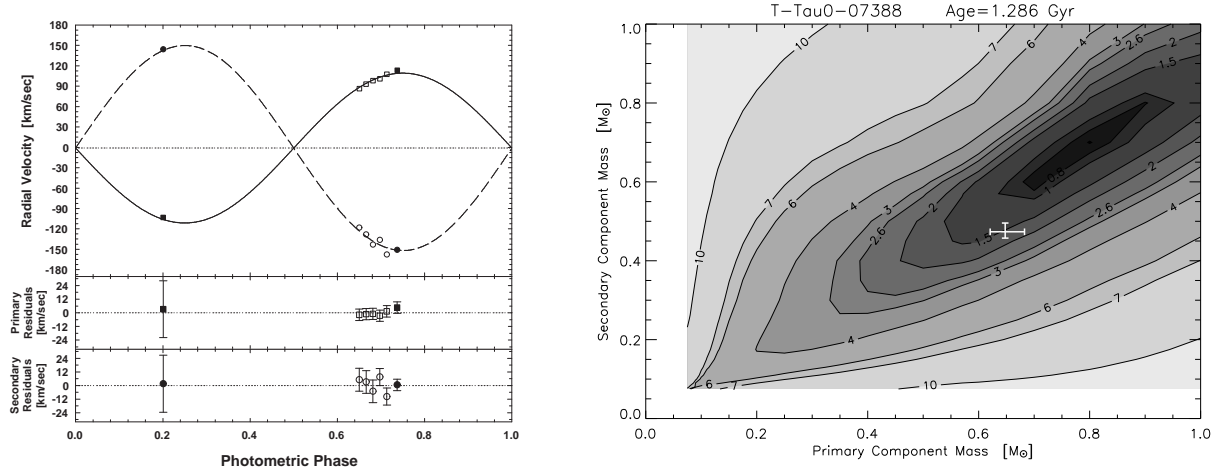


Fig. 7.8.— The phased RVs of T-Tau0-07388 are shown with the best-fit circular orbit model. The filled symbols indicate a NIRSPEC measurements, while the unfilled symbols indicate TRES measurements. The square symbols indicate the primary component's RVs and the solid line is their fitted model, while the circular symbols indicate the secondary component RVs and the dashed line is their fitted model. The MECI likelihood contours are compared with the RV solution (error bars).

Table 7.8. Catalog information of T-Tau0-07388

Parameter	Value
α (J2000)	04:10:04.977
δ (J2000)	29:31:02.33
USNO-B B -mag	16.635 \pm 0.2
GSC2.3 V -mag	14.38 \pm 0.26
USNO-B R -mag	13.750 \pm 0.2
CMC14 r' -mag	14.115 \pm 0.05
2MASS J -mag	11.131 \pm 0.015
2MASS H -mag	10.375 \pm 0.015
2MASS K_s -mag	10.133 \pm 0.015
USNO-B μ_α [mas yr $^{-1}$]	-36 \pm 2
USNO-B μ_δ [mas yr $^{-1}$]	-14 \pm 6
TrES third light [R -mag]	0.031 \pm 0.007

Table 7.9. Binary parameters of T-Tau0-07388

Parameter	Symbol	Value
Orbital Period [days]	P	0.6078486 $^{+0.0000033}_{-0.0000015}$
Epoch of eclipse [HJD]	t_0	2453736.924811 \pm 0.000080
Number of light curve data points	N_{LC}	6702
Number of RV data points	N_{RV}	7
MECI analysis primary mass [M_\odot]	M_A^{MECI}	0.80 \pm 0.13
MECI analysis secondary mass [M_\odot]	M_B^{MECI}	0.70 \pm 0.11
MECI analysis binary age [Gyr]	T^{MECI}	1.4 \pm 1.3
Primary RV amplitude [km s $^{-1}$]	K_A	110.23 \pm 1.06
Secondary RV amplitude [km s $^{-1}$]	K_B	150.83 \pm 2.40
Barycenteric RV, relative to GJ 182 [km s $^{-1}$]	V_γ	-1.10 \pm 1.02
DEBiL estimate of the projection factor	$\sin i$	0.9998 \pm 0.0055
Combined semimajor axis with projection factor [R_\odot]	$a \sin i$	3.137 $^{+0.040}_{-0.020}$
Primary mass with projection factor [M_\odot]	$M_A \sin^3 i$	0.647 $^{+0.033}_{-0.025}$
Secondary mass with projection factor [M_\odot]	$M_B \sin^3 i$	0.473 $^{+0.021}_{-0.014}$

7.2 Low-Mass Candidates with Fewer than Three RV Measurements

The following binaries have only one or two RV measurements, and their fitted models are therefore speculative at best. Nevertheless, for completeness we chose to present these systems as well, together with our best guess as to their properties. Our analysis of these systems repeated the procedure we outlined in section §7.1. However, because we did not have sufficient RV data to reliably determine both the primary and secondary RV amplitudes ($K_{A,B}$), as well as the Barycenteric RV (V_γ), as we did previously, we opted instead for a model of the sum of the components' RVs. This latter model has only a single free parameter, the sum of the RV amplitudes ($K_A + K_B$), and thus can be fit, in principle, using a single measurement of the difference between the components' RVs. Note that, as before, we determine the period (P) and epoch of eclipse (t_0) of the binary using the photometric LC.

Once we determined the sum of the RV amplitudes ($K_A + K_B$), we solve for $a \sin i$ using Equation 7.2, and then solve for $(M_A + M_B) \sin^3 i$, by summing both instances of Equation 7.3 and thus arriving at:

$$\begin{aligned} (M_A + M_B) \sin^3 i &= P(K_A + K_B)^3(1 - e^2)^{3/2}/2\pi G \simeq \\ &\simeq 1.0361 \cdot 10^{-7} M_\odot P_d(k_A + k_B)^3(1 - e^2)^{3/2}. \end{aligned} \quad (7.4)$$

As before, we assume that the orbits are circular and fix the eccentricity to $e = 0$, and use the DEBiL parameter fit to estimate the projection factor ($\sin i$).

Since in these cases we only know the sum of the components' masses, when comparing the RV results with the MECI analysis, we produce a solid diagonal line on the mass-mass contour plot, indicating all the mass pairings that solve Equation 7.4. We repeated this calculation for mass pairings at the 1σ uncertainty level, thus producing two additional diagonals, which we plot as dotted lines. Though we do not know the component's mass ratio (q) for these EBs, by the fact that at least one observed spectrum was seen to be double-lined, we may conclude that $q \gtrsim 0.5$ with a moderate degree of certainty.

Table 7.10. Measured radial velocities for EBs with fewer than three RV measurements

Target	Epoch (HJD)	Primary RV [km s ⁻¹]	Secondary RV [km s ⁻¹]	Template	Instrument	Comments
T-And0-04829	2,453,928.066849	98.89 ± 1.5	-29.92 ± 1.5	GJ 182	NIRSPEC	uncertain
–	2,453,929.095220	-77.06 ± 1.5	...	GJ 182	NIRSPEC	
T-And0-20382	2,453,931.061037	-24.22 ± 3.0	110.72 ± 10.0	GJ 182	NIRSPEC	offset to match GJ 182
–	2,454,377.855671	-47.24 ± 15.0	...	GX And A	TRES	
T-CrB0-14232	2,453,930.846256	67.26 ± 2.0	-102.47 ± 2.0	GJ 182	NIRSPEC	
T-Dra0-03021	2,453,929.882148	-25.04 ± 10.0	85.84 ± 10.0	GJ 182	NIRSPEC	
–	2,454,308.878115	-71.31 ± 10.0	...	GJ 182	NIRSPEC	
T-Dra0-07116	2,453,931.905448	25.89 ± 2.5	-47.58 ± 2.5	GJ 182	NIRSPEC	
–	2,454,308.890984	-77.08 ± 8.0	83.63 ± 4.0	GJ 182	NIRSPEC	

7.2.1 T-And0-04829

This binary was found to have a double-lined spectrum and nearly identical eclipses, which suggests that the components are likely similar. The RV model seems to predict components as small as M-dwarfs, while MECI suggests that the components may be as large as G-dwarfs. The binary's 2MASS colors are comparably red, supporting the low-mass hypothesis; however, the eclipse durations are comparably large, which supports the higher-mass hypothesis. Consequently, these contradictory results prevent us from arriving at any firm conclusions.

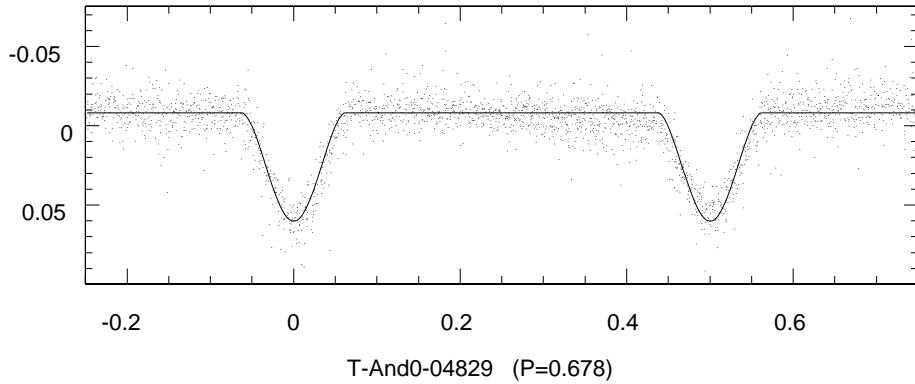
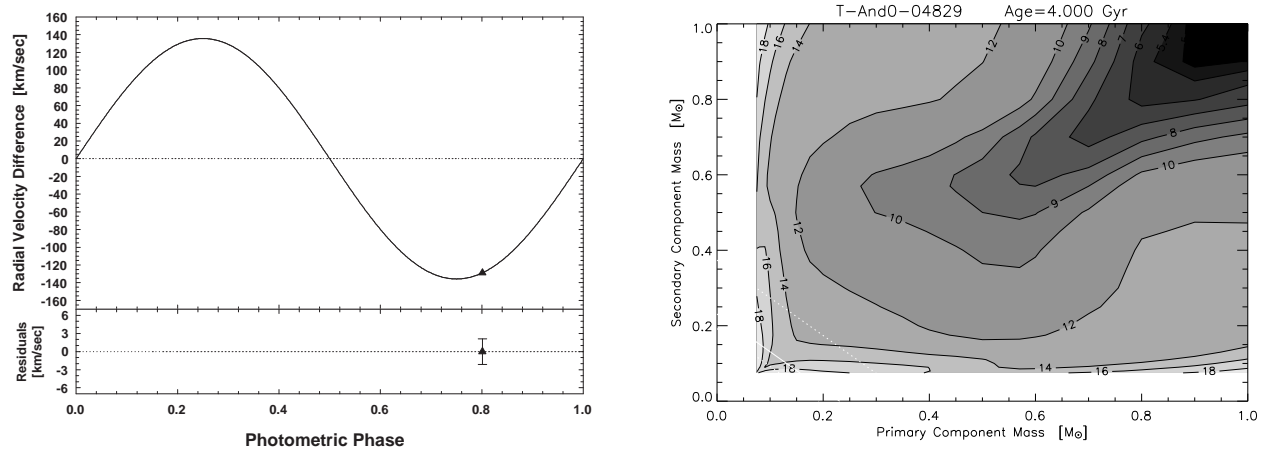


Fig. 7.9.— The phased TrES light curve (*r*-band), with the best-fit MECI model (solid line).



a. Phased RVs with model

b. MECI likelihood contours

Fig. 7.10.— The phased RVs of T-And0-04829 are shown with the best-fit circular orbit model to the difference between the component RVs.

Table 7.11. Catalog information of T-And0-04829

Parameter	Value
α (J2000)	01:15:15.228
δ (J2000)	47:45:58.97
USNO-B B -mag	13.610 \pm 0.2
GSC2.3 V -mag	12.33 \pm 0.29
USNO-B R -mag	11.730 \pm 0.2
CMC14 r' -mag	12.782 \pm 0.05
2MASS J -mag	10.970 \pm 0.015
2MASS H -mag	10.339 \pm 0.015
2MASS K_s -mag	10.162 \pm 0.015
UCAC μ_α [mas yr $^{-1}$]	-23.8 \pm 4.9
UCAC μ_δ [mas yr $^{-1}$]	44.7 \pm 4.9
TrES third light [R -mag]	0.011 \pm 0.003

Table 7.12. Binary parameters of T-And0-04829

Parameter	Symbol	Value
Orbital Period [days]	P	0.6778149 \pm 0.0000036
Epoch of eclipse [HJD]	t_0	2452906.767874 \pm 0.000081
Number of light curve data points	N_{LC}	2357
Number of RV data points	N_{RV}	1
Relative RV amplitude [km s $^{-1}$]	$K_A + K_B$	135.74 \pm 2.24
DEBiL estimate of the projection factor	$\sin i$	0.913 \pm 0.021
Combined semimajor axis with projection factor [R_\odot]	$a \sin i$	$1.82_{-0.10}^{+0.32}$
Mass sum with projection factor [M_\odot]	$(M_A + M_B) \sin^3 i$	$0.176_{-0.027}^{+0.108}$

7.2.2 T-And0-20382

Like T-And0-04829, this binary was found to have a double-lined spectrum and nearly identical eclipses, which suggests that the components are likely similar. The RV and MECI analyses are consistent with one another, and indicate that the components are K-dwarfs, however both analyses have large uncertainties that prevent a more specific identification. MECI is limited by poorly constrained eclipses, while the RV analysis is limited by both a poorly determined orbital period and a poorly determined RV measurement.

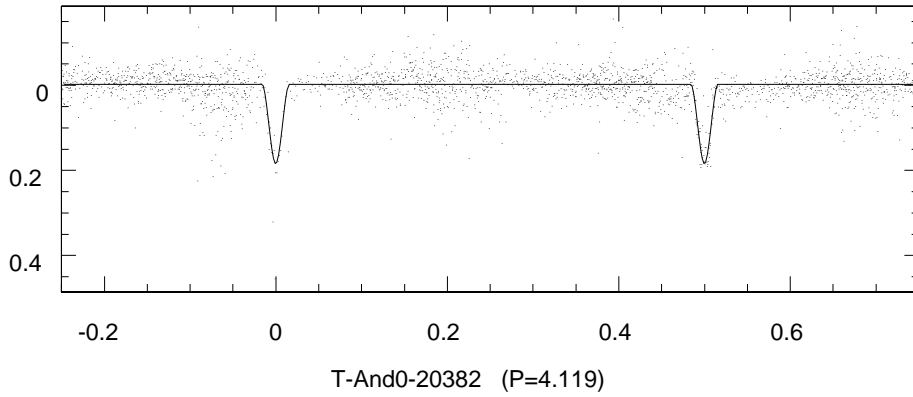
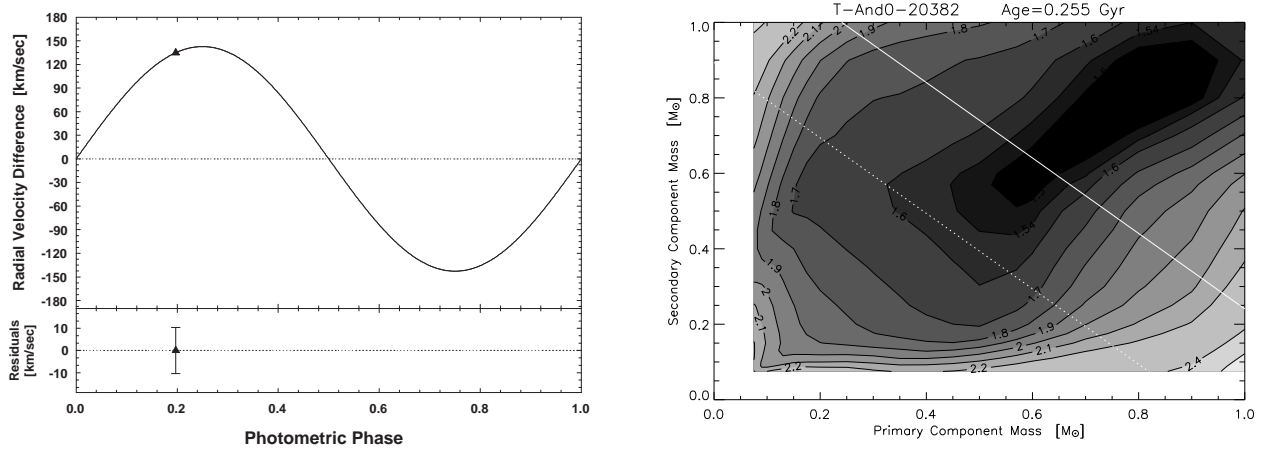


Fig. 7.11.— The phased TrES light curve (r -band), with the best-fit MECI model (solid line).



a. Phased RVs with model

b. MECI likelihood contours

Fig. 7.12.— The phased RVs of T-And0-20382 are shown with the best-fit circular orbit model to the difference between the component RVs.

Table 7.13. Catalog information of T-And0-20382

Parameter	Value
α (J2000)	01:22:08.780
δ (J2000)	46:59:55.41
USNO-B B -mag	16.190 \pm 0.2
GSC2.3 V -mag	14.88 \pm 0.33
USNO-B R -mag	14.685 \pm 0.2
CMC14 r' -mag	14.859 \pm 0.05
2MASS J -mag	13.154 \pm 0.015
2MASS H -mag	12.619 \pm 0.015
2MASS K_s -mag	12.440 \pm 0.015
UCAC μ_α [mas yr $^{-1}$]	9.0 \pm 5.7
UCAC μ_δ [mas yr $^{-1}$]	-3.5 \pm 5.6
TrES third light [R -mag]	0.333 \pm 0.050

Table 7.14. Binary parameters of T-And0-20382

Parameter	Symbol	Value
Orbital Period [days]	P	4.11975 \pm 0.00031
Epoch of eclipse [HJD]	t_0	2452949.7657 \pm 0.0046
Number of light curve data points	N_{LC}	5368
Number of RV data points	N_{RV}	1
MECI analysis primary mass [M_\odot]	M_A^{MECI}	0.81 \pm 0.60
MECI analysis secondary mass [M_\odot]	M_B^{MECI}	0.80 \pm 0.66
MECI analysis binary age [Gyr]	T^{MECI}	0.25 \pm 0.77
Relative RV amplitude [km s $^{-1}$]	$K_A + K_B$	142.7 \pm 11.0
DEBiL estimate of the projection factor	$\sin i$	1.0000 \pm 0.0057
Combined semimajor axis with projection factor [R_\odot]	$a \sin i$	11.6 $^{+10.2}_{-1.1}$
Mass sum with projection factor [M_\odot]	$(M_A + M_B) \sin^3 i$	1.2 $^{+6.9}_{-0.3}$

7.2.3 T-CrB0-14232

As with the two previous EBs, this binary was found to have a double-lined spectrum and nearly identical eclipses, which suggests that the components are likely similar.

As with T-And0-20382, the RV and MECI analyses are consistent with one another, though the RV analysis results have large uncertainties due to poorly determined orbital period and a poorly determined RV measurement. The MECI results, however, provide stronger mass constraints, suggesting that the EB components are both late K-dwarfs.

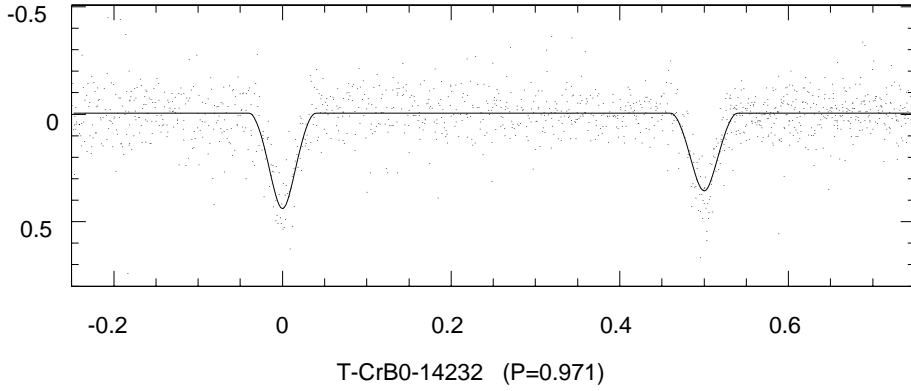
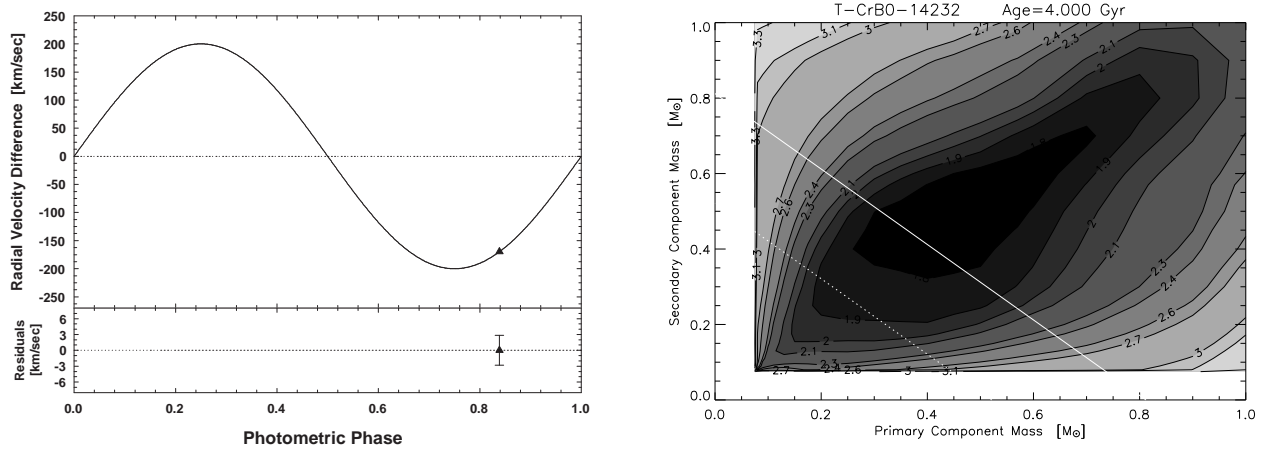


Fig. 7.13.— The phased TrES light curve (r -band), with the best-fit MECI model (solid line).



a. Phased RVs with model

b. MECI likelihood contours

Fig. 7.14.— The phased RVs of T-CrB0-14232 are shown with the best-fit circular orbit model to the difference between the component RVs.

Table 7.15. Catalog information of T-CrB0-14232

Parameter	Value
α (J2000)	16:10:22.495
δ (J2000)	33:57:52.33
USNO-B B -mag	17.985 \pm 0.2
GSC2.3 V -mag	16.27 \pm 0.31
USNO-B R -mag	16.170 \pm 0.2
CMC14 r' -mag	16.092 \pm 0.01
2MASS J -mag	13.367 \pm 0.015
2MASS H -mag	12.757 \pm 0.015
2MASS K_s -mag	12.511 \pm 0.015
USNO-B μ_α [mas yr $^{-1}$]	6 \pm 1
USNO-B μ_δ [mas yr $^{-1}$]	-4 \pm 3
TrES third light [R -mag]	0.252 \pm 0.039

Table 7.16. Binary parameters of T-CrB0-14232

Parameter	Symbol	Value
Orbital Period [days]	P	0.971305 \pm 0.000038
Epoch of eclipse [HJD]	t_0	2453514.79889 \pm 0.00055
Number of light curve data points	N_{LC}	1287
Number of RV data points	N_{RV}	1
MECI analysis primary mass [M_\odot]	M_A^{MECI}	0.59 \pm 0.28
MECI analysis secondary mass [M_\odot]	M_B^{MECI}	0.56 \pm 0.36
MECI analysis binary age [Gyr]	T^{MECI}	4.0 \pm 13.4
Relative RV amplitude [km s $^{-1}$]	$K_A + K_B$	200.00 \pm 3.33
DEBiL estimate of the projection factor	$\sin i$	0.997 \pm 0.013
Combined semimajor axis with projection factor [R_\odot]	$a \sin i$	$3.84^{+1.65}_{-0.52}$
Mass sum with projection factor [M_\odot]	$(M_A + M_B) \sin^3 i$	$0.81^{+1.54}_{-0.29}$

7.2.4 T-Dra0-03021

This binary was found to have disparate eclipses, which indicates that the component are not equal. Though the RV measurement was uncertain, the high signal-to-noise ratio of this EB's LC allowed us to determine its orbital period with high accuracy, thus reducing the RV analysis uncertainties. The RV analysis indicates that the components are early M-dwarfs, however the binary's 2MASS colors indicate that it is likely to be a K-dwarf binary. Furthermore, the eclipse durations are so long that they caused the MECI analysis to produce mass estimates that are out of range ($>1M_{\odot}$). Similar to the case of T-And0-04829, these contradictory results prevent us from arriving at any firm conclusion.

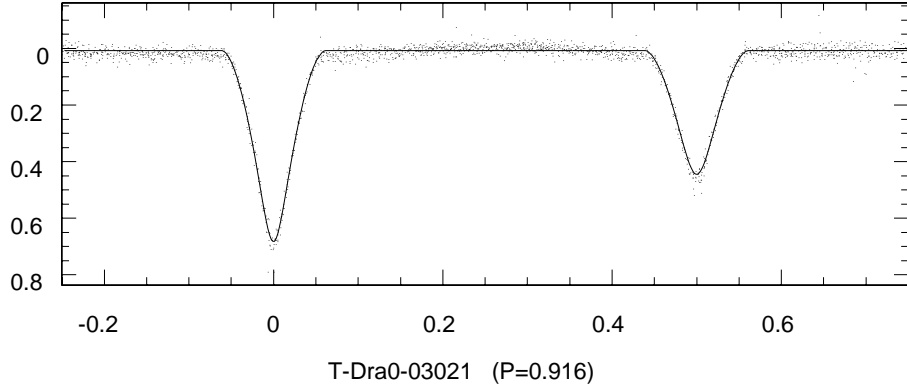


Fig. 7.15.— The phased TrES light curve (r -band), with the best-fit MECI model (solid line).

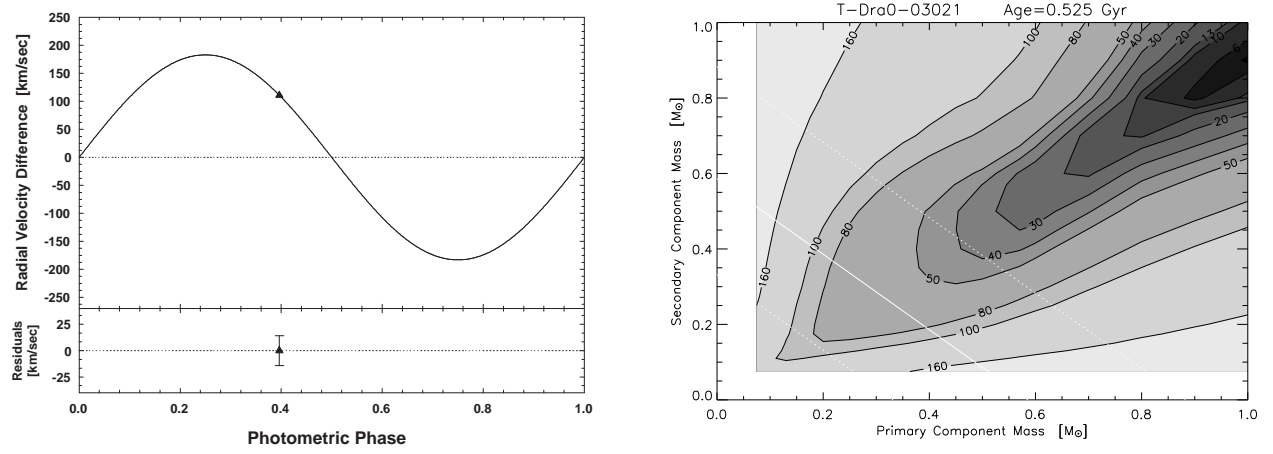


Fig. 7.16.— The phased RVs of T-Dra0-03021 are shown with the best-fit circular orbit model to the difference between the component RVs.

Table 7.17. Catalog information of T-Dra0-03021

Parameter	Value
α (J2000)	17:01:03.618
δ (J2000)	55:14:54.70
USNO-B B -mag	15.135 \pm 0.2
GSC2.3 V -mag	13.68 \pm 0.16
USNO-B R -mag	13.135 \pm 0.2
2MASS J -mag	11.498 \pm 0.015
2MASS H -mag	10.924 \pm 0.015
2MASS K_s -mag	10.771 \pm 0.015
USNO-B μ_α [mas yr $^{-1}$]	20 \pm 2
USNO-B μ_δ [mas yr $^{-1}$]	-20 \pm 2
TrES third light [R -mag]	0.045 \pm 0.011

Table 7.18. Binary parameters of T-Dra0-03021

Parameter	Symbol	Value
Orbital Period [days]	P	0.9159291 \pm 0.0000025
Epoch of eclipse [HJD]	t_0	2453128.081067 \pm 0.000051
Number of light curve data points	N_{LC}	2000
Number of RV data points	N_{RV}	1
Relative RV amplitude [km s $^{-1}$]	$K_A + K_B$	183.1 \pm 23.3
DEBiL estimate of the projection factor	$\sin i$	0.9978 \pm 0.0034
Combined semimajor axis with projection factor [R_\odot]	$a \sin i$	$3.31^{+0.54}_{-0.49}$
Mass sum with projection factor [M_\odot]	$(M_A + M_B) \sin^3 i$	$0.58^{+0.29}_{-0.25}$

7.2.5 T-Dra0-07116

As with previous EBs, this binary was found to have double-lined spectra and nearly identical eclipses, which suggests that the components are likely similar. Though this system has two RV measurements, they are spaced approximately a half a phase apart, thus preventing them from providing a strong verification of the RV model's phase. The RV and MECI analyses are comparably well constrained, but are marginally consistent with one another. The RV analysis indicates that the components are either early M-dwarfs or late K-dwarfs, while the MECI analysis suggests that they are likely K-dwarfs. We thus conclude that this system is probably a late K-dwarf binary.

In principle, since this system has two double-lined spectra, we can use the Wilson (1941) method to estimate the binary's mass ratio (q) and barycenteric RV (V_γ), independently of its orbital phase and period. With this method, one fits a linear regression to a plot of the binary components' RVs (see Figure 7.19), and determines $q = -1/b_1$, where b_1 is the slope of the regression. Similarly, $V_\gamma = b_0/(1 - b_1)$, where b_0 is the offset of the regression. Applying this method to T-Dra0-07116, we find that $q = 0.785 \pm 0.070$, and $V_\gamma = -6.4 \pm 1.9 \text{ km s}^{-1}$ relative to GJ 182. From this, we can estimate that $M_1 = 0.50 \pm 0.15 M_\odot$ and $M_2 = 0.38 \pm 0.12 M_\odot$. However, this small value of q is inconsistent with our previous conclusions that the binary components are similar (i.e. $q \approx 1$). We therefore chose not to adopt the Wilson method results, which with only two data points are not expected to be reliable.

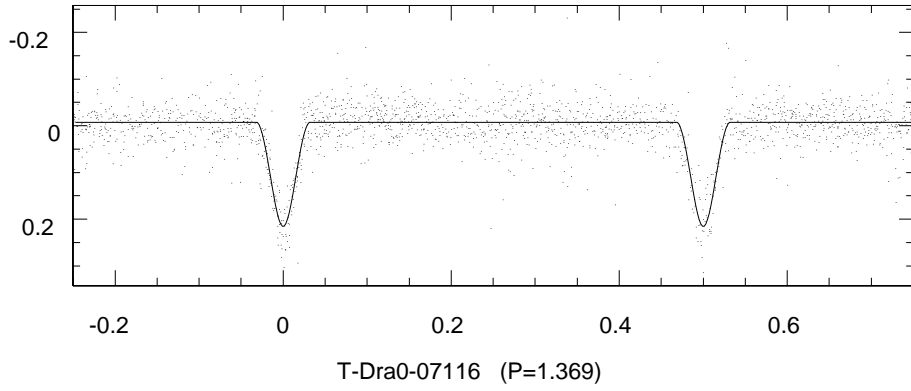
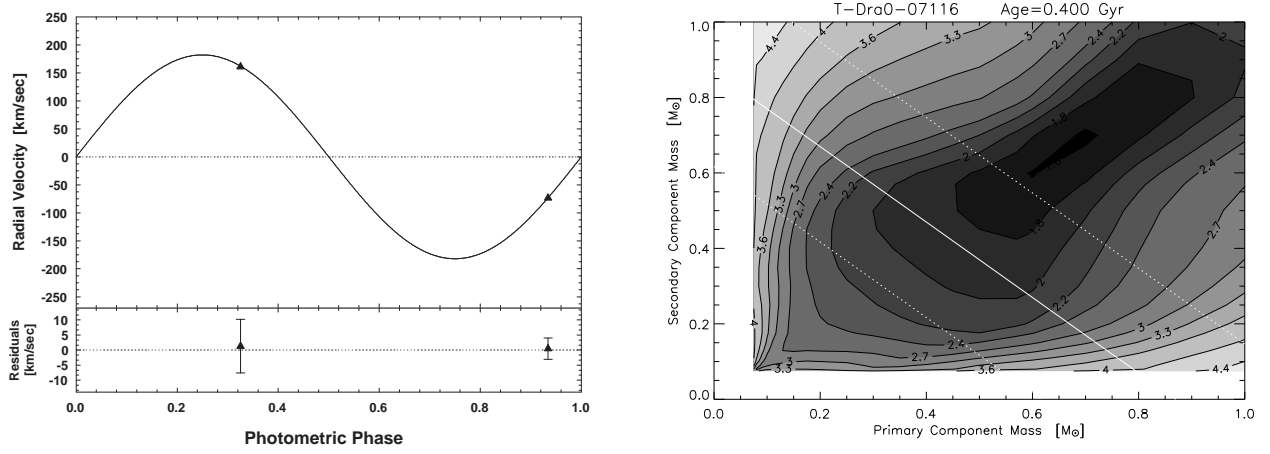


Fig. 7.17.— The phased TrES light curve (r -band), with the best-fit MECI model (solid line).



a. Phased RVs with model

b. MECI likelihood contours

Fig. 7.18.— The phased RVs of T-Dra0-07116 are shown with the best-fit circular orbit model to the difference between the component RVs.

Table 7.19. Catalog information of T-Dra0-07116

Parameter	Value
α (J2000)	17:02:53.025
δ (J2000)	55:07:47.44
USNO-B B -mag	16.805 \pm 0.2
GSC2.3 V -mag	15.33 \pm 0.16
USNO-B R -mag	14.350 \pm 0.2
2MASS J -mag	12.620 \pm 0.015
2MASS H -mag	11.964 \pm 0.015
2MASS K_s -mag	11.830 \pm 0.015
USNO-B μ_α [mas yr $^{-1}$]	-2 \pm 1
USNO-B μ_δ [mas yr $^{-1}$]	-16 \pm 1
TrES third light [R -mag]	0.258 \pm 0.049

Table 7.20. Binary parameters of T-Dra0-07116

Parameter	Symbol	Value
Orbital Period [days]	P	$1.368910^{+0.000026}_{-0.000019}$
Epoch of eclipse [HJD]	t_0	$2453517.2157^{+0.0073}_{-0.0054}$
Number of light curve data points	N_{LC}	2000
Number of RV data points	N_{RV}	2
MECI analysis primary mass [M_\odot]	M_A^{MECI}	0.71 \pm 0.21
MECI analysis secondary mass [M_\odot]	M_B^{MECI}	0.69 \pm 0.21
MECI analysis binary age [Gyr]	T^{MECI}	0.4 \pm 2.0
Relative RV amplitude [km s $^{-1}$]	$K_A + K_B$	182.03 \pm 6.63
DEBiL estimate of the projection factor	$\sin i$	0.9945 \pm 0.0072
Combined semimajor axis with projection factor [R_\odot]	$a \sin i$	$4.93^{+0.48}_{-0.52}$
Mass sum with projection factor [M_\odot]	$(M_A + M_B) \sin^3 i$	$0.86^{+0.27}_{-0.25}$

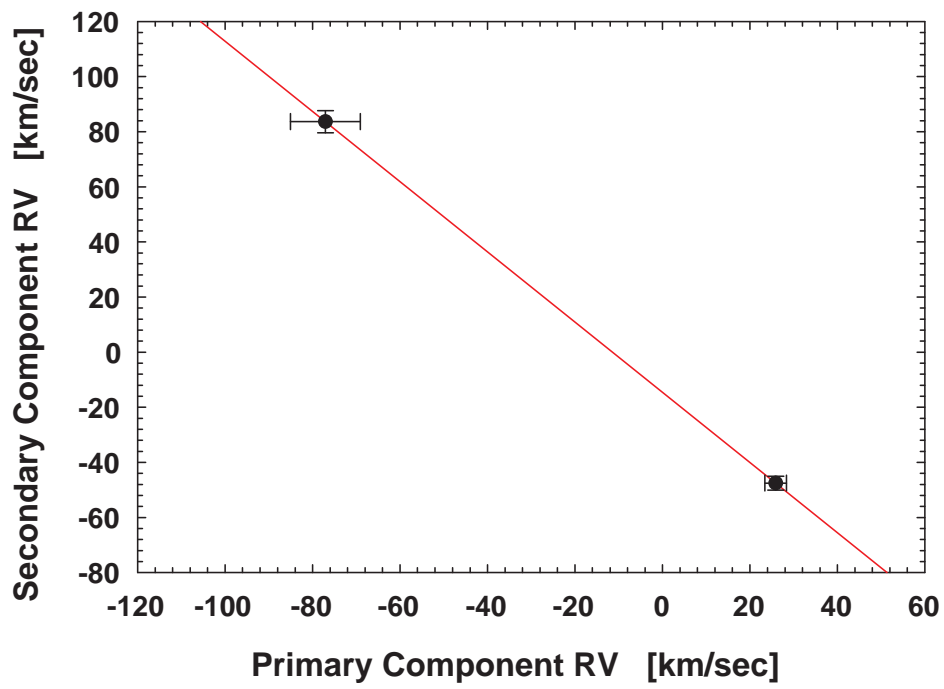


Fig. 7.19.— A linear regression of a plot of T-Dra0-07116 components' RVs. The slope and offset of this regression are used in the Wilson (1941) method to determine the binary's mass ratio and barycenteric RV.

7.3 T-Cas0-07656: A Pulsating Eclipsing Binary

T-Cas0-07656 is a pulsating EB that was located through a systematic search of previously identified EBs from ten TrES fields (see Tables 5.1 and 5.2). We selected LCs that exhibited strong residual periodicities, after subtracting the best-fit DEBiL model. To quantify these periodicities, we employed a version of the analysis of variances period finder [Schwarzenberg-Czerny (1989, 1996); see also sections §2.3.1 and §5.2], and ignored the original EB orbital period and its harmonics. After ranking the EBs by the periodicity strength of their residuals, we manually inspected the most promising candidates. Of these candidates we chose T-Cas0-07656 as the best case for an EB with a stable pulsation. The orbital period of T-Cas0-07656 was found to be $P = 1.560019 \pm 0.000044$ days, with an epoch of eclipse at $t_0 = 2453252.99121 \pm 0.00068$ HJD. However, it was not sufficiently detached to enable accurate component identification using MECI, though its colors indicate that the system is likely a late F-dwarf binary. Once the DEBiL model was subtracted from the LC, the residual was found to have a 0.1-magnitude fluctuation in the r -band. This fluctuation had a stable period of 1.9053 ± 0.0001 hours, suggesting that one of the EB components is likely a δ -Scuti type variable. As such, by comparing and combining the information gather through both the EB model and the pulsation model, one could perhaps introduce new constraints and insights into both these models.

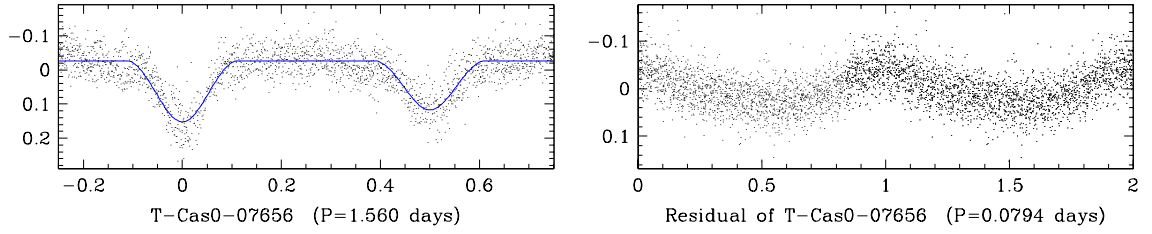


Fig. 7.20.— Left: The phased LC of T-Cas0-07656. Right: The phased residual of T-Cas0-07656, after subtracting the best-fit DEBiL model.

Table 7.21. Catalog information of T-Cas0-07656

Parameter	Value
α (J2000)	00:23:55.733
δ (J2000)	50:43:47.61
USNO-B B -mag	14.125 ± 0.2
GSC2.3 V -mag	13.03 ± 0.37
USNO-B R -mag	13.325 ± 0.2
2MASS J -mag	11.851 ± 0.015
2MASS H -mag	11.547 ± 0.015
2MASS K_s -mag	11.492 ± 0.015
UCAC μ_α [mas yr $^{-1}$]	6.0 ± 5.5
UCAC μ_δ [mas yr $^{-1}$]	-5.4 ± 5.5
TrES third light [R -mag]	0.034 ± 0.007

7.4 T-Cyg1-03378: A Binary with Large O-C Eclipse Timing Variations

T-Cyg1-03378 is an EB with large $O - C$ eclipse timing variation that was found in a systematic search through previously identified EBs from ten TrES fields (see Tables 5.1 and 5.2). In brief, for a given EB, we measured the timing of each of its eclipses, provided we had at least three observations. Fortunately, TrES operates at an effective 9-minute cadence, thus typically capturing 10-20 observations in each eclipse that is fully observed. For a given eclipse, we collect all the observations made while it was in progress, as well as a small number of out-of-eclipse observations made immediately before and after the eclipse. We then remove all outliers, and compare the remaining data to a generated DEBiL LC during this eclipse, adopting the EB parameters of the best-fit model. We compute the chi-squared value (χ^2) of the DEBiL LC for these data, and then repeat this computation in a range of time-offsets by varying the epoch of perihelion of the DEBiL model. We find the offset that minimizes the chi-squared value, and compute its 1σ uncertainty. This measurement is recorded as the timing $O - C$ during the center of the eclipse. We then repeat this procedure for all the eclipses in the given EB's LC (see Figure 7.21). Note that some LCs have long term trends that interfere with fitting some of the eclipses. To correct this, we normalize the magnitudes of the observations during an eclipse, so that the median of the out-of-eclipse observations remains constant. However, if only the ingress or egress of an eclipse are observed, then there results a degeneracy between the magnitude normalization and the eclipse offset, which produces large $O - C$ uncertainties.

Once all the $O - C$ of a given EB are recorded, we removed any linear trends, which are due to having assumed an inaccurate period¹. We then examined the de-trended timing variation for second order effects and for sinusoidal variations. EBs whose eclipse timing variations fit such a pattern significantly better than a straight line (i.e. an F-test), were selected to be examined manually. Of these selected systems, T-Cyg1-03378 was identified as having the most convincing sinusoidal timing variations.

T-Cyg1-03378 has an orbital period of $P = 2.05637567 \pm 0.00000104$ days, or possibly half that if the secondary eclipse is unseen, and an epoch of eclipse at $t_0 = 2453403.037891 \pm 0.000190$. It was found to have a 3.5-minute $O - C$ amplitude, repeating at a 25.6-day period (see Figure 7.21). This phenomenon is probably due to the orbital perturbations due to the gravitational pull of an unusually tight tertiary component. It is unlikely that such a short-period and high-amplitude timing variations would be due only to a light-time effect, as this would require a dim yet extraordinarily massive tertiary object. This system may offer a rare test case for the development of eclipse timing analysis methodologies, which may ultimately be used for extrasolar planet discovery (Holman & Murray 2005; Agol et al. 2005). Following this discovery of T-Cyg1-03378 in the TrES dataset, we obtained additional archival observations from PSST and HATNet (see Figure 7.23). These data have much larger $O - C$ uncertainties than TrES, however they also seem to show the same sinusoidal timing variations, though at certain times this pattern seems to be out of phase.

¹We also used this timing correction to fine-tune the periods of EBs (see §5.2).

Upon further examination, this EB was found to be in an optical binary, with the neighboring component being approximately 4" away. Because of their proximity, these two sources are blended in our photometric data, and we were unable to determine which of these sources is the EB. Furthermore, this blending significantly diluted the depth of the eclipses, thus explaining why the eclipse is only \sim 0.035 mag in *r*-band. We observed T-Cyg1-03378 using TRES, although we produced only single-lined spectra for both the optical binary components. This, however, may be a result of the fact that we were only able to observe this binary within a few hours if its eclipse. If the relative RVs between the components were less than a few tens of km s^{-1} , we would not be able to resolve the two template cross-correlation peaks. However, if this binary is indeed single-lined, then we may conclude that the secondary component is dim and low-mass, and thus the secondary eclipse is unseen and the correct period is half of the value listed above.

Finally, both the MECI analysis and the colors of T-Cyg1-03378 suggest that it is likely to be a late F-dwarf binary. However, the fact that this system has a significant amount of third light makes these determinations less certain. We thus strongly encourage additional observations be made of this system so that this intriguing EB may be better understood.

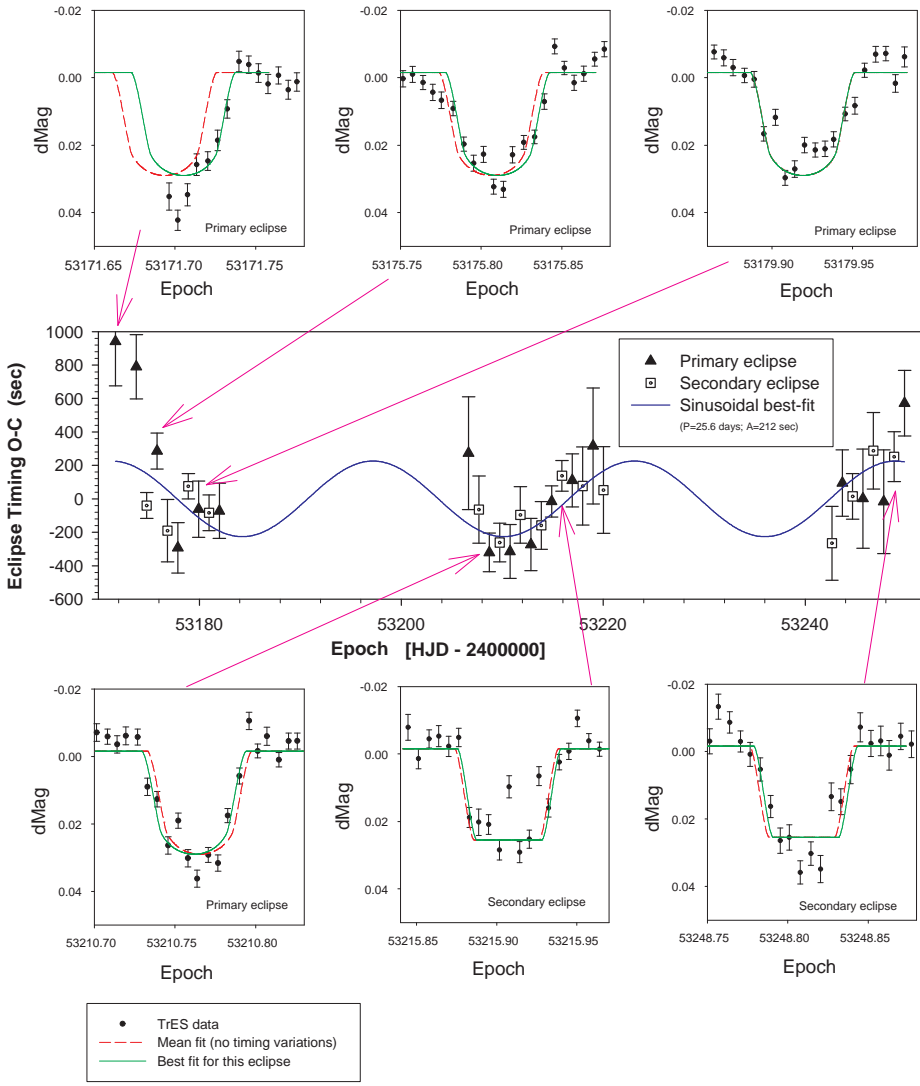


Fig. 7.21.— Measured $O - C$ eclipse timing variations found in the TrES LC of T-Cyg1-03378 (center), with details of six selected eclipses. Each of the detailed eclipses shows both the eclipse model with the best-fit offset to the individual eclipse data (dotted line), and the model whose offset is determined by extrapolating a fixed period (dashed line). The eclipse timing plot includes $O - C$ measurements of primary eclipses (triangle symbols) and $O - C$ measurements of secondary eclipses (square symbols). The solid line indicates the best-fit sinusoidal model to the TrES $O - C$ timing measurements.

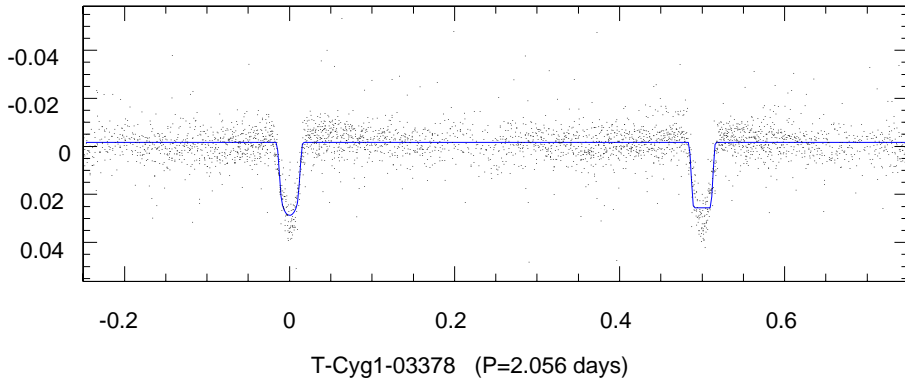


Fig. 7.22.— The phased TrES light curve (*r*-band), with the best-fit DEBiL model (solid line). The poor DEBiL model fit seems to be due to the fact that this LC contains significant third light, which dilutes the eclipses and makes them shallower than they are supposed to be.

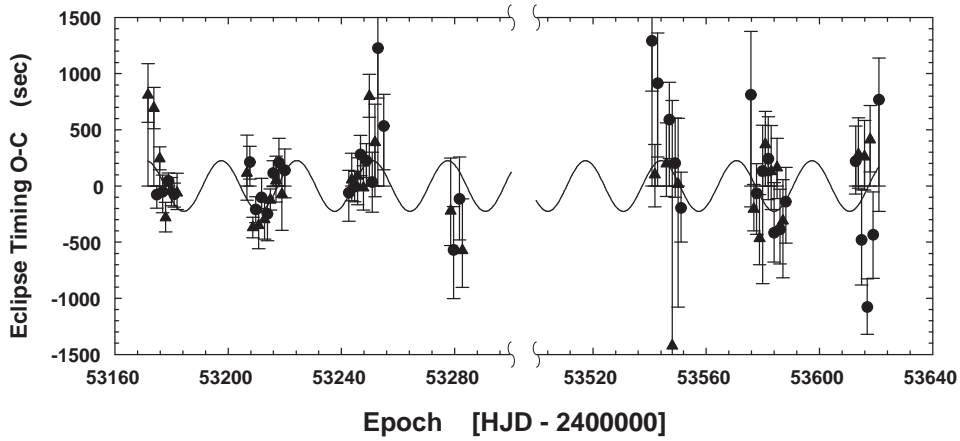


Fig. 7.23.— The $O-C$ eclipse timing variations found in a light curve constructed by combining TrES, PSST, and HATNet observations. The triangle symbols represent timing measurements of primary eclipses, while the circular symbols indicate timing measurements of secondary eclipses.

Table 7.22. Catalog information of T-Cyg1-03378

Parameter	Visual	Visual
	Component A	Component B
α (J2000)	20:10:32.489	20:10:32.832
δ (J2000)	47:33:16.95	47:33:14.64
USNO-B B -mag	12.385 \pm 0.2	...
GSC2.3 V -mag	11.99 \pm 0.33	...
USNO-B R -mag	11.470 \pm 0.2	...
CMC14 r' -mag	12.755 \pm 0.05	...
2MASS J -mag	11.643 \pm 0.015	12.164 \pm 0.015
2MASS H -mag	11.419 \pm 0.015	12.081 \pm 0.015
2MASS K_s -mag	11.351 \pm 0.015	12.029 \pm 0.015
USNO-B μ_α [mas yr $^{-1}$]	6 \pm 2	...
USNO-B μ_δ [mas yr $^{-1}$]	4 \pm 2	...
TrES third light [R -mag]	0.189 \pm 0.034	...

Table 7.23. T-Cyg1-03378 Eclipse Timing

Eclipse Type	Epoch (HJD)	O-C [sec]	Data Source
Secondary	2453171.6943	811 ⁺²⁷⁹ ₋₂₄₄	Sleuth
Secondary	2453173.7506	693 ⁺¹⁸⁵ ₋₁₈₄	Sleuth
Primary	2453174.7788	-78 ⁺⁷⁸ ₋₁₂₁	Sleuth
Secondary	2453175.8070	242 ⁺¹⁰⁶ ₋₉₉	Sleuth
Primary	2453176.8352	-52 ⁺¹⁵⁰ ₋₁₈₆	Sleuth
Secondary	2453177.8634	-281 ⁺¹³⁵ ₋₁₂₈	Sleuth
Primary	2453178.8916	44 ⁺⁷² ₋₇₂	Sleuth
Secondary	2453179.9198	-44 ⁺¹¹⁸ ₋₁₃₂	Sleuth
Primary	2453180.9480	-74 ⁺⁹⁹ ₋₁₁₆	Sleuth
Secondary	2453181.9762	-61 ⁺¹⁷³ ₋₁₅₀	Sleuth
Secondary	2453206.6527	116 ⁺³³⁹ ₋₂₄₂	Sleuth + PSST
Primary	2453207.6809	212 ⁺¹⁴¹ ₋₁₅₁	Sleuth + PSST
Secondary	2453208.7091	-371 ⁺⁹⁴ ₋₉₀	Sleuth + PSST
Primary	2453209.7373	-209 ⁺¹¹⁴ ₋₁₁₇	Sleuth
Secondary	2453210.7655	-350 ⁺¹⁵⁰ ₋₂₀₈	Sleuth
Primary	2453211.7937	-103 ⁺¹⁷¹ ₋₁₃₄	Sleuth + PSST
Secondary	2453212.8219	-298 ⁺¹⁹⁶ ₋₁₇₇	Sleuth
Primary	2453213.8501	-249 ⁺¹⁴⁴ ₋₂₃₉	Sleuth + HATNet
Secondary	2453214.8783	-123 ⁺⁹⁷ ₋₉₃	Sleuth + HATNet
Primary	2453215.9064	114 ⁺¹¹⁰ ₋₁₂₀	Sleuth + HATNet
Secondary	2453216.9346	48 ⁺²¹⁹ ₋₁₉₀	Sleuth + PSST
Primary	2453217.9628	207 ⁺²¹⁷ ₋₂₀₄	Sleuth + HATNet
Secondary	2453218.9910	-74 ⁺²²⁰ ₋₃₂₀	Sleuth + HATNet
Primary	2453220.0192	139 ⁺¹⁸⁹ ₋₂₄₄	Sleuth + HATNet
Primary	2453242.6394	-61 ⁺²⁰⁰ ₋₂₅₃	Sleuth + HATNet
Secondary	2453243.6676	55 ⁺²³⁶ ₋₁₈₆	Sleuth + HATNet
Primary	2453244.6958	-6 ⁺¹³⁵ ₋₁₃₄	Sleuth + HATNet
Secondary	2453245.7240	89 ⁺¹⁶³ ₋₂₅₆	Sleuth + HATNet
Primary	2453246.7522	280 ⁺¹⁷¹ ₋₁₈₇	Sleuth + HATNet
Secondary	2453247.7804	-16 ⁺¹⁹⁵ ₋₁₉₈	Sleuth + HATNet
Primary	2453248.8085	225 ⁺¹⁵³ ₋₁₅₀	Sleuth + HATNet
Secondary	2453249.8367	799 ⁺¹⁹⁵ ₋₁₈₆	Sleuth + HATNet
Primary	2453250.8649	34 ⁺²⁶⁵ ₋₂₆₈	HATNet
Secondary	2453251.8931	389 ⁺³⁴¹ ₋₄₈₄	HATNet
Primary	2453252.9213	1227 ⁺²⁹⁶ ₋₄₄₅	HATNet
Primary	2453254.9777	533 ⁺²⁸³ ₋₃₈₉	HATNet
Secondary	2453278.6261	-223 ⁺⁴⁷² ₋₃₀₈	HATNet
Primary	2453279.6543	-570 ⁺³⁸⁶ ₋₄₃₁	HATNet
Primary	2453281.7106	-115 ⁺³⁷⁴ ₋₃₆₅	HATNet
Secondary	2453282.7388	-574 ⁺⁴⁶⁰ ₋₃₂₉	HATNet
Primary	2453540.8147	1292 ⁺³¹⁵ ₋₄₄₇	HATNet

Table 7.23—Continued

Eclipse Type	Epoch (HJD)	O-C [sec]	Data Source
Secondary	2453541.8428	101 ⁺²⁶⁹ ₋₂₈₆	HATNet
Primary	2453542.8710	914 ⁺⁴⁴⁹ ₋₆₅₅	HATNet
Secondary	2453545.9556	197 ⁺³⁶⁶ ₋₂₈₉	HATNet
Primary	2453546.9838	590 ⁺³³³ ₋₃₄₇	HATNet
Secondary	2453548.0120	-1422 ⁺²¹⁸⁵ ₋₄₁₄	HATNet
Primary	2453549.0402	202 ⁺⁴⁰² ₋₃₀₂	HATNet
Secondary	2453550.0684	16 ⁺⁵⁸⁵ ₋₁₀₉₆	HATNet
Primary	2453551.0966	-196 ⁺³²⁰ ₋₃₀₃	HATNet
Primary	2453575.7731	811 ⁺⁵⁶⁶ ₋₉₉₆	HATNet
Secondary	2453576.8013	-205 ⁺²¹⁹ ₋₁₉₄	HATNet
Primary	2453577.8295	-67 ⁺²⁶⁶ ₋₃₆₄	HATNet
Secondary	2453578.8577	-467 ⁺³⁹¹ ₋₂₃₅	HATNet
Primary	2453579.8859	132 ⁺⁴⁰⁹ ₋₁₀₀₃	HATNet
Secondary	2453580.9141	370 ⁺²⁹⁶ ₋₂₇₇	HATNet
Primary	2453581.9423	241 ⁺³⁷⁵ ₋₃₆₂	HATNet
Secondary	2453582.9705	130 ⁺⁴⁰⁸ ₋₃₄₀	HATNet
Primary	2453583.9987	-417 ⁺⁴⁴⁷ ₋₂₅₈	HATNet
Secondary	2453585.0268	164 ⁺²⁶⁰ ₋₂₇₅	HATNet
Primary	2453586.0550	-387 ⁺³⁵⁷ ₋₃₀₆	HATNet
Secondary	2453587.0832	-310 ⁺³⁶⁶ ₋₅₀₉	HATNet
Primary	2453588.1114	-140 ⁺³⁰⁶ ₋₃₆₈	HATNet
Primary	2453612.7880	219 ⁺³¹⁵ ₋₂₉₁	HATNet
Secondary	2453613.8162	280 ⁺³²⁷ ₋₂₉₉	HATNet
Primary	2453614.8444	-481 ⁺⁴⁴⁷ ₋₄₀₁	HATNet
Secondary	2453615.8726	261 ⁺³²² ₋₂₉₇	HATNet
Primary	2453616.9008	-1078 ⁺²⁵¹ ₋₂₄₃	HATNet
Secondary	2453617.9289	413 ⁺³⁰³ ₋₂₈₈	HATNet
Primary	2453618.9571	-435 ⁺³⁸⁴ ₋₃₈₇	HATNet
Primary	2453621.0135	768 ⁺³⁷¹ ₋₉₉₅	HATNet

References

- Agol, E., Steffen, J., Sari, R., & Clarkson, W. 2005, MNRAS, 359, 567
- Aitken, R. G. 1964, *The Binary Stars* (New York: Dover Publication)
- Akerlof, C., et al. 2000, AJ, 119, 1901
- Alard, C. & Guibert, J. 1997, A&A, 326, 1
- Alard, C. & Lupton, R. H. 1998, ApJ, 503, 325
- Alard, C. 2000, A&AS, 144, 363
- Albrow, M. D., Gilliland, R. L., Brown, T. M., Edmonds, P. D., Guhathakurta, P., & Sarajedini, A. 2001, ApJ, 559, 1060
- Alcock, C., et al. 1997, AJ, 114, 326
- Alcock, C., et al. 1998, ApJ, 492, 190
- Alonso, R., et al. 2004, ApJ, 613, L153
- Andersen, J. 1991, A&A Rev., 3, 91
- Andersen, J. 1998, IAU Symp. 189: Fundamental Stellar Properties, 189, 99

- Antonello, E., Farinella, P., Guerrero, G., Mantegazza, L., & Paolicchi, P. 1980, Ap&SS, 72, 359
- Baglin, A., & The COROT Team 1998, New Eyes to See Inside the Sun and Stars, 185, 301
- Bakos, G. Á., Lázár, J., Papp, I., Sári, P., & Green, E. M. 2002, PASP, 114, 974
- Bakos, G. Á., Noyes, R. W., Kovács, G., Stanek, K. Z., Sasselov, D. D., & Domsa, I. 2004, PASP, 116, 266
- Baraffe, I., Chabrier, G., Allard, F., & Hauschildt, P. H. 1998, A&A, 337, 403
- Batten, A. H. 1973, Binary and multiple systems of stars (Oxford ; New York : Pergamon Press)
- Beaulieu, J. P., et al. 1995, A&A, 299, 168
- Becker, A. C., et al. 2008, MNRAS, 386, 416
- Berger, D. H., et al. 2006, ApJ, 644, 475
- Binnendijk, L. 1960, AJ, 65, 358
- Blake, C. H., Torres, G., Bloom, J. S., & Gaudi, B. S. 2007, ArXiv Astrophysics e-prints, arXiv:0707.3604
- Blake, C. H., Charbonneau, D., White, R. J., Torres, G., Marley, M. S., & Saumon, D. 2008, ApJ, 678, L125
- Bonanos, A. Z., et al. 2006, ApJ, 652, 313

Borucki, W. J., Koch, D. G., Dunham, E. W., & Jenkins, J. M. 1997, Planets Beyond the Solar System and the Next Generation of Space Missions, ASP Conference Series, 119, 153

Borucki, W. J., et al. 2003, Proc. SPIE, 4854, 129

Browning, M. K., & Basri, G. 2007, American Institute of Physics Conference Series, 948, 157

Carpenter, J. M. 2001, AJ, 121, 2851

Carretta, E., Gratton, R. G., Clementini, G., & Fusi Pecci, F. 2000, ApJ, 533, 215

Chabrier, G., & Baraffe, I. 2000, ARA&A, 38, 337

Chabrier, G., Gallardo, J., & Baraffe, I. 2007, A&A, 472, L17

Charbonneau, P. 1995, ApJS, 101, 309

Charbonneau, D., Brown, T. M., Latham, D. W., & Mayor, M. 2000, ApJ, 529, L45

Charbonneau, D., Brown, T. M., Burrows, A., & Laughlin, G. 2007, Protostars and Planets V (Tucson: University of Arizona Press), 701

Christian, D. J., et al. 2006, MNRAS, 372, 1117

Claret, A., & Cunha, N. C. S. 1997, A&A, 318, 187

Claret, A., & Willems, B. 2002, A&A, 388, 518

Claret, A. 1998, A&A, 335, 647

- Claret, A. 2000, A&A, 363, 1081
- Claret, A. 2003, A&A, 401, 657
- Claret, A., Diaz-Cordoves, J., & Gimenez, A. 1995, A&AS, 114, 247
- Cox, A. N. 2000, Allen's astrophysical quantities (New York: AIP Press; Springer)
- Crawford, J. A. 1955, ApJ, 121, 71
- Creevey, O. L., et al. 2005, ApJ, 625, L127
- Croots, A. P. S. 1992, ApJ, 399, L43
- Danby, J. M. A. 1964, Fundamentals of Celestial Mechanics (New York: Macmillan)
- Darwin, G. H. 1879, The Observatory, 3, 79
- Davidge, T. J., & Milone, E. F. 1984, ApJS, 55, 571
- de Loore, C. & Doom, C. 1992, Structure and Evolution of Single and Binary Stars, Astrophysics and Space Science Library, Vol. 179 (Dordrecht: Kluwer)
- Deeg, H. J., Doyle, L. R., Kozhevnikov, V. P., Blue, J. E., Martín, E. L., & Schneider, J. 2000, A&A, 358, L5
- Delfosse, X., Forveille, T., Perrier, C., & Mayor, M. 1998, A&A, 331, 581
- Delfosse, X., Forveille, T., Mayor, M., Burnet, M., & Perrier, C. 1999, A&A, 341, L63

Derekas, A., Kiss, L. L., & Bedding, T. R. 2007, ArXiv Astrophysics e-prints, arXiv:astro-ph/0703137

Devor, J. 2004, American Astronomical Society Meeting Abstracts, 205

Devor, J. 2005, ApJ, 628, 411

Devor, J., & Charbonneau, D. 2006a, Ap&SS, 304, 351

Devor, J., & Charbonneau, D. 2006b, ApJ, 653, 648

Devor, J., Charbonneau, D., O'Donovan, F. T., Mandushev, G., & Torres G. 2008, AJ, 135, 850

Dunham, E. W., Mandushev, G. I., Taylor, B. W., & Oetiker, B. 2004, PASP, 116, 1072

Duquennoy, A., & Mayor, M. 1991, A&A, 248, 485

Eggleton, P. P. 1983, ApJ, 268, 368

Etzel, P. B. 1981, Photometric and Spectroscopic Binary Systems (Dordrecht: Reidel), 111

Etzel, P. B. 1991, International Amateur-Professional Photoelectric Photometry Communications, 45, 25

Evans, D. W., Irwin, M. J., & Helmer, L. 2002, A&A, 395, 347

Farinella, P., Luzny, F., Mantegazza, L., & Paolicchi, P. 1979, ApJ, 234, 973

Galan, M. J., & Cobos, F. J. 1987, Revista Mexicana de Astronomia y Astrofisica, 14, 767

- Gilmore, G., Perryman, M. A. C., Lindegren, L., et al. 1998, Proc. SPIE Conf., 3350, 541
- Girardi, L., Grebel, E. K., Odenkirchen, M., & Chiosi, C. 2004, A&A, 422, 205
- Gorda, S. Y. & Svechnikov, M. A. 1998, Astronomy Reports, 42, 793
- Gratton, R. G., Bragaglia, A., Carretta, E., Clementini, G., Desidera, S., Grundahl, F., & Lucatello, S. 2003, A&A, 408, 529
- Gray, D. F. 1992, The Observation and Analysis of Stellar Photospheres (Cambridge, UK: Cambridge Univ. Press), 368
- Grundahl, F., Stetson, P. B., & Andersen, M. I. 2002, A&A, 395, 481
- Guinan, E. F., Bradstreet, D. H., & Dewarf, L. E. 1996, ASP Conf. Ser. 90: The Origins, Evolution, and Destinies of Binary Stars in Clusters, 90, 196
- Hebb, L., Wyse, R. F. G., Gilmore, G., & Holtzman, J. 2006, AJ, 131, 555
- Henry, G. W., Marcy, G. W., Butler, R. P., & Vogt, S. S. 2000, ApJ, 529, L41
- Holland, J. H. 1975, Adaptation in Natural and Artificial Systems (Ann Arbor, MI: University of Michigan Press)
- Holman, M. J., & Murray, N. W. 2005, Science, 307, 1288
- Horne, K. 1986, PASP, 98, 609
- Hut, P. 1981, A&A, 99, 126
- Iben, I., Jr., & Tutukov, A. V. 1984, ApJS, 54, 335

- Kaiser, N., et al. 2002, Proc. SPIE, 4836, 154
- Kallrath, J., & Milone, E. F. 1999, Eclipsing binary stars : modeling and analysis (New York : Springer), 169
- Kaluzny, J., Stanek, K. Z., Krockenberger, M., Sasselov, D. D., Tonry, J. L., & Mateo, M. 1998, AJ, 115, 1016
- Kim, Y., Demarque, P., Yi, S. K., & Alexander, D. R. 2002, ApJS, 143, 499
- Kirkpatrick, S., Gelatt, C. D., & Vecchi, M. P. 1983, Science, 220, 671
- Kleinmann, S. G., et al. 1994, Ap&SS, 217, 11
- Kopal, Z. 1959, The International Astrophysics Series (London: Chapman & Hall)
- Kopal, Z. 1990, Mathematical Theory of Stellar Eclipses (Dordrecht, Netherlands: Kluwer Academic Publishers)
- Kovács, G., Zucker, S., & Mazeh, T. 2002, A&A, 391, 369
- Kron, G. E. 1952, ApJ, 115, 301
- Kukarkin B. V., Parengo P. P. 1948, General Catalogue of Variable Stars, Nauka Publ. House, Moscow
- Kurucz, R. L. 1992, IAU Symp. 149: The Stellar Populations of Galaxies, 149, 225
- Lacy, C. H. S., Torres, G., Claret, A., Stefanik, R. P., Latham, D. W., & Sabby, J. A. 2000, AJ, 119, 1389
- Lacy, C. H. S., Torres, G., Claret, A., & Sabby, J. A. 2002, AJ, 123, 1013

- Lacy, C. H. S., Torres, G., Claret, A., & Sabby, J. A. 2003, AJ, 126, 1905
- Lacy, C. H. 1977a, ApJ, 218, 444
- Lacy, C. H. 1977b, ApJS, 34, 479
- Lane, B. F., Boden, A. F., & Kulkarni, S. R. 2001, ApJ, 551, L81
- Latham, D. W. 1992, ASP Conf. Ser. 32: IAU Colloq. 135: Complementary Approaches to Double and Multiple Star Research, 32, 110
- Liu, Q.-Y., & Yang, Y.-L. 2003, Chinese Journal of Astronomy and Astrophysics, 3, 142
- López-Morales, M., & Ribas, I. 2005, ApJ, 631, 1120
- López-Morales, M., Orosz, J. A., Shaw, J. S., Havelka, L., Arevalo, M. J., McIntyre, T., & Lazaro, C. 2006, ArXiv Astrophysics e-prints, arXiv:astro-ph/0610225
- López-Morales, M. 2007, ApJ, 660, 732
- Maceroni, C., & Montalbán, J. 2004, A&A, 426, 577
- Maceroni, C., & Rucinski, S. M. 1997, PASP, 109, 782
- Mallén-Ornelas, G., Seager, S., Yee, H. K. C., Minniti, D., Gladders, M. D., Mallén-Fullerton, G. M., & Brown, T. M. 2003, ApJ, 582, 1123
- Mandel, K., & Agol, E. 2002, ApJ, 580, L171
- Mandushev, G., et al. 2005, ApJ, 621, 1061

- Maxted, P. F. L., Marsh, T. R., Morales-Rueda, L., Barstow, M. A., Dobbie, P. D., Schreiber, M. R., Dhillon, V. S., & Brinkworth, C. S. 2004, MNRAS, 355, 1143
- Maxted, P. F. L., O'Donoghue, D., Morales-Rueda, L., Napiwotzki, R., & Smalley, B. 2007, MNRAS, 376, 919
- Mazeh, T. 2008, EAS Publications Series, 29, 1
- Mazeh, T., et al. 2000, ApJ, 532, L55
- Mazeh, T., Tamuz, O., North, P. 2005, Close Binaries in the 21st Century: New Opportunities and Challenges, 45
- Mazeh, T., Tamuz, O., & North, P. 2006, MNRAS, 367, 1531
- McCullough, P. R., et al. 2006, ApJ, 648, 1228
- McLaughlin, D. B. 1924, ApJ, 60, 22
- McLean, I. S., et al. 1998, Proc. SPIE, 3354, 566
- McLean, I. S., Graham, J. R., Becklin, E. E., Figer, D. F., Larkin, J. E., Levenson, N. A., & Teplitz, H. I. 2000, Proc. SPIE, 4008, 1048
- Meibom, S., & Mathieu, R. D. 2005, ApJ, 620, 970
- Mergenthaler, J. 1950, Wroclaw Cont., 4, 1
- Metcalfe, T. S. 1999, AJ, 117, 2503
- Metcalfe, T. S., Mathieu, R. D., Latham, D. W., & Torres, G. 1996, ApJ, 456, 356

- Milone, E. F. 1986, ApJS, 61, 455
- Mkrtichian, D. E., et al. 2004, A&A, 419, 1015
- Monet, D. G., et al. 2003, AJ, 125, 984
- Montes, D., López-Santiago, J., Gálvez, M. C., Fernández-Figueroa, M. J., De Castro, E., & Cornide, M. 2001, MNRAS, 328, 45
- Morrison, J. E., Röser, S., McLean, B., Bucciarelli, B., & Lasker, B. 2001, AJ, 121, 1752
- Nelder, J. A., & Mead 1965, R., Computer Journal, 7, 308
- Nelson, B., & Davis, W. D. 1972, ApJ, 174, 617
- North, P., & Zahn, J.-P. 2003, A&A, 405, 677
- O'Connell, D. J. K. 1951, Publications of the Riverview College Observatory, 2, 85
- O'Donovan, F. T., Charbonneau, D., & Kotredes, L. 2004, The Search for Other Worlds, AIP Conference Proceedings, 713, 169
- O'Donovan, F. T., et al. 2006, ApJ, 644, 1237
- O'Donovan, F. T., et al. 2007, ApJ, 662, 658
- Otten, R. H. J. M., & van Ginneken, L.P.P.P. 1989, The Annealing Algorithm (Dordrecht: Kluwer)
- Paczynski, B. 1986, ApJ, 304, 1

- Paczynski, B. 1997, The Extragalactic Distance Scale, Space Telescope Science Institute Series (Cambridge, UK: Cambridge Univ. Press), 273
- Percival, S. M., Salaris, M., van Wyk, F., & Kilkenny, D. 2002, ApJ, 573, 174
- Perrin, G. 2003, Ap&SS, 286, 197
- Phillips, A. C., & Davis, L. E. 1995, ASP Conf. Ser. 77, Astronomical Data Analysis and Software System IV (San Francisco: ASP), 297
- Pilecki, B., & Szczygiel, D. M. 2007, Informational Bulletin on Variable Stars, 5768, 1
- Pizzolato, N., Maggio, A., Micela, G., Sciortino, S., & Ventura, P. 2003, A&A, 397, 147
- Pojmanski, G. 1997, Acta Astronomica, 47, 467
- Popper, D. M. 1981, Revista Mexicana de Astronomia y Astrofisica, 6, 99
- Popper, D. M. & Etzel, P. B. 1981, AJ, 86, 102
- Pourbaix, D., et al. 2004, A&A, 424, 727
- Press, W. H., Teukolsky, S. A., Vetterling, W. T., & Flannery, B. P. 1992, Numerical Recipes in C. The Art of Scientific Computing (Cambridge, UK: Cambridge Univ. Press)
- Prša, A., & Zwitter, T. 2005, ApJ, 628, 426
- Reid, N. 1998, AJ, 115, 204
- Ribas, I. 2003, A&A, 398, 239

- Ribas, I. 2006, Ap&SS, 304, 87
- Rossiter, R. A. 1924, ApJ, 60, 15
- Russell, H. N. 1912a, ApJ, 35, 315
- Russell, H. N. 1912b, ApJ, 36, 54
- Russell, I. H. N., & Shapley, H. 1912a, ApJ, 36, 239
- Russell, H. N., & Shapley, H. 1912b, ApJ, 36, 385
- Salim, S., & Gould, A. 2003, ApJ, 582, 1011
- Samus, N. N. 2006, Astronomical and Astrophysical Transactions, 25, 223
- Schlegel, D. J., Finkbeiner, D. P., & Davis, M. 1998, ApJ, 500, 525
- Schwarzenberg-Czerny, A. 1989, MNRAS, 241, 153
- Schwarzenberg-Czerny, A. 1996, ApJ, 460, L107
- Seager, S. & Mallén-Ornelas, G. 2003, ApJ, 585, 1038
- Skrutskie, M. F., et al. 2006, AJ, 131, 1163
- Southworth, J., Maxted, P. F. L., & Smalley, B. 2004a, MNRAS, 351, 1277
- Southworth, J., Zucker, S., Maxted, P. F. L., & Smalley, B. 2004b, MNRAS, 355, 986
- Southworth, J., Smalley, B., Maxted, P. F. L., Claret, A., & Etzel, P. B. 2005, MNRAS, 363, 529

- Stebbing, J. 1910, ApJ, 32, 185
- Struve, O. 1948, PASP, 60, 160
- Sumi, T. 2004, MNRAS, 349, 193
- Szalay, A. & Gray, J. 2001, Science, 293, 2037
- Szentgyorgyi, A. H., & Fűrész, G. 2007, Revista Mexicana de Astronomia y Astrofisica Conference Series, 28, 129
- Ségransan, D., Kervella, P., Forveille, T., & Queloz, D. 2003, A&A, 397, L5
- Tamuz, O., Mazeh, T., & North, P. 2006, MNRAS, 367, 1521
- Tassoul, J.-L. 1988, ApJ, 324, L71
- Torres, G., & Ribas, I. 2002, ApJ, 567, 1140
- Torres, G., Lacy, C. H., Marschall, L. A., Sheets, H. A., & Mader, J. A. 2006, ApJ, 640, 1018
- Tsesevich, V. P. 1973, Eclipsing Variable Stars (New York: J. Wiley)
- Tyson, J. A. 2002, Proc. SPIE, 4836, 10
- Udalski, A. 2003, Acta Astronomica, 53, 291
- Udalski, A., et al. 1994, Acta Astronomica, 44, 165
- Udalski, A., Kubiak, M., & Szymanski, M. 1997, Acta Astronomica, 47, 319
- Udalski, A., et al. 2002, Acta Astronomica, 52, 217

- Vallée, J. P. 2005, AJ, 130, 569
- Vanderbilt, D., & Louie, S. G. 1983, Journal of Comp. Phys., 56, 259
- Voges et al. 1999, A&AS, 349, 389
- Wambsganss, J. 2006, Saas-Fee Advanced Course 33: Gravitational Lensing: Strong, Weak and Micro (Berlin: Springer), 453
- Wilson, O. C. 1941, ApJ, 93, 29
- Wilson, R. E. 1979, ApJ, 234, 1054
- Wilson, R. E. 1994, PASP, 106, 921
- Wilson, R. E. & Devinney, E. J. 1971, ApJ, 166, 605
- Wozniak, P. R. 2000, Acta Astronomica, 50, 421
- Wozniak, P. R., Udalski, A., Szymanski, M., Kubiak, M., Pietrzynski, G., Soszynski, I., & Zebrun, K. 2002, Acta Astronomica, 52, 129
- Wyithe, J. S. B. & Wilson, R. E. 2001, ApJ, 559, 260
- Wyithe, J. S. B. & Wilson, R. E. 2002, ApJ, 571, 293
- Yi, S., Demarque, P., Kim, Y.-C., Lee, Y.-W., Ree, C. H., Lejeune, T., & Barnes, S. 2001, ApJS, 136, 417
- Young, T. B., Hidas, M. G., Webb, J. K., Ashley, M. C. B., Christiansen, J. L., Derekas, A., & Nutto, C. 2006, MNRAS, 370, 1529

Zacharias, N., Urban, S. E., Zacharias, M. I., Wycoff, G. L., Hall, D. M., Monet, D. G., & Rafferty, T. J. 2004, AJ, 127, 3043

Zahn, J.-P. 1975, A&A, 41, 329

Zahn, J.-P. 1977, A&A, 57, 383

Zahn, J.-P. 1978, A&A, 67, 162

Zahn, J.-P. 1994, A&A, 288, 829

Zahn, J.-P., & Bouchet, L. 1989, A&A, 223, 112

Zucker, S. 2003, MNRAS, 342, 1291

Zucker, S., & Alexander, T. 2007, ApJ, 654, L83

Zucker, S., Mazeh, T., & Alexander, T. 2007, ApJ, 670, 1326